



**UNIVERSIDADE FEDERAL DO CEARÁ**  
**CENTRO DE TECNOLOGIA**  
**DEPARTAMENTO DE ENGENHARIA AMBIENTAL E HIDRÁULICA**  
**PROGRAMA DE PÓS-GRADUAÇÃO EM ENGENHARIA CIVIL**

**KONSTANTINOS POLEMIS JÚNIOR**

**EMPIRICAL METHODS TO ESTIMATE MECHANICAL PROPERTIES OF  
JOINTED ROCK MASSES AND A PROPOSAL FOR A GEOPHYSICAL  
METHOD TO ASSIST GEOLOGICAL DISCONTINUITY  
CHARACTERIZATION**

**FORTALEZA**

**2019**

KONSTANTINOS POLEMIS JÚNIOR

EMPIRICAL METHODS TO ESTIMATE MECHANICAL PROPERTIES OF  
JOINTED ROCK MASSES AND A PROPOSAL FOR A GEOPHYSICAL METHOD  
TO ASSIST GEOLOGICAL DISCONTINUITY CHARACTERIZATION

Dissertação apresentada ao Programa de Pós-Graduação em Engenharia Civil da Universidade Federal do Ceará, como requisito parcial à obtenção do Título de Mestre em Engenharia Civil. Área de concentração: Geotecnia.

Orientador: Prof. Dr. Francisco Chagas da Silva Filho.

Coorientador: Prof. Dr. Francisco Pinheiro Lima Filho.

FORTALEZA

2019

Dados Internacionais de Catalogação na Publicação  
Universidade Federal do Ceará  
Biblioteca Universitária  
Gerada automaticamente pelo módulo Catalog, mediante os dados fornecidos pelo(a) autor(a)

---

- P821e Polemis Júnior, Konstantinos.  
Empirical methods to estimate mechanical properties of jointed rock masses and a proposal for a geophysical method to assist geological discontinuity characterization / Konstantinos Polemis Júnior. – 2019.  
205 f. : il. color.
- Dissertação (mestrado) – Universidade Federal do Ceará, Centro de Tecnologia, Programa de Pós-Graduação em Engenharia Civil: Geotecnia, Fortaleza, 2019.  
Orientação: Prof. Dr. Francisco Chagas Silva Filho.  
Coorientação: Prof. Dr. Francisco Pinheiro Lima Filho.
1. Rock mass classification systems. 2. Rock mass strength. 3. Rock mass deformation modulus. 4. Ground-penetrating radar (GPR). I. Título.

---

CDD 624.15

KONSTANTINOS POLEMIS JÚNIOR

EMPIRICAL METHODS TO ESTIMATE MECHANICAL PROPERTIES OF  
JOINTED ROCK MASSES AND A PROPOSAL FOR A GEOPHYSICAL METHOD  
TO ASSIST GEOLOGICAL DISCONTINUITY CHARACTERIZATION

Dissertation presented to the Graduate Program in Civil Engineering of the Federal University of Ceará, as a partial requirement to obtain a master's degree in Civil Engineering. Concentration area: Geotechnics.

Approved in: 29/11/2019.

EXAMINATION BOARD

---

Prof. Francisco Chagas da Silva Filho, Ph.D. (Advisor)  
Federal University of Ceará (UFC)

---

Prof. Francisco Pinheiro Lima Filho, Ph.D. (Co-advisor)  
Federal University of Rio Grande do Norte (UFRN)

---

Prof. Silvrano Adonias Dantas Neto, Ph.D. (Internal Examiner)  
Federal University of Ceará (UFC)

---

Prof. Marcos Aurélio Marques Noronha, Ph.D. (External Examiner)  
Federal University of Santa Catarina (UFSC)

This dissertation is dedicated to all my friends and family, especially to my mother, Gláucia Polemis, and my grandfather, Francisco das Chagas (*in memoriam*).

## ACKNOWLEDGMENTS

To my advisor, Prof. Dr. Francisco Chagas da Silva Filho, for the continuous support of my dissertation study and related research, for his patience, motivation, and immense knowledge. His guidance helped me in all the time of research and writing of this dissertation. Thank you, professor!

To my co-advisor, Prof. Dr. Francisco Pinheiro Lima Filho, for embracing this research together with me and Prof. Chagas, giving me all the support necessary to achieve the desired results during this dissertation. There are not enough words to measure how grateful I am for all the learning I have had with you. My truly thank you!

To the National Council for Scientific and Technological Development (CNPq), for their financial support.

To the participants of the examining board, Prof. Dr. Silvrano Adonias Dantas (internal examiner) and Prof. Dr. Neto Prof. Marcos Aurélio Marques Noronha (external examiner), thank you for the availability and time spent on reading this dissertation study.

To the researchers of the Stratigraphic Analysis Laboratory (LAE), headed by Prof. Pinheiro, in particular, to the researchers João Andrade dos Reis Jr, Washington Luiz Evangelista Teixeira, and Yoe Alain Reyes Pérez, who guided me during the GPR data acquisition and its processing.

To my lovely companion, Larissa Zaira, that gave me all the support from the backstage of this dissertation, especially at times when things didn't go the way I wanted them to. Thank you, darling!

To all my classmates for sharing amazing moments of learning and friendship during our master program time.

To the researchers from the Climate Risk Management Group (GRC), headed by Prof. Francisco de Assis, that received me in their laboratory during the last months of this research. I am very grateful to have spent this last research period with all of you.

Last but not least, I would like to thank my family: my mother, Gláucia Polemis, and to my brother, Leonidas Batista, for supporting me spiritually throughout writing this dissertation and my life in general.

“Education is the great engine of personal development. It is through education that the daughter of a peasant can become a doctor, that the son of a mine worker can become the head of the mine, that a child of farm workers can become the president of a great nation. It is what we make out of what we have, not what we are given, that separates one person from another.”

**Nelson Rolihlahla Mandela**

## RESUMO

A engenharia das rochas é a ciência aplicada as atividades humanas utilizando as rochas como material de engenharia para diversos fins, tais como o suporte para túneis, mineração a céu aberto, escavações subterrâneas, poços de mineração, entre outras. Tem como base a mecânica das rochas, que estuda o comportamento mecânico das rochas em respostas a mudanças em seu campo de tensões causados por forças sobre elas, onde leva-se em consideração as características da parte intacta das rochas e as discontinuidades geológicas que possam ocorrer em seu meio. Por conta de suas características anisotrópicas e heterogêneas, que se manifestam principalmente por conta do efeito escala existente em maciços fraturados, estimar as propriedades mecânicas desse geomaterial pode ser visto com uma tarefa complexa e onerosa em comparação a outros materiais utilizados pela engenharia. Como alternativa, métodos empíricos baseados em sistemas de classificações de maciços rochosos (RMCS), como por exemplo o RMR, Q e o GSI, vem sendo amplamente utilizados pela engenharia das rochas na prática para estimar esses parâmetros, mais especificamente a compressão uniaxial e o módulo de deformação de maciços fraturados, para fins de modelagens numéricas. Tendo em vista a quantidade numerosa de modelos propostos, esse trabalho avaliou-se os métodos mais recorrentes na literatura baseados nos índices de RQD, RMR, Q e GSI, avaliando seus comportamentos para 46 cenários de maciços rochosos diferentes, previamente caracterizados e classificados. Como parte dos resultados obtidos durante as análises comparativas, pode-se perceber que as correlações não normalizadas superestimaram os valores dos módulos de deformação em comparação as correlações normalizadas, principalmente para maciços rochosos com certa qualidade, onde a diferença foi mais acentuada. Ao final desse trabalho foi proposto também uma metodologia para auxiliar na caracterização de maciços rochosos em campo, através do uso do radar de penetração no solo (GPR), para fins de classificações. Como estudo de caso, realizou-se uma análise comparativa entre as respostas obtidas através de um mapeamento geológico das fraturas de um afloramento rochoso na região da barragem do Castanhão, auxiliado por um veículo aéreo não tripulado (VANT), com as informações das discontinuidades subterrâneas do maciço imageadas pelo GPR. Com base nos resultados, pode-se verificar que após os processamentos básicos e avançados dos dados coletados em campo pelo GPR, o método geofísico apresenta-se como uma potencial ferramenta para visualização de fraturas subterrâneas para fins de caracterização.



**Palavras-chave:** Sistemas de classificações de maciços rochosos. Resistência de maciço rochosos. Módulo de deformação de maciços rochosos. Radar de penetração no solo (GPR).

## ABSTRACT

Rock engineering is the applied science related to human activities using the rock as an engineering material for different purposes, such as tunnels support, open-pit mine, underground excavation, mining shafts, among others. Its foundation lies in rock mechanics, which studies the mechanical behavior of this geomaterial in response to any change in the stress field of the rocks caused by the forces acting on them, taking into account the individual characteristics of the intact rock and the geological discontinuities within its medium. Because of the anisotropic and heterogeneous characteristics of the material, arising especially from the scale effect existing in jointed rock masses, estimating their mechanical properties can be seen as a complex and expensive task. As an alternative, empirical methods based on rock mass classification systems (RMCS), e.g., RMR, Q and GSI systems, have been widely used for rock engineering practice purposes, including for deriving the compressive strength,  $\sigma_{cm}$ , and deformation modulus of the material,  $E_{rm}$ , especially for numerical modeling. Once there are a significant number of empirical methods suggested for this purpose, this study evaluated the most known correlations based on the RQD index, RMR number, Q-value, and GSI number, using 46 scenarios of different rock mass quality previously characterized and classified. As part of the results found, it was noticed that non-normalized correlations yielded overestimated values of deformation modulus in direct comparison to the normalized one, especially for better rock mass quality scenarios, where the difference was way more significative. This study also proposed the usage of a geophysical technique, the ground-penetrating radar (GPR), as an auxiliary survey tool for in situ rock mass characterization, for rock mass classification purposes. As a case of study, a comparative analysis between a geological mapping of discontinuities identified using an unmanned aerial vehicle (UAV) from an outcrop and the underground discontinuity imaging using the GPR was conducted in the Castanhão dam region. Based on the results derived after basic and advanced processing of the raw data collected in loco, it was confirmed the capacity of the geophysical method for mapping discontinuities with high resolution for rock mass characterization purposes.

**Keywords:** Rock mass classification systems. Rock mass strength. Rock mass deformation modulus. Ground-penetrating radar (GPR).

## LIST OF FIGURES

<b>Figure 2.1</b>	- Illustration of the scale effect in rocks in a hypothetical rock mass surrounding an underground excavation .....	25
<b>Figure 2.2</b>	- Illustration of the stress-strain curve of a brittle (left) and ductile (right) behavior under the uniaxial compression test .....	26
<b>Figure 2.3</b>	- Range of Young's modulus of some rock types .....	28
<b>Figure 2.4</b>	- Range of Poisson's ratio of some rock types .....	28
<b>Figure 2.5</b>	- Two-dimensional schematic representation of the parameters that describe the discontinuities within a rock mass .....	30
<b>Figure 2.6</b>	- Definition of dip and dip direction in an isometric view of plane ....	31
<b>Figure 2.7</b>	- Illustration of apparent measurement from a rock face .....	33
<b>Figure 2.8</b>	- Typical roughness profiles .....	35
<b>Figure 2.9</b>	- Standard roughness profiles for Joint Roughness Coefficient (JRC) .....	36
<b>Figure 2.10</b>	- Procedure for measurement of rock quality designation RQD .....	44
<b>Figure 2.11</b>	- Relationship between RQD and mean discontinuity spacing .....	45
<b>Figure 2.12</b>	- Relationship between RQD and mean discontinuity frequency .....	45
<b>Figure 2.13</b>	- Ratings from strength of intact rock in the RMR system .....	49
<b>Figure 2.14</b>	- Ratings for RQD in the RMR system .....	49
<b>Figure 2.15</b>	- Ratings for discontinuity spacing in the RMR system .....	50
<b>Figure 2.16</b>	- Input chart for combined rating of the RQD and discontinuity spacing based on the rock discontinuity density .....	50
<b>Figure 2.17</b>	- The Geological Strength Index (GSI) chart designed by Hoek and Marinos (2000) .....	61
<b>Figure 3.1</b>	- Correlation between $E_{rm}/E_i$ and RQD proposed by Coon and Merritt (1970) .....	66
<b>Figure 3.2</b>	- Correlations between $E_{rm}/E_i$ and RQD suggested by AASHTO (2002) .....	66
<b>Figure 3.3</b>	- Correlations between $E_{rm}/E_i$ and RQD proposed by Zhang and Einstein (2004) .....	67
<b>Figure 3.4</b>	- Graphical comparison between the empirical methods developed by Kulhawy and Goodman (1987), AASHTO (2002) and Zhang (2010) to estimate rock mass strength using RQD .....	68

<b>Figure 3.5</b>	- Correlations proposed by Bieniawski (1978) to estimate $E_{rm}$ based on the RMR .....	71
<b>Figure 3.6</b>	- Graphical comparison between the correlations proposed by Bieniawski (1978) and Serafim and Pereira to estimate $E_{rm}$ based on the RMR .....	72
<b>Figure 3.7</b>	- Graphical representation of the correlations developed by Nicholson and Bieniawski (1990), left, and Mitri et al. (1994), right, varying $E_i$ from 20 to 80 GPa .....	73
<b>Figure 3.8</b>	- Graphical comparison between the correlations proposed by Read et al. (1999) and Serafim and Pereira (1983) to estimate $E_{rm}$ based on the RMR values .....	74
<b>Figure 3.9</b>	- Relationship between $E_{rm}$ and RMR suggested by Gokceoglu et al. (2003) using regression analysis on a new database .....	74
<b>Figure 3.10</b>	- Graphical representation of the correlation proposed for Lowson and Bieniawski (2013) to estimate $E_{rm}$ for $RMR > 56$ .....	76
<b>Figure 3.11</b>	- Graphical representation of several correlations proposed to estimate $\sigma_{cm}/\sigma_{ci}$ using RMR plotted against the data derived from Aydan and Kawamoto (2000) .....	78
<b>Figure 3.12</b>	- Graphical representation of the correlation proposed by Barton et al. (1980, 1981) to estimate $E_{rm}$ using Q-value .....	80
<b>Figure 3.13</b>	- Graphical comparison between the correlations proposed by Barton (1995), Bieniawski (1978) and Serafim and Pereira (1983) to estimate the deformation modulus of rock mass based on the RMR and Q-value .....	81
<b>Figure 3.14</b>	- Modified version of Barton's (1995) correlation proposed by Barton (2002) using the range of the unconfined compressive strength ( $\sigma_{ci}$ , UCS) grades from Table 2.8 .....	82
<b>Figure 3.15</b>	- Graphical representation of the correlation proposed by Hoek and Brown (1997) to estimate $E_{rm}$ using GSI for different values of UCS .....	84
<b>Figure 3.16</b>	- Plot of the simplified Hoek and Diederichs equation in relation to the measured rock mass modulus data from a) Hoek and Diederichs (2006) and b) Bieniawski (1978) and Serafim (1978) .....	87
<b>Figure 3.17</b>	- Generalized Hoek and Diederichs equation plotted against the normalized in situ rock mass deformation modulus presented by Hoek and Diederichs (2006) .....	87
<b>Figure 3.18</b>	- Plotting of the unconfined compressive strength of rock mass data presented by Aydan and Kawamoto (2000) against the correlation proposed by a) Hoek <i>et al.</i> (2002) and b) Hoek (2004, apud Zhang, 2010) .....	90
<b>Figure 3.19</b>	- Box plot graph of estimated $E_{rm}$ values of scenarios from SG-I .....	94
<b>Figure 3.20</b>	- Box plot graph of estimated $E_{rm}$ values of scenarios from SG-II .....	95

<b>Figure 3.21</b>	- Box plot graph of estimated $E_{rm}$ values of scenarios from SG-III ...	95
<b>Figure 3.22</b>	- Estimated average values of rock mass deformation for non-normalized (NN) and normalized (N) empirical correlations .....	96
<b>Figure 3.23</b>	- $E_{rm}$ values estimated using RQD (a), RMR (b), Q (c) and GSI (d) - based methods plotted with the average results from all methods .	98
<b>Figure 3.24</b>	- Box plot graph of estimated $\sigma_{cm}$ values of scenarios from SG-I .....	99
<b>Figure 3.25</b>	- Box plot graph of estimated $\sigma_{cm}$ values of scenarios from SG-II .....	100
<b>Figure 3.26</b>	- Box plot graph of estimated $\sigma_{cm}$ values of scenarios from SG-III ...	100
<b>Figure 3.27</b>	- Average values of compressive strength estimated by the empirical methods for the SG-I, SG-II and SG-III groups .....	101
<b>Figure 3.28</b>	- $\sigma_{cm}$ values estimated using RQD (a), RMR (b), Q (c) and GSI (d) - based methods plotted with the average results from all methods .	103
<b>Figure 4.1</b>	- Modes of operation for ground-penetrating radar data acquisition: a) common offset; b) common source; c) common depth-point; and d) common receiver .....	110
<b>Figure 4.2</b>	- Illustration of the reflection profiling mode for GPR data acquisition .....	111
<b>Figure 4.3</b>	- Two dimension GPR profile derived from Figure 4.2 .....	113
<b>Figure 4.4</b>	- GPR data processing flow of a common-offset reflection data .....	119
<b>Figure 4.5</b>	- Castanhão Dam layout .....	122
<b>Figure 4.6</b>	- Paleo Channel (a) and Paleo Channel Junior (b) .....	122
<b>Figure 4.7</b>	- Study area location .....	123
<b>Figure 4.8</b>	- A topographic survey using geodetic GPS, left, and the elevation measured in which the GPR survey line was positioned, right .....	125
<b>Figure 4.9</b>	- A georeferenced image of the location where the geophysical survey was conducted .....	126
<b>Figure 4.10</b>	- GPR survey using the 200 (left) and 400MHz (right) antenna frequency .....	127
<b>Figure 4.11</b>	- Estimation of the velocity using hyperbolic fitting .....	129
<b>Figure 4.12</b>	- GPR signal before and after data processing (200 MHz) .....	129
<b>Figure 4.13</b>	- GPR signal before and after data processing (400 MHz) .....	130
<b>Figure 4.14</b>	- Processed 200 MHz data .....	131
<b>Figure 4.15</b>	- Processed 400 MHz data .....	131

<b>Figure 4.16</b> - Processed 200 MHz data (analogous to Figure 4.14, but with the color palette used by the seismic) .....	132
<b>Figure 4.17</b> - Processed 400 MHz data (analogous to Figure 4.15, but with the color palette used by the seismic) .....	132
<b>Figure 4.18</b> - Attribute 01 – Variance (200 MHz) .....	133
<b>Figure 4.19</b> - Attribute 01 – Variance (400 MHz) .....	133
<b>Figure 4.20</b> - Attribute 02 – Amplitude (200 MHz) .....	134
<b>Figure 4.21</b> - Attribute 02 – Amplitude (400 MHz) .....	134
<b>Figure 4.22</b> - Attribute 03 – Outcrop (200 MHz) .....	135
<b>Figure 4.23</b> - Attribute 04 – Outcrop (400 MHz) .....	135
<b>Figure 4.24</b> - Rock slope surveyed with depth achieved by the ground-penetrating radar .....	136
<b>Figure 4.25</b> - Comparative analysis between the geological features observed on the external outcrop and its analogs subsurface information imaged by the 200 MHz GPR (basic and advanced data processing) .....	138
<b>Figure A.1</b> - Frequency histogram of RQD index database (S1 to S46) .....	155
<b>Figure A.2</b> - Frequency histogram of RMR number database (S1 to S46) .....	156
<b>Figure A.3</b> - Frequency histogram of Q-value database (S1 to S46) .....	157
<b>Figure A.4</b> - Frequency histogram of GSI number database (S1 to S46) .....	158
<b>Figure B.5</b> - Deformation modulus calculated for scenario 1 .....	159
<b>Figure B.6</b> - Deformation modulus calculated for scenario 2 .....	159
<b>Figure B.7</b> - Deformation modulus calculated for scenario 3 .....	159
<b>Figure B.8</b> - Deformation modulus calculated for scenario 4 .....	160
<b>Figure B.9</b> - Deformation modulus calculated for scenario 5 .....	160
<b>Figure B.10</b> - Deformation modulus calculated for scenario 6 .....	160
<b>Figure B.11</b> - Deformation modulus calculated for scenario 7 .....	161
<b>Figure B.12</b> - Deformation modulus calculated for scenario 8 .....	161
<b>Figure B.13</b> - Deformation modulus calculated for scenario 9 .....	161
<b>Figure B.14</b> - Deformation modulus calculated for scenario 10 .....	162

<b>Figure B.15</b> - Deformation modulus calculated for scenario 11 .....	162
<b>Figure B.16</b> - Deformation modulus calculated for scenario 12 .....	162
<b>Figure B.17</b> - Deformation modulus calculated for scenario 13 .....	163
<b>Figure B.18</b> - Deformation modulus calculated for scenario 14 .....	163
<b>Figure B.19</b> - Deformation modulus calculated for scenario 15 .....	163
<b>Figure B.20</b> - Deformation modulus calculated for scenario 16 .....	164
<b>Figure B.21</b> - Deformation modulus calculated for scenario 17 .....	164
<b>Figure B.22</b> - Deformation modulus calculated for scenario 18 .....	164
<b>Figure B.23</b> - Deformation modulus calculated for scenario 19 .....	165
<b>Figure B.24</b> - Deformation modulus calculated for scenario 20 .....	165
<b>Figure B.25</b> - Deformation modulus calculated for scenario 21 .....	165
<b>Figure B.26</b> - Deformation modulus calculated for scenario 22 .....	166
<b>Figure B.27</b> - Deformation modulus calculated for scenario 23 .....	166
<b>Figure B.28</b> - Deformation modulus calculated for scenario 24 .....	166
<b>Figure B.29</b> - Deformation modulus calculated for scenario 25 .....	167
<b>Figure B.30</b> - Deformation modulus calculated for scenario 26 .....	167
<b>Figure B.31</b> - Deformation modulus calculated for scenario 27 .....	167
<b>Figure B.32</b> - Deformation modulus calculated for scenario 28 .....	168
<b>Figure B.33</b> - Deformation modulus calculated for scenario 29 .....	168
<b>Figure B.34</b> - Deformation modulus calculated for scenario 30 .....	168
<b>Figure B.35</b> - Deformation modulus calculated for scenario 31 .....	169
<b>Figure B.36</b> - Deformation modulus calculated for scenario 32 .....	169
<b>Figure B.37</b> - Deformation modulus calculated for scenario 33 .....	169
<b>Figure B.38</b> - Deformation modulus calculated for scenario 34 .....	170
<b>Figure B.39</b> - Deformation modulus calculated for scenario 35 .....	170
<b>Figure B.40</b> - Deformation modulus calculated for scenario 36 .....	170

<b>Figure B.41</b> - Deformation modulus calculated for scenario 37 .....	171
<b>Figure B.42</b> - Deformation modulus calculated for scenario 38 .....	171
<b>Figure B.43</b> - Deformation modulus calculated for scenario 39 .....	171
<b>Figure B.44</b> - Deformation modulus calculated for scenario 40 .....	172
<b>Figure B.45</b> - Deformation modulus calculated for scenario 41 .....	172
<b>Figure B.46</b> - Deformation modulus calculated for scenario 42 .....	172
<b>Figure B.47</b> - Deformation modulus calculated for scenario 43 .....	173
<b>Figure B.48</b> - Deformation modulus calculated for scenario 44 .....	173
<b>Figure B.49</b> - Deformation modulus calculated for scenario 45 .....	173
<b>Figure B.50</b> - Deformation modulus calculated for scenario 46 .....	174
<b>Figure D.51</b> - Compressive strength calculated for scenario 1 .....	181
<b>Figure D.52</b> - Compressive strength calculated for scenario 2 .....	181
<b>Figure D.53</b> - Compressive strength calculated for scenario 3 .....	181
<b>Figure D.54</b> - Compressive strength calculated for scenario 4 .....	182
<b>Figure D.55</b> - Compressive strength calculated for scenario 5 .....	182
<b>Figure D.56</b> - Compressive strength calculated for scenario 6 .....	182
<b>Figure D.57</b> - Compressive strength calculated for scenario 7 .....	183
<b>Figure D.58</b> - Compressive strength calculated for scenario 8 .....	183
<b>Figure D.59</b> - Compressive strength calculated for scenario 9 .....	183
<b>Figure D.60</b> - Compressive strength calculated for scenario 10 .....	184
<b>Figure D.61</b> - Compressive strength calculated for scenario 11 .....	184
<b>Figure D.62</b> - Compressive strength calculated for scenario 12 .....	184
<b>Figure D.63</b> - Compressive strength calculated for scenario 13 .....	185
<b>Figure D.64</b> - Compressive strength calculated for scenario 14 .....	185
<b>Figure D.65</b> - Compressive strength calculated for scenario 15 .....	185
<b>Figure D.66</b> - Compressive strength calculated for scenario 16 .....	186



<b>Figure D.67</b> - Compressive strength calculated for scenario 17 .....	186
<b>Figure D.68</b> - Compressive strength calculated for scenario 18 .....	186
<b>Figure D.69</b> - Compressive strength calculated for scenario 19 .....	187
<b>Figure D.70</b> - Compressive strength calculated for scenario 20 .....	187
<b>Figure D.71</b> - Compressive strength calculated for scenario 21 .....	187
<b>Figure D.72</b> - Compressive strength calculated for scenario 22 .....	188
<b>Figure D.73</b> - Compressive strength calculated for scenario 23 .....	188
<b>Figure D.74</b> - Compressive strength calculated for scenario 24 .....	188
<b>Figure D.75</b> - Compressive strength calculated for scenario 25 .....	189
<b>Figure D.76</b> - Compressive strength calculated for scenario 26 .....	189
<b>Figure D.77</b> - Compressive strength calculated for scenario 27 .....	189
<b>Figure D.78</b> - Compressive strength calculated for scenario 28 .....	190
<b>Figure D.79</b> - Compressive strength calculated for scenario 29 .....	190
<b>Figure D.80</b> - Compressive strength calculated for scenario 30 .....	190
<b>Figure D.81</b> - Compressive strength calculated for scenario 31 .....	191
<b>Figure D.82</b> - Compressive strength calculated for scenario 32 .....	191
<b>Figure D.83</b> - Compressive strength calculated for scenario 33 .....	191
<b>Figure D.84</b> - Compressive strength calculated for scenario 34 .....	192
<b>Figure D.85</b> - Compressive strength calculated for scenario 35 .....	192
<b>Figure D.86</b> - Compressive strength calculated for scenario 36 .....	192
<b>Figure D.87</b> - Compressive strength calculated for scenario 37 .....	193
<b>Figure D.88</b> - Compressive strength calculated for scenario 38 .....	193
<b>Figure D.89</b> - Compressive strength calculated for scenario 39 .....	193
<b>Figure D.90</b> - Compressive strength calculated for scenario 40 .....	194
<b>Figure D.91</b> - Compressive strength calculated for scenario 41 .....	194
<b>Figure D.92</b> - Compressive strength calculated for scenario 42 .....	194

<b>Figure D.93</b> - Compressive strength calculated for scenario 43 .....	195
<b>Figure D.94</b> - Compressive strength calculated for scenario 44 .....	195
<b>Figure D.95</b> - Compressive strength calculated for scenario 45 .....	195
<b>Figure D.96</b> - Compressive strength calculated for scenario 46 .....	196

## LIST OF TABLES

<b>Table 2.1</b>	- Typical range of uniaxial compressive strength for intact rock for different types of rocks .....	27
<b>Table 2.2</b>	- Index properties of intact rock .....	29
<b>Table 2.3</b>	- Negative influence of the orientation of discontinuities for different engineering applications .....	32
<b>Table 2.4</b>	- Discontinuity spacing description .....	32
<b>Table 2.5</b>	- Discontinuity persistence description .....	34
<b>Table 2.6</b>	- Roughness classes .....	35
<b>Table 2.7</b>	- Relationship between $J_r$ and JRC for block sizes of 20 and 100 cm	36
<b>Table 2.8</b>	- Strength estimation using field identification – Grades R0 to R6 ....	38
<b>Table 2.9</b>	- Apertures description of the discontinuities .....	39
<b>Table 2.10</b>	- Strength estimation using field identification – Grades S1 to S6 ....	40
<b>Table 2.11</b>	- Seepage rating in unfilled discontinuities .....	41
<b>Table 2.12</b>	- Seepage rating in filled discontinuities .....	41
<b>Table 2.13</b>	- Classification of the rock mass based on RQD range values .....	43
<b>Table 2.14</b>	- Correlation between RQD and velocity index .....	46
<b>Table 2.15</b>	- The uniaxial compressive strength of intact rock - 1° RMR parameter .....	47
<b>Table 2.16</b>	- The rock quality designation (RQD) - 2° RMR parameter .....	47
<b>Table 2.17</b>	- Spacing of discontinuities - 3° RMR parameter .....	47
<b>Table 2.18</b>	- Conditions of discontinuities - 4° RMR parameter .....	48
<b>Table 2.19</b>	- Groundwater conditions - 5° RMR parameter .....	48
<b>Table 2.20</b>	- Guidelines for classification of discontinuity conditions for Geomechanics Classification .....	51
<b>Table 2.21</b>	- Rating adjustment for discontinuity orientations - 6° RMR parameter .....	51
<b>Table 2.22</b>	- Rock mass classes from Geomechanics Classification .....	51
<b>Table 2.23</b>	- Meaning of rock mass classes from Geomechanics Classification .	52

<b>Table 2.24</b>	- Rock mass classes from Q-system .....	53
<b>Table 2.25</b>	- Rock quality designation (RQD) for Q-system .....	53
<b>Table 2.26</b>	- Joint set number (Jn) for Q-system .....	53
<b>Table 2.27</b>	- Joint roughness number (Jr) for Q-system .....	54
<b>Table 2.28</b>	- Joint alteration number (Ja) for Q-system – Part 1 .....	55
<b>Table 2.29</b>	- Joint alteration number (Ja) for Q-system – Part 2 .....	55
<b>Table 2.30</b>	- Joint alteration number (Ja) for Q-system – Part 3 .....	55
<b>Table 2.31</b>	- Joint water reduction factor (Jw) for Q-system .....	56
<b>Table 2.32</b>	- Stress reduction factor (SRF) for Q-system – Part 1 .....	56
<b>Table 2.33</b>	- Stress reduction factor (SRF) for Q-system – Part 2 .....	57
<b>Table 2.34</b>	- Stress reduction factor (SRF) for Q-system – Part 3 .....	57
<b>Table 2.35</b>	- Stress reduction factor (SRF) for Q-system – Part 4 .....	57
<b>Table 2.36</b>	- Blockiness of the rock mass and its description used in Geological Strength Index (GSI) system .....	59
<b>Table 2.37</b>	- Surface conditions and its description used in Geological Strength Index (GSI) system .....	60
<b>Table 3.1</b>	- The relationship between $\sigma_{cm}/\sigma_{ci}$ and RQD proposed by Kulhawy and Goodman (1987) .....	68
<b>Table 3.2</b>	- Correlations proposed by Galera et al. (2007) to estimate rock mass modulus using RMR .....	75
<b>Table 3.3</b>	- Rock mass conditions in relation to factor D .....	85
<b>Table 3.4</b>	- Guidelines for estimating factor D .....	86
<b>Table 3.5</b>	- Values of MR for different rocks .....	89
<b>Table 3.6</b>	- Database of 46 scenarios of rock masses selected .....	91
<b>Table 3.7</b>	- Descriptive statistics of SG-I, SG-II, and SG-III .....	93
<b>Table 4.1</b>	- Input rock mass parameters used by RQD, RMR, Q and GSI .....	106
<b>Table 4.2</b>	- Electromagnetic characteristics of common geological materials ..	116
<b>Table 4.3</b>	- Probing depth as function of antenna frequency .....	117
<b>Table 4.4</b>	- Brief description of GPR data processing techniques from Figure 4.4 .....	120

<b>Table 4.5</b>	- GPR data acquisition parameters for the 200 and 400 MHz antennas survey .....	128
<b>Table A.1</b>	- Descriptive statistics of RQD index database (S1 to S46) .....	155
<b>Table A.2</b>	- Descriptive statistics of RMR number database (S1 to S46) .....	156
<b>Table A.3</b>	- Descriptive statistics of Q-value database (S1 to S46) .....	157
<b>Table A.4</b>	- Descriptive statistics of GSI number database (S1 to S46) .....	158
<b>Table C.5</b>	- Mean relative error (MRE) of SG-I group in percentage (from deformation modulus estimated data) .....	175
<b>Table C.6</b>	- Mean relative error (MRE) of SG-II group in percentage (from deformation modulus estimated data) .....	176
<b>Table C.7</b>	- Mean relative error (MRE) of SG-III group in percentage (from deformation modulus estimated data) .....	177
<b>Table C.8</b>	- Median relative error (MdRE) of SG-I group in percentage (from deformation modulus estimated data) .....	178
<b>Table C.9</b>	- Median relative error (MdRE) of SG-II group in percentage (from deformation modulus estimated data) .....	179
<b>Table C.10</b>	- Median relative error (MdRE) of SG-III group in percentage (from deformation modulus estimated data) .....	180
<b>Table E.11</b>	- Mean relative error (MRE) of SG-I group in percentage (from compressive strength estimated data) .....	197
<b>Table E.12</b>	- Mean relative error (MRE) of SG-II group in percentage (from compressive strength estimated data) .....	198
<b>Table E.13</b>	- Mean relative error (MRE) of SG-III group in percentage (from compressive strength estimated data) .....	199
<b>Table E.14</b>	- Median relative error (MdRE) of SG-I group in percentage (from compressive strength estimated data) .....	200
<b>Table E.15</b>	- Median relative error (MdRE) of SG-II group in percentage (from compressive strength estimated data) .....	201
<b>Table E.16</b>	- Median relative error (MdRE) of SG-III group in percentage (from compressive strength estimated data) .....	202

## SUMMARY

<b>1</b>	<b>INTRODUCTION .....</b>	<b>21</b>
<b>1.1</b>	<b>Research Objectives .....</b>	<b>22</b>
<b>1.2</b>	<b>Dissertation Structure .....</b>	<b>22</b>
<b>2</b>	<b>OVERVIEW OF ROCK MASS AS AN ENGINEERING MATERIAL AND ITS CLASSIFICATION SCHEME SYSTEMS .....</b>	<b>24</b>
<b>2.1</b>	<b>Rock masses .....</b>	<b>24</b>
<b>2.2</b>	<b>Intact Rock.....</b>	<b>25</b>
<b>2.3</b>	<b>Discontinuities.....</b>	<b>29</b>
<b>2.3.1</b>	<b><i>Orientation.....</i></b>	<b>30</b>
<b>2.3.2</b>	<b><i>Spacing.....</i></b>	<b>31</b>
<b>2.3.3</b>	<b><i>Persistence.....</i></b>	<b>33</b>
<b>2.3.4</b>	<b><i>Roughness.....</i></b>	<b>34</b>
<b>2.3.5</b>	<b><i>Wall strength.....</i></b>	<b>37</b>
<b>2.3.6</b>	<b><i>Aperture.....</i></b>	<b>38</b>
<b>2.3.7</b>	<b><i>Filling.....</i></b>	<b>39</b>
<b>2.3.8</b>	<b><i>Seepage.....</i></b>	<b>40</b>
<b>2.4</b>	<b>Rock Mass Classification Systems .....</b>	<b>40</b>
<b>2.4.1</b>	<b><i>Rock Quality Designation Index.....</i></b>	<b>42</b>
<b>2.4.2</b>	<b><i>Rock Mass Rating System.....</i></b>	<b>46</b>
<b>2.4.3</b>	<b><i>Tunnelling Quality Index.....</i></b>	<b>52</b>
<b>2.4.4</b>	<b><i>Geological Strength Index.....</i></b>	<b>58</b>
<b>2.4.5</b>	<b><i>Correlations between the classification schemes.....</i></b>	<b>61</b>
<b>2.5</b>	<b>Conclusions .....</b>	<b>62</b>
<b>3</b>	<b>EMPIRICAL METHODS BASED ON CLASSIFICATION SCHEMES TO ESTIMATE ROCK MASS STRENGTH AND DEFORMATION PARAMETERS FOR NUMERICAL MODELING PURPOSES .....</b>	<b>64</b>

3.1	Deere's RQD index .....	64
3.1.1	<i>Rock Mass Deformability Correlations Based on RQD</i> .....	65
3.1.2	<i>Rock Mass Strength Correlations Based on RQD</i> .....	68
3.2	Bieniawski's RMR number .....	69
3.2.1	<i>Rock Mass Deformability Correlations Based on RMR number</i> .....	70
3.2.2	<i>Rock Mass Strength Correlations Based on RMR number</i> .....	77
3.3	Barton's Q-value.....	79
3.3.1	<i>Rock Mass Deformability Correlations Based on Q-value</i> .....	79
3.3.2	<i>Rock Mass Strength Correlations Based on Q-value</i> .....	82
3.4	Hoek's GSI number.....	83
3.4.1	<i>Rock Mass Deformability Correlations Based on GSI number</i> .....	83
3.4.2	<i>Rock Mass Strength Correlations Based on GSI number</i> .....	88
3.5	Comparative Analysis of the Empirical Correlations .....	90
3.5.1	<i>Comparative analysis – <math>E_{rm}</math></i> .....	92
3.5.2	<i>Comparative analysis – <math>\sigma_{cm}</math></i> .....	97
3.6	Conclusions .....	102
4	<b>APPLICATION OF GROUND-PENETRATING RADAR (GPR) TO DISCONTINUITY IMAGING FOR ROCK MASS CHARACTERIZATION PURPOSES</b> .....	105
4.1	Introduction.....	105
4.2	Ground-Penetrating Radar (GPR) .....	108
4.2.1	<i>The GPR Technique</i> .....	109
4.2.2	<i>GPR EM Waves Theory</i> .....	112
4.2.3	<i>GPR Signal Behavior</i> .....	113
4.2.4	<i>Depth of Penetration</i> .....	117
4.2.5	<i>GPR Data Processing and Analysis</i> .....	118
4.2.6	<i>Interpretation of GPR data</i> .....	120
4.3	Study Area .....	121

4.3.1	<i>Castanhão Dam</i> .....	121
4.3.2	<i>Geological Settings – Castanhão Spillway</i> .....	124
4.4	<b>Material and Methods</b> .....	124
4.4.1	<i>Topographic survey</i> .....	125
4.4.2	<i>GPR Data Acquisition</i> .....	127
4.4.3	<i>GPR Data Processing</i> .....	128
4.4.4	<i>GPR Data Interpretation</i> .....	136
4.5	<b>Comparative Analysis</b> .....	137
4.6	<b>Conclusions</b> .....	138
5	<b>CONCLUSIONS AND SUGGESTIONS FOR FUTURE RESEARCH</b> ....	141
5.1	<b>Final Conclusions</b> .....	141
5.2	<b>Future Research Suggestions</b> .....	142
	<b>REFERENCES</b> .....	143
	<b>APPENDIX A - DESCRIPTIVE STATISTICS OF THE DATABASE</b> ....	155
	<b>APPENDIX B - DEFORMATION MODULUS (<math>E_{RM}</math>) RESULTS</b> .....	159
	<b>APPENDIX C - MEAN AND MEDIAN RELATIVE ERROR – DEFORMATION MODULUS</b> .....	175
	<b>APPENDIX D - COMPRESSIVE STRENGTH (<math>\Sigma_{CM}</math>) RESULTS</b> .....	181
	<b>APPENDIX E - MEAN AND MEDIAN RELATIVE ERROR – COMPRESSIVE STRENGTH</b> .....	197



## 1 INTRODUCTION

Rock engineering is the applied science related to human activities using the rocks as an engineering material for different purposes, such as the dam foundations, tunnels support, open-pit mines, underground excavations, mining shafts, among others. Its foundation lies in rock mechanics, which studies the mechanical behavior of this geomaterial in response to any change in the stress field of the rocks caused by the forces acting on them.

The common term used for describing the rocks, from the point of view of engineering practices is the rock mass, which refers to the intact part of the rock and geological discontinuities that may exist within its interior, where the individual characteristic of both affects directly the mechanical behavior of the material. For the intact part, the uniaxial (or unconfined) compressive strength,  $\sigma_{ci}$ , and the deformation modulus,  $E_i$ , are the most relevant parameters, while, for the discontinuities, which is defined by the International Society of Rock Mechanics (ISRM) as any break within the rock mass having zero or low tensile strength, it is taken into account its orientation, spacing, persistence, roughness, wall strength, aperture, filling, and seepage (ISRM, 1978).

Because of the anisotropic and heterogeneous characteristics of the material arising from the presence of geological breaks within the medium, estimating the mechanical parameters of rock masses, in order to predict its behavior under any change of its stress field, is a much more complex task when compared to other common engineering material, such as concrete, metal and even the soil. In common, those materials can be tested in a laboratory, however, the rock mass, due to the existence of scale effect, have their properties estimated using in situ tests, which are very expensive and not so common in practice, or using indirect methodologies for this purpose (HOEK, 2012).

Among these indirect methodologies, correlations derived from rock mass classification schemes are probably the most used in rock engineering practices. These classifications take into consideration, in general, the main features related to the intact rock and discontinuities for describing the quality of rock masses. They were designed first as an engineering tool based on past experience to be a guide for rock engineering practices, especially for underground excavations, however, due to its good acceptance

by the rock mechanic community, its use has expanded considerably, and now they are widely used in the early stages of most rock engineering projects (ZHANG, 2016).

In regard to the relevance of rock mass classification systems for rock engineering, this dissertation study will present some important subjects related to them, such as a review of the concepts behind the main methodologies used to classify rocks, e.g., RQD, RMR, Q, and GSI, a comparative analysis of the main empirical methods developed over the years for estimating the mechanical parameters using these systems as the input parameter for numerical modeling, and, finally, a proposal for a geophysical method for enhancing rock mass characterization for rock mass classification purposes.

### **1.1 Research Objectives**

The general objectives of this dissertation is to examine the reliability of the suggested empirical methods for estimating the rock mass strength,  $\sigma_{cm}$ , and deformation modulus,  $E_{rm}$ , based on the rock mass quality using the classification schemes as input parameters for numerical modeling, and a proposal for a geophysical technique, the ground-penetrating radar (GPR), to enhance in situ rock mass characterization for classification schemes purposes. In order to their achievement, the specific objectives are presented as follow:

- i. To evaluate the methodologies used in the most noticed rock mass classification systems as well as their main input parameters requirement;
- ii. To assess the predicted values for these methods based on the rock mass quality derived from different real rock mass scenarios previously characterized and classified according to RQD, RMR, Q, and GSI methodologies.
- iii. To apply the ground-penetrating radar (GPR) method in a previously selected location to study the behavior of subsurface imaging information and how it can be useful for rock mass characterization.

### **1.2 Dissertation Structure**

This dissertation presents three major studies divided into three separated chapters, besides this first introductory one, where each of them is connected to the subject of rock engineering and the rock mass classification systems (RMCS). Although

there is this virtual connection among them, each chapter is presented as an independent study, with an introduction, an analysis of their content and a conclusion, for publication purposes.

The first study, which is formally written in chapter two of this dissertation, describes a review of the main aspects related to the rock mass classification systems, including a discussion of the main features concerning the intact rock and discontinuities and their importance for the classification schemes. The methodologies proposed by Deere *et al.* (1967), Bieniawski (1973), Barton *et al.* (1974), and Hoek (1994) for the rock mass quality assessment are also presented and discussed on it

In chapter 3, the following study is concerned with the evaluation of the different empirical methods proposed to estimate the mechanical parameters of the rock mass, based on RMCS, necessary for mostly numerical modeling, i.e., the compressive strength and the deformation modulus. In this regard, 46 scenarios of different rock mass quality, previously characterized and classified using Deere's, Bieniawski's, Barton's, and Hoek's methodologies, are used for the comparative analysis among these empirical correlations.

The last chapter of this dissertation study, in turn, will present the ground-penetrating radar as an auxiliary rock engineering tool for enhancing the rock mass characterization, especially for assessing the underground discontinuity conditions of the rock masses for rock mass classification purposes. A case study was conducted in the Castanhão Dam, where a rock mass outcrop was sounding using two different antennas frequency.

## 2 OVERVIEW OF ROCK MASS AS AN ENGINEERING MATERIAL AND ITS CLASSIFICATION SCHEME SYSTEMS

Classification schemes developed for rock engineering practice are an important tool used for assessing the rock mass quality, taking into account the properties of the intact rock and the discontinuities. This chapter presents an overview of the rock mass as an engineering material, reviewing some properties and characteristics related to the intact pieces of rocks and the geological discontinuities, often used as input parameters in the rock classification schemes. Later, the main methodologies used for classifying the rock mass for engineering purposes are presented, focusing on the Rock Quality Designation (RQD), Rock Mass Rating (RMR) system, Q-system, and the Geological Strength Index (GSI) systems.

### 2.1 Rock masses

Bieniawski (1989) describes rock mass as an assemblage of intact rock blocks separated by geological discontinuities, like joints, faults, and bedding planes. Rock masses often have heterogeneous<sup>1</sup> and anisotropic<sup>2</sup> behavior, although they also can be treated as homogeneous<sup>3</sup> and isotropic<sup>4</sup>. This second condition occurs, conforming Hoek (1994), in cases where the rock mass is heavily jointed or free of joints (intact rock).

Figure 2.1 is a schematic representation, presented by Hoek and Brown (1980) and used in many rock mechanics books and papers to explain the occurrence of the scale effect in rocks. It shows the transition from intact rock to heavily jointed mass with increasing the rock domain analyzed in a hypothetical rock mass surrounding an underground excavation. Depending on the scale that a specific rock mass is analyzed, it may have different discontinuities arrangement or even no discontinuities at all.

Along with the characteristics of the intact blocks of rocks, the discontinuities features will reflect in the strength and stiffness of the rock mass. Therefore, the characterization of intact part and discontinuities conditions are a common and necessary practice for evaluating the mechanical behavior of the rock mass when subjected to changes in its initial stress conditions.

---

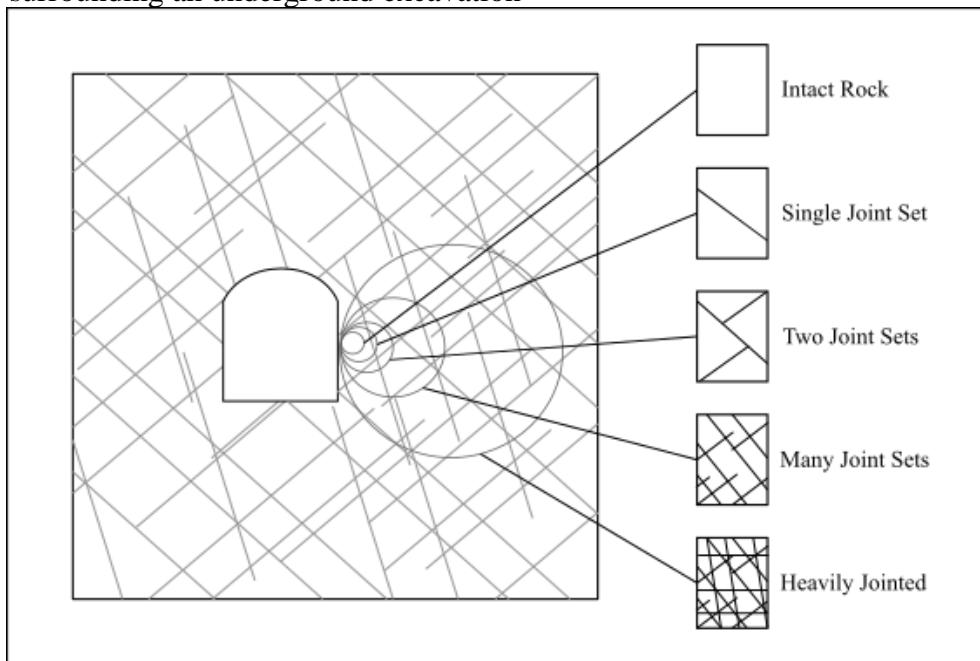
<sup>1</sup> Different property values at all locations.

<sup>2</sup> Different property values in different directions.

<sup>3</sup> The same property values at all locations.

<sup>4</sup> The same property values in different directions.

**Figure 2.1** - Illustration of the scale effect in rocks in a hypothetical rock mass surrounding an underground excavation



Source: adapted from Hoek and Brown (1980).

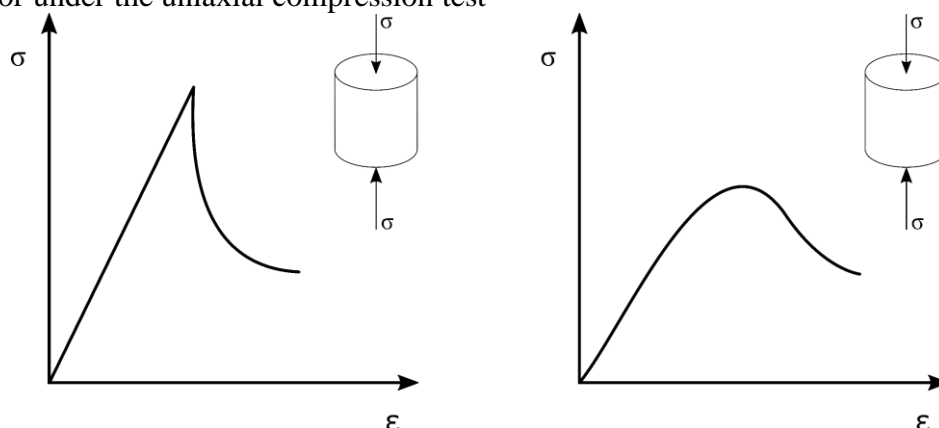
The next sections will discuss some properties and characteristics related to the intact pieces of rocks and the discontinuities that will be necessary later for understanding the rock mass classification schemes.

## 2.2 Intact Rock

Intact rock is the terminology used in rock mechanics to describe the unbroken rock blocks that are separated by the discontinuities in the rock mass. Although the characteristics of the discontinuities play an important role in determining the rock mass strength and deformability, the properties of the intact rock should not be ignored, as pointed out by Bieniawski (1989). According to this author, the intact rock may strongly influence the rock mass behavior in cases where the discontinuities are widely spaced, or the intact rock is weak and altered.

The strength and deformation characteristics of the intact rocks, as reported by Vallejo and Ferrer (2011), are reflected of their physical properties, which are the result of their geological formation and their mineralogical composition and fabric. Hoek (1994) mentions that for most hard igneous and metamorphic rocks failure can be classified as brittle, i.e. occurs a sudden reduction in strength after the compressive strength is reached, while weak sedimentary rocks show ductile behavior, characterized by the little or no strength reduction after reaching the limiting stress level (Figure 2.2).

**Figure 2.2** - Illustration of the stress-strain curve of a brittle (left) and ductile (right) behavior under the uniaxial compression test



Source: adapted from Vallejo and Ferrer (2011).

The mechanical properties of intact rock are the responsible for its behavior under changes of stresses. From these properties, the uniaxial compressive strength ( $\sigma_{ci}$  or UCS<sup>5</sup>) and the elastic deformation moduli, i.e. Young's modulus (E) and Poisson's ratio ( $\nu$ ), are the most applicable.

The uniaxial compressive strength corresponds to the maximum stress which the rock can carry under axial compression, measured on an unconfined cylindrical specimen in the laboratory (VALLEJO AND FERRER, 2011). ISRM (1979) describes the procedures to measure the uniaxial compressive strength in the laboratory, through the UCS test, where its value is the result of the maximum load carried by the specimen during the test divided by the original cross-sectional area, Eq. 2.1.

$$\sigma_{ci} = \frac{P}{A} \quad 2.1$$

where  $\sigma_{ci}$  is the uniaxial compressive strength of the intact; P is the peak load; and A is the cross-sectional area of the rock specimen.

According to Hudson and Harrison (1997), the uniaxial compressive strength is probably the most widely used and quoted rock parameter. To understand its importance in the rock mass behavior, the UCS is an input parameter for different classification schemes, and it is one of the variables present in the Hoek-Brown failure criterion.

<sup>5</sup> UCS is commonly used in the literature as an acronym of uniaxial compressive strength, but there also several authors that refers it as an acronym to the unconfined compressive strength.

The American Association of State Highway and Transportation Officials (AASHTO) in the Standard Specification for Highway Bridges (AASHTO, 2002) gives the typical range values of uniaxial compressive strength for intact rock for different types of rocks, as summarized in Table 2.1.

**Table 2.1** - Typical range of uniaxial compressive strength for intact rock for different types of rocks

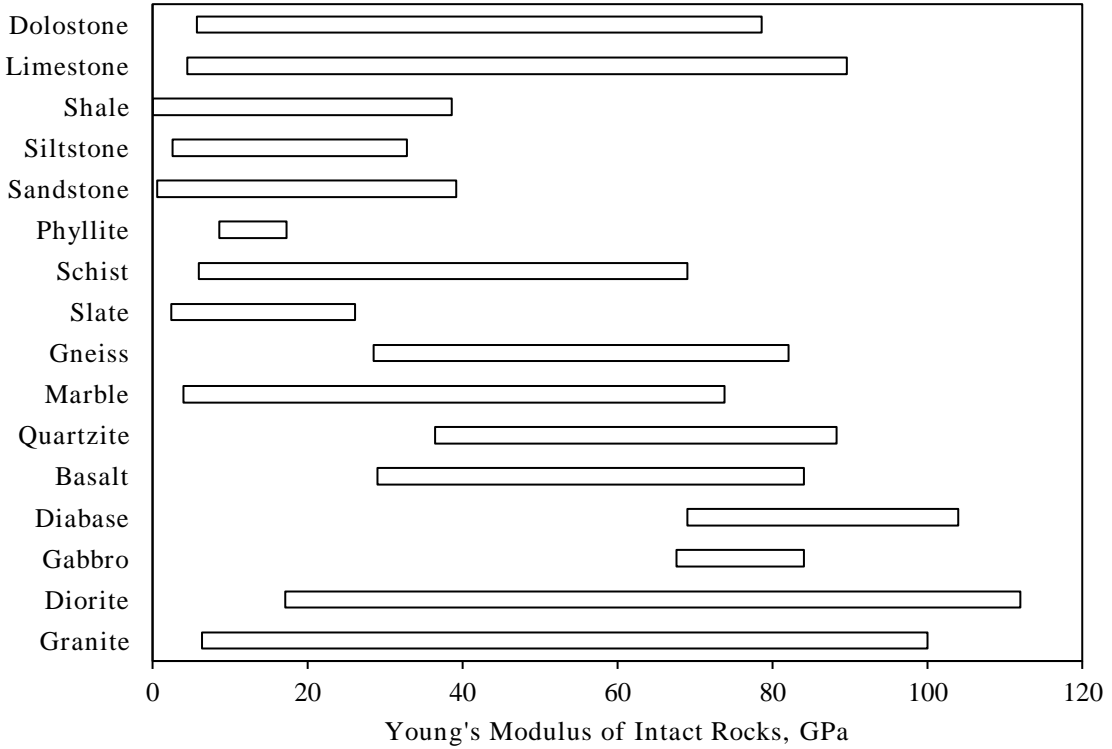
Category	General Description	Rock Type	Uniaxial Compressive Strength, MPa
A	Carbonate rocks with well-developed crystal cleavage	Dolostone	33 – 310
		Limestone	24 – 290
		Carbonatite	38 – 69
		Marble	38 – 241
		Tactite-Skarn	131 - 338
B	Lithified argillaceous rock	Argillite	29 – 145
		Claystone	1 – 8
		Marlstone	52 – 193
		Phyllite	24 – 241
		Siltstone	10 – 117
		Shale	7 – 35
		Slate	145 – 207
C	Arenaceous rocks with strong crystals and poor cleavage	Conglomerate	33 – 221
		Sandstone	67 – 172
		Quartzite	62 – 379
D	Fine-grained igneous crystalline rock	Andesite	97 – 179
		Diabase	21 – 572
E	Coarse-grained igneous and metamorphic crystalline rock	Amphibolite	117 – 276
		Gabbro	124 – 310
		Gneiss	24 – 310
		Granite	15 – 338
		Quartzdiorite	10 – 97
		Quartzmonzonite	131 – 159
		Schist	10 – 145
Syenite	179 – 427		

Source: modified from AASHTO (2002).

Regard to Young's modulus and Poisson's ratio, according to Pariseau (2017), they may be determined static and dynamically, where the first one is determined most often in practice. ISRM (1979) suggests the procedures to measure these elastic

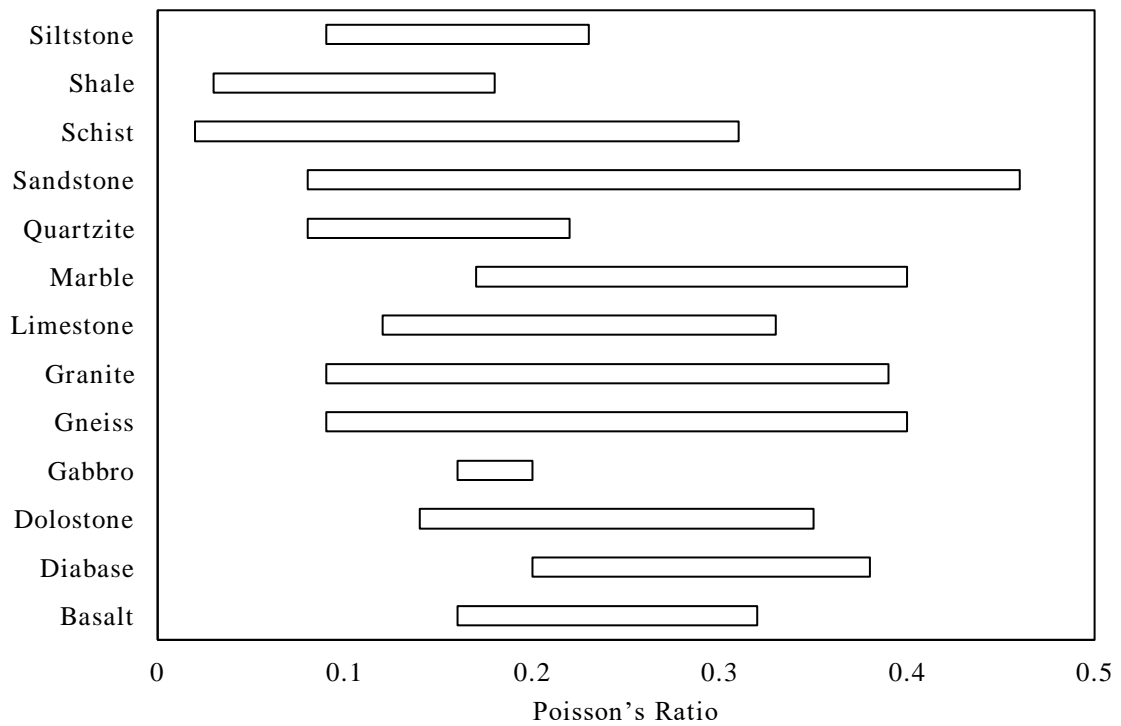
properties using the uniaxial compression test. The typical range values of these mechanical properties for intact rock are presented in Figures 2.3 and 2.4, respectively.

**Figure 2.3** - Range of Young's modulus of some rock types



Source: adapted from AASHTO (2002).

**Figure 2.4** - Range of Poisson's ratio of some rock types



Source: adapted from AASHTO (2002).



Besides the mechanical properties of intact rock, Goodman (1989) and Zhang (2016) listed a specific group, termed as the index properties (see Table 2.2), which can help classify specimens of rock for applications related primarily to the behavior of the rock itself as opposed to the rock mass.

This study will not detail how these properties can be determined, for more information, the author recommends the following references: Ulusay and Hudson (2007) and Ulusay (2014), which are suggested standards for field tests and measurements in situ published by the International Society for Rock Mechanics (ISRM). Also, correlations among some of them, developed by different authors, are found in Goodman (1989) and Zhang (2016).

**Table 2.2 - Index properties of intact rock**

<b>Index property</b>	<b>Symbol</b>
Porosity	n
Density	p
Sonic wave velocity	$v_p, v_s$
Point load stress	$I_s$
Schmidt hammer rebound number	R
Slake durability index	$I_d (2)$
Needle penetration index	NPI
Shore scleroscope hardness	H
Water content	w
Permeability coefficient	k

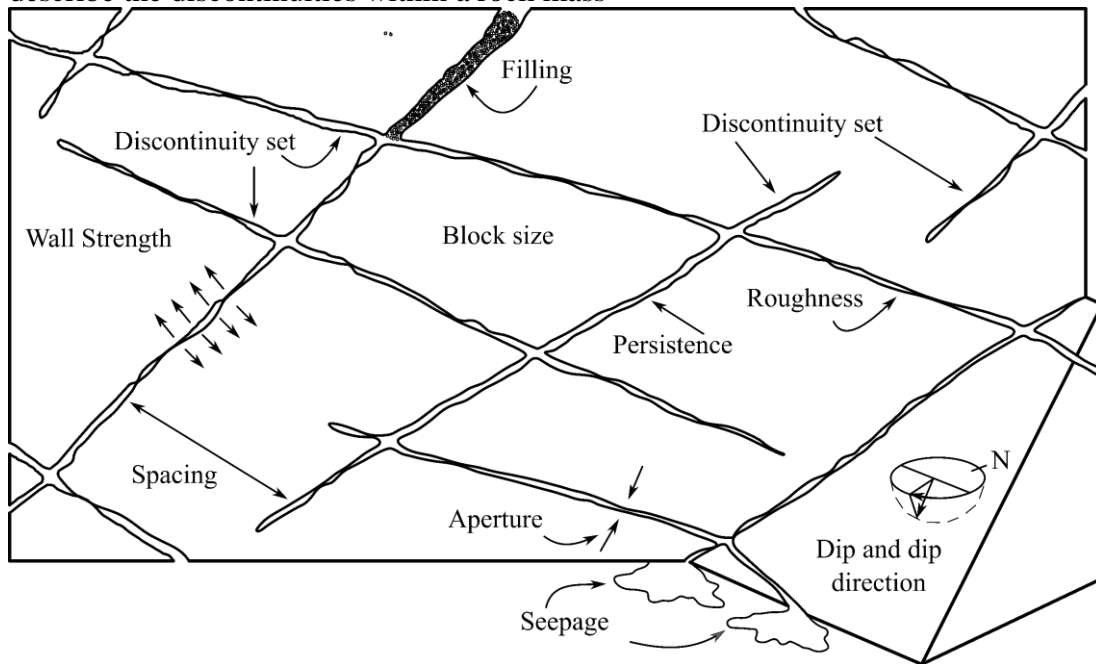
Source: Goodman (1989), Zhang (2016).

### 2.3 Discontinuities

Discontinuity in a rock mass is a break in the rock continuum having zero or minimum effectively tensile strength (HUDSON; HARRISON, 1997). In rock mechanics, it is the generic term used to describe most types of joints<sup>6</sup>, bedding planes, foliation, cleavage, schistosity, and faults (ISRM, 1978; SIVAKUGAN *et al.*, 2013). The usage of a single term to represent all breaks in the rock mass, while avoiding any inferences concerning their geological origins, contributed to its acceptance by the rock mechanics community since the first publications (PRIEST, 1993).

<sup>6</sup> Joints are the most common and geotechnically significant discontinuity in rocks (ZHANG, 2016).

**Figure 2.5** - Two-dimensional schematic representation of the parameters that describe the discontinuities within a rock mass



Source: adapted from Hudson and Harrison (1997).

According to Vallejo and Ferrer (2011), the rock mass properties, including their strength, deformational, and hydraulic behavior, are influenced by the presence of discontinuities in the medium. The level of influence of the discontinuities on the rock mass behavior will depend on their characteristics.

ISRM (1979) listed the following several parameters to describe discontinuities: (1) orientation; (2) spacing; (3) persistence, or continuity; (4) roughness; (5) wall strength; (6) aperture; (7) filling, or infilling; and (8) seepage. Their 2D schematic representation in a rock mass is illustrated in Figure 2.5.

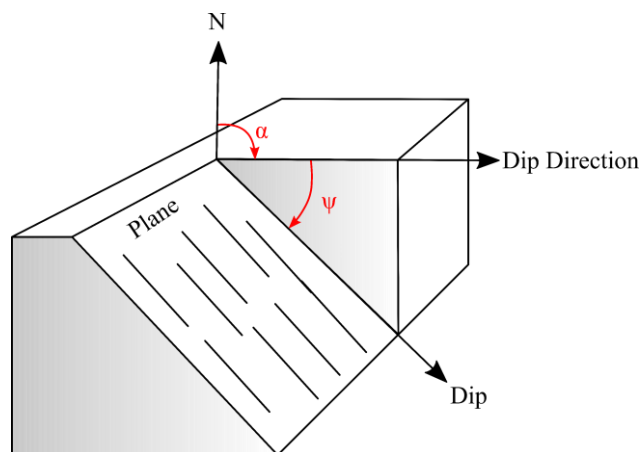
### 2.3.1 Orientation

The orientation of a discontinuity represents its attitude in space, described by the dip direction ( $\alpha$ ), measuring clockwise from true north, and the dip ( $\psi$ ) of the line of steepest declination in its plane, measuring from horizontal, illustrated by Figure 2.8 (ISRM, 1978). The dip direction and dip value vary from  $0^\circ$  to  $360^\circ$  and  $0^\circ$  to  $90^\circ$ , respectively, conforming (VALLEJO; FERRER, 2011).

Although discontinuities often have an irregular or curved geometry, the orientation is measured in a scale at which the whole, or a portion of it, is sufficiently

planar, using a simple compass-clinometer device (PRIEST, 1993). In some cases, the strike<sup>7</sup> of the discontinuity are recorded rather the dip direction (ZHANG, 2016).

**Figure 2.6** - Definition of dip and dip direction in an isometric view of plane



Source: adapted from Wyllie (2018).

As reported by ISRM (1978), the orientation of discontinuities relative to an engineering structure may induce unstable conditions or excessive deformation developing. For example, in rock slopes, such as those present in an open pit mine, their primary modes of failure (plane, wedge and toppling failure) depend on the discontinuity's orientation in general (DEB; VERMA, 2016). Table 2.3 illustrates different scenarios of engineering application in which the unfavorable orientation conditions will result in unstable conditions.

Bieniawski (1989) uses the influence of the discontinuity orientation in his rock mass classification system, the Rock Mass Rating (RMR) system, to adjust the overall RMR of a rock mass. This adjustment is determined by a qualitative description of the orientation, from very favorable to very unfavorable, varying according to engineering application, i.e., tunnels and mines, foundations, and slopes.

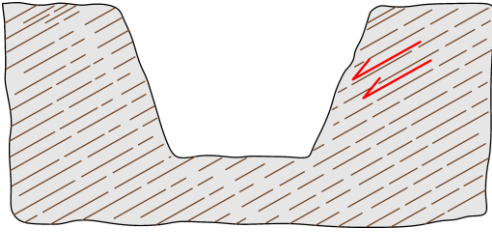
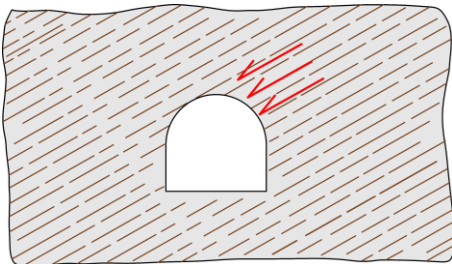
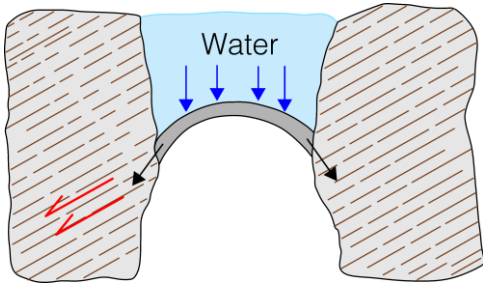
### 2.3.2 Spacing

Spacing is the perpendicular distance between adjacent discontinuities, which normally refers to the mean or modal spacing of a set of joints (ISRM, 1978). It controls the size of individual blocks of intact rock and has a direct impact on the rock mass

<sup>7</sup> The angle formed between a horizontal line drawn on the discontinuity plane and magnetic north (VALLEJO; FERRER, 2011).

behavior. Table 2.4 presents the terminology to describe discontinuities spacing suggested by ISRM (1978).

**Table 2.3** - Negative influence of the orientation of discontinuities for different engineering applications

Engineering Application	Note
	In surface excavations, e.g., for highway construction, the stability of a slope depends on its orientation in relation to discontinuities.
	In cases of tunneling design, the presence of discontinuities with pronounced dips running parallel to the tunnel axis, as illustrated on the side, are equally unfavorable.
	The presence of discontinuities parallel to the direction of the resultant force transmitted by an arch dam and the reservoir may cause problems of stability.

Source: adapted from Vallejo and Ferrer (2011).

**Table 2.4** - Discontinuity spacing description

Description	Spacing (mm)
Extremely close spacing	< 20
Very close spacing	20 – 60
Close spacing	60 – 200
Moderate spacing	200 – 600
Wide spacing	600 – 2000
Very wide spacing	2000 – 6000
Extremely wide spacing	> 6000

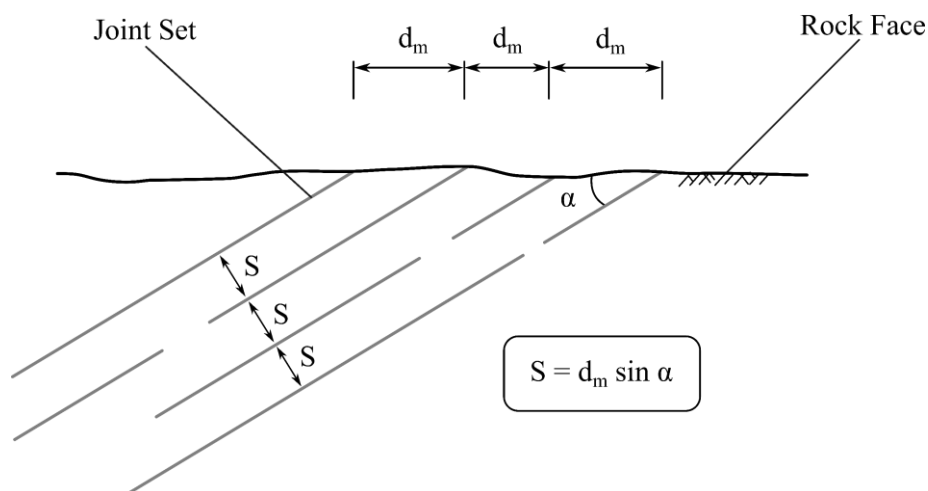
Source: ISRM (1978).

The spacing of a joint set is measured on the accessible surfaces of rock outcrops using measuring tape of at least 3m length (ISRM, 1978). In cases where it is not possible to record a perpendicular spacing measurement, Figure 2.7, it is necessary to use a direction bias correction to estimate the true spacing, using a compass and clinometer. The true spacing is then estimated using the Eq. 2.2.

$$S = d_m \sin \alpha \quad 2.2$$

where  $S$  is the true spacing;  $d_m$  is the apparent measurement; and  $\alpha$  is the angle between the line of apparent measurement and the strike of the joint set.

**Figure 2.7** - Illustration of apparent measurement from a rock face



Source: adapted from Wyllie (2018).

According to Priest (1993), discontinuity spacing is used to estimate the quality of a rock mass for classifications schemes. In Bieniawski's system (Bieniawski, 1989), the spacing of discontinuities is one of the six parameters to determine the RMR. The GSI, obtained through the GSI basic chart for jointed rock masses (HOEK; MARINOS, 2000), depends on the rock mass blockiness, which is influenced by the spacing of discontinuities.

### 2.3.3 Persistence

ISRM (1978) defines persistence as the areal extent or size of a discontinuity within a plane. Together with spacing, this parameter defines the size of blocks and the length of potential sliding surfaces (WYLLIE, 2018). Although it is an import

discontinuity characteristic, it is probably the most difficult to determine. According to Priest (1993), it is only possible to trace and to measure the complete area of each discontinuity if the rock mass could be completely dismantling.

Persistence can be measured using measuring tape of at least 10 m length, where efforts should be made for measuring the discontinuity length in the direction of dip and in the direction of strike (ISRM, 1978). The Table 2.5 shows the description of the persistence based on its modal trace lengths.

**Table 2.5 - Discontinuity persistence description**

<b>Description</b>	<b>Trace length (m)</b>
Very low persistence	< 1
Low persistence	1 – 3
Medium persistence	3 – 10
High persistence	10 – 20
Very high persistence	> 20

Source: ISRM (1978).

#### 2.3.4 Roughness

The roughness of a discontinuity is a measure of the inherent surface waviness and unevenness of the discontinuity relative to its mean plane (ISRM, 1978). The waviness term refers to large scale undulations which, if interlocked and in contact, cause dilation during shear displacement, once they are too large to be sheared off. The unevenness term, on the other hand, refers to small scale roughness that tends to be damaged during shear displacement, excepting in cases that discontinuity walls are of high strength and/or the stress levels are low, so that dilation can also occur on these small scale features (ISRM, 1978).

According to Sivakugan *et al.* (2013), the waviness can be defined as stepped, undulating, or planar, while the unevenness can be rough, smooth, or slickensided. The description of the roughness, therefore, is based on two scales of observation and can be classified into nine different classes, described in Table 2.6. The roughness profiles for these nine classes are illustrated in Figure 2.10.

The roughness of a discontinuity is an important parameter to estimate the shear stress of its walls, especially in cases where it is unfilled and is not displaced and remains interlocked (WILLIE, 2018). It is expressed numerically as a function of the Joint Roughness Coefficient (JRC), developed by Barton (1973), which is measured by

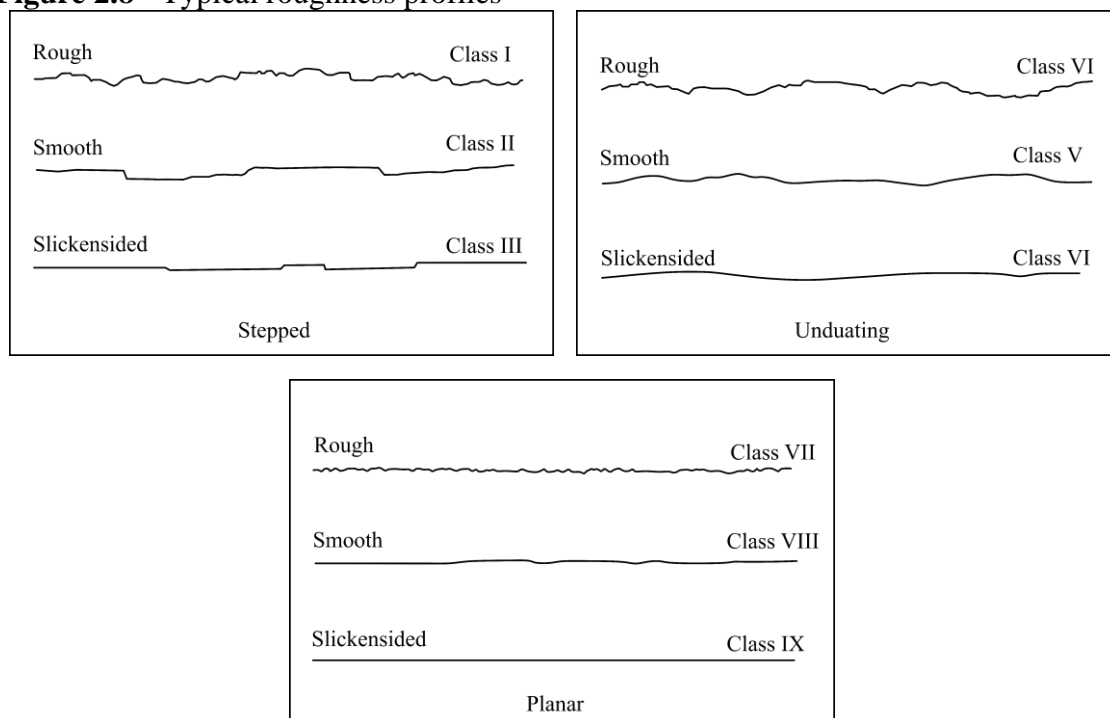
comparing the profile of a discontinuity surface with the standard roughness profiles, Figure 2.9, from Barton and Choubey (1977).

**Table 2.6 - Roughness classes**

Class	Unevenness	Waviness
I	Rough	Stepped
II	Smooth	Stepped
III	Slickensided	Stepped
IV	Rough	Undulating
V	Smooth	Undulating
VI	Slickensided	Undulating
VII	Rough	Planar
VIII	Smooth	Planar
IX	Slickensided	Planar

Source: ISRM (1978).

**Figure 2.8 - Typical roughness profiles**

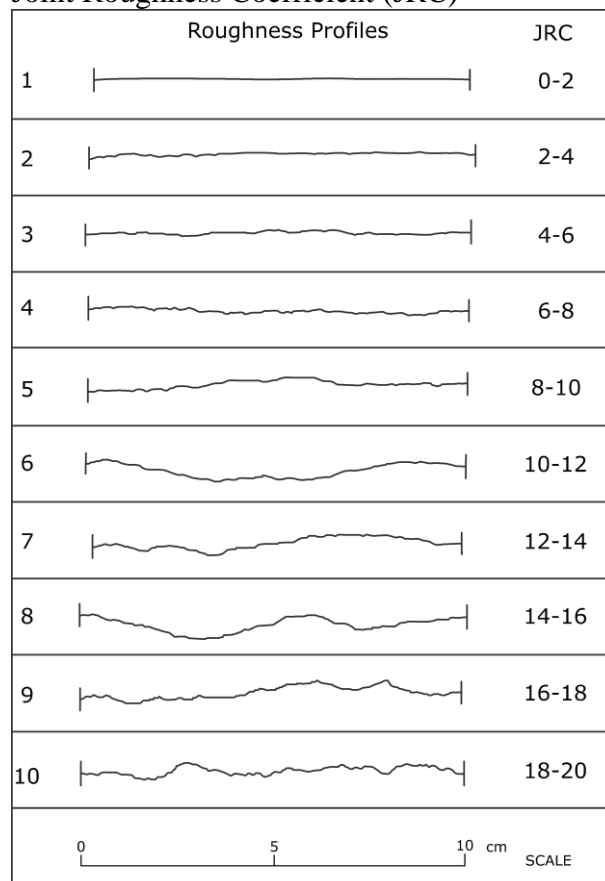


Source: adapted from ISRM (1978).

The rock mass classification designed by Barton *et al.* (1974), the Q-system, uses the roughness characteristics of the most unfavorable discontinuity as one of its six input parameters, the joint roughness number,  $J_r$ . The  $J_r$  parameter quantification will be discussed further, after introducing the Q-system, however, it also can be estimating using

the relationship with the JRC parameter, as reported by Barton (1987), described in Table 2.7.

**Figure 2.9** - Standard roughness profiles for Joint Roughness Coefficient (JRC)



Source: adapted from Barton and Choubey (1977).

**Table 2.7** - Relationship between  $J_r$  and JRC for block sizes of 20 and 100 cm

Class <sup>a</sup>	$J_r$	JRC <sub>20</sub> <sup>b</sup>	JRC <sub>100</sub> <sup>b</sup>
I	4	20	11
II	3	14	9
III	2	11	8
IV	3	14	9
V	2	11	8
VI	1.5	7	6
VII	1.5	2.5	2.3
VIII	1.0	1.5	0.9
IX	0.5	0.5	0,6

<sup>a</sup> Roughness classes (ISRM, 1978)

<sup>b</sup> JRC<sub>n</sub> values for 20 cm and 100 cm block size

Source: adapted from Barton (1987).



### 2.3.5 Wall strength

Wall strength refers to the compression strength of the rock comprising the walls of a discontinuity, and it is often expressed numerically by the joint wall compression strength (JCS), introduced by Barton (1973). Barton and Choubey (1977) explain that the JCS parameter has an influence on the strength and deformation properties of the rock mass, especially if the walls are in direct contact, i.e., unfilled joints conditions.

Along with the JRC constant, the JCS is one of the input parameters of the empirical nonlinear equation of peak shear strength developed by Barton (1973), which were modified by Barton and Choubey (1977) and more recently by Barton and Bandis (1990), expressed by the Eq. 2.3.

$$\tau = \sigma_n \tan \left[ \text{JRC} \log \left( \frac{\text{JCS}}{\sigma_n} \right) + \phi_r \right] \quad 2.3$$

where  $\tau$  is the shear strength;  $\sigma_n$  is the normal stress; JRC is the joint roughness coefficient; JCS is the joint wall compression strength; and  $\phi_r$  is the residual friction angle, which can be estimating using the follow relation:

$$\phi_r = (\phi_b - 20^\circ) + 20^\circ \left( \frac{r}{R} \right) \quad 2.4$$

where  $\phi_b$  is the basic friction angle of the material; R is the Schmidt rebound number on dry unweathered sawn surfaces; and r is the Schmidt rebound number on wet joint surfaces.

In cases that joints are completely unweathered, Barton and Choubey (1977) mention that the wall strength of a discontinuity will be equal to the unconfined compression strength of the unweathered rock ( $\sigma_c$ ), where it can be estimated using the Point Load Strength test<sup>8</sup>, or even using field identification as described by the Table 2.8, presented by ISRM (1978). In cases of rock mass in a stage of weathering, the JCS will be lower than  $\sigma_c$ , and it is recommended using the Schmidt hammer test to determine the JCS parameter.

---

<sup>8</sup> A suggested method for determining the Point Load Strength test is described by Ulusay and Hudson (2007).

Through the correlation chart for Schmidt (L) hammer, according to ISRM (1978), relating rock density, compressive strength, and rebound number, it is possible determining the wall strength. This chart is presented by Deere and Miller (1966), based on the second author's Ph.D. thesis. Later it was involved in Eq. 2.5, introduced by Barton and Choubey (1977).

$$\log(\sigma_c) = 0.00088 y_d R + 1.01 \quad 2.5$$

where  $\sigma_c$  is the unconfined compression strength of surface in MPa; R is the Schmidt hammer rebound number; and  $y_d$  is the dry density of rock in  $\text{kN/m}^3$ .

**Table 2.8** - Strength estimation using field identification – Grades R0 to R6

Grade	Description	Field identification	$\sigma_c$ (MPa)
R0	Extremely weak	Indented by thumbnail.	0.25 – 1.0
R1	Very weak	Crumbles under firm blows of geological hammer. Can be peeled with a pocket knife.	1.0 – 5.0
R2	Weak	Can be peeled with a pocket knife with difficulty. Shallow indentations made by a firm blow with point of geological hammer.	5.0 – 25
R3	Medium strong	Cannot be scraped or peeled with a pocket knife. Specimen can be fractured with a single firm blow of geological hammer.	25 – 50
R4	Strong	Specimen requires more than one blow of geological hammer to fracture.	50 – 100
R5	Very strong	Specimen requires many blows of geological hammer to fracture.	100 – 250
R6	Extremely strong	Specimen can only be chipped with the geological hammer.	> 250

Source: ISRM (1978).

### 2.3.6 Aperture

ISRM (1978) defines aperture as the perpendicular distance between rock walls of an open discontinuity, in which the intervening space is air or water filled. It has an influence on the deformability, shear strength and hydraulic conductivity of discontinuities (ZHANG, 2016). In cases that a discontinuity is filled, e.g., with clay, this

term aperture has no more meaning, and the perpendicular distance between the rock walls should be described in terms of the width of the infill (SIVAKUGAN *et al.*, 2013).

The aperture can be measured using a measuring tape of at least 3 m length, calibrated in mm and aided by equipment for washing the rock exposure and white spray paint. In cases of apertures visible in an outcrop, these should be greater than those within the rock mass, due to the processes of stress relief and weathering that a rock exposure is submitted. A much more reliable indication of undisturbed apertures may be estimated in tunnels that are machine bored (ISRM, 1979). Table 2.9 presents the descriptions of the apertures suggested by the International Society for Rock Mechanics.

**Table 2.9** - Apertures description of the discontinuities

Aperture (mm)	Description
< 0.1	Very tight
0.1 – 0.25	Tight
0.25 – 0.5	Partly open
0.5 – 2.5	Open
2.5 – 10	Moderately wide
> 10	Wide
1 – 10	Very wide
10 – 100	Extremely wide
> 1 m	Cavernous

Source: ISRM (1978).

### 2.3.7 Filling

Filling, or infilling (WYLLIE, 2018), is characterized in rock mechanics as the material that separates the adjacent rock walls of a discontinuity, e.g., calcite, chlorite, clay, silt, fault gouge, and breccia. In cases of discontinuities that are filled, as mentioned before, it has the perpendicular distance between the adjacent rock wall termed as the width of the infilled discontinuity (ISRM, 1978; WYLLIE, 2018).

The physical behavior of the filled discontinuities, regarding their shear strength, deformability, and permeability, will vary according to the following factors: (1) mineralogy of infilling material; (2) grading or particular size; (3) over-consolidation ratio; (4) water content and permeability; (5) previous shear displacement; (6) wall roughness; (7) width; and (8) fracturing or crushing of wall rock. The procedures to estimate these features are described in ISRM (1978).

In the case of estimating the filling strength, ISRM (1978) suggests using the Table 2.10, where the undrained shear strengths are equal to one half of the given uniaxial compressive strength (S1 to S6).

**Table 2.10** - Strength estimation using field identification – Grades S1 to S6

<b>Grade</b>	<b>Description</b>	<b>Field identification</b>	<b><math>\sigma_c</math> (MPa)</b>
S1	Very soft clay	Easily penetrated several inches by fist	< 0.025
S2	Soft clay	Easily penetrated several inches by thumb	0.025 – 0.05
S3	Firm clay	Can be penetrated several inches by thumb with moderate effort	0.05 – 0.10
S4	Stiff clay	Readily indented by thumb but penetrated only with great effort	0.10 – 0.25
S5	Very stiff clay	Readily indented by thumbnail	0.25 – 0.50
S6	Hard clay	Indented with difficulty by thumbnail	> 0.5

Source: ISRM (1978).

### 2.3.8 Seepage

Seepage is the water flow and free moisture visible in individual discontinuities, or in the rock mass. It occurs often through discontinuities, defined as the secondary permeability, but it also can occur through the pores from the intact rock blocks, defined as the primary permeability. The primary permeability is more frequent in the sedimentary rocks (ISRM, 1978).

The prediction of seepage conditions of a rock mass in the preliminary stages may give an overall view of the stability or construction difficulties. A description of the seepage from individual unfilled and filled discontinuities, or from specific sets exposed in a tunnel or in an outcrop, can be done using the Tables 2.11 and 2.12.

## 2.4 Rock Mass Classification Systems

In any practice of rock engineering, in general, a reliable estimation of the rock mass behavior under changing stress conditions is fundamental for a safe and economical design project. However, this is a complex and difficult task, due to the heterogeneous and anisotropic characteristics of the rock material.

**Table 2.11** - Seepage rating in unfilled discontinuities

<b>Rating</b>	<b>Description</b>
I	The discontinuity is very tight and dry, water flow along it does not appear possible
II	The discontinuity is dry with no evidence of water flow
III	The discontinuity is dry but shows evidence of water flow, e.g., rust staining
IV	The discontinuity is damp, but no free water is present
V	The discontinuity shows seepage, occasional drops of water, but no continuous flow
VI	The discontinuity shows a continuous flow of water – estimate L/min and describe pressure, that is, low, medium, high

Source: ISRM (1978).

**Table 2.12** - Seepage rating in filled discontinuities

<b>Rating</b>	<b>Discontinuity characteristics</b>
I	The filling materials are heavily consolidated and dry, significant flow appears unlikely to very low permeability
II	The filling materials are damp, but no free water is present
III	The filling materials are wet, occasional drops of water
IV	The filling materials show signs of outwash, continuous flow of water (estimate L/min)
V	The filling materials are washed out locally, considerable water flow along out-wash channels (estimate L/min and describe pressure, that is, low medium, high)
VI	The filling materials are washed out completely, very high water pressures experienced, especially on first exposure (estimate L/min and describe pressure, that is, low, medium, high)

Source: ISRM (1978).

Different from others engineering sciences, such as in civil and mechanical engineering, where laboratory testing techniques have played a large role in determining the material's mechanical properties, quantifying rock mass strength and deformability for rock engineering purposes only in a laboratory is an impractical task (HOEK, 2012). As reported by Hoek (2012), the practice of testing rock specimens in laboratory allows only estimating a very small fraction of one percent of the rock mass volume.

Dealing with this limitation, different rock mass classification systems (RMCS) were proposed to be used as a guide for different rock engineering applications, based on past experience.

A summary of the general objectives of the RMCS are described by Bieniawski (1989):

- I. Identifying the most significant parameters responsible for influence the rock mass behavior;
- II. Dividing a rock mass into several classes with similar characteristics;
- III. Providing a basis for understanding the characteristics of each rock mass class;
- IV. Relating rock conditions experiences encountered in at other sites with the present site conditions;
- V. Deriving quantitative data and guidelines for engineering design; and
- VI. Providing a better communication between engineers and geologists.

Among the main rock mass classification systems published by the time in which this dissertation was written, the most recognized systems by the rock mechanics community are: (1) the Rock Load Classification (TERZAGHI, 1946); (2) the Rock Quality Designation (RQD) (DEERE *et al.*, 1967); (3) the Rock Structure Rating (RSR) concept (WICKHAM *et al.*, 1972, 1974); (4) the Rock Mass Rating (RMR) system (BIENIAWSKI, 1973, 1976, 1979, 1989); (5) the Q-system (BARTON *et al.*, 1974, BARTON, 2002); (6) the Geological Strength Index (GSI) system (HOEK, 1994; HOEK *et al.*, 1995; HOEK AND BROWN, 1997; MARINOS; HOEK, 2000); and (7) the Rock Mass Index (RMI) system (PALMSTRÖM, 1995, 1996a,b).

This study will be focusing on describing the classification schemes most cited in the literature, that is, RQD, RMR, Q and GSI systems, which are also used as an input parameter by different empirical methods for estimating the mechanical parameters of rock masses, as will be discussed later on this dissertation.

#### 2.4.1 Rock Quality Designation Index

The rock quality designation (RQD) was developed by Don Deere in 1964, however it was just formal presented by Deere *et al.* (1967), as reported by Deere and Deere (1988). This index was designed for use during early site evaluation to predict tunneling conditions (DEERE AND DEERE, 1989).

According to Deere *et al.* (1967), the RQD is defined as a modified borehole core recovery percentage in which all the pieces of sound core over 4 in (10 cm) are counted as recovery. The lengths of these sound core pieces are counted and divided by

the length of the core run (Eq. 2.6), where its value can be used as an index for estimating the engineering behavior of the rock mass (DEERE *et al.*, 1967).

$$\text{RQD (\%)} = \frac{\sum \text{lengths of sound core pieces } \geq 4 \text{ in } (\cong 10 \text{ cm})}{\text{Total length of the core run}} \quad 2.6$$

Deere and Deere (1989) mentioned that 10 cm requisite length was chosen after they considered it as a reasonably lower limit for fair quality rock mass within three or four joint sets of close to moderate spacing. However, in cases where a core piece has a length longer than RQD threshold length of 10 cm, it should not be considered if the core is not hard and sound, as reported by the International Society for Rock Mechanics (1978).

The RQD index ranges from 0 to 100%, where a high RQD values will identify a rock mass with good quality, while an RQD ranging from 0 to 50% are indicative of poor quality rock mass (DEERE *et al.*, 1967). A correlation of the description of the rock quality and RQD index is shown in Table 2.13, and Figure 2.10 illustrates a procedure for measurement of RQD, described by Deere and Deere (1988).

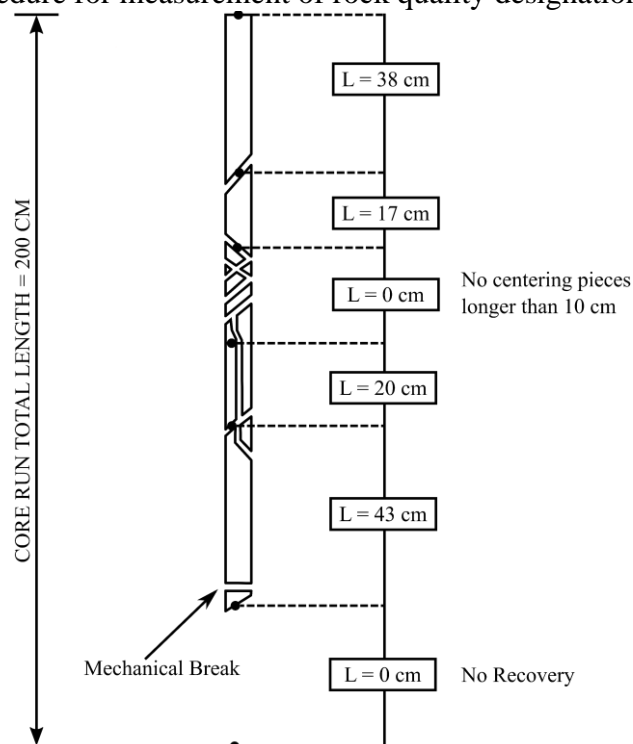
**Table 2.13** - Classification of the rock mass based on RQD range values

RQD (%)	Rock Mass Quality
0 – 25	Very poor
25 – 50	Poor
50 – 75	Fair
75 – 90	Good
90 – 100	Excellent

Source: Deere *et al.* (1967).

Although the RQD index is not sufficient on its own for a full description of a rock mass, as mentioned by Bieniawski (1989), it is an important rating parameter in several classification systems, e.g., the Rock Mass Rating system and the Q-system. It also can be used to estimate the deformation modulus and unconfined compressive strength of rock masses, as will be described in advance. Therefore, in this study, the RQD index will be considered as rock mechanics system.

**Figure 2.10** - Procedure for measurement of rock quality designation RQD



Source: adapted from Deere and Deere (1989).

Besides the original procedure for measuring RQD, as reported by Deere and Deere (1988), several empirical correlations were developed to estimate the borehole core quality index based on scanline surveys<sup>9</sup>.

During the 1970s, Priest and Hudson (1976) and Hudson and Priest (1979) suggested a relationship between the rock quality designation and mean discontinuity frequency per meter, expressed by Eq. 2.7. This expression was obtained through a negative exponential distribution of discontinuity value obtained from field scanline measurements carried out by the authors. Figure 2.11 shows the behavior of this correlation for the RQD and the mean discontinuity spacing.

$$\text{RQD} = 100e^{-0.1\lambda}(0.1\lambda + 1) \quad 2.7$$

where  $\lambda$  is the mean discontinuity frequency per unit length.

In case that average number of discontinuity per meter is between 6 and 16, i.e., mean discontinuity spacing of 167 mm and 62,5 mm, the relationship between RQD

<sup>9</sup> Technique in which a line is drawn over an outcropped rock surface and all the discontinuities intersecting it are described and measured (CHAMINÉ *et al.*, 2015).

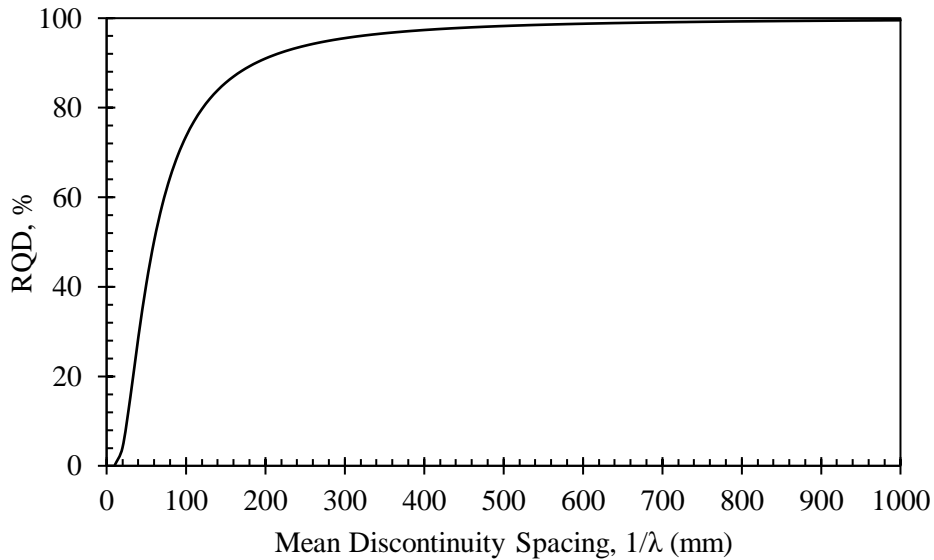


and  $\lambda$  is approximately linear, as illustrated in Figure 2.12, thus the Eq. 2.7 can be reduced into Eq. 2.8 (Priest and Hudson, 1976).

$$\text{RQD} = -3.68\lambda + 110.4$$

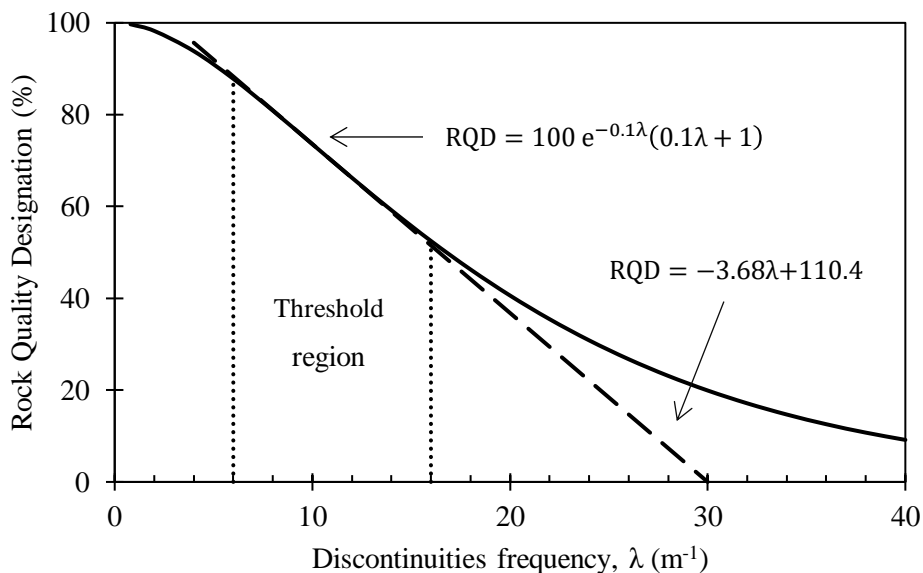
2.8

**Figure 2.11** - Relationship between RQD and mean discontinuity spacing



Source: Priest and Hudson (1976).

**Figure 2.12** - Relationship between RQD and mean discontinuity frequency



Source: Priest and Hudson (1976).

Although the practicality of the Priest and Hudson's correlation, it was only designed for long scanline measurements. In order to estimate the RQD for a finite (short) scanline length, Sen and Kazi (1984) proposed the following expression:

$$RQD = \frac{100}{1 - e^{-0.1\lambda} - \lambda L e^{-0.1\lambda}} [e^{-0.1\lambda}(0.1\lambda + 1) - e^{-0.1\lambda}(\lambda L + 1)] \quad 2.9$$

where L is the length of the scanline.

Seismic velocity also can be used to estimate RQD. In the same publication in which the RQD concept was formal published, Deere *et al.* (1967) proposed a correlation between RQD and the velocity index, which is the square of the ratio of in situ seismic compressional velocity<sup>10</sup> (P-wave velocity) to the laboratory compressional sonic velocity<sup>11</sup>, expressed by Eq. 2.10. Table 2.14 shows the correlation of velocity index and RQD, presented by Coon and Merritt (1970).

$$RQD = \left( \frac{V_{pf}}{V_{pl}} \right)^2 \times 100\% \quad 2.10$$

where  $V_{pf}$  is the P-wave velocity of the in situ rock mass and  $V_{pl}$  is the P-wave velocity of the intact rock measured in laboratory.

**Table 2.14** - Correlation between RQD and velocity index

RQD (%)	Rock Mass Quality	Velocity Index
0 – 25	Very poor	0 – 0.20
25 – 50	Poor	0.20 – 0.40
50 – 75	Fair	0.40 – 0.60
75 – 90	Good	0.60 – 0.80
90 – 100	Excellent	0.80 – 1.00

Source: Coon and Merritt (1970).

#### 2.4.2 Rock Mass Rating System

The Rock Mass Rating (RMR) system, also known as the Geomechanics Classification, was introduced by Bieniawski (1973). Over the years this system was modified in order to conform with international standards and procedures, besides to new case histories that became available after the publication of the original version. The last

<sup>10</sup> The field velocities may be taken through seismic refraction, cross-hole, or downhole technique (DEERE; DEERE, 1989).

<sup>11</sup> The laboratory velocity is measured by a sonic test on a saturated core cylinder under a 3000 psi axial load (COON; MERRITT, 1970).

considerable review of the RMR system was made by Bieniawski (1989), which, according to the author, maintained the same principle proposed by the original version.

The RMR system classify the rock mass using the following six parameters: (1) the uniaxial compressive strength of intact rock,  $\sigma_{ci}$  or UCS (see Table 2.15); (2) the rock quality designation, RQD (see Table 2.16); (3) the spacing of discontinuities (see Table 2.17); (4) the condition of discontinuities (see Table 2.18); (5) the groundwater conditions (see Table 2.19); and (6) the orientation of discontinuities (see Table 2.21). Each of these parameters will attribute a rating for the rock mass, which combined they generate the overall RMR value of it.

**Table 2.15** - The uniaxial compressive strength of intact rock - 1° RMR parameter

Uniaxial Compressive Strength, MPa	Point Load Strength Index, MPa	Rating
> 250	> 10	15
100 – 250	4 – 10	12
50 – 100	2 – 4	7
25 – 50	1 – 2	5
5 – 25	N/A	2
1 – 5	N/A	1
< 1	N/A	0

Source: adapted from Bieniawski (1989).

**Table 2.16** - The rock quality designation (RQD) - 2° RMR parameter

RQD (%)	Rating
90 – 100	20
75 – 90	17
50 – 75	13
25 – 50	8
< 25	3

Source: adapted from Bieniawski (1989).

**Table 2.17** - Spacing of discontinuities - 3° RMR parameter

Spacing (mm)	Rating
> 2000	20
600 – 2000	15
200 – 600	10
60 – 200	8
> 60	5

Source: adapted from Bieniawski (1989).

**Table 2.18** - Conditions of discontinuities - 4° RMR parameter

<b>Condition of discontinuities</b>	<b>Rating</b>
Very rough surfaces; not continuous; no separation; unweathered wall rock	30
Slightly rough surfaces; separation < 1 mm; slightly weathered walls	25
Slightly rough surfaces; separation < 1 mm; highly weathered wall	20
Slickensided surfaces; or gouge < 5 mm thick; or separation 1- 5 mm; continuous	10
Soft gouge > 5 mm thick; or separation > 5 mm; continuous	0

Source: adapted from Bieniawski (1989).

**Table 2.19** - Groundwater conditions - 5° RMR parameter

<b>Inflow per 10 m tunnel length (L/min)</b>	<b>Joint Water Pressure Major Principal Stress</b>	<b>General Conditions</b>	<b>Rating</b>
None	0	Completely Dry	15
< 10	< 0.1	Damp	10
10 – 25	0.1 – 0.2	Wet	7
25 – 125	0.2 – 0.5	Dripping	4
> 125	> 5	Flowing	0

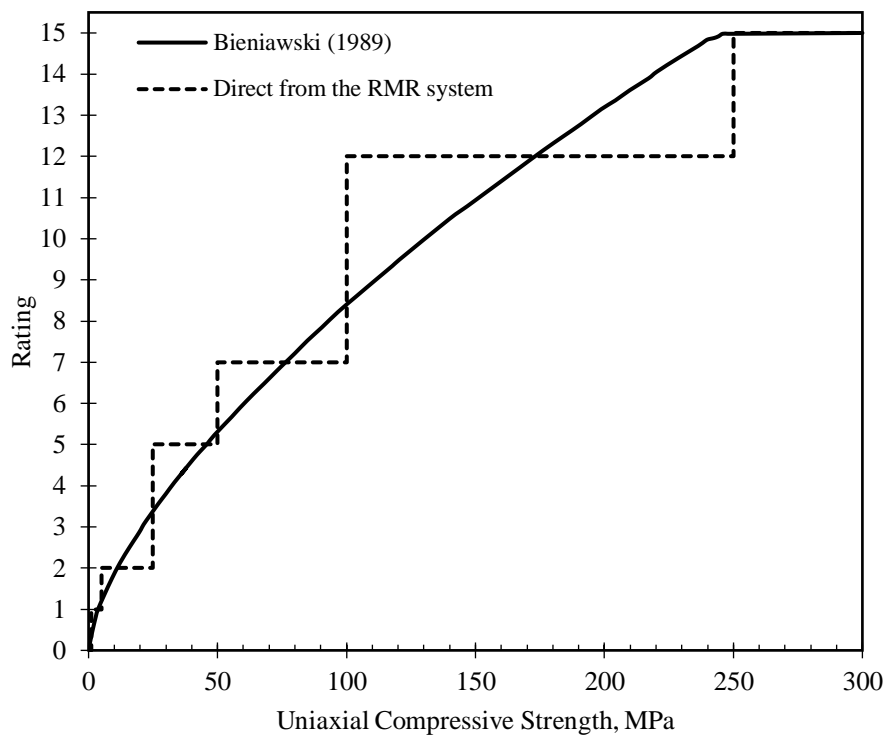
Source: adapted from Bieniawski (1989).

The first five parameters of the RMR system are grouped into five ranges of values, described through Table 2.15 to 2.19, where a higher rating indicating better rock mass quality. In order to remove the impression that abrupt changes in ratings occur between categories for the uniaxial compressive strength of intact rock, the RQD and the spacing of discontinuities, Bieniawski (1989) suggested using the charts given in Figures 2.13 to 2.15.

In the absence of the rock quality designation values, Lawson and Bieniawski (2013) suggested a new parameter, the discontinuity density parameter, which combines the ratings of the discontinuity and the RQD. Figure 2.16 presents the chart for estimating the discontinuity density parameter rating.

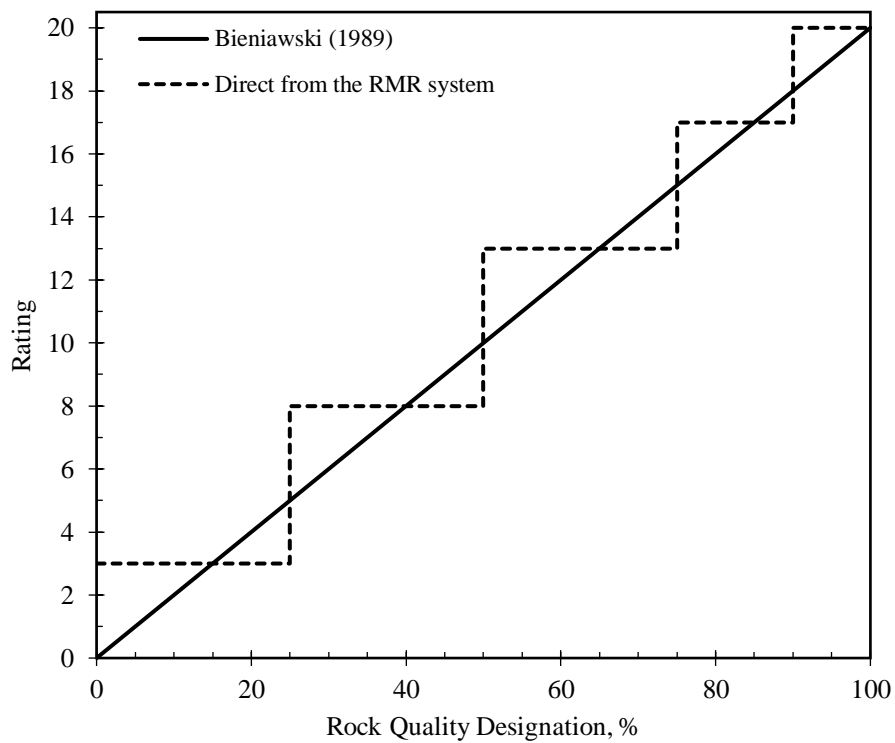
To assist the rating estimation of the discontinuity conditions, Bieniawski (1989) recommends using the guidelines presented in Table 2.20. In this table, some conditions are mutually exclusive, e.g., if infilling is present, thus the roughness is irrelevant.

**Figure 2.13** - Ratings for strength of intact rock in the RMR system



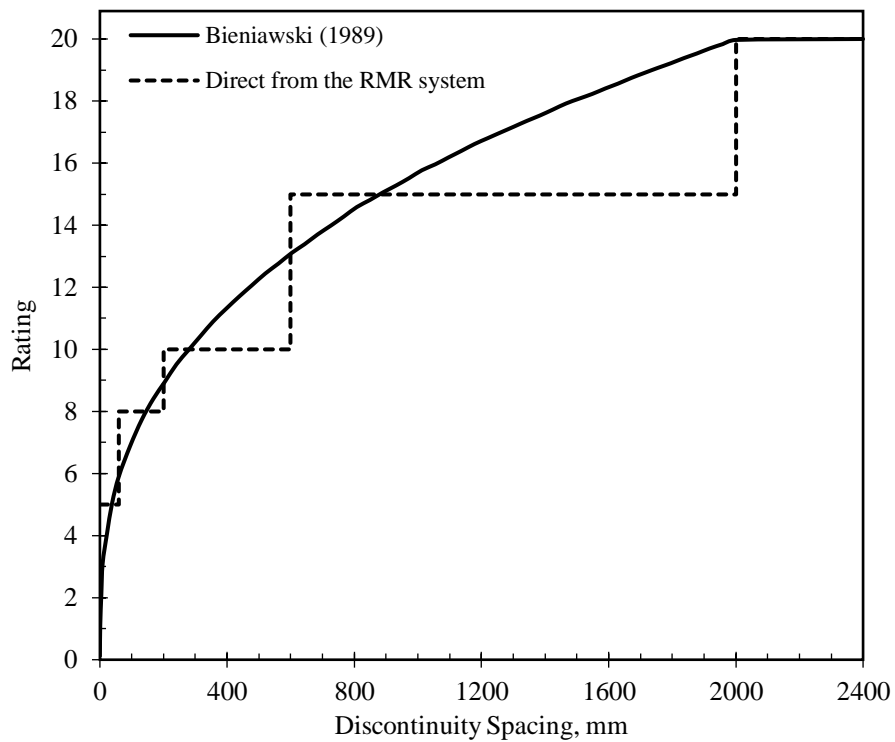
Source: adapted from Bieniawski (1989).

**Figure 2.14** - Ratings for RQD in the RMR system



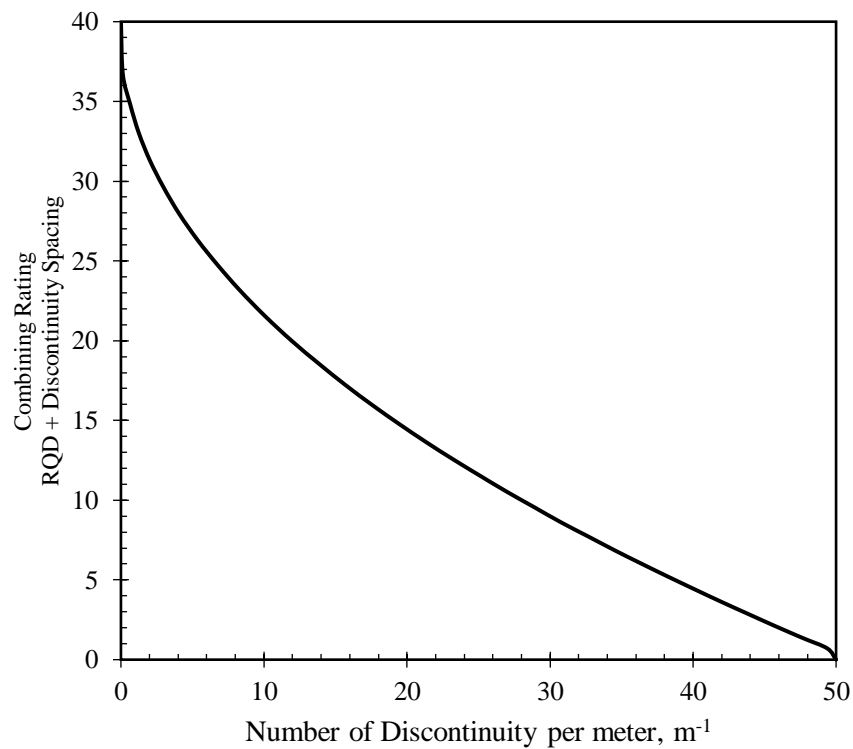
Source: adapted from Bieniawski (1989).

**Figure 2.15** - Ratings for discontinuity spacing in the RMR system



Source: adapted from Bieniawski (1989).

**Figure 2.16** - Input chart for combined rating of the RQD and discontinuity spacing based on the rock discontinuity density



Source: adapted Lowson and Bieniawski (2013).

**Table 2.20** - Guidelines for classification of discontinuity conditions for Geomechanics Classification

<b>Parameter</b>	<b>Ratings</b>				
Persistence	<1m 6	1-3 m 4	3-10 m 2	10-20 m 1	>20 m 0
Aperture	None 6	<0.1 mm 5	0.1-1 mm 4	1-5 mm 1	>5 mm 0
Roughness	Very Rough 6	Rough 5	Slightly Rough 3	Smooth 1	Slickensided 0
Infilling	None 6	HF <5 mm 4	HF >5 mm 2	SF <5 mm 2	SF >5 mm 0
Weathering	Unweathered 6	Slightly weathered 5	Moderately weathered 3	Highly weathered 1	Decomposed 0

HF and SF are hard and soft filling, respectively

Source: adapted from Bieniawski (1989).

The sixth and last parameter used in Bieniawski's system, the orientation of discontinuity, is an adjustment factor which affects the overall RMR of the rock mass, depending on how favorable or unfavorable the discontinuity orientation is in respect to the project. Table 2.21 presents the rating adjustment suggested by Bieniawski (1989) for discontinuity orientations.

**Table 2.21** - Rating adjustment for discontinuity orientations - 6° RMR parameter

<b>Orientation of discontinuities</b>	<b>Very Favorable</b>	<b>Favorable</b>	<b>Fair</b>	<b>Unfavorable</b>	<b>Very Unfavorable</b>
Tunnels and mines	0	-2	-5	-10	-12
Foundation	0	-2	-7	-15	-25
Slopes	0	-5	-25	-50	-60

Source: adapted from Bieniawski (1989).

**Table 2.22** - Rock mass classes from Geomechanics Classification

<b>Class</b>	<b>Rating</b>	<b>Description</b>
I	100 – 81	Very good rock
II	80 – 61	Good rock
III	60 – 41	Fair rock
IV	40 – 21	Poor rock
V	21 – 0	Very poor rock

Source: adapted from Bieniawski (1989).

**Table 2.23** - Meaning of rock mass classes from Geomechanics Classification

Class	Average stand-up time	c (KPa)	$\phi$ (deg)
I	20 year for 15 m span	> 400	> 45
II	1 year for 10 m span	300 – 400	35 – 45
III	1 week for 5 m span	200 – 300	25 – 35
IV	10 hours for 2.5 m span	100 – 200	15 – 25
V	30 min for 1 m span	<100	< 15

c is the cohesion of the rock mass.

$\phi$  is the friction angle of the rock mass.

Source: adapted from Bieniawski (1989).

After the first five parameters are rated and summed, and the adjustment rating is defined, the rock mass can be classified into five different rock mass classes (I, II, III, IV, and V), conforming Table 2.22. Table 2.23 presents the practical meaning of each rock mass class, relating it to specific engineering problems.

#### 2.4.3 Tunnelling Quality Index

The Q-system was designed by Barton *et al.* (1974) and later reviewed by Barton (2002). It is a rock mass classification based on a rock mass quality parameter, the Q-value, used primarily to characterize the rock mass and to assist the tunnel support design. The numerical value of Q ranges on a scale from 0.001, for exceptionally poor rock mass quality, up to 1000, for exceptionally good rock mass quality, Table 2.24, and is estimated using the following empirical equation:

$$Q = \frac{RQD}{J_n} \times \frac{J_r}{J_a} \times \frac{J_w}{SRF} \quad 2.11$$

where RQD is the rock quality designation;  $J_n$  is the rating for number of joint sets;  $J_r$  is the rating for joint surface roughness;  $J_a$  is the rating for joint alteration;  $J_w$  is the rating for water reduction factor; and SRF is the rating for stress reduction factor.

The first quotient in Eq. 2.11,  $RQD/J_n$ , represents the overall structure of the rock mass, representing a crude measure of the relative block size, which its value ranges from 0.5 to 200 (BARTON *et al.*, 1974). The RQD rating is presented in Table 2.25, very similar to those used by the RMR system. The  $J_n$  value is estimated using Table 2.26, in



which higher values of  $J_n$  are assigned for very jointed rock masses, while low values for massive rock masses.

**Table 2.24** - Rock mass classes from Q-system

<b>Rock Mass Classification</b>	<b>Q-value</b>
Exceptionally good	1000 – 400
Extremely good	400 – 100
Very good	100 – 40
Good	40 – 10
Fair	10 – 4
Poor	4 – 1
Very poor	1 – 0.1
Extremely poor	0.1 – 0.01
Exceptionally poor	0.01 – 0.001

Source: adapted from Barton *et al.* (1973).

**Table 2.25** - Rock quality designation (RQD) for Q-system

<b>Rock quality designation</b>	<b>RQD (%)</b>
A Very poor	0 – 25
B Poor	25 – 50
C Fair	50 – 75
D Good	75 – 90
E Excellent	90 – 100

i) For  $RQD \leq 10$  (including 0), a nominal value of 10 is used to evaluate Q

ii) RQD intervals of 5, i.e., 100, 95, 90, etc., are sufficiently accurate

Source: adapted from Barton (2002).

**Table 2.26** - Joint set number ( $J_n$ ) for Q-system

<b>Joint set number</b>	<b><math>J_n</math></b>
A Massive, no or few joint	0.5 – 1
B One joint set	2
C One joint set plus random joints	3
D Two joint sets	4
E Two joint sets plus random joints	6
F Three joint sets	9
G Three joint sets plus random joints	12
H Four or more joint sets, random, heavily jointed, etc.	15
J Crushed rock, earthlike	20

i) For tunnel intersections, use  $3.0 \times J_n$

ii) For portals use  $2.0 \times J_n$

Source: adapted from Barton (2002).

The second quotient in Q-system correlation,  $J_r/J_a$ , according to Barton *et al.* (1974), represents the roughness and frictional characteristics of the discontinuity walls or filling materials, where the function  $\tan^{-1}(J_r/J_a)$  gives a fair approximation to the actual shear strength. The  $J_r$  parameter is estimated based on the joint roughness conditions, using Table 2.27, while the  $J_a$  is determined through Tables 2.28 to 2.30, conforming to the joint alteration conditions within the rock mass.

The third and last quotation in Eq. 2.11,  $J_w/SRF$ , is defined by Barton (2002) as an active stress term, which is the relative effect of water, faulting, strength/stress ratio, squeezing, or swelling. The  $J_w$  parameter is a measure of water pressure that influences the shear strength directly, once the presence of water can reduce the effective normal stress (Barton *et al.*, 1974). This parameter is estimated using the Table 2.31, ranging from 0.05 to 1.0, where for dry conditions it will be assigned with high values, while for inflow conditions this parameter value will be lower, depending on the inflow intensity.

The SRF is a total stress parameter, defined by the Tables 2.32 to 2.35, ranging from 0.5 to 400, with 0.5 being the most favorable condition, i.e., high stress and very tight structure, and 400 being the most unfavorable condition, i.e., heavy rock burst.

**Table 2.27 - Joint roughness number ( $J_r$ ) for Q-system**

Joint roughness number	$J_r$
<b>(a) Rock-wall contact, and (b) rock wall contact before 10 cm shear</b>	
A Discontinuous joints	4
B Rough or irregular, undulating	3
C Smooth, undulating	2
D Slickensided, undulating	1.5
E Rough or irregular, planar	1.5
F Smooth, planar	1.0
G Slickensided, planar	0.5
<b>(b) No rock-wall contact when sheared</b>	
H Zone containing lay minerals thick enough to prevent rock-wall contact	1.0
J Sand, gravely or crushed zone thick enough to prevent rock-wall contact	1.0
i) Add 1.0 if the mean spacing of the relevant joint set is greater than 3 m	
ii) $J_r = 0.5$ can be used for planar, slickensided joints having lineation, provided the lineations are oriented for minimum strength	

Source: adapted from Barton (2002).

**Table 2.28** - Joint alteration number ( $J_a$ ) for Q-system – Part 1

Joint alteration number	$\phi_r$ (°)	$J_a$
<b>(a) Rock-wall contact (no mineral fillings, only coatings)</b>		
A	Tightly healed, hard, non-softening, impermeable filling, i.e., quartz or epidote	- 0.75
B	Unaltered joint walls, surface staining only	25-35 1.0
C	Slightly altered joint walls, non-softening mineral coating, sandy particles, clay-free disintegrated rock, etc.	25-30 2.0
D	Silty- or sandy-clay coating, small clay fraction (non-softening)	20-25 3.0
E	Softening or low friction clay mineral coating, i.e., kaolinite or mica; also, chlorite, talc, gypsum, graphite, etc., and small quantities of swelling clays	8-16 4.0

Source: adapted from Barton (2002).

**Table 2.29** - Joint alteration number ( $J_a$ ) for Q-system – Part 2

Joint alteration number	$\phi_r$ (°)	$J_a$
<b>(b) Rock-wall contact before 10cm shear (thin mineral fillings)</b>		
F	Sandy particles, clay-free disintegrated rock, etc.	25-30 4.0
G	Strongly over-consolidated non-softening clay mineral fillings (continuous, but < 5mm thickness)	16-24 6.0
H	Medium or low over-consolidation, softening, clay mineral fillings (continuous, but <5 mm thickness)	12-16 8.0
J	Swelling-clay fillings, i.e., montmorillonite (continuous, but <5mm); value of $J_a$ depends on per cent of swelling clay-size particles, and access to water, etc.	6-12 8-12

Source: adapted from Barton (2002).

**Table 2.30** - Joint alteration number ( $J_a$ ) for Q-system – Part 3

Joint alteration number	$\phi_r$ (°)	$J_a$
<b>(c) No rock-wall contact when sheared (thick mineral fillings)</b>		
KLM	Zones or bands of disintegrated or crushed rock and clay (see G, H, and J for description of clay conditions)	6-24 6, 8 or 8-12
N	Zone or bands of silty- or sandy-clay, small clay fraction (non-softening)	- 5.0
OPR	Thick, continuous zone or bands of clay (see G, H, J for description of clay condition)-	6-24 10, 13, or 13-20

Source: adapted from Barton (2002).

**Table 2.31** - Joint water reduction factor ( $J_w$ ) for Q-system

Joint water reduction	$P_w$ (KPa)	$J_w$
A Dry excavation or minor inflow, i.e., < 51 L/min locally	< 1	1.0
B Medium inflow or pressure, occasional outwash of joint fillings	1-2.5	0.66
C Large inflow or high pressure in competent rock with unfilled joints	2.5-10	0.5
D Large inflow or high pressure, considerable outwash of joint fillings	2.5-10	0.33
E Exceptionally high inflow or water pressure at blasting, decaying with time	> 10	0.2-0.1
F Exceptionally high inflow or water pressure continuing without noticeable decay	> 10	0.1-0.05

i)  $P_w$  is the approximate water pressure  
ii) C to F are crude estimates  
iii) Increase  $J_w$  parameter if drainage measures are installed

Source: adapted from Barton (2002).

**Table 2.32** - Stress reduction factor (SRF) for Q-system – Part 1

Stress Reduction factor	SRF
<b>(a) Weakness zones intersecting excavation, which may cause loosening of rock mass when tunnel is excavated</b>	
A Multiple occurrences of weakness zones containing lay or chemically disintegrated rock, very loose surround rock (any depth)	10
B Single weakness zones containing clay or chemically disintegrated rock ( depth of excavation $\leq$ 50m)	5
C Single weakness zones containing clay or chemically disintegrated rock ( depth of excavation > 50m)	2.5
D Single weakness zones in competent rock (clay-free), loose surrounding rock (any depth)	7.5
E Single shear zones in competent rock; clay free (depth of excavation $\leq$ 50m)	5.0
F Single shear zones in competent rock; clay free (depth of excavation > 50m)	2.5
G Loose, open joints, heavily jointed, etc. (any depth)	5.0

i) Reduce these values of SRF by 25-50% if the relevant shear zones only influence but do not intersect the excavation. This will also be relevant for characterization.

Source: adapted from Barton (2002).

**Table 2.33** - Stress reduction factor (SRF) for Q-system – Part 2

<b>Stress Reduction factor</b>		$\sigma_c / \sigma_1$	$\sigma_\theta / \sigma_c$	<b>SRF</b>
<b>(b) Competent rock, rock stress problems</b>				
H	Low stress, near surface, open joints	> 200	< 0.01	2.5
J	Medium stress, favorable stress condition	200-10	0.01-0.3	1
K	High stress, very tight structure. Usually favorable to stability, may be unfavorable to stability, may be unfavorable for wall stability	10-5	0.3-0.4	0.5-2
L	Moderate slabbing after > 1h in massive rock	5-3	0.5-0.65	5-50
M	Slabbing and rock burst after a few minutes in massive rock	3-2	0.65-1	50-200
N	Heavy rock burst (strain-burst) and immediate dynamic deformations in massive rock	< 2	> 1	200-400
i) For strong anisotropic virgin stress field (if measured), when $5 \leq \sigma_1 / \sigma_3 \leq 10$ , reduce $\sigma_c$ to $0,75\sigma_c$ ; when $\sigma_1 / \sigma_3 > 10$ , reduce $\sigma_c$ to $0,5\sigma_c$ – where $\sigma_c$ is the unconfined compression strength; $\sigma_1$ and $\sigma_3$ are the major and minor principal stress; and $\sigma_\theta$ is the maximum tangential stress (estimated from elastic theory).				
ii) Cases L, M and N are usually most relevant for support design of deep tunnel excavations in hard massive rock masses, with RQD/ $J_n$ ratios from about 50-200.				

Source: adapted from Barton (2002).

**Table 2.34** - Stress reduction factor (SRF) for Q-system – Part 3

<b>Stress Reduction factor</b>		$\sigma_\theta / \sigma_c$	<b>SRF</b>
<b>(c) Squeezing rock; plastic flow of incompetent rock under the influence of high rock pressure</b>			
O	Mild squeezing rock pressure	1-5	5-10
P	Heavy squeezing rock pressure	> 5	10-20
i) Reduce these values of SRF by 25-50% if the relevant shear zones only influence but do not intersect the excavation. This will also be relevant for characterization.			

Source: adapted from Barton (2002).

**Table 2.35** - Stress reduction factor (SRF) for Q-system – Part 4

<b>Stress Reduction factor</b>		<b>SRF</b>
<b>(d) Swelling rock; chemical swelling activity depending on presence of water</b>		
R	Mild swelling rock pressure	5-10
S	Heavy swelling rock pressure	10-15
i) Reduce these values of SRF by 25-50% if the relevant shear zones only influence but do not intersect the excavation. This will also be relevant for characterization.		

Source: adapted from Barton (2002).

Barton (1995, 2002) suggest normalizing the Q-value to include rocks that could be weaker or stronger than the assumed hard rock from the original Barton's system. Then, a new Q-value correlation is given by:

$$Q_c = \left[ \frac{\text{RQD}}{J_n} \times \frac{J_r}{J_a} \times \frac{J_w}{\text{SRF}} \right] \frac{\sigma_{ci}}{100} \quad 2.12$$

where  $Q_c$  is a normalized value of  $Q$  and  $\sigma_{ci}$  is the unconfined compressive strength of the intact rock in MPa.

Based on this new empirical correlation, Barton (2002) derived a frictional, FC, and cohesive component, CC, Eqs. 2.9 and 2.10, respectively, of the rock mass. Although the author considers unwise to present FC and CC as analog parameters of the angle of internal friction,  $\phi$ , and cohesion,  $c$ , from the Mohr-Coulomb failure criterion, he suggested that these shear-strength-like components are more accurate than the fixed  $\phi$  and  $c$  values obtained in Table 2.22, suggested by Bieniawski (1989).

$$\text{FC} = \tan^{-1} \left( \frac{J_r}{J_a} \times J_w \right) \quad 2.13$$

where FC is the frictional component of a rock mass in  $^\circ$ .

$$\text{CC} = \frac{\text{RQD}}{J_n} \times \frac{1}{\text{SRF}} \times \frac{\sigma_{ci}}{100} \quad 2.14$$

where CC is the cohesive component of a rock mass in MPa.

#### 2.4.4 Geological Strength Index

The Geological Strength Index (GSI) is a rock mass classification system used to describe a rock mass qualitatively based on geological observations. It was introduced first by Hoek (1994) and Hoek *et al.* (1995), where the authors proposed using the GSI number to estimate the empirical constants<sup>12</sup> of the Hoek-Brown failure criterion (Eqs. 2.15 to 2.18).

$$\sigma'_1 = \sigma'_3 + \sigma_{ci} \left( m_b \frac{\sigma'_3}{\sigma_{ci}} + s \right)^a \quad 2.15$$

---

<sup>12</sup> Before GSI was introduced, the Hoek-Brown empirical constants were calculated using expressions based on the RMR value.

$$m_b = m_i \exp\left(\frac{GSI - 100}{28 - 14D}\right) \quad 2.16$$

$$s = \exp\left(\frac{GSI - 100}{9 - 3D}\right) \quad 2.17$$

$$a = \frac{1}{2} + \frac{1}{6} \left[ \exp\left(-\frac{GSI}{15}\right) - \exp\left(-\frac{20}{3}\right) \right] \quad 2.18$$

where  $\sigma'_1$  and  $\sigma'_3$  are the major and minor effective principal stress at failure, respectively;  $m_i$  and  $m_b$  is the value of the Hoek-Brown constant for the intact rock and rock mass, respectively;  $s$  and  $a$  are constants which depend upon the characteristics of the rock mass; GSI is the Geological Strength Index of the rock mass; and  $D$  is the disturbance factor.

According to Hoek and Brown (2018), the GSI system incorporates the two major parameters that most influence the mechanical properties of a rock mass: (1) the overall structure, also known as the blockiness, and (2) the surface condition of discontinuities. The first parameter is inherent to the interlocking characteristics of the rock pieces, ranging from intact to laminated conditions, Table 3.36, while the second stands for the conditions of the discontinuities, ranging from very good to very poor conditions, Table 2.37.

**Table 2.36** - Blockiness of the rock mass and its description used in Geological Strength Index (GSI) system

Class	Blockiness	Description
B-I	Intact or massive	Intact rock specimens or massive in situ rock with few widely spaced discontinuities
B-II	Blocky	Well interlocked undisturbed rock mass consisting of cubical blocks formed by three intersecting discontinuity set
B-III	Very blocky	Interlocked, partially disturbed mass with multi-faceted angular blocks formed by 4 or more joint sets
B-IV	Block, disturbed, seamy	Folded with angular blocks formed by many intersecting discontinuity sets; persistence of bedding planes or schistosity
B-V	Disintegrated	Poorly interlocked, heavily broken rock mass with mixture of angular and rounded rock pieces
B-VI	Laminated, sheared	Lack of blockiness due to close spacing of weak schistosity or shear planes

Source: adapted from Hoek and Marinos (2000).

**Table 2.37** - Surface conditions and its description used in Geological Strength Index (GSI) system

Class	Surface Conditions	Description
D-I	Very good	Very rough, fresh unweathered surfaces
D-II	Good	Rough, slightly weathered, iron stained surfaces
D-III	Fair	Smooth, moderately, weathered and altered surfaces
D-IV	Poor	Slickensided, highly weathered surfaces with compact coatings or fillings or angular fragments
D-V	Very Poor	Slickensided, highly weathered surfaces with soft clay coating or fillings

Source: adapted from Hoek and Marinos (2000).

Figure 2.17 presents the traditional GSI chart<sup>13</sup>, derived from the studies of Hoek and Brown (1997) and Marinos and Hoek (2000), which is used to estimate the GSI from a rock mass taking the descriptions presented in Tables 2.35 and 2.36 into account.

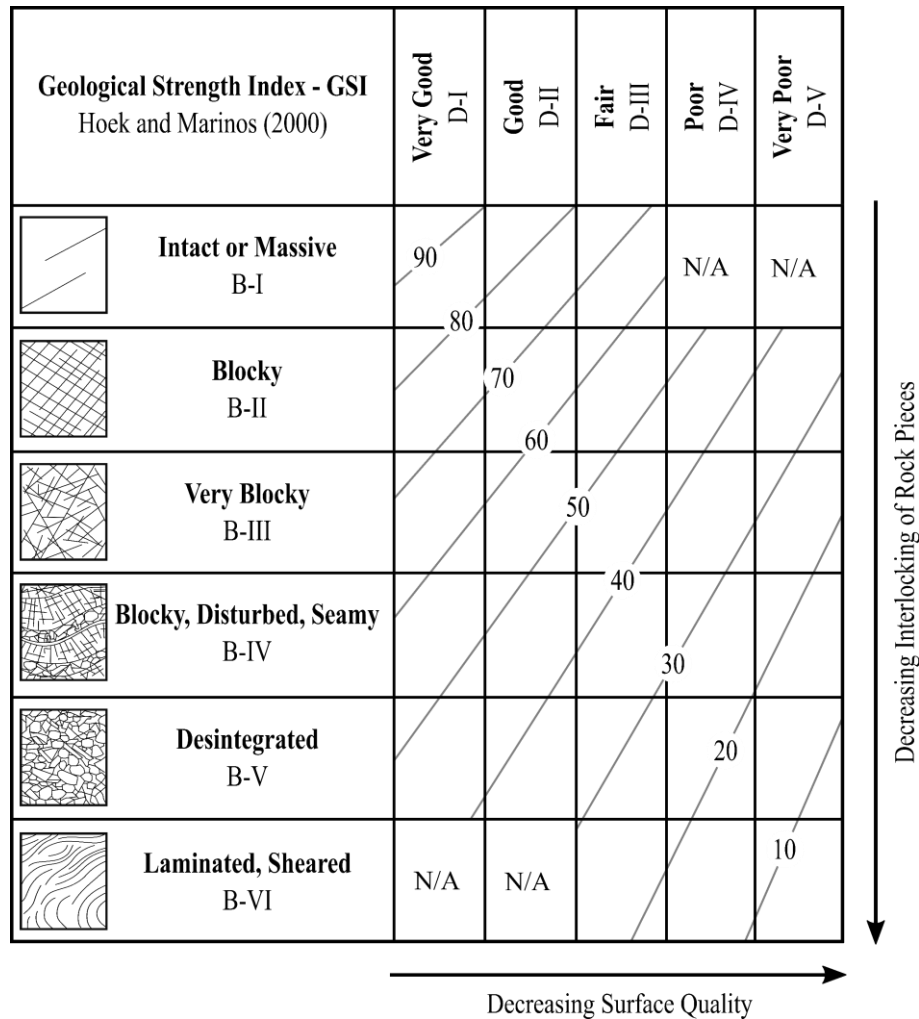
The GSI system should be used primarily when the rock mass contains a sufficient number of randomly oriented joints resulting in an isotropic behavior of the rock mass (MARINOS *et al.*, 2005). In cases where the failure is controlled by three-dimensional geometry of intersecting features in the rock mass, the GSI should not be used, as reported by Hoek and Brown (2019). In these scenarios, the authors suggest that stability analysis for calculating the factors of safety of sliding blocks or wedges should be applied instead of Hoek's classification schemes.

Although there are plenty of empirical methods for estimating the rock mass strength and deformation parameters using the rock mass classification system, as will be discussed next chapter, the GSI is the only directly linked to these engineering parameters, including the Mohr-Coulomb and Hoek-Brown strength criteria parameters, as reported by Cai *et al.* (2004). These authors applied the GSI system to characterize the jointed rock masses at Kannagawa and Kazunogawa underground powerhouses in Japan, and they founded that both the means and variances of cohesion, angle of internal friction, and deformation modulus predicted from the quantified GSI classification scheme were in good agreement with field data.

<sup>13</sup> For heterogeneous and tectonically disturbed rock masses, such as Flysch, it is recommended using the chart proposed by Marinos and Hoek (2001).



**Figure 2.17** - The Geological Strength Index (GSI) chart designed by Hoek and Marinos (2000)



Source: adapted from Marinos *et al.* (2005).

#### 2.4.5 Correlations between the classification schemes

It is a common practice in many rock engineering projects to use different rock mass classification schemes for determining the engineering qualities of rock masses by the engineering and geological staff. As a result of this, based on the field data obtained from different case histories, several authors proposed some correlations among the classification schemes discussed in this chapter (BIENIAWSKI, 1976; ABAD *et al.*, 1983; HOEK, 1994; BARTON, 1995; SOUFI *et al.*, 2018).

Among the RMR-Q correlation, Bieniawski's (1976) and Barton's (1995) correlations, Eq. 2.19 and 2.20, respectively, are highlighted in this dissertation.

$$\text{RMR} = 9 \ln Q + 44 \leftrightarrow Q = \exp\left(\frac{\text{RMR} - 44}{9}\right) \quad 2.19$$

$$\text{RMR} = 15 \log Q + 50 \leftrightarrow Q = 10^{\frac{\text{RMR}-50}{15}} \quad 2.20$$

Regarding the GSI-based correlations, Hoek (1994) recommends the following correlations for estimating the RMR number and the Q-value, respectively:

$$\text{GSI} = \text{RMR} - 5 \quad 2.21$$

$$\text{GSI} = 9 \ln Q + 44 \quad 2.22$$

Eq. 2.21 should be used if the RMR number is estimated from Bieniawski's 1989 classification scheme, assuming the rock mass completely dry and with the orientation of discontinuities very favorable to the project. In cases where GSI is estimated from Bieniawski's 1976 classification scheme, their values should be assumed the same, considering the rock mass completely dry and with the orientation of discontinuities very favorable to the project as well.

To use Eq. 2.22, the Q-value should be calculated using Eq. 2.11 assuming the joint water reduction factor (Jw) and the stress reduction factor (SRF) as a value of 1 for both parameters.

## 2.5 Conclusions

Since the mechanical behavior of rock masses is directly influenced by the conditions of the intact rock blocks and the geological discontinuities, several classification schemes based on both features were proposed to build up a picture of the rock mass to predict its quality for engineering purposes, including estimating its strength and deformation parameters. This chapter presented the most widely classification systems, i.e., RQD, RMR, Q, and GSI, used for describing qualitatively the rock mass.

Among these rock mass classification schemes, RQD is a single parameter-based, taking into account only the density of discontinuities. The RMR and Q systems, on the other hand, are based on six parameters, dealing with the similar conditions of the discontinuities (spacing, aperture, roughness, infilling, and weathering), but given

different weightings. The main difference between these systems lies in the fact that the RMR system takes the compressive strength into account, while Q-system considers the stress condition given as the stress reduction factor (SRF) parameter.

The Geological Strength Index (GSI) system, in comparison to the other classification schemes, is an essentially qualitative tool that relies more on geological observation and less on numerical values. It is the only system that was developed primarily to link to the mechanical parameters of the rock mass.

### 3 EMPIRICAL METHODS BASED ON CLASSIFICATION SCHEMES TO ESTIMATE ROCK MASS STRENGTH AND DEFORMATION PARAMETERS FOR NUMERICAL MODELING PURPOSES

In rock engineering practices, including underground excavations, open-pit mines, road cuts, and foundations of structures to be built on rocks, estimating the design input parameters such as strength and deformation parameters of the rock mass is a necessary step in any numerical modeling. Among the most commonly used methods for this purpose, using empirical correlations based on classification schemes systems are the most cost-effective (CAI *et al.*, 2004, 2007; HOEK; DIEDERICHS, 2006; ZHANG, 2010, 2017; VÁSÁRHELYI; KOVÁCS, 2017; PANTHEE *et al.*, 2018)

This chapter will review the most known empirical methods existing in the literature for estimating the compressive strength,  $\sigma_{cm}$ , and deformation modulus,  $E_{rm}$ , of rock masses based on the following classification methodologies: Rock Quality Designation (RQD), Rock Mass Rating (RMR) system, Q-system and Geological Strength Index (GSI) system. In order to evaluate them, a comparative analysis between these methods is performed using 46 scenarios of different quality rock masses, previously characterized and classified using RQD, RMR, Q, and GSI systems.

#### 3.1 Deere's RQD index

The rock quality designation (RQD) index is a measurement of the borehole core quality, which was designed by Dr. Don Deere in 1964 and formal presented in the Deere *et al.* (1967) publication (DEERE; DEERE, 1988). It is described as the ratio of the sum of the length of sound pieces with 10 cm or longer to the total length of the core run in percentage, conforming Eq. 2.6. Once it provides an unambiguous numerical value and it is relatively easy to calculate, as mentioned by Priest (1993), it was widely accepted as a measure of discontinuity spacing and incorporated directly by important rock mass classification systems, e.g., Rock Mass Rating (RMR) system and Q-system. The Geological Strength Index (GSI) system also rely on this parameter indirectly as reported by Hoek *et al.* (2013).

Next, the most common empirical RQD-based methods for estimating the deformation modulus,  $E_{rm}$ , and compressive strength,  $\sigma_{cm}$ , of jointed rock masses are presented.

### 3.1.1 Rock Mass Deformability Correlations Based on RQD

In the late 1960s, it was investigated by several authors the relationship between the rock quality designation and the in situ modulus of deformation (DEERE ; DEERE, 1988, 1989). The first empirical correlation published in this period, associating these rock mass parameters, was introduced by Coon and Merritt (1970). It was derived from field and laboratory measurements at different dams, including those presented in the Deere *et al.* (1967) publication, and is described as the following equation:

$$\frac{E_{rm}}{E_i} = 0.0231RQD - 1.32 \quad 3.1$$

where  $E_{rm}$  is the in situ rock mass modulus and  $E_i$  is the intact rock modulus.

The correlation proposed by Coon and Merritt (1970) is presented in terms of the ratio of the intact modulus to the in situ rock mass modulus,  $E_{rm}/E_i$ . Although it showed a reasonable correlation between  $E_{rm}/E_i$  and RQD, with a correlation coefficient of 0.554, it is only valid for RQD values higher than 57% approximately, as can be seen in Figure 3.1. To estimate the rock mass modulus for lower RQD values, the Standard Specification for Highway Bridges (AASHTO, 2002) recommended the following correlation, previously designed by Gardner (1987):

$$E_{rm} = \alpha_E E_i \quad 3.2$$

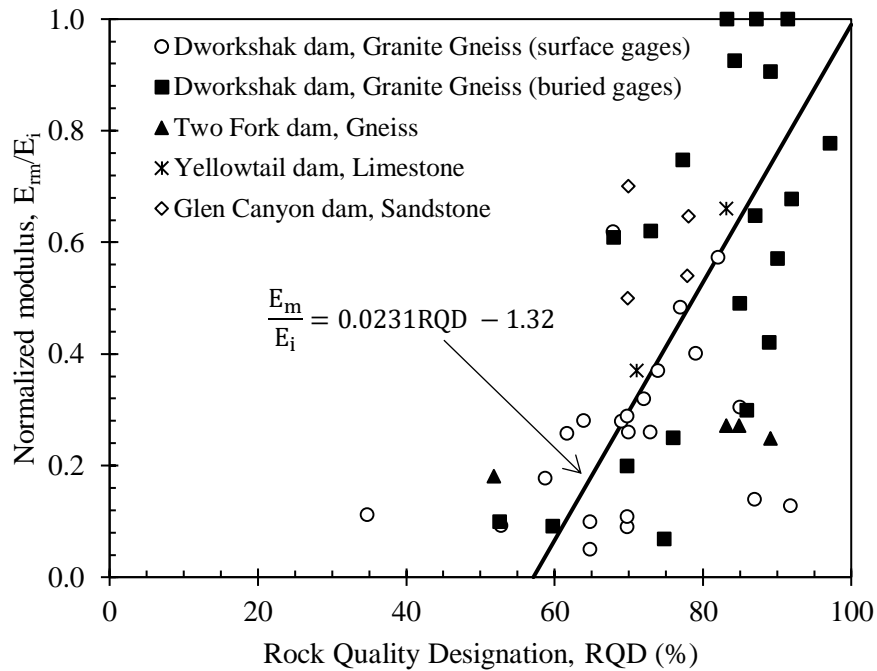
where  $\alpha_E$  is the reduction factor which accounts for frequency of discontinuities by the RQD, and is expressed as:

$$\alpha_E = 0.0231(RQD) - 1.32 \geq 0.15 \quad 3.3$$

For preliminary analysis, when in situ test results are not available, AASHTO (2002) suggested using  $\alpha_E = 0.15$ . Figure 3.2 illustrates the behavior of the Eq. 3.1 and 3.2 plotted against the in situ deformability data reported by Coon and Merritt (1970) and Bieniawski (1978). The main limitations of using the above relationships to estimate  $E_{rm}$  through the RQD index was discussed by Zhang and Einstein (2004). According to the authors, for RQD values lower than 60%, these correlations are not suitable, once only an arbitrary value of the normalized modulus  $E_{rm}/E_i$  can be selected in this range ( $\alpha_E = 0.15$ ).

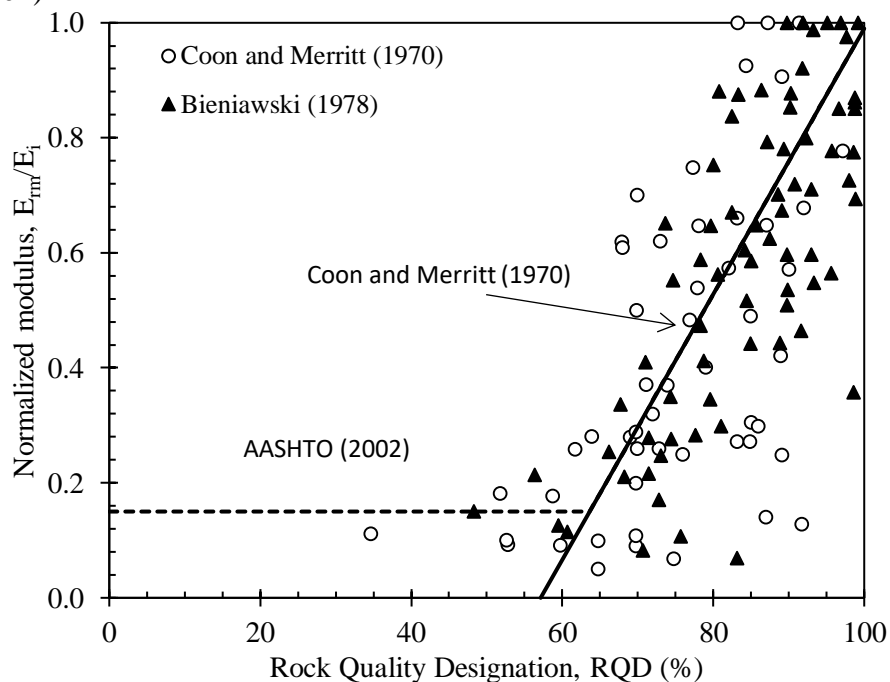
In cases where RQD = 100%, the rock mass modulus is assumed to be equal to the intact modulus, which is considered unsafe in design practice, since there may be discontinuities in rock masses even for RQD = 100%, as mentioned by Zhang and Einstein (2004).

**Figure 3.1** - Correlation between  $E_{rm}/E_i$  and RQD proposed by Coon and Merritt (1970)



Source: Coon and Merritt (1970).

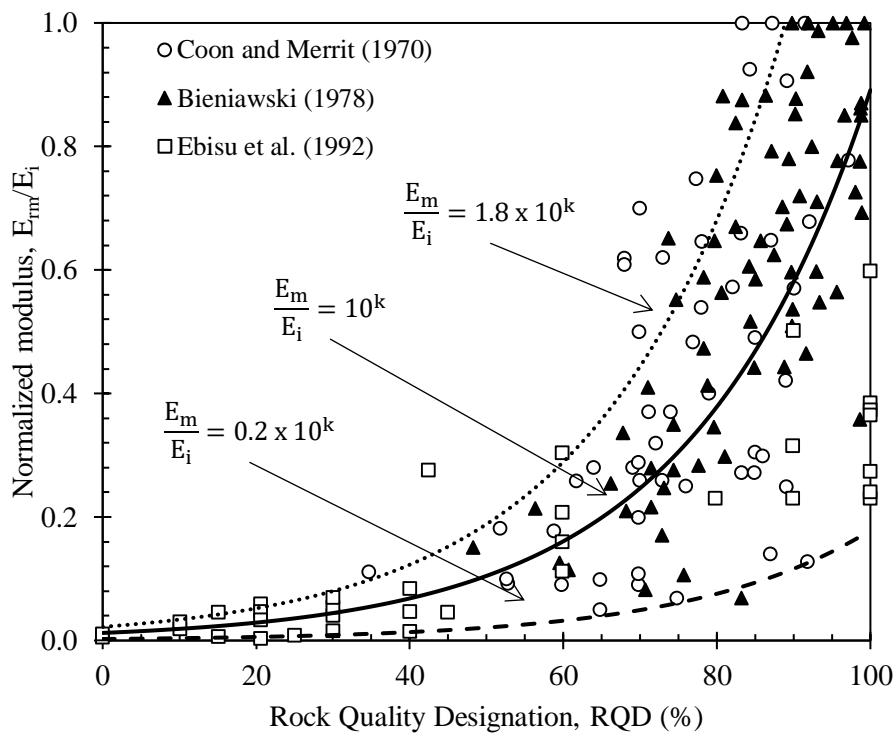
**Figure 3.2** - Correlations between  $E_{rm}/E_i$  and RQD suggested by AASHTO (2002)



Source: elaborated by the author.

To overcome the limitations of the previous correlations, Zhang and Einstein (2004) expanded the database to cover the entire RQD range and proposed a new correlation, Eq. 3.4, with a coefficient of regression of 0.76. The authors also proposed two other correlations, an upper bound correlation, Eq. 3.5, and a lower bound correlation, Eq. 3.6. Figure 3.3 presents these correlations plotted along with the new database, that include information about the following rocks: mudstone, siltstone, sandstone, shale, dolerite, granite, limestone, greywacke, gneiss and granite gneiss.

**Figure 3.3** - Correlations between  $E_{rm}/E_i$  and RQD proposed by Zhang and Einstein (2004)



Source: Zhang and Einstein (2004).

$$\frac{E_{rm}}{E_i} = 10^k \quad 3.4$$

$$\frac{E_{rm}}{E_i} = 1.8 \times 10^k \quad 3.5$$

$$\frac{E_{rm}}{E_i} = 0.2 \times 10^k \quad 3.6$$

where  $k$  is given by:

$$k = 0.0186 \times \text{RQD} - 1.91$$

3.7

### 3.1.2 Rock Mass Strength Correlations Based on RQD

Although using the RQD index to estimate the rock mass strength is not a common practice, once the discontinuity spacing is only one of the many factors that influence it, some correlations were suggested along the years for this purpose.

Kulhawy and Goodman (1987) were one of the first authors to suggest an empirical relationship between the unconfined compressive strength of rock masses,  $\sigma_{cm}$ , and the unconfined strength of intact rock,  $\sigma_{ci}$ , using the RQD index. They suggested, as a first approximation, that  $\sigma_{cm}$  should be assumed as 33% of the  $\sigma_{ci}$  for RQD values lower than 70%. When RQD is greater than or equal to 70%, they indicated a linear relationship between the unconfined compressive strength ratio,  $\sigma_{cm}/\sigma_{ci}$ , and the RQD, considering that  $\sigma_{cm}$  would reach 80% of the  $\sigma_{ci}$ , for RQD equal to 100%. Table 3.1 presents the summary of these empirical relationships described by Kulhawy and Goodman (1987).

**Table 3.1** – The relationship between  $\sigma_{cm}/\sigma_{ci}$  and RQD proposed by Kulhawy and Goodman (1987)

Conditions	Correlation	Eq.
RQD < 70%	$\frac{\sigma_{cm}}{\sigma_{ci}} = 0.33$	3.8
$70\% \leq \text{RQD} \leq 100\%$	$\frac{\sigma_{cm}}{\sigma_{ci}} = 0.0157\text{RQD} - 0.77$	3.9
RQD = 100%	$\frac{\sigma_{cm}}{\sigma_{ci}} = 0.8$	3.10

where  $\sigma_{cm}$  is the unconfined compressive strength of rock mass and  $\sigma_{ci}$  is the unconfined strength of intact rock

Source: Kulhawy and Goodman (1987).

AASHTO (2002) suggested using the Eq. 3.11 to estimate the unconfined compressive strength ratio using the rock quality designation. This correlation is very similar to the Eq. 3.2, where the reduction factor,  $\alpha_E$ , is estimating using the Eq. 3.3.

$$\sigma_{cm} = \alpha_E \sigma_{ci} \quad 3.11$$

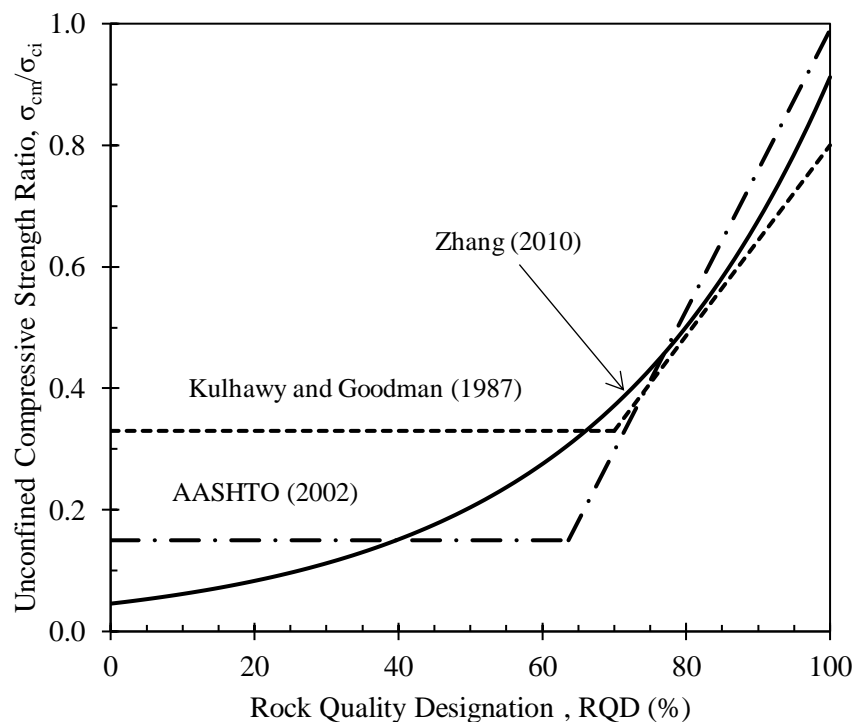


More recently, Zhang (2010), after analyzing the relation between the unconfined compressive strength ratio,  $\sigma_{cm}/\sigma_{ci}$ , and the deformation modulus ratio,  $E_{rm}/E_i$ , which were discussed before by Ramamurthy (1993), Singh *et al.* (1998), and Singh and Rao (2005), suggested a new correlation, given by:

$$\frac{\sigma_{cm}}{\sigma_{ci}} = 10^{0.013RQD-1.34} \quad 3.12$$

According to Zhang (2010), Eq. 3.12 provides a convenient way for estimating the unconfined compressive strength of joint rock masses, but it should be applied with care, once RQD is only one of the many factors that affect the strength of the rock mass. Figure 3.4 illustrates the comparison of the correlations proposed by Kulhawy and Goodman (1987), AASHTO (2002), and Zhang (2010).

**Figure 3.4** - Graphical comparison between the empirical methods developed by Kulhawy and Goodman (1987), AASHTO (2002) and Zhang (2010) to estimate rock mas strength using RQD



Source: Zhang (2010).

### 3.2 Bieniawski's RMR number

The Rock Mass Rating (RMR) system, also known as Geomechanics Classification, was introduced first by Bieniawski (1973, 1976, 1979, 1989) to be a useful

communication means among engineers and geologists concerned with the design problems in jointed rock masses, allowing to quantify the rock mass quality using the following measurable parameters:

- 1 Uniaxial compressive strength of intact rock (see Table 2.15);
- 2 Rock quality designation, RQD (see Table 2.16);
- 3 Spacing of discontinuities (see Table 2.17);
- 4 Condition of discontinuities (see Table 2.18);
- 5 Groundwater conditions (see Table 2.19); and
- 6 The orientation of discontinuities (see Table 2.21).

In this section is presented the empirical methods suggested for estimating the rock mass strength and deformability using the value obtained from the Geomechanics Classification.

### 3.2.1 Rock Mass Deformability Correlations Based on RMR number

Despite the fact that several correlations were proposed to estimate the rock mass deformability using the RQD index, it is noticeable that those correlations were developed using a large scatter of results from the relationship between RQD and the ratio of  $E_{rm}$  to  $E_i$  (Figures 3.1 to 3.3). In order to derive an empirical correlation that could give a better correlation coefficient, avoiding a large scatter of the data, Bieniawski (1978) proposed the following relationship based on the RMR and the in situ modulus of deformation of rock mass:

$$E_{rm}[\text{GPa}] = 1.76 \text{ RMR} - 84.3 \quad \mathbf{3.13}$$

where  $E_{rm}$  is the deformation modulus of rock mass in GPa and RMR is the rock mass rating in accordance with the Geomechanics Classification.

Eq. 3.13, as reported by Bieniawski (1978), presented a correlation coefficient of 0.9612 and yielded the prediction error<sup>14</sup> of 17.8%. Due to its high accuracy correlation, the author suggested rounded off its coefficients and introduced a simple equation, Eq. 3.14, that could be remembered and sufficiently accurate for a preliminary

---

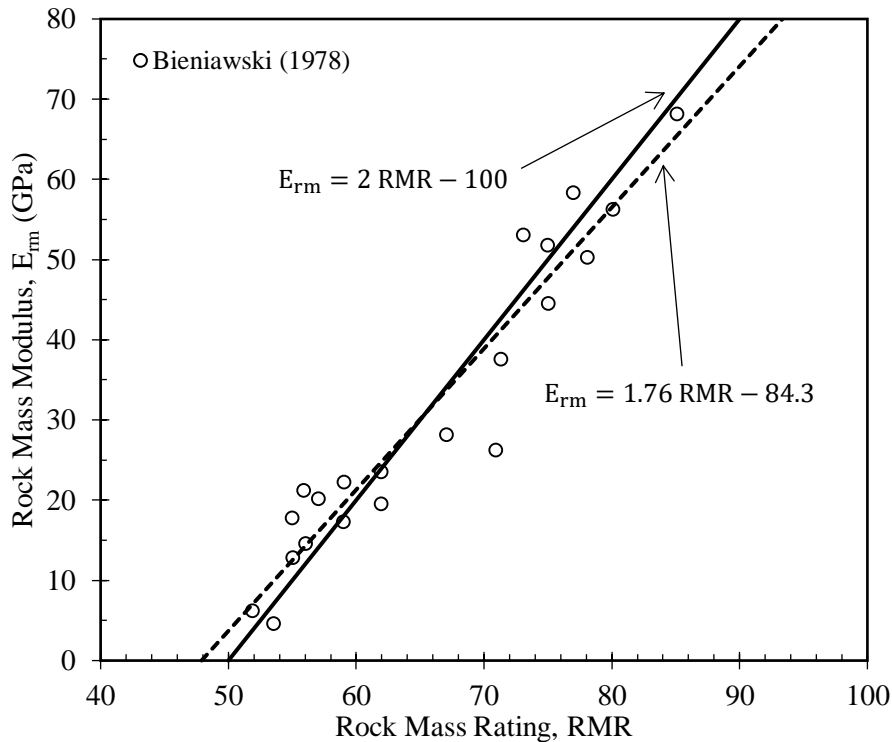
<sup>14</sup> The difference between the observed value and the predicted value expressed as a percentage of the predicted value.

assessment of rock masses. Figure 3.5 presents the correlations proposed by Bieniawski (1978) with the measured field data reported by the author.

$$E_{rm}[\text{GPa}] = 2 \text{ RMR} - 100$$

3.14

**Figure 3.5** - Correlations proposed by Bieniawski (1978) to estimate  $E_{rm}$  based on the RMR



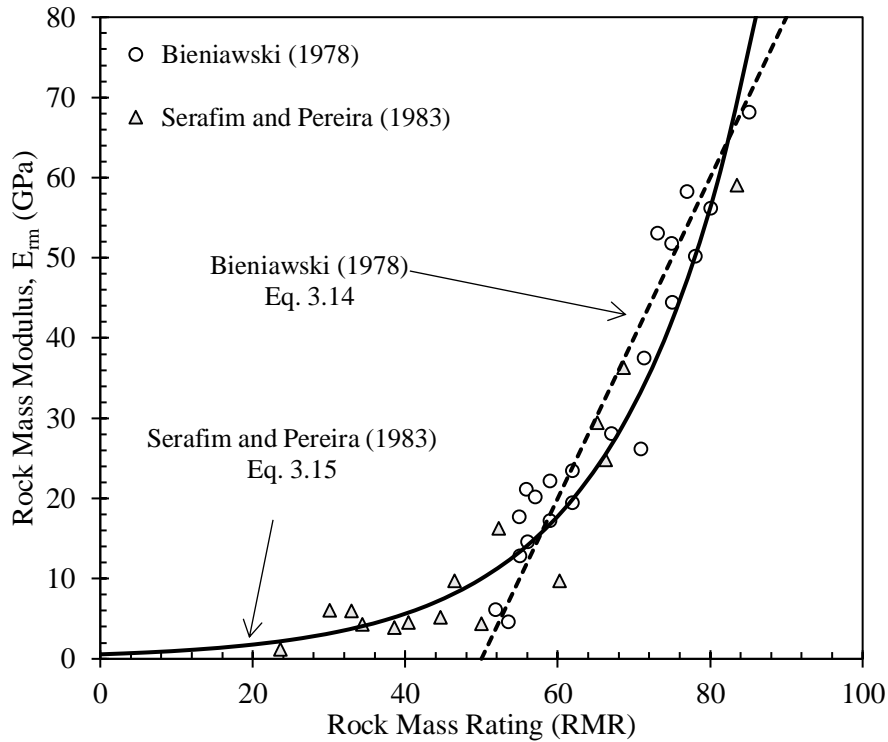
Source: Bieniawski (1978).

The correlation proposed by Bieniawski (1978), Eq. 3.14, is only applied for rock masses with RMR greater than 50, in other words, it is not suitable for poor and very poor rock masses (see Table 2.22). This limitation was later circumvented by the correlation introduced by Serafim and Pereira (1983), Eq. 3.15, after the authors provided more results for rock masses with RMR lower than 50 (Bieniawski, 1989). Figure 3.6 presents a comparison between the behavior of the correlations proposed by Bieniawski (1978) and Serafim and Pereira (1983) in relation to both data.

$$E_{rm}[\text{GPa}] = 10 \frac{\text{RMR} - 10}{40}$$

3.15

**Figure 3.6** - Graphical comparison between the correlations proposed by Bieniawski (1978) and Serafim and Pereira to estimate  $E_{rm}$  based on the RMR



Source: Bieniawski (1989).

Nicholson and Bieniawski (1990) suggested later a new correlation, Eq. 3.16, taking the RMR and the stiffness of the intact rock into account. According to the authors, their correlation recognizes the approximate nature of the ratio of  $E_{rm}$  to  $E_i$  (i.e.,  $E_{rm}/E_i \leq 1$ ).

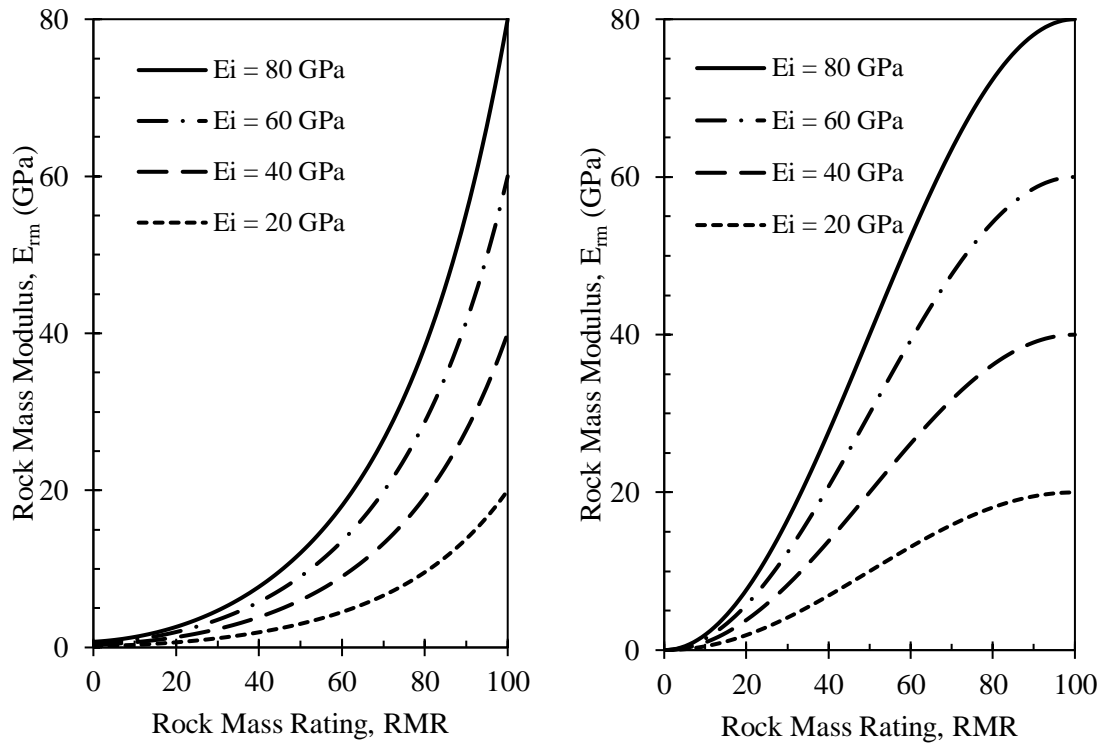
$$\frac{E_{rm}}{E_i} = \frac{1}{100} \left[ 0.0028 \text{RMR}^2 + 0.9 \exp\left(\frac{\text{RMR}}{22.82}\right) \right] \quad 3.16$$

Mitri *et al.* (1994) also proposed a correlation considering the relationship between the deformation modulus ratio and the rock mass rating number, and is given by:

$$\frac{E_{rm}}{E_i} = 0.5 \left\{ 1 - \left[ \cos\left(\pi \times \frac{\text{RMR}}{100}\right) \right] \right\} \quad 3.17$$

Figure 3.7 presents the behavior of the correlations proposed by Nicholson and Bieniawski (1990) and Mitri *et al.* (1994) for a range of intact rock modulus values (20, 40, 60 and, 80 GPa)

**Figure 3.7** - Graphical representation of the correlations developed by Nicholson and Bieniawski (1990), left, and Mitri *et al.* (1994), right, varying  $E_i$  from 20 to 80 GPa



Source: elaborated by the author.

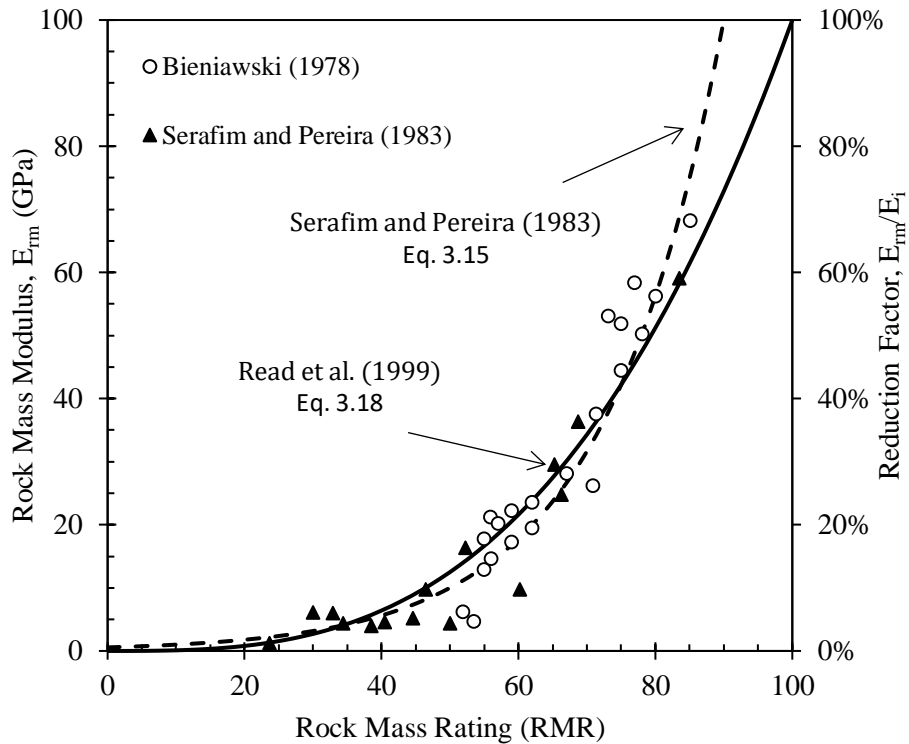
In the 9<sup>th</sup> ISRM Congress in Paris, France, Read *et al.* (1999) suggested a modification in the correlations proposed by Serafim and Pereira (1983). According to the authors, for rock masses with RMR values close to 100, the Eq. 3.15 will give high values of the deformability modulus of the rock mass, predicting, therefore, values of the intact rock mass modulus higher than its measured values. To overcome this issue, Read *et al.* (1999) introduced the correlation expressed by Eq. 3.18, where, as reported by them, it gives a more realistic rock mass deformability at  $RMR = 100$ . Figure 3.8 shows the behavior of this correlation in comparison to Serafim and Pereira's (1978) correlation.

$$E_{rm}[\text{GPa}] = 0.1 \times \left(\frac{RMR}{10}\right)^3 \quad 3.18$$

Based on a new experimental database obtained from several locations, i.e., Deriner (Artvin) and Emenek (Karaman) dam sites, Gokceoglu *et al.* (2003) performed a series of simple regression to obtain a new empirical relation between the deformation modulus of rock mass and the RMR, which is given by:

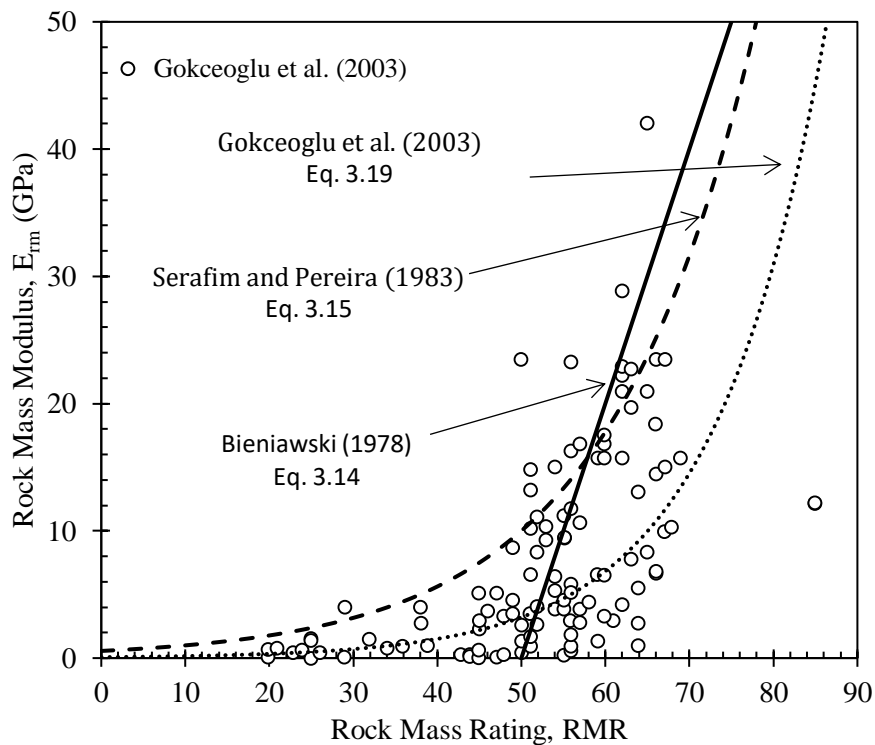
$$E_{rm}[\text{GPa}] = 0.0736e^{0.0755 RMR} \quad 3.19$$

**Figure 3.8** - Graphical comparison between the correlations proposed by Read *et al.* (1999) and Serafim and Pereira (1983) to estimate  $E_{rm}$  based on the RMR values



Source: Read *et al.* (1999).

**Figure 3.9** - Relationship between  $E_{rm}$  and RMR suggested by Gokceoglu *et al.* (2003) using regression analysis on a new database



Source: Gokceoglu *et al.* (2003).

Figure 3.9 exhibits a graphical comparison between the correlations proposed by Gokceoglu *et al.* (2003), Bieniawski (1978) and Serafim and Pereira (1983), in relation to the new database presented by Gokceoglu *et al.* (2003).

Sonmez *et al.* (2006) by a trial and error method proposed another empirical equation, Eq. 3.20, to be used for a full range of RMR values, i.e., from a very weak rock masses to massive rock mass. According to the authors, their correlation would be useful as a preliminary tool for predicting the deformation modulus of a rock mass for the design stage of a rock engineering project, e.g., tunnels, deep slopes, and dams.

$$E_{rm} = E_i \times 10^S \quad 3.20$$

where S is given by:

$$S = \frac{(RMR - 100)(100 - RMR)}{4000 \exp\left(\frac{-RMR}{100}\right)} \quad 3.21$$

Due to the scattering behavior of the measured field data reported by Bieniawski (1978) and Serafim and Pereira (1983), Galera *et al.* (2007) suggested a correlation for RMR values equal or lower than 50, Eq. 3.22, and another for RMR values greater than 50, Eq. 3.23.

They also proposed a new correlation, Eq. 3.24, considering 98 experimental data, for a full range of values of RMR. Table 3.2 presents a summary of these correlations and the threshold RMR range values for their usage.

**Table 3.2** – Correlations proposed by Galera *et al.* (2007) to estimate rock mass modulus using RMR

Condition	Correlation	Eq.
$RMR \leq 50$	$E_{rm}[\text{GPa}] = 0.0876 \text{ RMR}$	3.22
$RMR > 50$	$E_{rm}[\text{GPa}] = 0.0876 \text{ RMR} + 1.056(\text{RMR} - 50) + 0.015(\text{RMR} - 50)^2$	3.23
Full range of RMR	$\frac{E_{rm}}{E_i} = e^{\frac{\text{RMR}-100}{36}}$	3.24

Source: Galera *et al.* (2007).

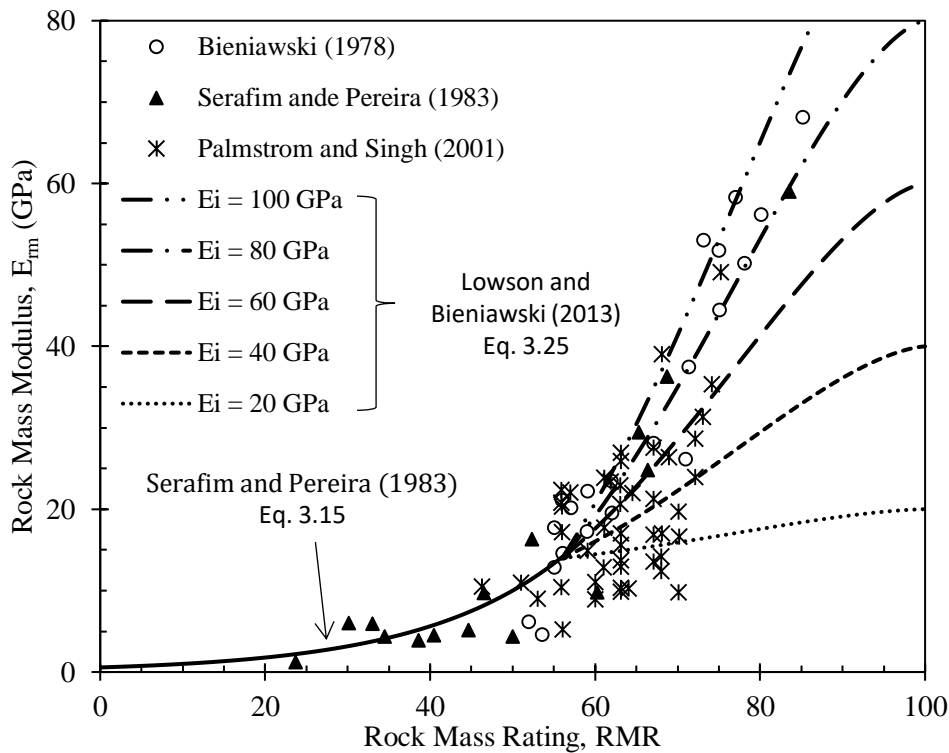
Recently, Lawson and Bieniawski (2013) suggested using a new empirical method for estimated  $E_{rm}$  for RMR greater than 56, given by Eq. 3.25. For RMR values range lower than this, the authors recommend using the correlation proposed by Serafim and Pereira (1983).

According to the authors, at high RMR values, the intact modulus would dominate the deformations, whereas, at low RMR values, the deformations would be controlled by weathering and joint infilling. Therefore, the approach of using two correlations to cover the low and high ranges of RMR would avoid overestimation or underestimation values of rock mass modulus.

Figure 3.10 presents a graphical representation of the correlation developed by Lawson and Bieniawski (2013) plotted against the field data obtained from Bieniawski (1978), Serafim and Pereira (1983) and Palmström and Singh (2001).

$$E_{rm} = 14 + (E_i - 14) \left[ 1 - \left( \frac{100 - RMR}{44} \right)^{\frac{RMR}{70}} \right] \quad 3.25$$

**Figure 3.10** - Graphical representation of the correlation proposed for Lawson and Bieniawski (2013) to estimate  $E_{rm}$  for RMR > 56



Source: Lawson and Bieniawski (2013).



### 3.2.2 Rock Mass Strength Correlations Based on RMR number

If the usage of RQD to estimate the rock mass strength is not a common practice, once this index provides just a small picture of the rock mass characteristics, as discussed earlier, relationships between RMR and  $\sigma_{cm}$  have been widely accepted and used by the rock mechanics community. Most of the correlations are expressed in terms of the unconfined compressive strength ratio, i.e.,  $\sigma_{cm}/\sigma_{ci}$ , and, according to Ván and Vásárhelyi (2010) and Vásárhelyi and Kovács (2017), they have the following guise:

$$\frac{\sigma_{cm}}{\sigma_{ci}} = \exp\left(\frac{\text{RMR} - 100}{B}\right) \quad 3.26$$

where  $\sigma_{cm}$  and  $\sigma_{ci}$  is the unconfined strength of the rock mass and intact rock, respectively and B is a constant.

The first noticeable relationship between  $\sigma_{cm}/\sigma_{ci}$  and RMR was presented by Yudhbir *et al.* (1983) during the 5<sup>th</sup> ISRM Congress in Melbourne, Australia. In the same publication that the authors proposed their empirical failure criterion for rock masses, they suggested the following empirical correlation:

$$\frac{\sigma_{cm}}{\sigma_{ci}} = \exp(0.0765 \text{ RMR} - 7.65) = \exp\left(\frac{\text{RMR} - 100}{13.07}\right) \quad 3.27$$

Prof. T. Ramamurthy, in the 8<sup>th</sup> annual lecture of the Indian Geotechnical Society, suggested the following empirical correlation for predicting the in situ rock mass strength when RMR rating is known (Ramamurthy, 1985):

$$\frac{\sigma_{cm}}{\sigma_{ci}} = \exp\left(\frac{\text{RMR} - 100}{18.75}\right) \quad 3.28$$

Kalamaras and Bieniawski (1995), Sheorey (1997) and Ramamurthy (2004) suggested very close correlations, which are given by Eqs. 3.29 to 3.31, respectively.

$$\frac{\sigma_{cm}}{\sigma_{ci}} = \exp\left(\frac{\text{RMR} - 100}{24}\right) \quad 3.29$$

$$\frac{\sigma_{cm}}{\sigma_{ci}} = \exp\left(\frac{RMR - 100}{20}\right) \quad 3.30$$

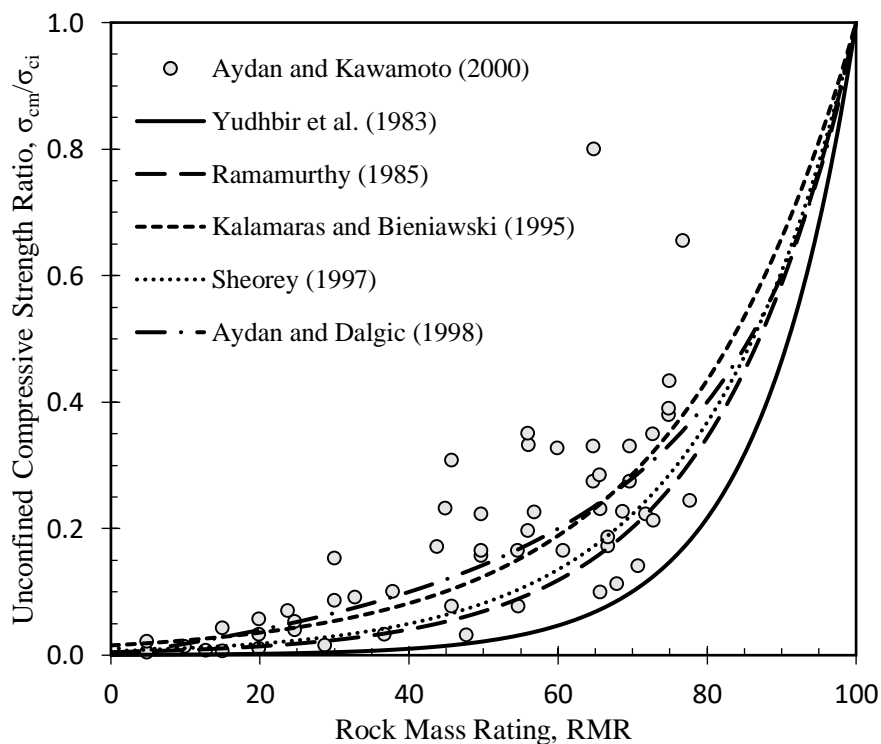
$$\frac{\sigma_{cm}}{\sigma_{ci}} = \exp\left(\frac{RMR - 100}{25}\right) \quad 3.31$$

Aydan and Dalgic (1998) proposed the following correlation based on a number of field measurements:

$$\frac{\sigma_{cm}}{\sigma_{ci}} = \frac{RMR}{RMR + 6(100 - RMR)} \quad 3.32$$

A graphical comparison between the correlations developed by Yudhbir *et al.* (1983), Ramamurthy (1985), Kalamaras and Bieniawski (1995), Sheorey (1997), and Aydan and Dalgic (1998) are presented in Figure 3.11 with field measurements from Aydan and Kawamoto (2000), which including data from Aydan and Dalgic (1998).

**Figure 3.11** - Graphical representation of several correlations proposed to estimate  $\sigma_{cm}/\sigma_{ci}$  using RMR plotted against the data derived from Aydan and Kawamoto (2000)



Source: elaborated by the author.

### 3.3 Barton's Q-value

The Q-system was conceived by Barton *et al.* (1974) for tunneling stability, in which is based on a numerical assessment of the rock mass quality, similar to the RMR system, using the following six parameters:

- 1 Rock quality designation, RQD (see Table 2.25);
- 2 Joint set number,  $J_n$  (see Table 2.26);
- 3 Joint roughness,  $J_r$  (see Table 2.27);
- 4 Joint alteration number,  $J_a$  (see Tables 2.28 to 2.30);
- 5 Joint water reduction factor,  $J_w$  (see Table 2.31); and
- 6 Stress reduction factor, SRF (see Tables 2.32 to 2.35).

According to Barton and Bieniawski (2008), the numerical value derived through Barton's system, the Q-value, Eq. 2.11, can be used as a tool for assessing the rock mass strength and deformability through empirical correlations, as will be discussed next.

#### 3.3.1 Rock Mass Deformability Correlations Based on Q-value

The first correlation proposed to estimate the deformation modulus of rock mass using the Q-value was introduced by Barton *et al.* (1980, 1981), written according to the following equation:

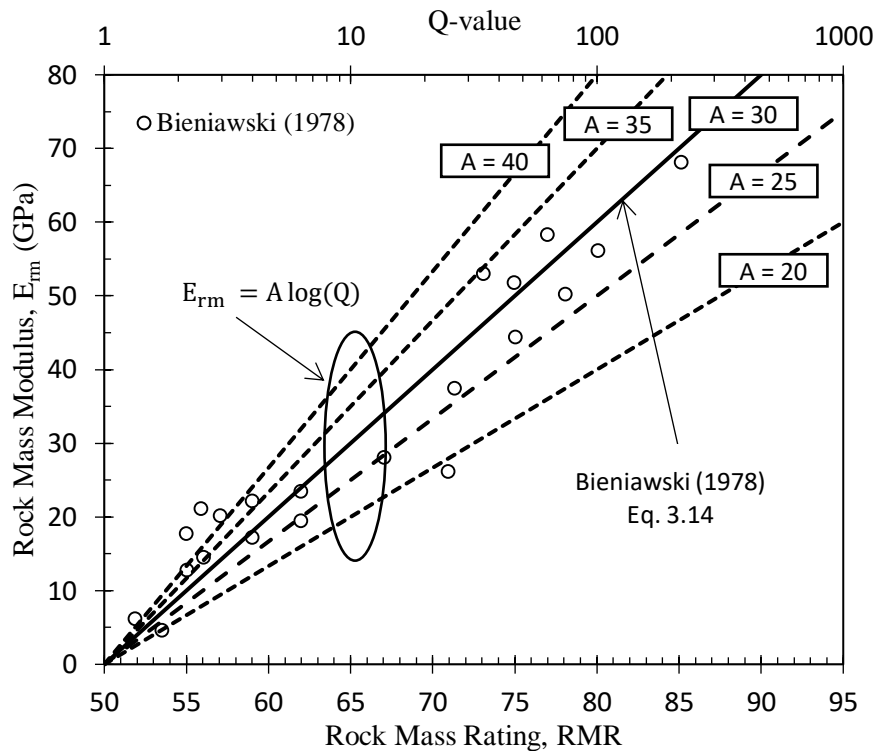
$$E_{rm} = A \log(Q) \quad 3.33$$

where  $E_{rm}$  is deformation modulus of rock mass in GPa; Q is the Q-value in accordance with the Q-system; and A is an empirical constant, in which a value of 40 was assumed by Barton *et al.* (1980,1981), while Grimstad and Barton (1993) suggested  $A = 25$ .

By setting the constant  $A = 30$  and using the relationship between RMR and Q, Eq. 3.34, the Eq. 3.33 will give similar results to correlation proposed by Bieniawski (1978), as can be observed in Figure 3.12. Similar to the correlation proposed by Bieniawski (1978), Eq. 3.33 is also only applicable for rocks with considerable quality, that is, Q-values greater than 1.

$$RMR = 15 \log(Q) + 50 \quad 3.34$$

**Figure 3.12** - Graphical representation of the correlation proposed by Barton *et al.* (1980, 1981) to estimate  $E_{rm}$  using Q-value



Source: elaborated by the author.

Later, with the new database provided by Serafim and Pereira (1983), covering the range of rock mass with poor quality, Barton (1995) introduced a new correlation between in situ deformation modulus and Q-value, given by Eq. 3.35.

$$E_{rm}[\text{GPa}] = 10 \times Q^{1/3} \quad 3.35$$

Figure 3.13 presents a comparison between Eq. 3.39 and the correlations proposed by Bieniawski (1978) and Serafim and Pereira (1983). For rock masses with poor quality ( $RMR < 50$  and  $Q < 1$ ), Eq. 3.39 behaves similarly to the Serafim and Pereira's empirical relationship. While, for rock mass with better quality, Barton's correlation presents more conservative values compared to those obtained from Bieniawski's equation.

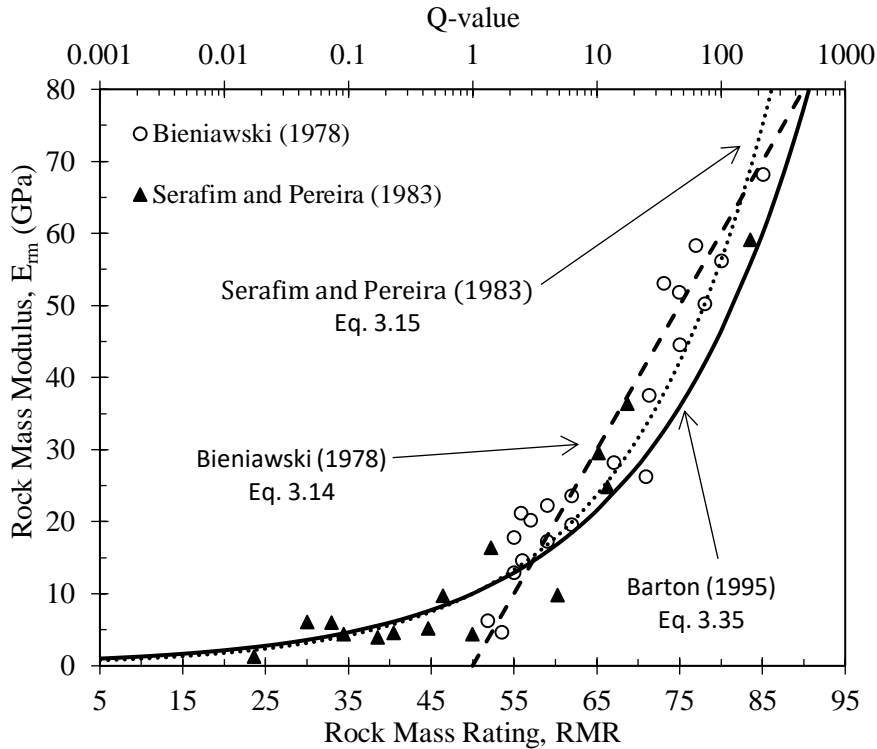
Due to the similarity of the curves from the empirical correlations proposed by Barton (1995) and Serafim and Pereira (1983) for poor rock masses, the correlation proposed by Serafim and Pereira can be rewritten in term of Q-value as:

$$E_{rm}[\text{GPa}] = 10^{(0.375 \log Q + 1)} \quad 3.36$$

Palmström and Singh (2001) suggested the following modification in Eq. 3.37 for Q-values ranging from 1 to 30:

$$E_{rm}[\text{GPa}] = 8 \times Q^{0.4} \quad 3.37$$

**Figure 3.13** - Graphical comparison between the correlations proposed by Barton (1995), Bieniawski (1978) and Serafim and Pereira (1983) to estimate the deformation modulus of rock mass based on the RMR and Q-value



Source: Barton (1995).

Later, in the last review of the Q-system, Barton (2002) suggested an improvement of Eq. 3.35 by replacing the Q-value for a modified version,  $Q_c$ , first introduced by Barton (1995), which takes the effect of the unconfined compressive strength of intact rock,  $\sigma_{ci}$ , into account, Eq. 3.38.

$$Q_c = Q \times \frac{\sigma_{ci}}{100} \quad 3.38$$

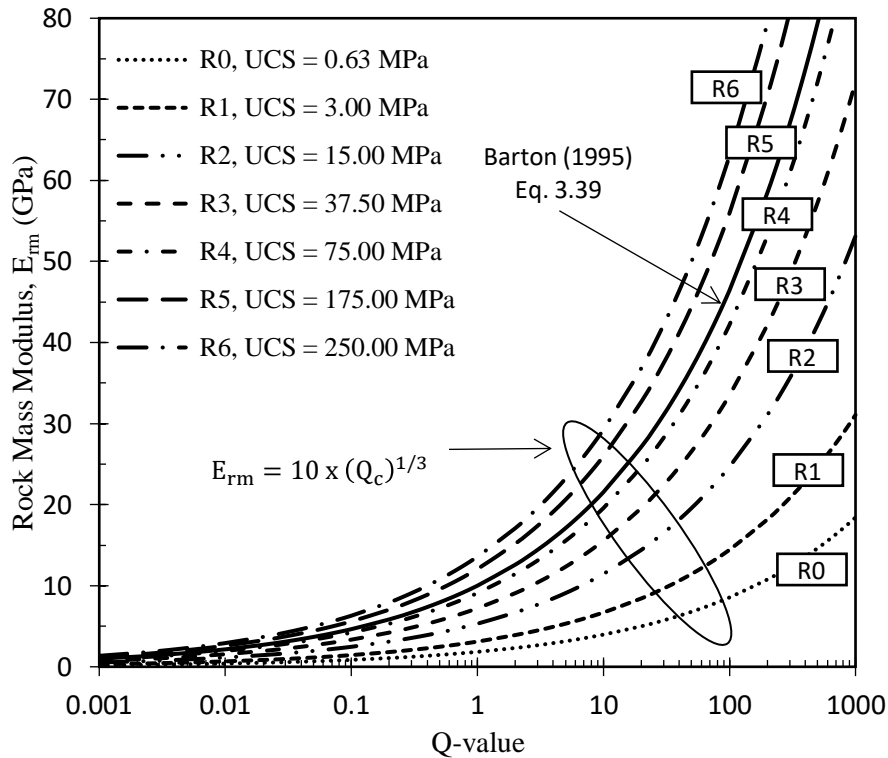
where  $Q_c$  is a normalized value of Q and  $\sigma_{ci}$  is the unconfined compressive strength of the intact rock in MPa.

Therefore, the updated version of Eq. 3.35 suggested by Barton (2002) is given by:

$$E_{rm} = 10 (Q_c)^{1/3} = 10 \left( Q \times \frac{\sigma_{ci}}{100} \right)^{1/3} \quad 3.39$$

The behavior of the Eq. 3.39 for different values of  $\sigma_{ci}$ , ranging from R0 to R6 (see Table 2.8), is presented in Figure 3.14.

**Figure 3.14** - Modified version of Barton's (1995) correlation proposed by Barton (2002) using the range of the unconfined compressive strength ( $\sigma_{ci}$ , UCS) grades from Table 2.8



Source: elaborated by the author.

### 3.3.2 Rock Mass Strength Correlations Based on Q-value

Most of the empirical correlations proposed to estimate the rock mass strength using the Q-value, including those presented by Bhasin and Grimstad (1996), Singh *et al.* (1997), and Singh and Goel (1999, 2011), are based on the equation first introduced by Singh (1993), which is given by:

$$\sigma_{cm} = 7 \gamma (Q)^{1/3} \quad 3.40$$

where  $\sigma_{cm}$  is the uniaxial compressive strength of the rock mass in MPa and  $\gamma$  is the rock mass density in  $t/m^3$  (or  $g/cm^3$ ).

The recently updated form of the above correlation was proposed by Barton (2002), who suggested the following empirical equation:

$$\sigma_{cm} = 5 \gamma (Q_c)^{1/3} = 5 \gamma \left( Q \times \frac{\sigma_{ci}}{100} \right)^{1/3} \quad 3.41$$

where  $\sigma_{ci}$  is the uniaxial compressive strength of the intact rock mass in MPa.

### 3.4 Hoek's GSI number

The Geological Strength Index (GSI) system is a geological tool developed by Hoek (1994) and Hoek *et al.* (1995) to be used to characterize a rock mass through visual inspections at the site. This system is based on an index, the GSI number, which takes into account the two principal factors that most influence the mechanical properties of a rock mass, i.e., the overall structure of the rock mass (the rock mass blockiness) and surface conditions of discontinuities (HOEK; BROWN, 2019).

Among the main rock mass classification systems, including those described throughout this chapter, the GSI system is the only that is directly linked to the engineering parameters used in practice, such as the cohesive strength and the angle of friction of Mohr-Coulomb criterion and the strength parameters of Hoek-Brown criterion, besides the in situ rock mass modulus (CAI *et al.*, 2004).

This section presents the empirical methods that were suggested along the years for estimating the rock mass strength and the rock mass modulus of deformation using Hoek's index.

#### 3.4.1 Rock Mass Deformability Correlations Based on GSI number

Hoek and Brown (1997) based upon practical observations and back analysis of excavations in poor quality rock masses suggested the following correlation for estimating the deformation modulus of rock mass using the GSI:

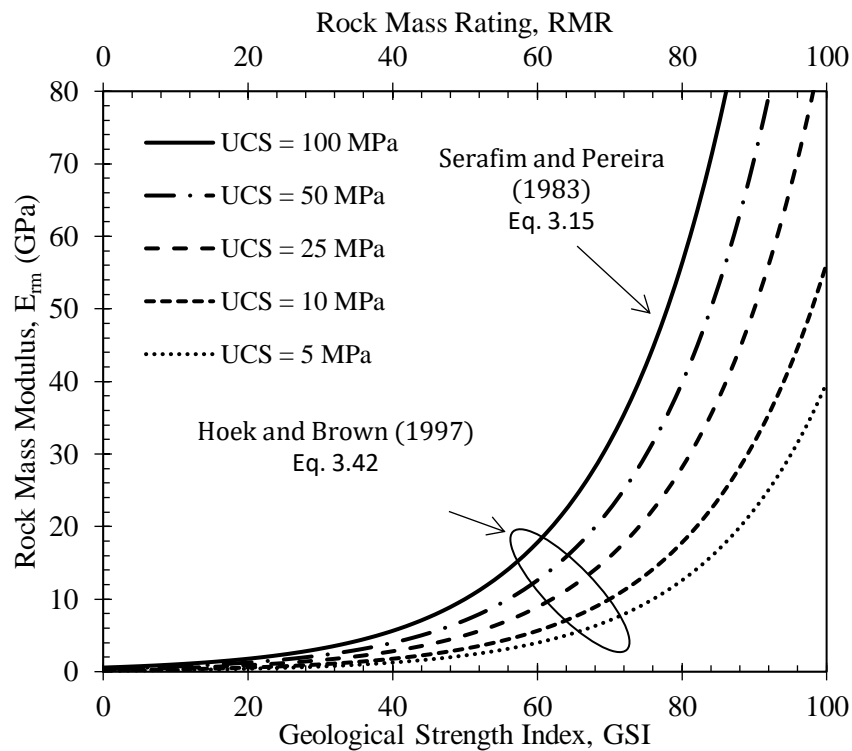
$$E_{rm} = \sqrt{\frac{\sigma_{ci}}{100}} 10^{\frac{GSI-10}{40}} \quad 3.42$$

where  $E_{rm}$  is the deformation modulus of rock mass in GPa;  $\sigma_{ci}$  is the unconfined compressive strength of the intact rock in MPa; and GSI is the numerical value of Hoek's system obtained through the GSI chart (see Figure 2.17).

As reported by Hoek and Brown (1997), the authors modified Eq. 3.15 by substituting RMR for GSI and adding into the equation the term  $\sqrt{\sigma_{ci}/100}$ , which would reduce the  $E_{rm}$  progressively as the value of  $\sigma_{ci}$  falls below 100 MPa. This reduction, as reported by them, is based upon the deformation response of the rock mass in relation to its quality. For better quality rock masses, the deformation is controlled by the discontinuities, while, for poorer quality rock masses, the overall deformation takes the intact rock pieces stiffness into account.

Figure 3.15 presents the graphical representation of Eq. 3.42 for different values of the intact rock unconfined compressive strength.

**Figure 3.15** - Graphical representation of the correlation proposed by Hoek and Brown (1997) to estimate  $E_{rm}$  using GSI for different values of UCS



Source: elaborated by the author.

Later, in the 2002 review of the Hoek-Brown failure criterion, Hoek *et al.* (2002) introduced a new parameter, the factor  $D$ , which depends upon the degree of disturbance that a rock mass has been subjected, such as blast damage and/or stress relaxation, and suggested using Eq. 3.47 as an improvement of the Hoek and Brown's 1997 equation for  $\sigma_{ci} \leq 100$  MPa.

$$E_{rm}[\text{GPa}] = \left(1 - \frac{D}{2}\right) \sqrt{\frac{\sigma_{ci}}{100}} 10^{\frac{\text{GSI}-10}{40}} \quad 3.43$$



where  $D$  is the disturbance factor which ranges from 0 for undisturbed to 1 for disturbed rock masses (see Table 3.3).

In cases where  $\sigma_{ci} > 100$  MPa, Hoek *et al.* (2002) suggested using Eq. 3.44.

$$E_{rm}[\text{GPa}] = \left(1 - \frac{D}{2}\right) 10^{\frac{GSI-10}{40}} \quad 3.44$$

Table 3.3 gives a general rock mass conditions for a range of values of factor  $D$ , while Table 3.4 presents the guidelines introduced by Hoek *et al.* (2002) and later updated by Hoek and Brown (2018) for estimating this disturbance factor.

**Table 3.3 – Rock mass conditions in relation to factor  $D$**

Factor $D$	Conditions of the rock mass
1.0	Rock mass fully undisturbed
0.5	Rock mass partially disturbed
0.0	Rock mass undisturbed

Source: elaborated by the author.

Similar to Eq. 3.19, Gokceoglu *et al.* (2003) also proposed a correlation to estimate the rock mass deformation modulus using GSI, which is given by:

$$E_{rm}[\text{GPa}] = 0.1451e^{0.0654 \text{ GSI}} \quad 3.45$$

Recently, based on an analysis of in situ rock mass modulus measurements for a wide range of rock types from China and Taiwan, Hoek and Diederichs (2006) proposed two empirical correlations for estimating the value of rock mass deformation modulus taking the geological strength index and the effects of disturbance due to blasting and/or stress relief into account.

The first correlation, also known as the simplified Hoek and Diederichs equation, is given by:

$$E_{rm}[\text{GPa}] = 100 \left( \frac{1 - D/2}{1 + e^{(75+25D-GSI)/11}} \right) \quad 3.46$$

The simplified Hoek and Diederichs equation, as can be observed in Figure 3.16a, covers all range of measured rock mass modulus of deformation data. Hoek and

Diederichs (2006) recommend using this simplified correlation when reliable property data for the intact rock is not available. In a comparison with the measured field data reported by Bieniawski (1978) and Serafim and Pereira (1983), Eq. 3.46 gives a good fit to this data for  $D = 0$ , Figure 3.16b.

**Table 3.4** - Guidelines for estimating factor D

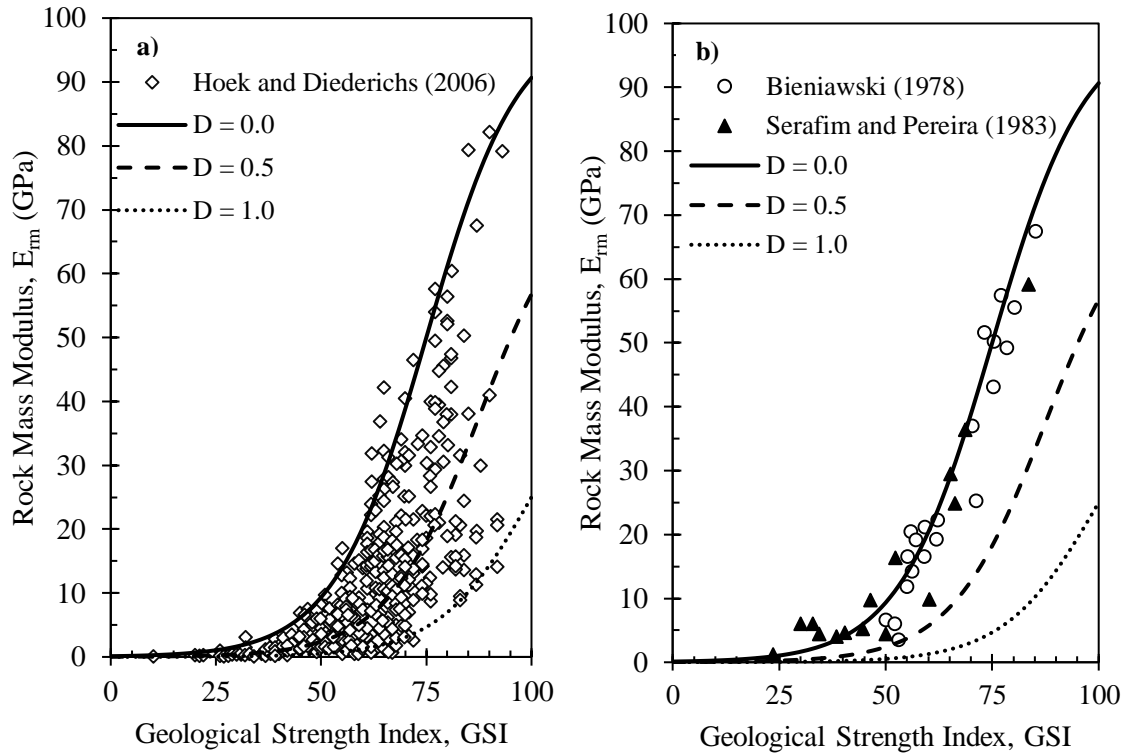
Description of rock mass	Suggested value of D
Excellent quality-controlled blasting or excavation by a road-header or tunnel boring machine results in minimal disturbance to the confined rock mass surrounding a tunnel.	$D = 0$
Mechanical or manual excavation in poor quality rock masses gives minimal disturbance to the surrounding rock mass. Where squeezing problems result in significant floor heave, disturbance can be severe unless a temporary invert, as shown in the photograph, is placed.	$D = 0$ ; $D = 0.5$ with no invert.
Poor control of drilling alignment, charge design and detonation sequencing results in very poor blasting in a hard rock tunnel with severe damage, extending 2 or 3 m, in the surrounding rock mass.	$D = 1.0$ at surface with a linear decrease to $D = 0$ at $\pm 2$ m.
Small-scale blasting in civil engineering slopes results in modest rock mass damage when controlled blasting is used, as shown on the left-hand side of the photograph. Uncontrolled production blasting can result in significant damage to the rock face.	$D = 0.5$ for controlled presplit or smooth wall blasting; $D = 1.0$ for production blasting.
In some weak rock masses, excavation can be carried out by ripping and dozing. Damage to the slopes is due primarily to stress relief. Very large open pit mine slopes suffer significant disturbance due to heavy production blasting and stress relief from overburden removal.	$D = 0.7$ for mechanical excavation effects of stress reduction damage; $D = 1.0$ for production blasting.

Source: Hoek and Brown (2018).

In cases where reliable estimates of the intact rock modulus or intact rock strength are available, Hoek and Diederichs (2006) recommend using the second correlation derived in their study, also known as the generalized Hoek and Diederichs equation, which is given by:

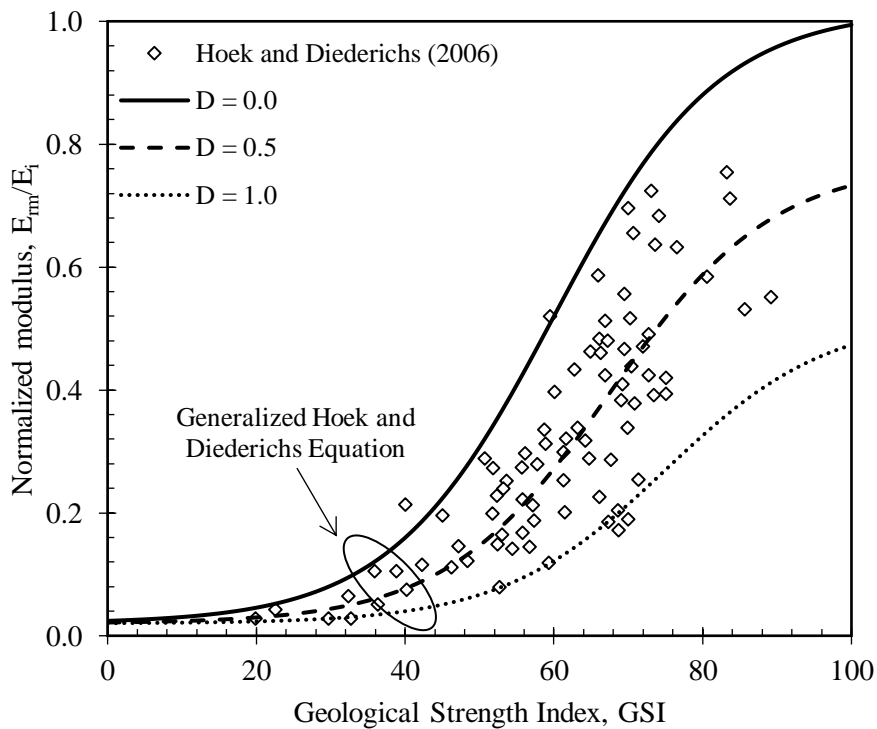
$$E_{rm} = E_i \left( 0.02 + \frac{1 - D/2}{1 + e^{(60+15D-GSI)/11}} \right) \quad 3.47$$

**Figure 3.16** - Plot of the simplified Hoek and Diederichs equation in relation to the measured rock mass modulus data from a) Hoek and Diederichs (2006) and b) Bieniawski (1978) and Serafim (1978)



Source: Hoek and Diederichs (2006).

**Figure 3.17** - Generalized Hoek and Diederichs equation plotted against the normalized in situ rock mass deformation modulus presented by Hoek and Diederichs (2006)



Source: Hoek and Diederichs (2006).

For calculating the intact rock modulus,  $E_i$ , used in the generalized Hoek and Diederichs equation, Hoek and Diederichs (2006) suggesting using Eq. 3.48, which is based on the modulus ratio, MR. This correlation should be used in cases when  $E_i$  is not available at the moment, or it is difficult to get an undisturbed rock sample for direct measurements. Table 3.5 shows the values of MR for different rocks, considering its type, class, group, and texture.

$$E_i = MR\sigma_{ci} \quad 3.48$$

Figure 3.17 illustrates the behavior of Eq. 3.47 plotted against normalized in situ rock mass deformation modulus, where each data point represents the average of multiple tests at the same site in the same rock mass, as reported by Hoek and Diederichs (2006).

### 3.4.2 Rock Mass Strength Correlations Based on GSI number

Hoek *et al.* (2002) derived from the generalized Hoek-Brown criterion, Eq. 2.10, by setting the minor principal stress at failure,  $\sigma_3$ , equal to zero ( $\sigma_3 = 0$ ), the following equation to estimate the unconfined compressive strength of rock masses:

$$\frac{\sigma_{cm}}{\sigma_{ci}} = \exp\left(\frac{GSI - 100}{9 - 3D}\right) \left[ \frac{1}{2} + \frac{1}{6} \left( e^{\frac{-GSI}{15}} - e^{\frac{-20}{3}} \right) \right] \quad 3.49$$

where  $\sigma_{cm}$  and  $\sigma_{ci}$  is the unconfined strength of the rock mass and intact rock.

Eq. 3.49 gives conservative values when compared to the data reported by Aydan and Kawamoto (2000), as can be observed in Figure 3.18a, even for undisturbed rock masses, that is,  $D = 0$ .

However, later, in personal communication with Zhang (2010), Dr. Evert Hoek suggested a relationship between the unconfined compressive strength ratio and the GSI, given by Eq. 3.55. This suggested relationship, as can be seen in Figure 3.18b, gives a better fit to the Aydan and Kawamoto's (2000) data.

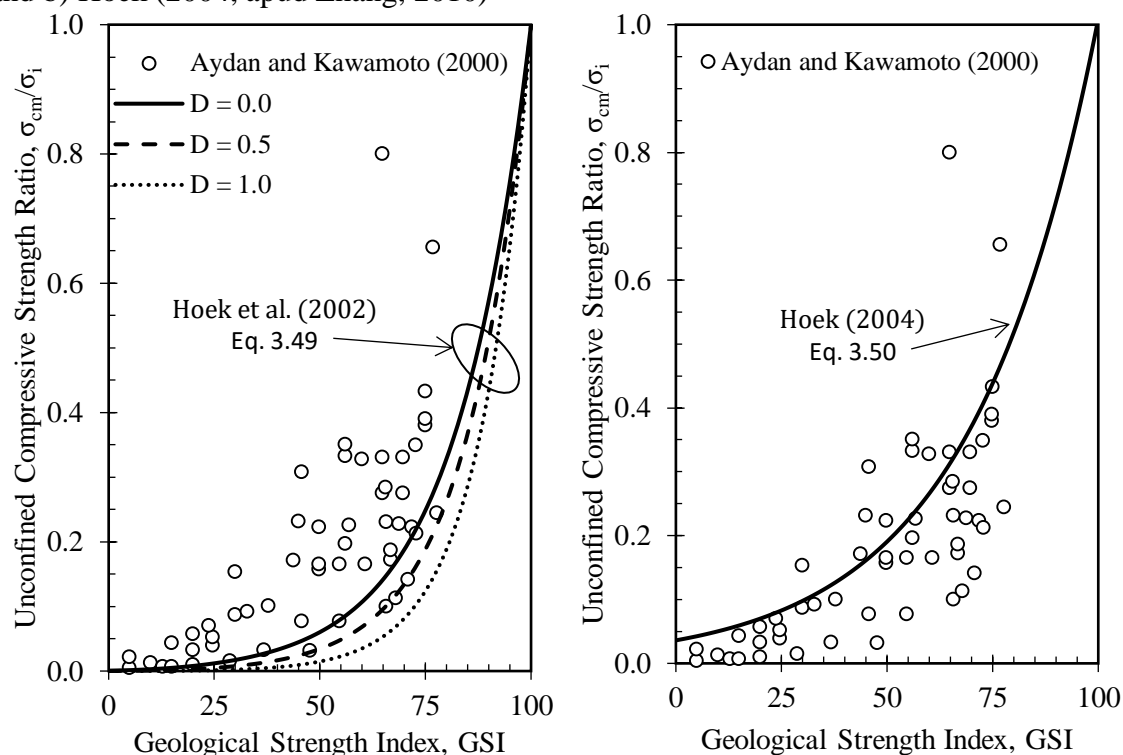
$$\frac{\sigma_{cm}}{\sigma_{ci}} = 0.036e^{\frac{GSI}{30}} \quad 3.50$$

**Table 3.5** - Values of MR for different rocks

Rock type	Class	Group	Texture			
			Coarse	Medium	Fine	Very Fine
Sedimentary	Clastic		Conglomerates 300-400	Sandstones 200-350	Siltstones 350-400	Claystones 200-300
			Breccias 230-350		Greywackes 350	Shales 150-250 Marls 150-200
	Non-Clastic	Carbonates	Crystalline Limestones 400-600	Sparitic Limestones 600-800	Micritic Limestones 800-1000	Dolomites 350-500
		Evaporites		Gypsum 350	Anhydrite 350	
Organic					Chalk 1000 +	
Metamorphic	Non-Foliated		Marble 700-1000	Hornfels 400-700 Metasandstone 200-300	Quartzites 300-450	
	Slightly Foliate		Migmatite 350-400	Amphibolites 400-500	Gneiss 300-750	
	Foliated			Schists 250-1100	Phyllites / Mica Schist 300-800	Slates 400-600
Igneous	Plutonic	Light	Granite 300-550 Granodiorite 400-450	Diorite 300-350		
		Dark	Gabbro 400-500 Norite 350-400	Dolerite 300-500		
	Hypabyssal		Porphyries 400		Diabase 300-450	Peridotite 250-300
	Volcanic	Lava		Rhyolite 300-500 Andesite 300-500	Dacite 350-450 Basalt 250-450	
Pyroclastic		Agglomerate 400-600	Volcanic Breccia 500	Tuff 200-400		

Source: Hoek and Diederichs (2006).

**Figure 3.18** - Plotting of the unconfined compressive strength of rock mass data presented by Aydan and Kawamoto (2000) against the correlation proposed by a) Hoek *et al.* (2002) and b) Hoek (2004, apud Zhang, 2010)



Source: Hoek and Diederichs (2006).

### 3.5 Comparative Analysis of the Empirical Correlations

To compare the behavior of the empirical correlations presented above, they were used for estimating the deformation modulus and the compressive strength of rock masses from a large database with 46 scenarios. The chosen database was based on 5 main criteria: (1) lithology type variability; (2) rock masses quality variability; (3) rock masses previously classified with at least 3 of the 4 schemes (RQD, RMR, Q, and GSI); (4) properties of the intact rock estimated in laboratory, such as the intact rock strength and deformation modulus; and (5) applications of the rock mass sites for different engineering purposes, such as underground excavation and dams.

Table 3.6 presents the database collected in the following literature: Cosar (2004), Bieniawski (1990), Shafiei and Duesseault (2008), Shafiei *et al.* (2007), Shafiei *et al.* (2008), Heydari *et al.* (2019), Genis *et al.* (2007) and Genis (2010), Dalgiç (2002), Özsan and Akin (2002), Kocbay and Kilic (2006), Özsan and Karpuz (1996), Gurocak *et al.* (2007), Basarir *et al.* (2005), Rasouli (2009), Riaz *et al.* (2016), Basarir (2006), and Sapigini *et al.* (2003). Appendix A presents the statistical analysis thereof.

**Table 3.6** – Database of 46 scenarios of rock masses selected

Scenarios	Rock Type	RMR	Q	GSI	RQD (%)	UCS (MPa)	E <sub>i</sub> (GPa)	ρ (g/cc)
S1 <sup>1</sup>	Schist	31	0.010	32	2.0	20.0	14.00 <sup>c</sup>	2.79 <sup>d</sup>
S2 <sup>1</sup>	Schist	34	0.480	39	21.1	21.0	14.70 <sup>c</sup>	2.79 <sup>d</sup>
S3 <sup>1</sup>	Schist	44	0.090	40	13.3	79.0	55.30 <sup>c</sup>	2.79 <sup>d</sup>
S4 <sup>1</sup>	Schist	31	0.200	38	16.1	32.0	22.40 <sup>c</sup>	2.79 <sup>d</sup>
S5 <sup>1</sup>	Schist	34	0.540	40	19.9	24.0	16.80 <sup>c</sup>	2.79 <sup>d</sup>
S6 <sup>1</sup>	Limestone	36	0.180	37	12.2	13.0	9.10 <sup>c</sup>	2.56 <sup>d</sup>
S7 <sup>1</sup>	Conglomerate	58	18.750	52	93.5	15.0	6.00 <sup>c</sup>	2.60 <sup>d</sup>
S8 <sup>2</sup>	Shale	70	19.990	77	80.0	55.0	15.00	2.65
S9 <sup>2</sup>	Basalt	74	11.250	79	90.0	70.0	32.00	2.75
S10 <sup>3</sup>	Limestone	59	6.150	55	94.0	50.0	26.00	2.6
S11 <sup>3</sup>	Evaporitic	52	1.400	45	78.0	30.0	18.00	2.3
S12 <sup>4</sup>	Sandstone	55	5.340	66	80.0	95.0	40.00	2.73
S13 <sup>4</sup>	Sandstone	30	0.410	45	42.0	20.0	11.60	2.56
S14 <sup>4</sup>	Slate	42	1.930	53	59.0	44.0	41.90	2.77
S15 <sup>5</sup>	Conglomerate	16	0.031	15	35.0	5.1	3.00	2.65
S16 <sup>6</sup>	Conglomerate	65	12.600	70	80.0	57.0	19.95 <sup>c</sup>	2.7
S17 <sup>6</sup>	Shale	50	1.100	49	40.0	38.0	11.40 <sup>c</sup>	2.74
S18 <sup>7</sup>	Phyllite	27	0.040	28	26.0	30.0	18.00 <sup>c</sup>	2.90
S19 <sup>7</sup>	Phyllite	11	0.002	13	10.0	1.5	0.90 <sup>c</sup>	1.99
S20 <sup>7</sup>	Breccia	24	0.045	28	28.0	15.0	4.35 <sup>c</sup>	2.12
S21 <sup>7</sup>	Granodiorite	36	0.600	38	50.0	30.8	13.30	2.73
S22 <sup>7</sup>	Granodiorite	29	0.330	33	24.0	26.0	10.40 <sup>c</sup>	2.34
S23 <sup>8</sup>	Sandstone	58	3.415 <sup>a</sup>	53	50.0	55.0	31.00	2.7
S24 <sup>8</sup>	Mudstone	46	0.540 <sup>a</sup>	41	50.0	31.0	12.00	2.79
S25 <sup>9</sup>	Basalt	38	0.630	43	15.0	142.0	40.00	2.45
S26 <sup>9</sup>	Andesite	34	0.560	41	41.0	93.0	41.20	2.42
S27 <sup>9</sup>	Tuff	21	0.110	31	10.0	24.0	11.60	2.03
S28 <sup>10</sup>	Basalt	36	0.130	31 <sup>b</sup>	60.0	52.7	39.25	2.65
S29 <sup>11</sup>	SSP	30	0.120	25 <sup>b</sup>	44.0	43.97	26.38 <sup>c</sup>	2.75
S30 <sup>11</sup>	Quartzite	50	1.170	45 <sup>b</sup>	58.0	104.3	39.11 <sup>c</sup>	2.65
S31 <sup>12</sup>	Basalt	56	1.030	48	62.0	40.6	30.91	2.61
S32 <sup>12</sup>	Tuff	34	0.156	32	25.0	8.2	2.23	1.68
S33 <sup>13</sup>	Limestone	48	1.880	43	69.0	62.3	31.42	2.66
S34 <sup>13</sup>	Sandstone	38	0.450	33	34.0	64.7	27.20	2.70
S35 <sup>13</sup>	Diabase	24	0.120	19	28.0	32.3	23.50	2.70
S36 <sup>14</sup>	Schist	28	0.020	22	10.0	24.3	12.91	2.37
S37 <sup>14</sup>	Andesite	41	0.197	35	21.0	169.8	17.28	2.92

**Table 3.6** – Database of 46 scenarios of rock masses selected

Scenarios	Rock Type	RMR	Q	GSI	RQD (%)	UCS (MPa)	E <sub>i</sub> (GPa)	ρ (g/cc)
S38 <sup>14</sup>	Schist	34	0.021	30	12.0	68.1	11.62	2.73
S39 <sup>15</sup>	Schist	46	0.425	38	16.0	20.0	13.50	2.6
S40 <sup>15</sup>	Marble	43	1.183	40	21.5	50.0	42.50	2.6
S41 <sup>15</sup>	Schist	48	1.435	42	43.5	20.0	13.50	2.6
S42 <sup>15</sup>	MP	33	0.392	32	19.0	40.0	22.00	2.6
S43 <sup>15</sup>	Schist	23	0.100	26	10.0	20.0	13.50	2.6
S44 <sup>16</sup>	Granite	24	0.800	19	N/A	74.0	31.45 <sup>c</sup>	2.7
S45 <sup>16</sup>	Diorite	21	0.050	16	N/A	60.0	25.50 <sup>c</sup>	2.68
S46 <sup>17</sup>	Gneiss	69	17.800	80	N/A	85.0	44.63 <sup>c</sup>	2.85

SSP = Schist, slate and phyllite.

MP = Marble and phyllite.

N/A = not available results.

<sup>a</sup> Estimated using Barton's (1995) correlation, Eq. 2.20.

<sup>b</sup> Estimated using Hoek's (1994) correlation, Eq. 2.21.

<sup>c</sup> Estimated using Hoek and Diederichs' (2006) correlation, 3.48.

<sup>d</sup> Estimated using data from AASHTO (2002) and Zhang (2016).

Source: <sup>1</sup>Cosar (2004), <sup>2</sup>Bieniawski (1990), <sup>3</sup>Shafiei and Duesseault (2008), <sup>4</sup>Shafiei *et al.* (2007), <sup>5</sup>Shafiei *et al.* (2008), <sup>6</sup>Heydari *et al.* (2019), <sup>7</sup>Genis *et al.* (2007) and Genis (2010), <sup>8</sup>Dalgıç (2002), <sup>9</sup>Özsan and Akin (2002), <sup>10</sup>Kocbay and Kilic (2006), <sup>11</sup>Özsan and Karpuz (1996), <sup>12</sup>Gurocak *et al.* (2007), <sup>13</sup>Basarir *et al.* (2005), <sup>14</sup>Rasouli (2009), <sup>15</sup>Riaz *et al.* (2016), <sup>16</sup>Basarir (2006), <sup>17</sup>Sapigini *et al.* (2003).

To enhance the comparative analysis of the empirical methods, the 46 scenarios were divided into three different groups, SG-I, SG-II, and SG-III, taking into account the similarity of the rock mass quality. SG-I is composed of scenarios with lower quality rock masses: S1, S4, S6, S13, S15, S18, S19, S19, S20, S22, S27, S29, S32, S35, S36, S38, S43, S44, and S45. SG-II, in turn, is composed of scenarios with intermediate quality rock masses: S2, S3, S6, S11, S17, S21, S24, S25, S26, S28, S34, S37, S39, S40, S41, and S42. SG-III, finally, is composed of scenarios with better quality rock masses: S7, S8, S9, S10, S12, S14, S16, S23, S30, S31, S33, and S46. Table 3.7 gives the descriptive statistics of each group. The complete descriptive

### 3.5.1 Comparative analysis – E<sub>rm</sub>

The first analysis took into account the variation of the estimated deformation modulus, E<sub>rm</sub>, for the scenarios of each group using the classification schemes based correlations. Regarding the results of the SG-I group scenarios, in some cases, there were empirical methods estimating values up to 4 and 8 times the mean and median results, respectively, mainly for the poorest rock masses.



**Table 3.7** - Descriptive statistics of SG-I, SG-II, and SG-III

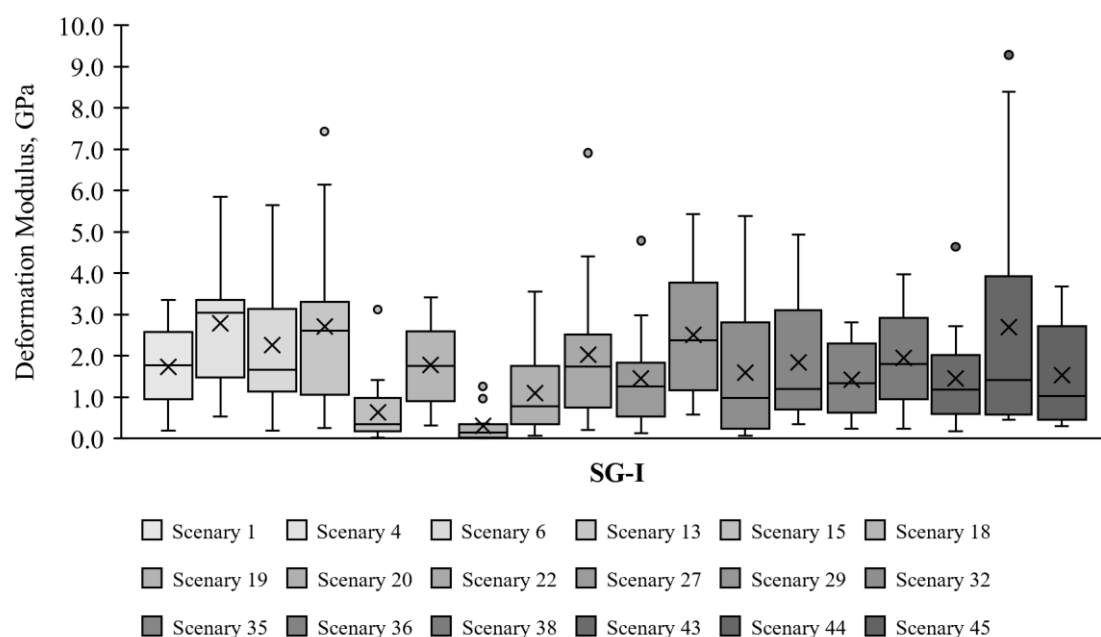
Data		SG-I	SG-II	SG-III
<b>RQD (%)</b>	Max.	44.00	78.00	94.00
	Min.	2.00	13.34	50.00
	Mean	20.89	33.96	74.14
<b>RMR</b>	Max.	36.00	52.00	74.00
	Min.	11.00	33.00	42.00
	Mean	26.33	40.81	58.67
<b>Q</b>	Max.	0.800	1.435	19.990
	Min.	0.002	0.090	1.030
	Mean	0.152	0.635	8.443
<b>GSI</b>	Max.	45.00	49.00	80.00
	Min.	13.00	31.00	43.00
	Mean	27.17	39.16	60.08

Source: elaborated by the author.

Among the empirical methods that overestimated the  $E_{rm}$  values, the correlation proposed by Barton (1995), Eq. 3.35, estimated the highest value in 78% of the scenarios from SG-I, followed by the correlations proposed by Serafim and Pereira (1993), Eq. 3.15, and Mitri *et al.* (1994), Eq. 3.17. On the other hand, Zhang and Einstein's (2004) and Sonmez *et al.*'s (2006) correlations estimated the lowest deformation modulus among the others, followed by the proposed method of Nicholson and Bieniawski (1990), Eq. 3.16, and both methods of Gokceoglu *et al.* (2003), Eqs. 3.19 and 3.45. The generalized Hoek and Diederichs equation, Eq. 3.47, also resulted in low values of  $E_{rm}$ .

The correlations that presented the closest results to the median values for each scenario of SG-I were from: Gardner (1987), Eq. 3.2, Galera *et al.* (2007), Eq. 3.22, Hoek *et al.* (2002), Eq. 3.43, and Hoek and Diederichs (2006), Eq. 3.46. Figure 3.19 shows the box-whisker plots displaying the range of deformation modulus estimated for the SG-I group.

Regard to the group with intermediate quality rock masses scenarios, SG-II, the empirical methods proposed by Mitri *et al.* (1994), Eq. 3.17, Barton (1995), Eq. 3.35, and Read *et al.* (1999), Eq. 3.18, estimated the upper-bounded deformation modulus values in this group. Barton (1995) overestimate  $E_{rm}$  for the poorest rock mass scenarios in this group, while Read *et al.* (1999) for the intermediate, and, finally, Mitri *et al.* (1994) for the scenarios with better quality rock masses.

**Figure 3.19** - Box plot graph of estimated  $E_{rm}$  values of scenarios from SG-I

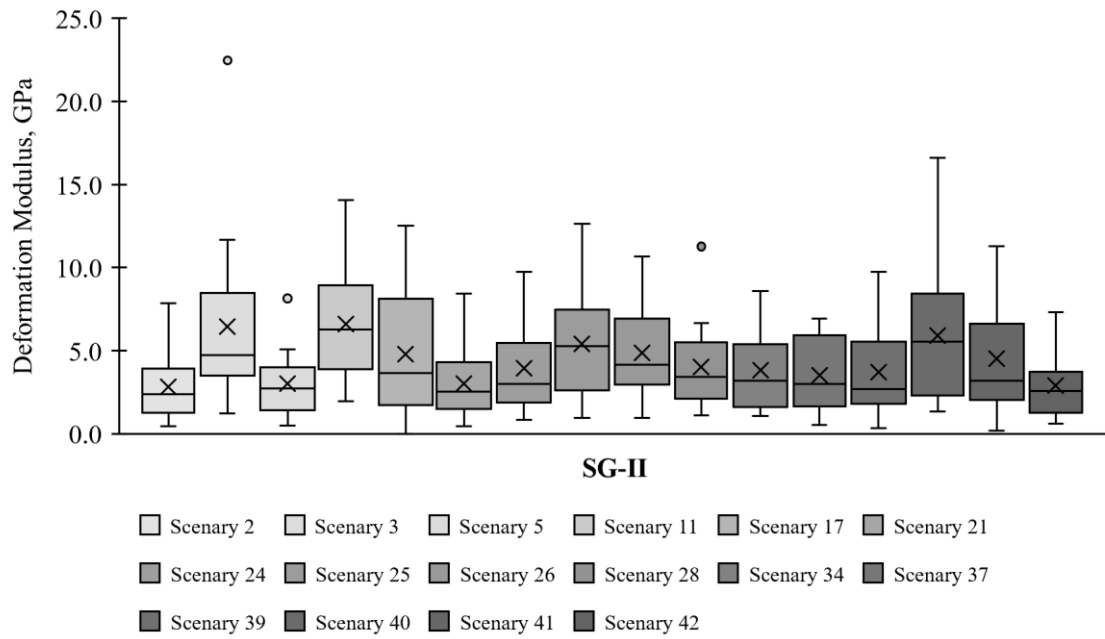
Source: elaborated by the author.

Analyzing the empirical methods that underestimated the  $E_{rm}$  for this group, the proposed method by Zhang and Einstein (2004), Eq. 3.4, and Sonmez *et al.* (2006), Eq. 3.20, estimated the lower-bounded deformation modulus values, repeating what happened in the SG-I. The correlations proposed by Barton (2002), Eq. 3.39, and Hoek and Diederichs (2006), Eq. 3.46, estimated the average  $E_{rm}$  values in this group, followed closed by Galera *et al.*'s (2007) method. Figure 3.20 shows the box-whisker plots giving the range of deformation modulus estimated for the SG-II group.

Finally, for the group with better rock mass quality, SG-III, Figure 3.21 presents the range of deformation values estimated by the appropriated empirical methods. The simplified Hoek and Diederichs' (2006) correlation, Eq. 3.46, estimated the highest values of  $E_{rm}$  for the rock masses with the best quality in this group, i.e., S8, S9, S16, and S46. The correlations proposed by Bieniawski (1978), Eqs. 3.13 and 3.14, also estimated high values of deformation modulus for these scenarios.

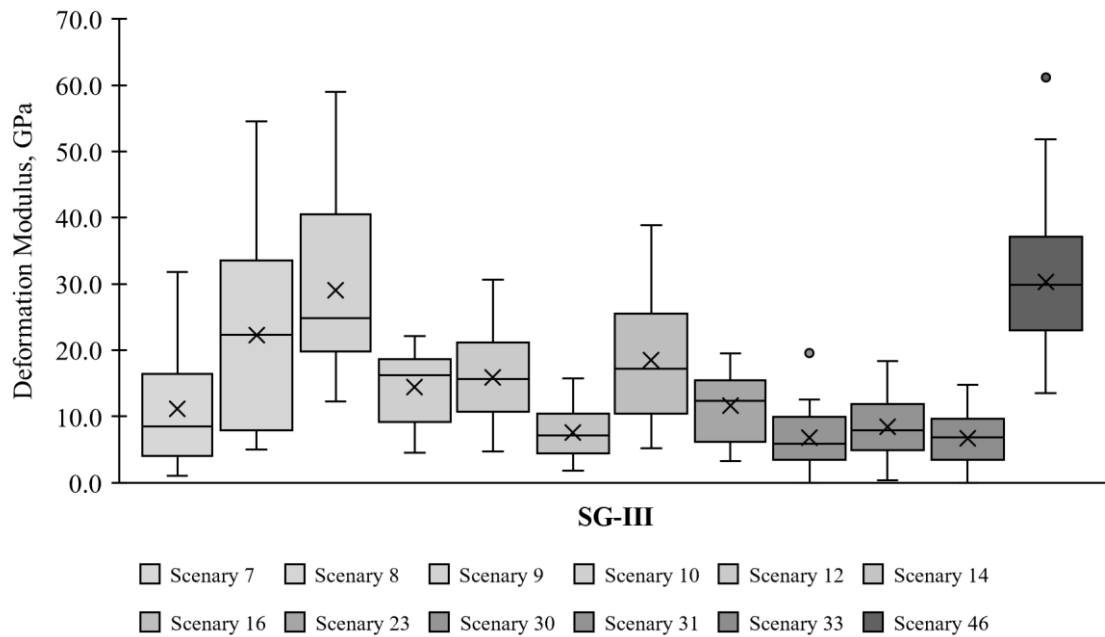
On the other hand, the empirical method proposed by Sonmez *et al.* (2006), Eq. 3.20, estimated again the lower values, this time followed by Nicholson and Bieniawski's (1990), 3.16 and Gokceoglu *et al.* (2003), Eq. 3.19, methods. For this scenario group, the correlations proposed by Serafim and Pereira (1983), Eq. 3.15, Galera *et al.* (2007), Eq. 3.23, and Barton (2002), Eq. 3.39, estimated the average values.

**Figure 3.20** - Box plot graph of estimated  $E_{rm}$  values of scenarios from SG-II



Source: elaborated by the author.

**Figure 3.21** - Box plot graph of estimated  $E_{rm}$  values of scenarios from SG-III



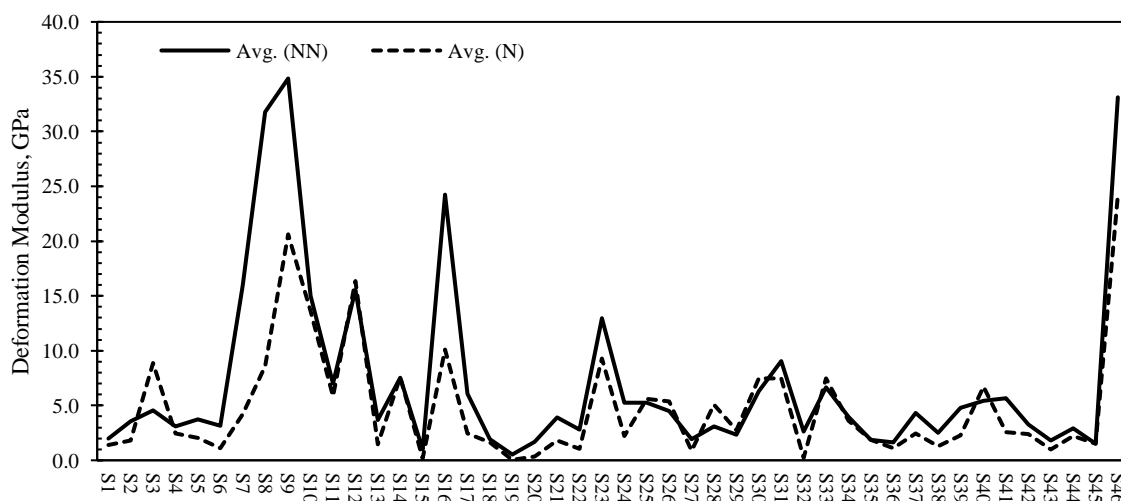
Source: elaborated by the author.

Based on the results commented above, it is possible to observe that non-normalized empirical methods, i.e., correlations expressed in terms of the deformation ratio ( $E_{rm}/E_i$ ), generally result in higher deformation modulus values when compared to the results obtained by normalized correlations. To check this behavior, Figure 3.22

shows a comparison of the estimated values average using the normalized correlations (that is, Eq. 3.1, Eq. 3.2, Eq. 3.4, Eq. 3.16, Eq. 3.17, Eq. 3.20, Eq. 3.24, Eq. 3.25, and Eq. 3.47) with the non-normalized methods (that is, Eq. 3.13, Eq. 3.14, Eq. 3.15, Eq. 3.18, Eq. 3.19, Eq. 3.22, Eq. 3.23, Eq. 3.35, Eq. 3.37, Eq. 3.39, Eq. 3.43, Eq. 3.44, Eq. 3.45, and Eq. 3.46).

From the results presented in Figure 3.22, for the scenarios with good rock mass quality, e.g., S8, S9, S16 and S46, a higher peak of deformation modulus estimated using the non-normalized equations when compared with the normalized ones can be observed. For low quality rock mass scenarios, the difference absolute difference between both types of methods are much smaller, as can be observed in S1, S2, S4, S15 and S36, for example.

**Figure 3.22** - Estimated average values of rock mass deformation for non-normalized (NN) and normalized (N) empirical correlations



Source: elaborated by the author.

For the third and final analysis, it was taken into account the behavior of the estimated deformation modulus values based on the same type of classification for each scenario. Figures 3.23a, 3.23b, 3.23c, and 3.23d present the estimate  $E_{rm}$  values calculated using RQD, RMR, Q, and GSI - based methods.

Regarding the RQD-based methods, for the scenarios with rock masses with  $RQD > 64\%$ , the correlations proposed by Coon and Merritt (1970), Eq. 3.1, and its modified version suggested by Gardner (1987), Eq. 3.2, estimated higher values of deformation modulus when compared to Zhang and Einstein's (2004) correlation, Eq. 3.4. For RQD values lower than 64%, the correlation proposed by Gardner (1987), which

gives an arbitrary value for the deformation ratio,  $E_{rm}/E_i$ , of 0.15, yielded  $E_{rm}$  higher than Zhang and Einstein's (2004) empirical method in almost all rock mass quality scenarios, other than S11, S12 and S31. In a direct comparison to the average value of the estimated values calculated by the other methods, in most of the scenarios, the RQD-based method resulted in lower values, especially for the good quality rock mass scenarios.

About the RMR-based empirical methods, the correlation proposed by Nicholson and Bieniawski (1990), Eq. 3.16, Gokceoglu *et al.* (2003), Eq. 3.19, and Sonmez *et al.* (2006), Eq. 3.20, estimated the low values of  $E_{rm}$  among the others. On the other hand, Mitri *et al.*'s (1994) correlation resulted in high values of deformation modulus for poor-to-medium rock mass quality, i.e.,  $30 < \text{RMR} < 50$ . For better rock mass with better quality, the correlations proposed by Bieniawski (1984) and Read *et al.* (1994) estimated high values of  $E_{rm}$ , that is,  $\text{RMR} > 50$ .

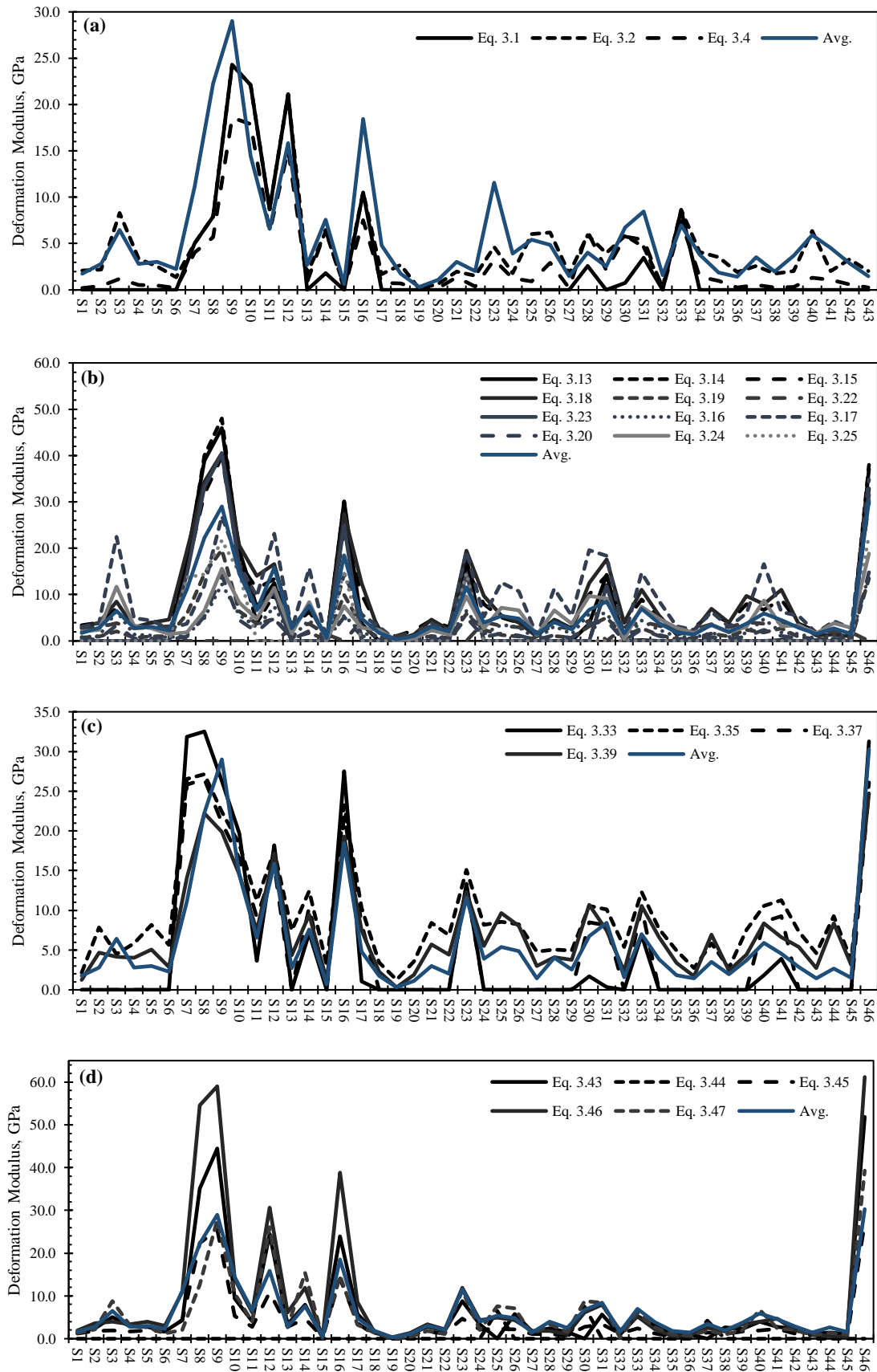
For the empirical methods that used Barton *et al.*'s (1974) Q-value as an input parameter to estimate the deformation modulus of rock masses, the correlation proposed by Barton (1995), Eq. 3.35, yielded the highest values among the others, especially for low-to-medium quality rock mass scenarios. For the scenarios with medium-to-good rock mass quality, Barton's (2002) empirical method, Eq. 3.39, stood out for giving average values of deformation modulus, closest to the average value of the estimated values calculated by the other methods. Grimstad and Barton's (1993) and Palmström and Singh's (2001) also presented values similar to the average, but only for a few cases of good rock mass quality scenarios.

To conclude this analysis, the GSI-based methods were the correlations with the greatest absolute variation, when compared to the other methods, mostly for the scenarios classified with  $\text{GSI} > 65$  (S8, S9, S12, S16, S46). While the simplified Hoek and Diederichs (2004) equation, Eq. 3.49, predicted the upper bound values, the generalized Hoek and Diederichs (2004), Eq. 3.50, resulted the lower bound values, among the other GSI-bases empirical correlations.

### 3.5.2 Comparative analysis – $\sigma_{cm}$

This section will compare the behavior of the empirical methods proposed for estimating the compressive strength of rock masses,  $\sigma_{cm}$ , using the database of 46 scenarios with rock masses with different qualities (Table 3.6), as analogous to the previously comparative analysis.

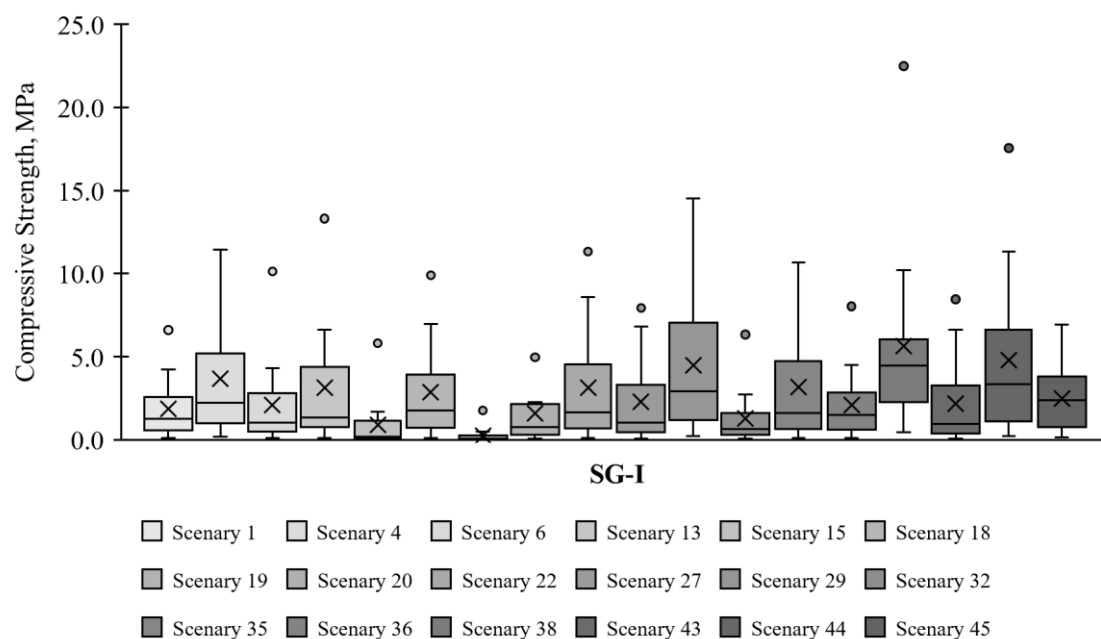
**Figure 3.23** -  $E_{rm}$  values estimated using RQD (a), RMR (b), Q (c) and GSI (d) - based methods plotted with the average results from all methods



Source: elaborated by the author.

Beginning with the scenarios from SG-I group, the correlations proposed by Kulhawy and Goodman (1987), Eq. 3.9, AASHTO (2002), Eq. 3.11, and Singh (1993), Eq. 3.40, estimated the highest values of compressive strength among the other methods. On the other hand, Yudhbir *et al.*'s (1983) and Hoek *et al.*'s (2002) methods, Eqs. 3.27 and 3.49, yielded the low bounded values, followed by the equations suggested by Ramamurthy (1985), Eq. 3.28, and Sheorey (1997), Eq. 3.30.

**Figure 3.24** - Box plot graph of estimated  $\sigma_{cm}$  values of scenarios from SG-I

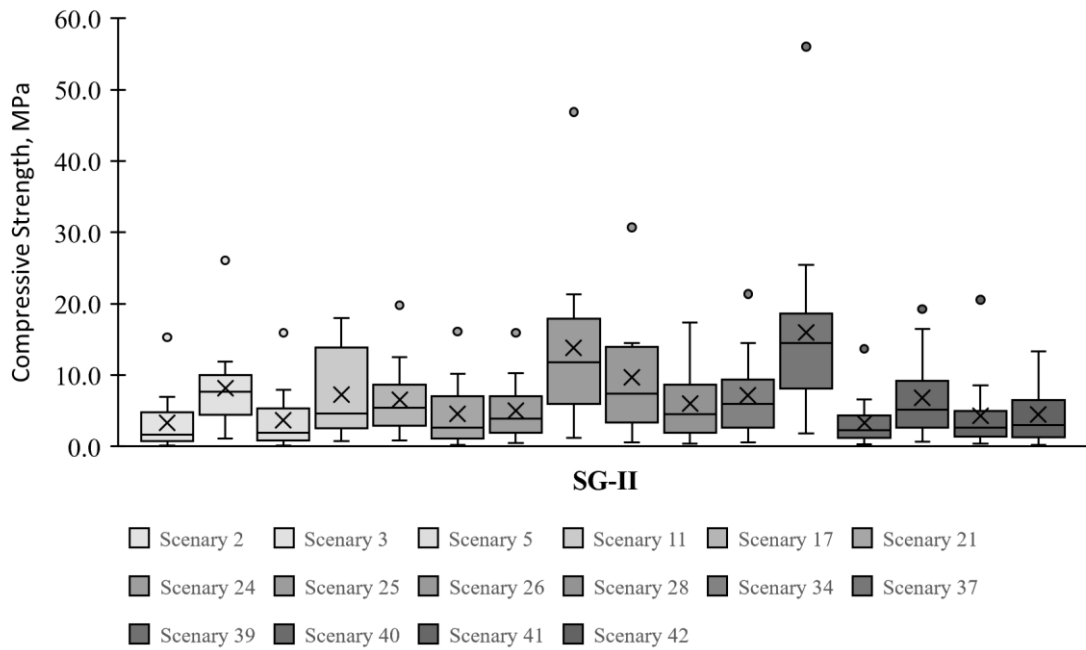


Source: elaborated by the author.

The correlations suggested by Aydan and Dalgic (1998), Eq. 3.32, for the weak rock mass scenarios, resulted in  $\sigma_{cm}$  values closest to the median for each scenario. In parallel with this behavior, Eqs. 3.29 and 3.31, derived from Kalamaras and Bieniawski's (1995) and Ramamurthy's (2004) studies, also calculated the central values of compressive strength for SG-I. Figure 3.24 presents the range of deformation values estimated by the appropriated empirical methods.

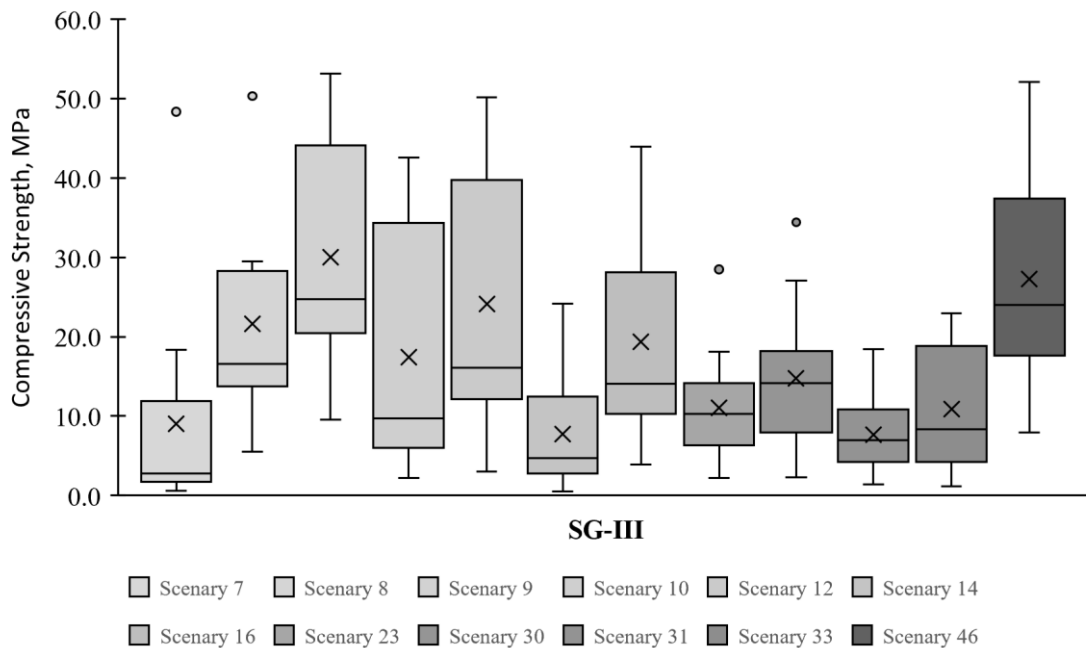
For the SG-II and SG-III groups, the proposed correlations for estimating the compressive strength followed the same behavior in comparison to the SG-I group, where the RQD-based methods together and Singh's (1993) correlation estimating the highest results, while Yudhbir *et al.*'s (1983), Ramamurthy (1985) and Hoek *et al.*'s (2002) equations estimated the most conservative results (see Figure 3.27).

**Figure 3.25** - Box plot graph of estimated  $\sigma_{cm}$  values of scenarios from SG-II



Source: elaborated by the author.

**Figure 3.26** - Box plot graph of estimated  $\sigma_{cm}$  values of scenarios from SG-III

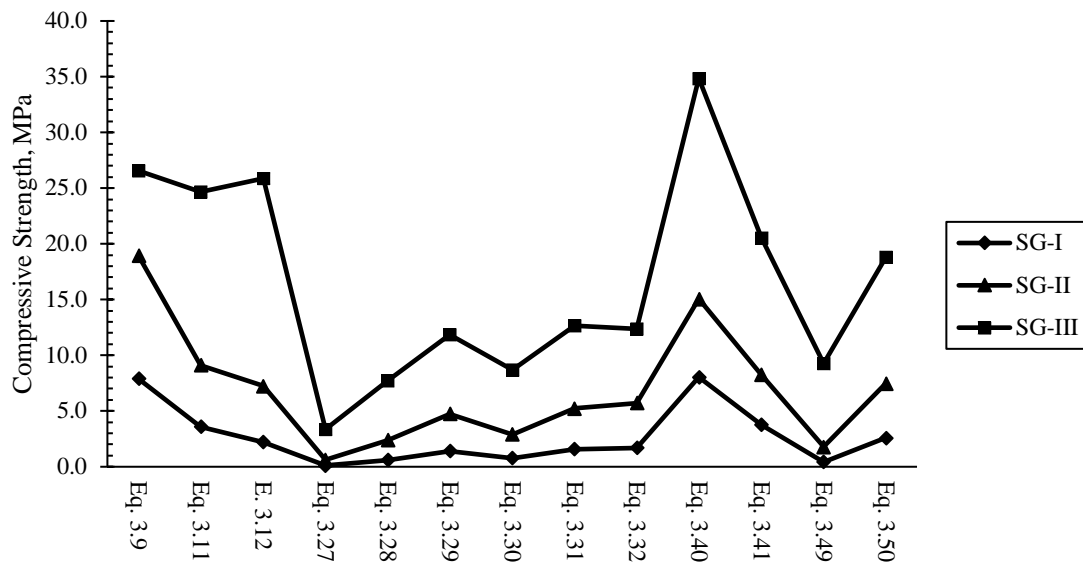


Source: elaborated by the author.

Next, for the correlations based on the same type of classification, Figures 3.28a, 3.28b, 3.28c, 3.29d shows the calculated values of compressive compared to the average values from all schemes-based methods.



**Figure 3.27** - Average values of compressive strength estimated by the empirical methods for the SG-I, SG-II and SG-III groups



Analyzing initially the RQD-based methods, the correlations proposed using Deere's index resulted in values above the average, as observed before. Among these methods, Zhang's (2010) equation, Eq. 3.12, yielded the low  $\sigma_{cm}$  values for rock mass with  $RQD < 40\%$  and  $RQD > 80\%$ , while, for the same range of rock mass quality, the proposed method by Kulhawy and Goodman (1987), Eq. 3.9, estimated the highest values. For rock masses with  $40 \leq RQD \leq 80\%$ , the suggested correlation by AASTHO (2002), Eq. 3.11, gave the most conservative values. This behavior can be observed in Figure 3.4.

Taking into the account the estimated values of compressive strength of rock masses calculated by the RMR-based methods, the correlations proposed by Yudhbir *et al.* (1983), Ramamurthy (1985), Kalamaras and Bieniawski (1995), Sheorey (1997), Ramamurthy (2004), and Aydan and Dalgic (1998), Eqs. 3.27 to 3.32, behaved similar for almost the full range of RMR values. For scenarios classified with RMR greater than 20 and less than 65, Eq. 3.32 estimated the highest value, followed by Eqs. 3.31, 3.29, 3.30, 3.28, while 3.27 estimated the most conservative values among the methods based on the Bieniawski system. In direct comparison with the average results obtained from the other correlations, all these equations estimated conservative values of compressive strength compared to the average results, as shown in Figure 3.28b.

Regard to the Q-based methods, as discussed during the first analysis, Singh's (1993) empirical method, Eq. 3.40, overestimated the compressive strength of rock masses, among the RQD-based correlations. On the other hand, Eq. 3.41, presented by

Barton (2002), estimated conservative values, similar to the average  $\sigma_{cm}$  estimated by the other correlations, as can be observed in Figure 3.28c.

To conclude this comparative analysis among the empirical methods based on classification schemes for estimating the compressive strength, Figure 3.28d presents the  $\sigma_{cm}$  results for all rock mass scenarios using Hoek's (1994) index-based methods, Eqs. 3.49 and 3.50. As can be noticed, the method derived from the generalized Hoek and Brown failure criterion, Eq. 3.49, estimated the most conservative values, while the suggested correlation presented by Zhang (2010), Eq. 50, after personal communication with Dr. Evert Hoek in 2005, yielded values a little higher than the overall average for all qualities rock mass scenarios.

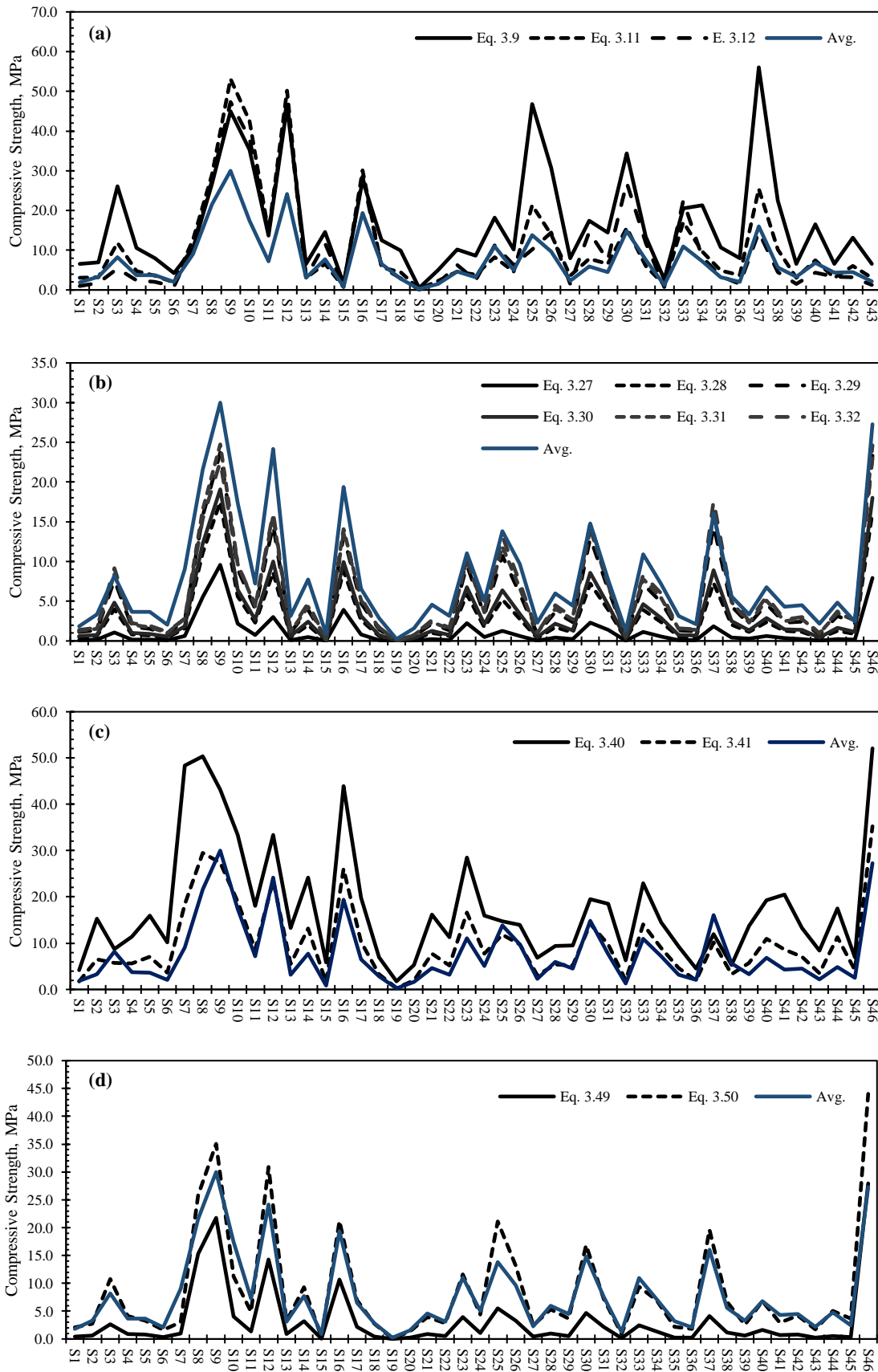
### 3.6 Conclusions

Estimating the mechanical properties of rock masses is a necessary step for any numerical modeling analysis for predicting the behavior of rock masses due to changes in their stress field, whether due to an underground excavation or the increase of load due to the settlement of a dam, for example. Among the various direct and indirect proposed methodologies for estimating rock mass deformation,  $E_{rm}$ , and compressive strength,  $\sigma_{cm}$ , methods based on rock mass classification systems are most cost-effective, especially during the early stages of most projects.

This chapter has reviewed an extensive number of publications suggesting empirical methods for estimating  $E_{rm}$  and  $\sigma_{cm}$ , using as input parameter rock mass quality index number derived from the following classification schemes: Rock Quality Designation (RQD), Rock Mass Rating (RMR), Q, and Geological Strength Index (GSI). To evaluate them, a comparative analysis between these methods was performed using 46 scenarios of different quality rock masses, previously characterized and classified. For the estimated values of deformation modulus, the following conclusions were derived from the comparative analysis:

- a. For rock mass scenarios with low-to-medium quality, the correlations suggested by Mitri *et al.* (1994), Barton (1995) and Read *et al.* (1999) yielded high values of  $E_{rm}$ , while, for rock mass scenarios with better quality, the simplified Hoek and Diederichs (2004) equation overestimated the deformation modulus when compared to the other methods, followed by Bieniawski's (1978) equations.

**Figure 3.28** -  $\sigma_{cm}$  values estimated using RQD (a), RMR (b), Q (c) and GSI (d) - based methods plotted with the average results from all methods



Source: elaborated by the author.

b. On the other hand, the correlation suggested by Sonmez *et al.* (2006) estimated the lower values of deformation modulus for all rock mass quality scenarios. The equations designed by Nicholson and Bieniawski (1990), Gokceoglu *et al.* (2003) and Zhang and Einstein's (2004) also resulted in  $E_{rm}$  values below the average. The empirical methods proposed by Hoek and Diederichs (2004), the generalized one, and Galera *et al.* (2007) gave the most central  $E_{rm}$  values.

c. Based upon the results presented above, it is perceptible that non-normalized correlations, in general, estimate higher deformation values when compared to normalized equations, i.e., expressed using deformation ratio ( $E_{rm}/E_i$ ). This difference is even greater in scenarios with higher quality rocks, where some correlations estimate deformation values higher than those of intact rock, e.g., S7, S8, S9, and S16 (see Appendix B). Therefore, the use of non-normalized correlations should be used with caution in cases of good quality rocks, especially where there are no measurements of intact rock stiffness.

d. Regarding the comparison of the  $E_{rm}$  values estimated based on the same classification scheme, the correlations proposed by Zhang and Einstein (2004), Galera *et al.* (2007), i.e., the normalized equation, Barton (2002), and Hoek and Diederichs (2006), i.e., the generalized equation, yielded the most central values. In cases where a few or only one classification was used to characterize the rock mass site, these correlations can be used for a first estimate of the mechanical behavior of the rock mass.

For estimating the strength of rock masses using the classification schemes based equations, the correlation proposed by Aydan and Dalgic (1998) and Hoek (2004 apud Zhang, 2010) gave the most average values, therefore, they should be used as a first approach for numerical modeling purposes. For a comparative analysis of the best and worst scenarios possible, the correlation suggested by Kulhawy and Goodman (1987) and Singh (1993), and Hoek *et al.* (2002) can be used as upper and lower boundary, respectively.

## 4 APPLICATION OF GROUND-PENETRATING RADAR (GPR) TO DISCONTINUITY IMAGING FOR ROCK MASS CHARACTERIZATION PURPOSES

Rock mass classification systems are an essential tool used in rock engineering practice for the assessment of rock mass quality. In general, these systems are based on the in situ rock mass characteristics, derived mostly from geological mapping and exploratory drilling. Although both techniques are widely used and accepted by the rock mechanics community for site characterization to estimate the input parameters necessary in these classification schemes, especially concerning the discontinuity conditions, additional survey techniques can be seen as an alternative to enhance the geological mapping and drilling methodologies.

This chapter will review the ground-penetrating radar (GPR) method as an auxiliary survey methodology for improving rock mass characterization and, consequently, rock mass classification, once this geophysical method allows the subsurface imaging. In the end, a case study that was carried out at the Castanhão dam region using the GPR, in the State of Ceará, in Brazil, is presented.

### 4.1 Introduction

Rock mass classification systems have been playing an important role in rock engineering for assessing the rock mass quality for engineering design purposes. In general, they take into account the characteristics of both the intact material and the discontinuities, where are assigned rating values for them, according to their relative importance to the system (BIENIAWSKI, 1989; HARRISON; HUDSON, 2000).

Among the many systems developed gradually over time to be used as an engineering tool to predict the behavior of the rock masses under different conditions of stresses, the methodologies proposed by Deere *et al.* (1967), Bieniawski (1973, 1976, 1979, 1989), Barton *et al.* (1974), and Hoek (1994), that is, the RQD, RMR, Q and GSI, respectively, are widely used in the rock engineering practices. They have been successfully applied to several rock engineering applications, including underground excavations, rock foundations, rock slopes excavations, and open-pit mining (SINGH; GOEL, 2011).

RQD, RMR, Q, and GSI, besides their primarily engineering design scopes, have been also used as a tool for estimating the mechanical properties of rock masses, e.g., the deformation modulus,  $E_m$ , and the unconfined compressive strength,  $\sigma_{cm}$ , using empirical methods proposed by different studies in the literature (COON; MERRITT, 1970; BIENIAWSKI, 1978; SERAFIM; PEREIRA, 1983; YUDHBIR *et al.*, 1983; RAMAMURTHY, 1985; GARDNER; 1987, KULHAWY; GOODMAN, 1987; NICHOLSON; BIENIAWSKI, 1990; GRIMSTAD; BARTON, 1993; SINGH, 1993; MITRI *et al.*, 1994; BARTON, 1995; HOEK; BROWN, 1997; KALAMARAS; BIENIAWSKI, 1997; SHEOREY, 1997; AYDAN; DALGIC, 1998; READ *et al.*, 1999; PALMSTRÖM, 2001; AASHTO, 2002; BARTON, 2002; HOEK *et al.*, 2002; GOKCEOGLU *et al.*, 2003; ZHANG; EINSTEIN, 2004; HOEK; DIEDERICHS, 2006; SONMEZ *et al.*, 2006; GALERA *et al.*, 2007; ZHANG, 2010; LOWSON; BIENIAWSKI, 2013). Estimating these parameters directly from empirical correlations based on classification schemes stand out as the most cost-effective in direct comparison to laboratory and in situ tests (CAI *et al.*, 2004; HOEK; DIEDERICHS, 2006; ZHANG; 2010; PANTHEE *et al.*, 2017).

Regard to the rock mass features used as input parameters in the classification schemes, they are the strength of the intact rock material ( $P_1$ ), the discontinuity frequency ( $P_2$ ) their conditions ( $P_3$ ), i.e., continuity, aperture, roughness, infilling and weathering, the groundwater conditions ( $P_4$ ), the orientation of the discontinuities ( $P_5$ ), and the in situ stresses ( $P_6$ ). Table 4.1 lists the parameters that are taken into consideration for RQD, RMR, Q, and GSI scheme methodologies.

**Table 4.1** - Input rock mass parameters used by RQD, RMR, Q and GSI

Input Parameters	Rock Mass Classification Systems			
	RQD	RMR	Q	GSI
$P_1$ – Strength of the intact rock material		X		
$P_2$ – Discontinuity frequency	X	X	X	X
$P_3$ – Discontinuity conditions		X	X	X
$P_4$ – Groundwater conditions		X	X	
$P_5$ – Discontinuity orientation		X		
$P_6$ – In situ stresses			X	

RQD = Rock Quality Designation.

RMR = Rock Mass Rating.

Q = Tunneling Quality Index.

GSI = Geological Strength Index.

Source: elaborated by the author.

All the parameters listed in Table 4.1 are assessed by site investigation techniques, more specifically through engineering geological mapping and drilling investigations, except for the strength of the intact rock material, which is normally determined by laboratory tests, e.g., unconfined compressive strength test or point load test.

Bieniawski (1989), about the geological mapping, pointed out it as probably the most used methodology for providing data for rock mass classifications, especially concerning the discontinuity features, where it depends upon the outcrops, excavated slopes, and tunnel faces as a source of information. Drilling investigations, on the other hand, are executed for examining the subsurface rock mass conditions, principally to match with the geological information derived from the outcrops, to check the groundwater conditions, and to extract intact rock samples necessary for laboratory tests. As a costly and invasive exploration technique of the subsurface, extra care should be taken in order to choose the potential locations for performing it.

Although the importance of using both geological and geotechnical methods for characterization rock masses for the classification purposes is unquestionable, there are some limitations concerning them that need to be taken into consideration. First, about the rock mass data obtained from the outcrops, they are directly influenced by the processes of subsurface relaxation, weathering, and alteration that a rock mass outcrop is subjected to. Usually, as discussed by Marinos *et al.* (2005), this limitation can be overcome by analyzing borehole cores, which is the complementary approach used for rock mass characterization, provided by the drilling investigations. However, this second method lies on three major limitations: 1) borehole cores only give one-dimensional information of the subsurface; 2) drilling investigations are costly destructive methods, therefore they are not allowed to be used in any location; and 3) they are susceptible to the uncertainty of the location choice.

As an alternative to improve the initial overall assessment of the site for rock mass classification purposes, especially because of the limitations regarding the drilling investigation discussed above, some geophysical exploration techniques can be used as a valuable supporting tool. In general, the geophysical methods are noted for being low cost and capable of investigating a subsurface quickly, using seismic refraction and reflection, electrical resistivity, and gravimetric and magnetic measurements form (HOEK; BROWN, 1980; BIENIAWSKI, 1989; VALLEJO; FERRER, 2001).

Among the traditional geophysical methods used for exploring the subsurface, the ground-penetrating radar has been standing out the over last two decades for providing a high-resolution underground imaging technique, where it has been widely used to map discontinuities for different applications (DAVIS; ANNAN, 1989; FRIEDEL *et al.*, 1991; TOSHIOKA *et al.*, 1995; WYATT; TEMPLES, 1996; GRASMUECK, 1996; GRANDJEAN; GOURRY, 1996; GORDNER, 2001; GRÉGORIE; HALLEUX, 2002; NASCIMENTO DA SILVA, 2004; THEUNE *et al.*, 2006; PORSANI *et al.*, 2006; KADIOGLU, 2008; DORN *et al.*, 2012; AROSIO, 2016; SARIDUBAK, 2016; ELKARMOTY *et al.*, 2017).

To show that the ground-penetrating radar method is a potential alternative characterization tool for improving the collection of information about the subsurface discontinuity conditions for rock mass classification purposes, this chapter will compare the geological information derived from an outcrop image using an unmanned aerial vehicle (UAV) to the subsurface information obtained from using GPR exploration surveys.

## 4.2 Ground-Penetrating Radar (GPR)

Ground-penetrating radar, GPR, is a nondestructive and well-accepted geophysical technique that uses short high-frequency-pulsed electromagnetic, EM, waves, normally from 10 to 1000 MHz, to probe the interior of natural geological materials, such as soil and rock masses, and human-made composites, such as concrete, asphalt, and other construction materials, based on changes in the EM properties, i.e., dielectric permittivity, electric conductivity, and magnetic permeability, of the investigated medium (ANNAN, 2003; 2005; 2009; DANIELS, 2004).

In a direct comparison to the other geophysical methods used to acquire the subsurface ground information, such as the seismic and sonar techniques, the GPR allows a higher resolution sounding capability, detecting features with an order of few tens of millimeters thickness at ranges of several meters (DAVIS; ANNAN, 1989). Another advantage of this technique, as reported by Vallejo and Ferrer (2011), lies on the speed in which the subsurface data can be collected. On the other hand, the main limitation of GPR is due to penetration depth limitation, especially in lossy dielectric materials, i.e., materials that tend to be conductive rather than resistive, as it will be discussed later.



The GPR technique has been successfully used for (DAVIS; ANNAN, 1989; ANNAN, 2003; DANIELS, 2005; NEAL, 2004; JOL, 2009; BRISTOW; JOL, 2003; PERSICO, 2014; BENEDETTO; PAJEWSKI, 2015; UTSI, 2017; LAI *et al.*, 2018): (1) mapping geologic features, such as bedrock depth, water table depth, soil stratigraphy (depth and thickness), faults and fracture zones within rock masses, and cavities in rock; (2) locating metallic and non-metallic utilities underground, such as cables, pipes and tanks; (3) mapping cavities or voids beneath road pavements, runways or behind tunnel linings; (4) archaeological and forensic investigation purposes; and (5) inspecting civil engineering constructions, such as concrete and masonry structures, highway bridges, and foundation of buildings.

This section will review some important aspects related to GPR, including some basic principles of operation, the types of survey methodologies employed, and the processing and interpretation data procedures.

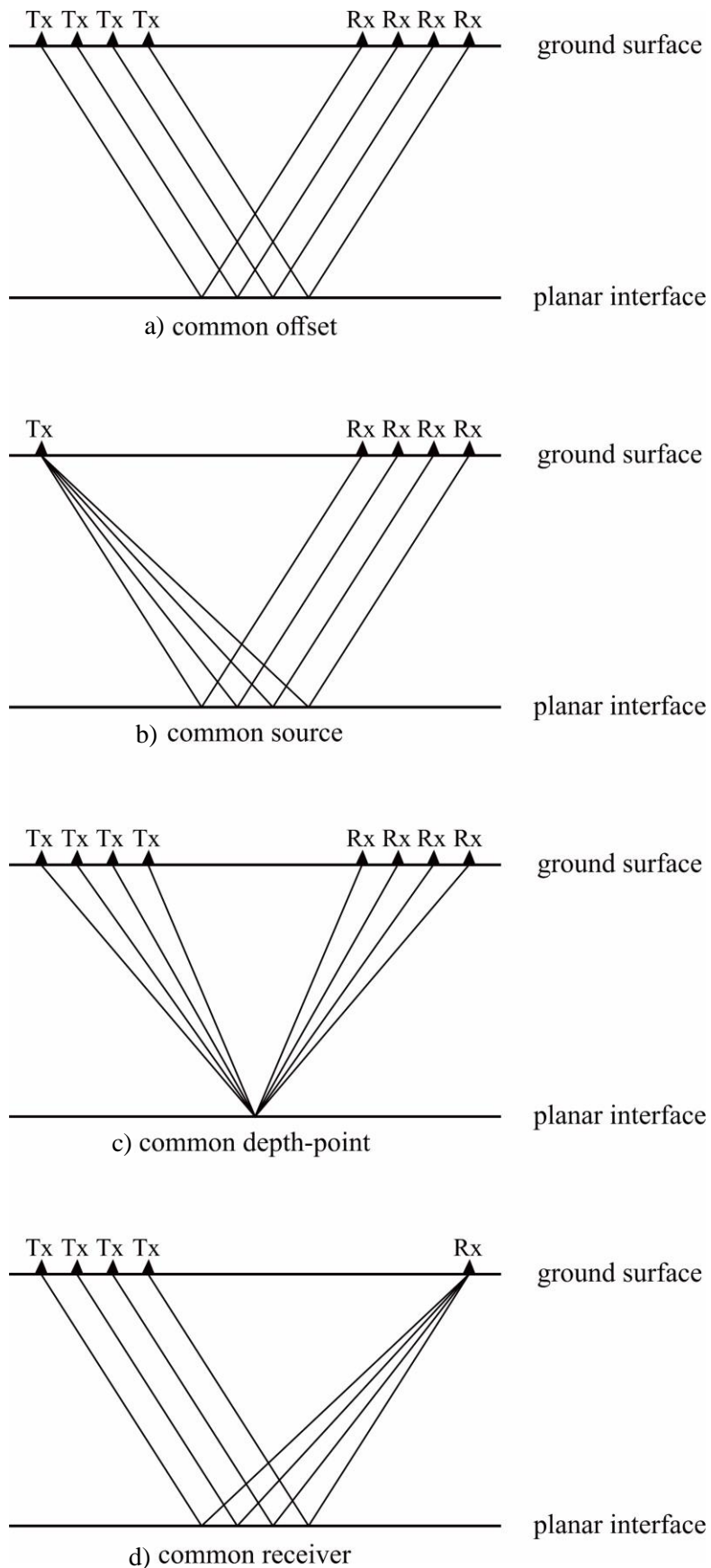
#### 4.2.1 The GPR Technique

Also known as ground-probing, sub-surface, and surface-penetrating radar, ground-penetrating radar is a non-invasive geophysical measurement technique that provides a high-resolution image of the subsurface based on the difference of EM properties within the medium (DANIELS, 2005). In this regard, GPR propagates low-power packets non-sinusoidal EM waves with frequency from 10 MHz to 4 GHz, which are reflect and detected by the radar when a discontinuity of the EM properties is detected (YELF, 2007; PERSICO, 2014).

With respect to the components of a GPR system, it comprises a control unit, one or more transmitter, Tx, and one receiver antenna, Rx, which can be shielded or unshielded, and suitable data storage and the display devices (ASTM, 2011; UTSI, 2017). The antennas are normally placed relatively close to the ground surface, where they can be coupled on a wheeled trolley or sled in order to protect the equipment and to speed up the survey (YELF, 2007). To compensate for the natural non-uniformity of the velocity of the operator during the survey with the radar, an odometer is usually equipped to the equipment (PERISCO, 2014).

The modes of operation for the ground-penetrating radar data acquisition can be classified as: common offset, common source, common depth-point and common receiver, as illustrated in Figure 4.1 (DANIELS, 2004).

**Figure 4.1** - Modes of operation for ground-penetrating radar data acquisition: a) common offset; b) common source; c) common depth-point; and d) common receiver

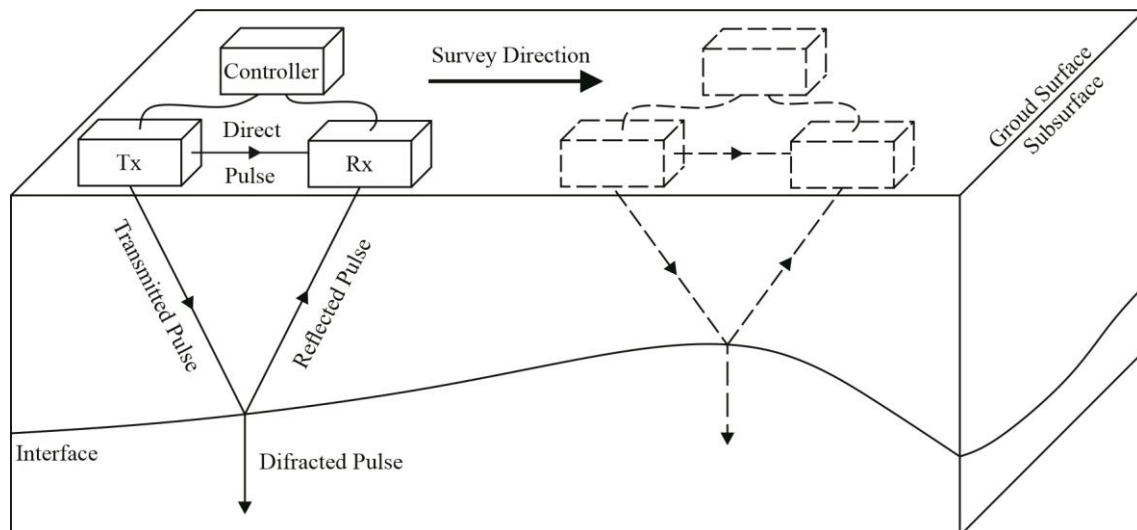


Source: Adapted from Daniels (2004).

The common offset mode Figure 4.1a, also known as the reflection profiling mode (DAVIS; ANNAN, 1989; ASTM, 2011; REYNOLDS, 2011; GOODMAN; PIRO, 2013), is the most used in practice for acquiring the subsurface data during a GPR survey. In this mode, one or more antennae are moved along the survey line on the ground surface simultaneously, where it is measured the two-way travel time that an output pulse emitted from the transmitting antenna (Tx) are reflected back to a receiving antenna (Rx) when an interface at which the electromagnetic properties of the medium changes occurs (see Figure 4.2). For every single fixed point, a scan giving the GPR reflections is displayed. As the antennae are moved, a series of scans are collected, resulting in a two-dimensional profile of the subsurface (Figure 4.3).

The common source and receiver modes, Figures 4.1b and 4.1d, respectively, are used for conducting velocity soundings. In these modes, the radar data are collected fixing the transmitter or the receiver antenna over an area where the principal reflector is and either horizontal or dipping only at very shallow angles (REYNOLDS, 2011). Because of these assumptions, these methods, which are termed in the literature as the Wide Angle Reflection and Refraction (WARR) sounding methods (DAVIS; ANNAN, 1989, ANNAN, 2003, 2005), are rarely performed in GPR studies (NEAL, 2004).

**Figure 4.2** - Illustration of the reflection profiling mode for GPR data acquisition



Source: elaborated by the author.

For the last, the common depth-point, Figure 4.1c, or common mid-point (CMP), is another sounding mode used for estimating the signal velocity in the ground (DAVIS; ANNAN, 1989). In contrast to the WARR mode, the CMP is commonly used

in practice as it avoids the assumption of having a planar reflector available at the GPR survey area. In this case, both transmitting and receiving antennae are moved away from each other at fixed intervals with a midpoint between them fixed.

#### 4.2.2 GPR EM Waves Theory

The ground-penetrating radar method relies heavily on the electromagnetic properties of the material, where the behavior of the GPR signal used for probing the interior of the materials is described by the Maxwell's equations, expressed as (ANNAN, 2003, 2005, 2009; CASSIDY, 2009):

$$\nabla \times \vec{E} = -\frac{\partial(\vec{B})}{\partial t} \quad 4.1$$

$$\nabla \times \vec{H} = \vec{J} + \frac{\partial(\vec{D})}{\partial t} \quad 4.2$$

$$\nabla \cdot \vec{D} = q \quad 4.3$$

$$\nabla \cdot \vec{B} = 0 \quad 4.4$$

where  $\vec{E}$  is electric field strength vector ( $V.m^{-1}$ );  $\vec{B}$  is the magnetic flux density vector (T);  $\vec{D}$  is the electric displacement vector ( $C.m^{-2}$ );  $\vec{H}$  is the magnetic field intensity ( $A.m^{-1}$ );  $q$  is the electric charge density ( $C.m^{-3}$ ); and  $\vec{J}$  is the electric current density vector ( $A.m^{-2}$ ).

These equations mathematically describe the physics of electromagnetic fields and are the foundation for the consideration of the propagation of EM waves (DANIELS, 2004). Conversely, as reported by Benedetto *et al.* (2017), the behavior of the survey medium in which the GPR signal is transmitted is described by the following constitutive equations:

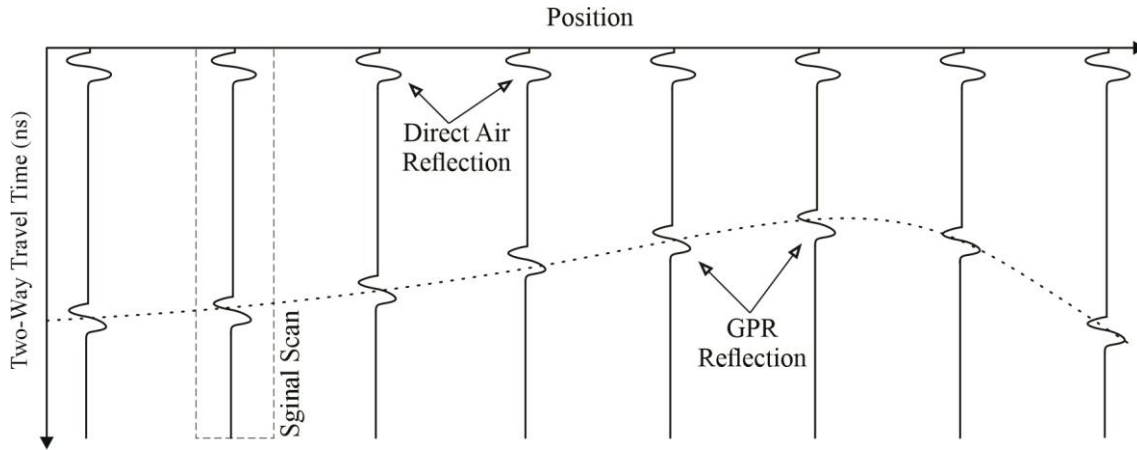
$$\vec{J} = \sigma \vec{E} \quad 4.5$$

$$\vec{D} = \epsilon \vec{E} \quad 4.6$$

$$\vec{B} = \mu\vec{H} \quad 4.7$$

where  $\sigma$  is the electric conductivity ( $S.m^{-1}$ ),  $\epsilon$  is dielectric permittivity ( $F.m^{-1}$ ), and  $\mu$  is the magnetic permeability ( $H.m^{-1}$ ).

**Figure 4.3** - Two dimension GPR profile derived from Figure 4.2



Source: elaborated by the author.

Maxwell's equations, Eqs. 4.1 to 4.4, combined with the constitutive relationships presented above, Eqs. 4.5 to 4.7, will describe the behavior of the GPR signal propagation into the ground. Next, it is reviewed how the EM properties of the medium, especially the dielectric permittivity and electric conductivity, influence important aspects in the GPR acquisition data, including the propagation velocity, the depth of penetration, and the attenuation of the EM waves in materials.

#### 4.2.3 GPR Signal Behavior

As earlier discussed, in a GPR data acquisition survey procedure using a common offset reflection profiling mode, Figure 4.1a, it is measured for every each predetermined position (a) the two-way travel time of the GPR signal, that is, the time required for the GPR energy waves travel downward from the transmitting antenna to a surface boundary with different EM properties (dielectric interface) and return to the receiving antenna, and (b) the amount of energy reflected due to the EM properties contrast in the subsurface. The behavior of the two measures is used to describe the

electromagnetic characteristics of the surveyed medium in which the GPR signal was propagated, and, consequently, imaging the subsurface.

Concerning to the two-way travel time (a), it is measured in terms of time, in nanoseconds, and can be converted to depth, which is more suitable for geological and engineering purposes, by determining or estimating the propagation velocity of the GPR pulses. This propagation velocity can be measured in the field using the WARR or CMP sounding methods, as presented before, or can be estimated through the following correlation (NEAL, 2004):

$$V_m = \frac{c}{\sqrt{\epsilon_r \mu_r \frac{1 + \sqrt{1 + \left(\frac{\sigma}{\omega \epsilon}\right)^2}}{2}}} \quad 4.8$$

where  $V_m$  is the propagation velocity through the material;  $c$  is the propagation velocity in a vacuum ( $3 \times 10^8$  m.s<sup>-1</sup>);  $\epsilon$  and  $\epsilon_r$  are the dielectric and relative permittivity, respectively;  $\mu_r$  is the relative magnetic permeability (= 1 for non-magnetic materials); and  $\sigma/\omega\epsilon$  is the loss factor, where  $\omega = 2\pi f$  is angular frequency (rad.s<sup>-1</sup>).

In a low-loss medium, i.e., materials where energy dissipation is small compared to energy storage (ANNAN, 2009), the loss factor is almost zero ( $\sigma/\omega\epsilon \approx 0$ ), so Eq. 4.8 can be reduced into Eq. 4.9. Due to its simplicity, this simplified relationship has been commonly used to find the propagation velocity when the assumptions are fulfilled (DAVIS; ANNAN; 1989; DANIELS, 2004, 2005; REYNOLDS, 2011).

$$V_m = \frac{c}{\sqrt{\epsilon_r}} \rightarrow V_m[\text{m.ns}^{-1}] = \frac{0.3}{\sqrt{\epsilon_r}} \quad 4.9$$

The relative permittivity,  $\epsilon_r$ , used in Eqs. 4.8 and 4.9, also termed as the relative dielectric permittivity or dielectric constant, is defined as the ratio of the dielectric permittivity of a material,  $\epsilon$ , to the permittivity of free space,  $\epsilon_0$  (Eq. 4.10).

In practice, the ground-penetrating radar users use the  $\epsilon_r$  rather than the  $\epsilon$ , as the relative permittivity is the real part of the dielectric constant (DAVIS; ANNAN; 1989, DANIELS, 2004; ANNAN, 2009).

$$\epsilon_r = \frac{\epsilon}{\epsilon_0} \quad 4.10$$

where  $\epsilon$  is the dielectric permittivity (F/m) and  $\epsilon_0$  is the permittivity of free space ( $8.854 \times 10^{-12}$  F/m).

Regard to the GPR signal reflections (b) they are governed by the EM material properties contrast, in which the proportion of energy reflected is given by the reflection coefficient,  $R$ , given as (NEAL, 2004; REYNOLDS, 2011):

$$R = \frac{\sqrt{\epsilon_{r2}} - \sqrt{\epsilon_{r1}}}{\sqrt{\epsilon_{r2}} + \sqrt{\epsilon_{r1}}} \quad 4.11$$

where  $R$  is the reflection coefficient and  $\epsilon_{r1}$  and  $\epsilon_{r2}$  are the respective dielectric constants of the material from layers 1 and 2.

The reflection coefficient ranges from  $-1$  to  $1$ , and its magnitude will determine how much of the transmitted wave is reflected back to the ground. If  $\epsilon_{r1}$  and  $\epsilon_{r2}$  are similar, most of the incident EM wave is transmitted through the dielectric interface, while, for a great contrast between the relative permittivity of the layers, most of the incident wave will be reflected (NEAL, 2004). Usually, in a geological setting, this contrast of relative permittivity is a function of (1) soil and rock material, (2) water content, and (3) bulk density (ASTM, 2011).

The reflection coefficient can also be estimated using the propagation velocities as follows:

$$R = \frac{V_2 - V_1}{V_2 + V_1} \quad 4.12$$

where  $V_1$  and  $V_2$  are the GPR wave velocities in layers 1 and 2, respectively.

Table 4.2 lists typical values of relative permittivity and propagation velocity, besides other electromagnetic characteristics, for some common geological subsurface materials. It is possible to observe that water is the material with the highest values of  $\epsilon_r$ , which explains the reason why the water table can be mapped easily in soils and rocks using the GPR technique.

**Table 4.2** - Electromagnetic characteristics of common geological materials

Material	Relative Permittivity	Conductivity (mS.m <sup>-1</sup> )	Velocity (m.ns <sup>-1</sup> )	Attenuation (dB.m <sup>-1</sup> )
Air	1	0	0.30	0
Distilled water	80	0.01	0.033	0.002
Fresh water	80	0.5	0.033	0.1
Seawater	80	3000	0.01	103
Dry sand	3-5	0.01	0.15	0.01
Saturated sand	20-30	1-10	0.06	0.03-0.3
Limestone	4-8	0.5-2	0.12	0.4-1
Shales	5-15	1-100	0.09	1-100
Silts	5-30	1-100	0.07	1-100
Clays	5-40	2-1000	0.06	1-300
Granite	4-6	0.01-1	0.13	0.01-1
Dry salt	5-6	0.01-1	0.13	0.01-1
Ice	3-4	0.01	0.16	0.01

Source: ANNAN (2005).

Among the material's electromagnetic properties described in Table 4.2, the attenuation constant,  $\alpha$ , is another important parameter used to describe the EM wave behavior in the medium. It is directly related to the GPR signal strength propagation in the medium and is often associated with the electrical conductivity,  $\sigma$ , once this parameter is one of the main responsible for causing the loss of EM wave energy transmitted (ASTM, 2011).

For materials that tend to be resistive rather than conductive (i.e., low values of electrical conductivity), e.g., dry sand, limestone, granite, and ice, the GPR signal attenuates less during its propagation in their mediums, consequently resulting in a penetration depth higher. On the other hand, materials with higher values of electrical conductivity (i.e., high values of electrical conductivity), e.g., seawater and clays, the GPR signal have their EM energy completely attenuated at depths almost near to the surface (ANNAN, 2003, 2005, 2009).

The attenuation constant can be estimated through the following correlation (REYNOLDS, 2011):

$$\alpha = \omega \sqrt{\left[\frac{\mu\epsilon}{2}\right] \left[\sqrt{1 + \frac{\sigma^2}{\omega^2\epsilon^2}} - 1\right]} \quad 4.13$$



Or, in cases of low-loss medium (DAVIS; ANNAN, 1989):

$$\alpha = \frac{1.69 \times 10^3 \sigma}{\epsilon_r} \quad 4.14$$

where  $\alpha$  is the attenuation constant ( $\text{dB.m}^{-1}$ ).

#### 4.2.4 Depth of Penetration

The main limitation concerning the ground-penetrating radar method is related to the probing depth, or penetration depth, especially when low-electrical-loss conditions are not prevalent (ANNAN, 2009). In general terms, the penetration depth is defined as the depth at the signal amplitude is no longer detectable, being a function of the electrical conductivity and the antennae frequency used during the GPR data acquisition (ANNAN, 2003).

As previously stated, for conditions that a subsurface surveyed tends to be more resistivity than conductivity, that is, the medium has low values of  $\sigma$ , the GPR signal can achieve greater probing depth before its complete attenuation when compared to a medium with lower resistivity. Therefore, penetration depths in materials such as sandstone and granite are expected to be higher than in materials like shales and clays, for example (REYNOLDS, 2011).

Besides the electrical conductivity of the surveyed medium, the antennae frequency plays an important role in determining the probing depth during a GPR survey. As reported by Neal (2004), the higher the antenna's frequency, the shallower the depth of penetration. Table 4.3, presented by ANNAN (2003), gives a big picture of the relationship between probing depth and antenna frequency.

**Table 4.3 - Probing depth as function of antenna frequency**

<b>Probing depth (m)</b>	<b>Antenna Frequency (MHz)</b>
0.5	1000
1.0	500
2.0	200
7.0	100
10.0	50
30.0	25
50.0	10

Source: ANNAN (2003).

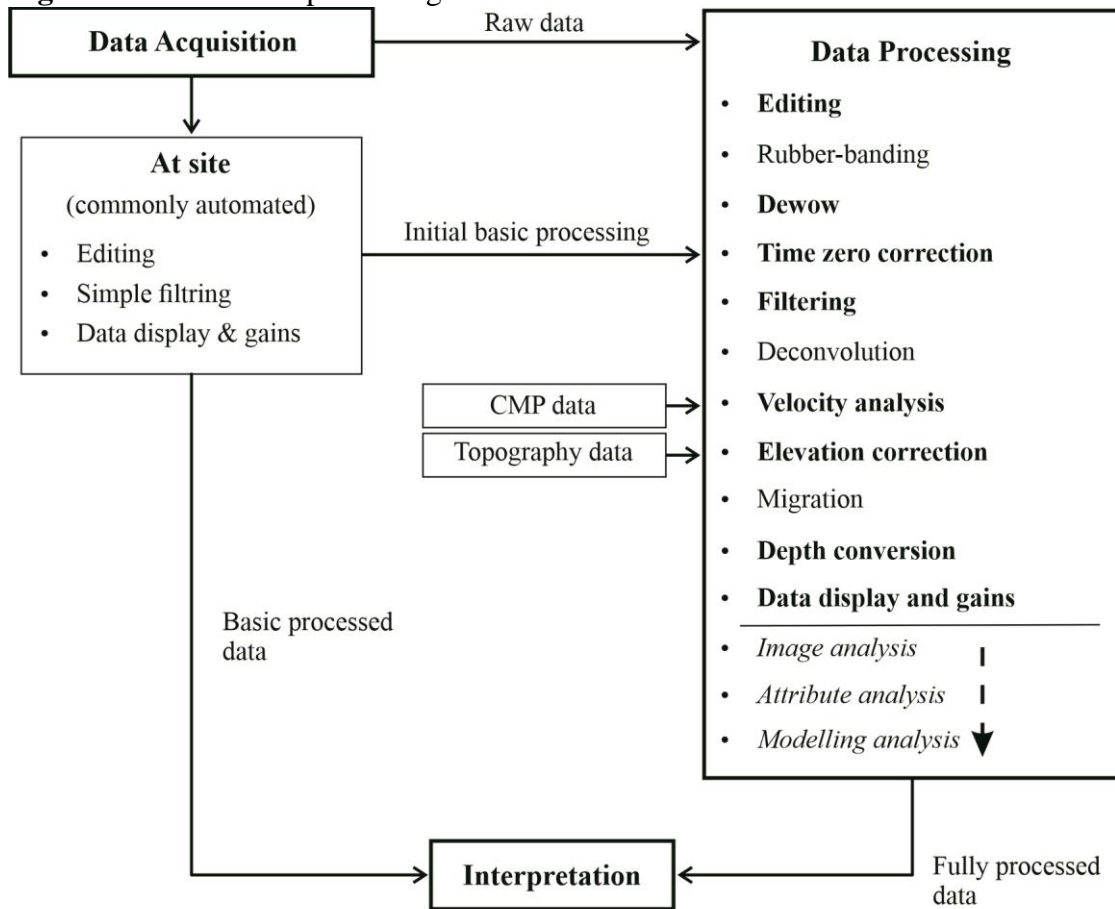
Although at first, it may seem advantageous to use a low-frequency antenna for probing the ground, once it allows for a greater depth range, the reduction of the antenna frequency directly affects, in a negative way, the GPR resolution. In other words, low-frequency antennas have a better penetration power but have a lower resolution, which can be critical for identifying some subsurface features. The chosen range of the GPR antennae frequency, consequently, is a tradeoff between resolution and penetration depth that needs to be considered carefully by the GPR operator before the acquisition survey (BAUDIN; HABIB, 2011).

#### 4.2.5 GPR Data Processing and Analysis

Once the GPR data acquisition is completed, digital signal processing is applied to the raw data as required (YELF, 2007). In this stage, several techniques can be applied to enhance the subsurface information, which includes removal of background noises, gain to increase GPR signal amplitude, topography surface correction, and velocity analysis and depth conversion, for example (CASSIDY, 2009). The general objective of data processing, in other words, is to present an image to readily be interpreted by the GPR operator/user (DANIELS, 2004).

For ground-penetrating radar data processing and signal analysis, there is common sense in the literature that, because of the number of methods existing for these purposes, the selection of techniques to treat the raw data will vary according to individual GPR surveyors (DANIELS, 2004; YELF, 2007; ANNAN, 2009; CASSIDY, 2009; UTSI, 2017). However, as a good GPR data processing practice, it is recommended to keep it simple and real as possible, to avoid processing steps unknown, and to be consistent and systematic to the processing flow route previously defined, as pointed out by Cassidy (2009).

Figure 4.4 shows a typical general processing flow sequence used with a GPR data acquisition of the common offset reflection mode, presented by Cassidy (2009). According to the author, the processing steps highlighted in bold, i.e., editing, dewow, time zero correction, filtering, velocity analysis, elevation correction, depth conversion, and data display and gains, might be considered essential, although not necessarily obligatory. A summary description of the GPR data processing is described in Table 4.4.

**Figure 4.4** - GPR data processing flow of a common-offset reflection data

Source: Adapted from Cassidy (2009).

Despite the basic data processing steps, which basically addresses some fundamental manipulations applied to the raw data in order to benefit the initial interpretation and data evaluation, as pointed out by Annan (2005), advanced imaging and analysis tools can be used as a powerful tool to facilitate the identification and characterization of the subsurface features, improving the overall quality and efficiency of interpretation (ZHAO et al, 2016).

Among these step-forward data processing techniques, attribute analysis, which has been often used by the seismic industry (WHITE, 1991) and it was fairly recently adopted by the GPR community (CASSIDY, 2009), is performed, in general, for highlight meaningful subsurface changes, including the physical properties of the medium surveyed, enhancing the GPR data for the interpretation analysis (ZHAO et al, 2013; MORRIS et al, 2019).

**Table 4.4** - Brief description of GPR data processing techniques from Figure 4.4

<b>Technique</b>	<b>Description</b>
<b>Editing</b>	Removal and correction of incoherent, noisy or missed GPR traces.
<b>Rubber-banding</b>	Correction of the horizontal scale by stretching or squeezing the data to ensure spatially uniform increments.
<b>Dewow</b>	Correction of low-frequency components from the raw data.
<b>Time-zero correction</b>	Correction of start time to match with surface position.
<b>Filtering</b>	Removal cultural or system noise and improve the visual quality of the data.
<b>Deconvolution</b>	Contraction of signal wavelets to “spikes” to enhance reflection events.
<b>Velocity analysis</b>	Determining GPR wave velocities, in situ (CMP, WARR) or as described in 4.2.3.
<b>Elevation correction</b>	Correction for the effects of topography.
<b>Migration</b>	Correction for the effects of survey geometry and spatial distribution of energy.
<b>Depth conversion</b>	Conversion of two-way travel times into depths, based on the propagation velocity, e.g., $D = V_m \times t/2$ , where $D$ is the depth, $V_m$ is the propagation velocity (see Eqs. 4.8 and 4.9), and $t$ is the two-way travel time.
<b>Display gains</b>	Selection of appropriate gains for data displays and interpretation.

Source: Cassidy (2009).

#### 4.2.6 Interpretation of GPR data

Once the GPR raw data collected is processed using the data processing techniques described above (basic or advanced), the next and last stage of the ground-penetrating technique concern with interpreting the results, usually given in a GPR profile, also known as radargram or B-scan, according to the survey purposes (DANIELS, 2005).

According to Annan (2003, 2005), interpretation is very application-dependent, where it is inherently to the experience and knowledge of the GPR interpreter. For the author, some aspects can be critical during the data interpretation, e.g., having a clear understanding of the survey objective, correlating GPR data with other sources, such as borehole information, and verifying if the subsurface image produced by the GPR is consistent to the in situ conditions, for example.

### 4.3 Study Area

To validate the ground-penetrating method as a reliable assessment tool for rock mass characterization, it was conducted a survey on a jointed rock mass slope near the Castanhão dam, in the State of Ceará, in Brazil. The choice of this location as the study area over others lies in different reasons, such as the fact that the dam was built on a jointed rock masses in addition to the importance of this construction to the hydric context of the region.

However, because of the appearance of two different geotechnical anomalies that were not previously detected during the earlier stages of the project, the Paleo Channel and the Paleo Channel Junior, compromising the final cost of the construction and its delay, it was also used as motivation for conducting this study in this region.

#### 4.3.1 Castanhão Dam

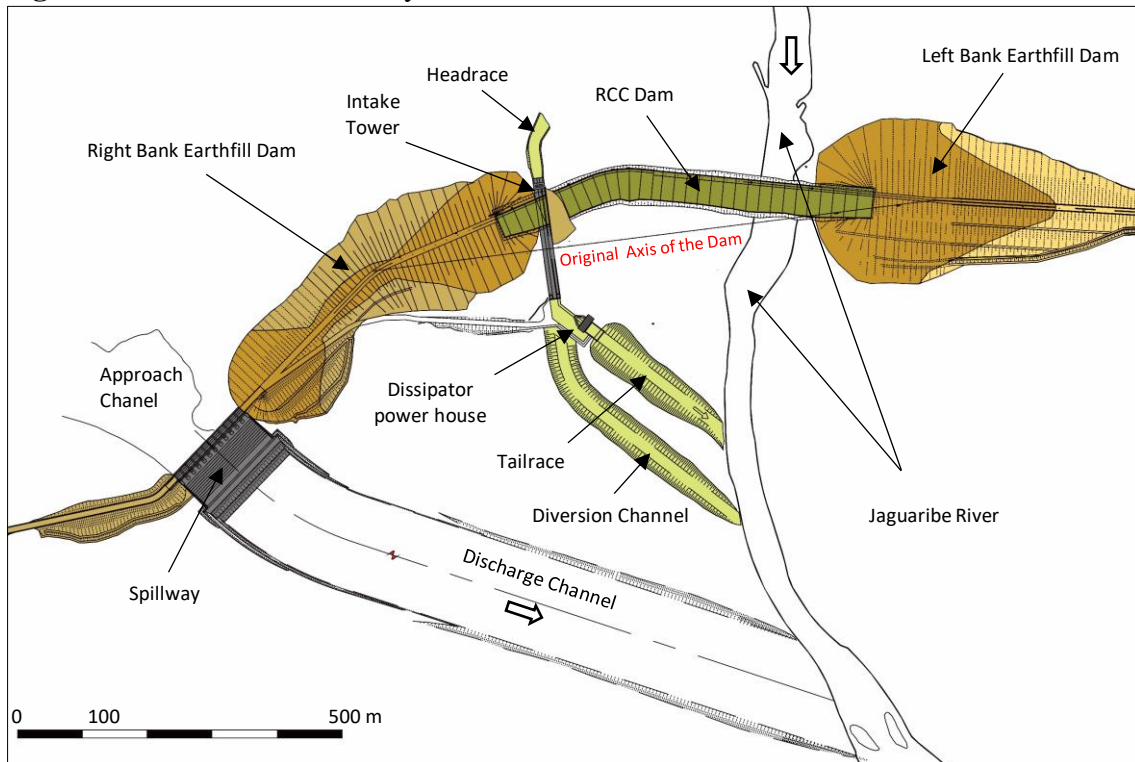
The Castanhão dam is a multipurpose dam constructed on the Jaguaribe river, in the area termed as Boqueirão do Cunha, in the State of Ceará, in the Northeast Region of Brazil, at 561261E and 9392314N (24S). It has a reservoir storage capacity of  $6.7 \times 10^9 \text{ m}^3$ , approximately  $2.4 \times 10^{11} \text{ ft}^3$ , and, among its main purposes, the dam is used to regulate the Jaguaribe river, control floods on the low Jaguaribe valley, and, most important, supply water for the riverine inhabitants and to the metropolitan area of the city of Fortaleza (CBDB, 2009).

The main components of the Castanhão complex are a roller-compacted concrete (RCC) dam with a maximum height of 72m, two bank earthfill dams located at both sides of the RCC structure, the auxiliary dam-dikes, a spillway with a maximum discharge of  $17,350 \text{ m}^3/\text{s}$  (10,000 year flood), a discharge channel, an intake tower, and a dissipator powerhouse (DNOCS, 2004). Figure 4.5 presents the Castanhão dam layout with these structural components.

As can be observed in Figure 4.5, the final layout of the project has a slightly different dam's axis when compared to the original one. The reason for this project change was due to a depression parallel to the river bed with dimension and characteristics peculiar enough, between the project stations 24C+0.00 and 26C+0.00. This anomaly was classified as Paleo Channel, Figure 4.6a, and was not previously detected during the exploration stage of the project, which was mostly done by geological field inspection

and drilling investigations (DNOCS, 2004). Later another depression on the bedrock between stations 114C+0.00 and 116C+0.00, with similar characteristics to the Paleo Channel but smaller, were found and classified as Paleo Channel Junior (Figure 4.6b).

**Figure 4.5 - Castanhão Dam layout**



Source: DNOCS (2004).

**Figure 4.6 - Paleo Channel (a) and Paleo Channel Junior (b)**

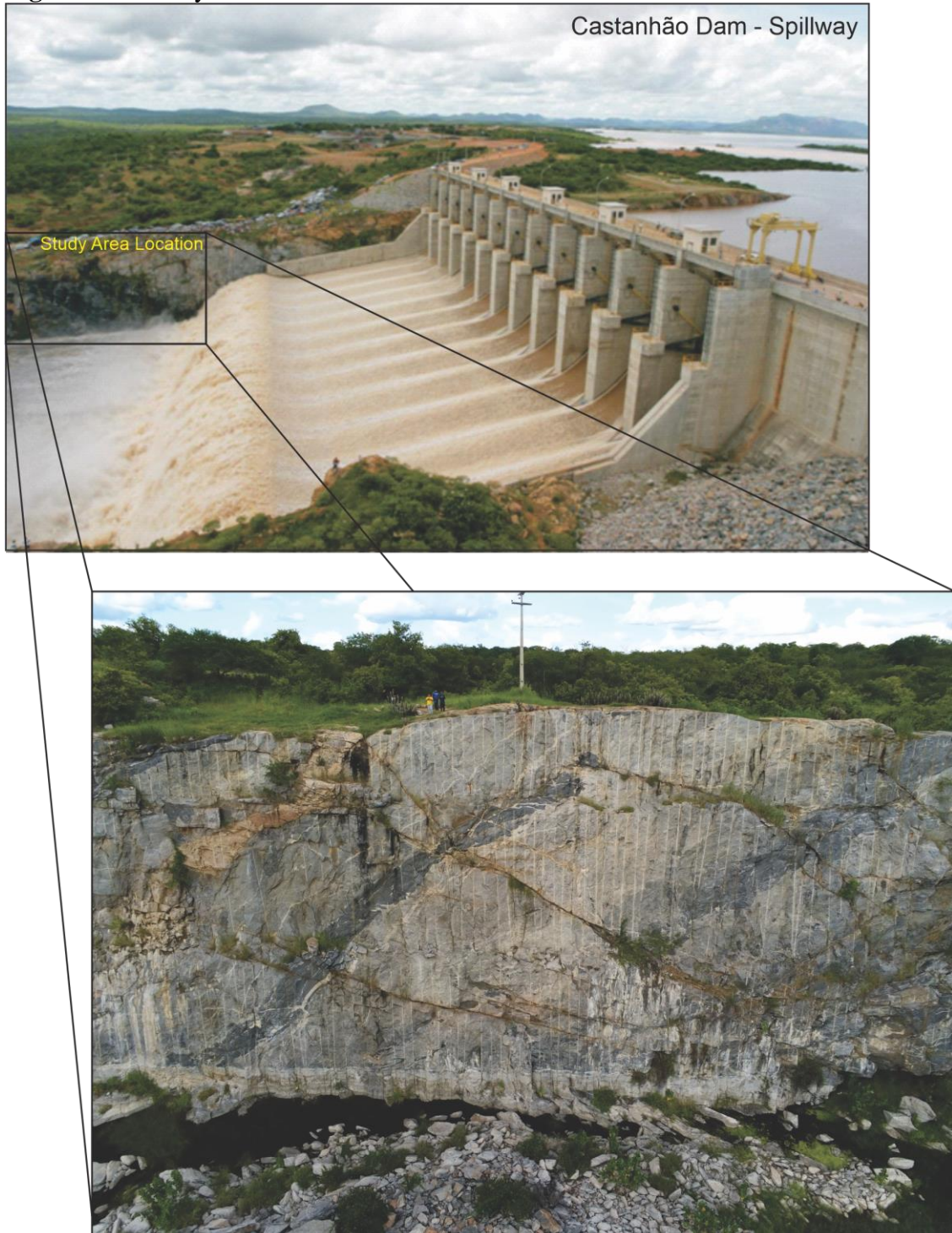


Source: DNOCS (2004).

The appearance of the Paleo Channel yielded in the interruption of the activities in this region, consequently delaying the finish of the dam construction. To minimize this delay caused by the Paleo Channel and to begin the reservoir filling in the rainy season of 2000, it was considered as an alternative possibility to build the central

section as a roller-compacted concrete (RCC) dam. This alternative solution resulted in some changes in the original location, such as moving the axis of the dam, as the dam was previously designed to be a single homogenous earthfill dam. In October of 2003, after 13 years, the Castanhão dam was concluded, becoming the largest multi-purpose dam in Latin America, according to the Brazilian Committee on Dams (2009).

**Figure 4.7 - Study area location**



Source: Adapted from CBDB (2009).

### 4.3.2 Geological Settings – Castanhão Spillway

The area selected for this study was the jointed rock mass slope at the right margin of the Castanhão dam spillway, located at 561412E and 9392366N (24S), as can be observed in Figure 4.7. The lithology of the area is formed predominantly by metamorphic rocks intersected in different places and by many times for quartz and feldspar granite veins. The gneiss rock mass presents variations according to the degree of metamorphism suffered by the original rock, in this case, an igneous rock.

From the lithological types encountered in the spillway region, there are mostly granitic gneisses with tones of color ranging from light to dark gray, where the quartz, feldspar, and biotite, in a smaller portion, are the predominated minerals. Their granulation is mainly fine to medium equigranular.

Regarding their fractures (discontinuities), they are present in different forms, mostly as horizontal (due to stress relief), vertical and sub-vertical (due to tension), where they can be founded filled with small parts of rocks, with air or just closed. The preferred directions by the fractures in this region are N/SW, N/NW and NW/SE, in agreement to the those reported by DNOCS (2004).

Regard to the granitic veins, they occur in the lenticular form, conceived by the filling with mineral material of pre-existing fractures. In granitic gneiss, the veins are relatively regular and clear. These veins are presented in pieces connected to each other and of varying thickness. They are found all the extension of the rock mass slope studied.

## 4.4 Material and Methods

For the evaluation of the ground-penetrating radar technique as a potential alternative tool to be used in conjunction with the traditional methods for the characterization of jointed rock masses, such as geological mapping and drilling exploration, the following procedures were performed at the previously selected location described above:

1. Topographic analysis of the chosen survey location;
2. Ground-penetrating radar survey for acquiring the subsurface data using different frequency antennas;
3. GPR raw data processing using basic and advanced methodologies;
4. Interpretation of the results derived from the previous processing stage.

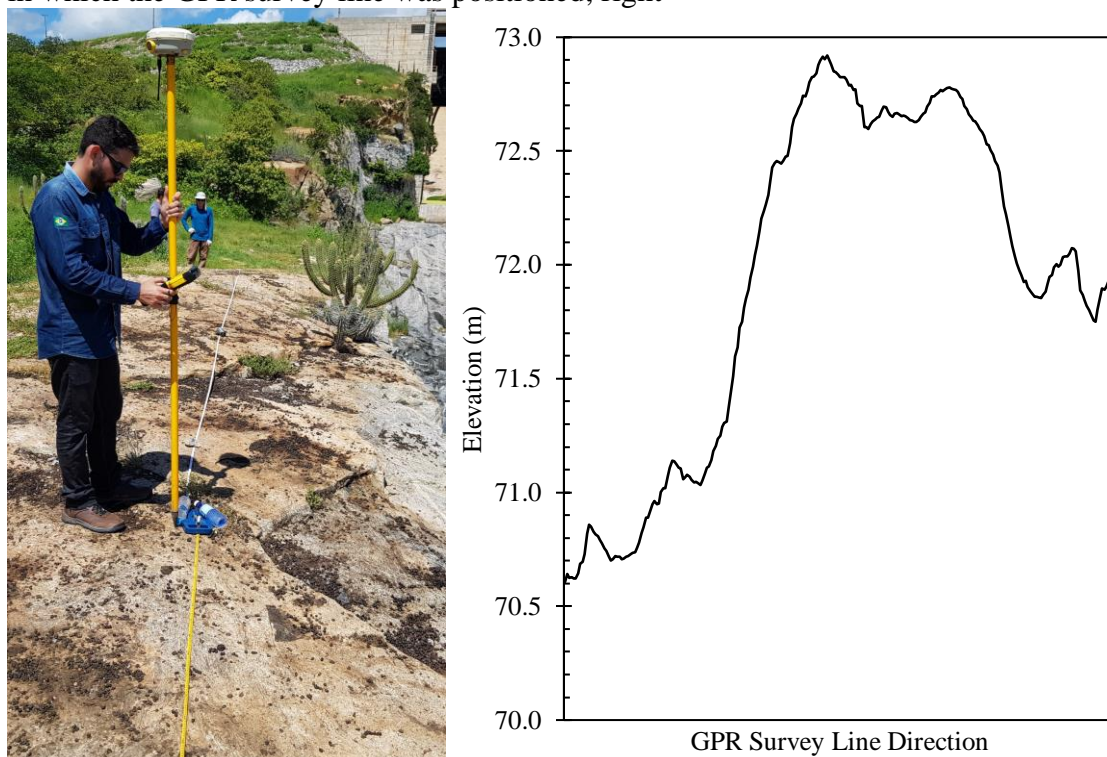


From the results obtained throughout these methodological steps, a comparative analysis will be performed in the next section to compare the results obtained from the GPR with those resulting from a visual inspection of the rock mass slope outcrop using an unmanned aerial vehicle (UAV).

#### 4.4.1 Topographic survey

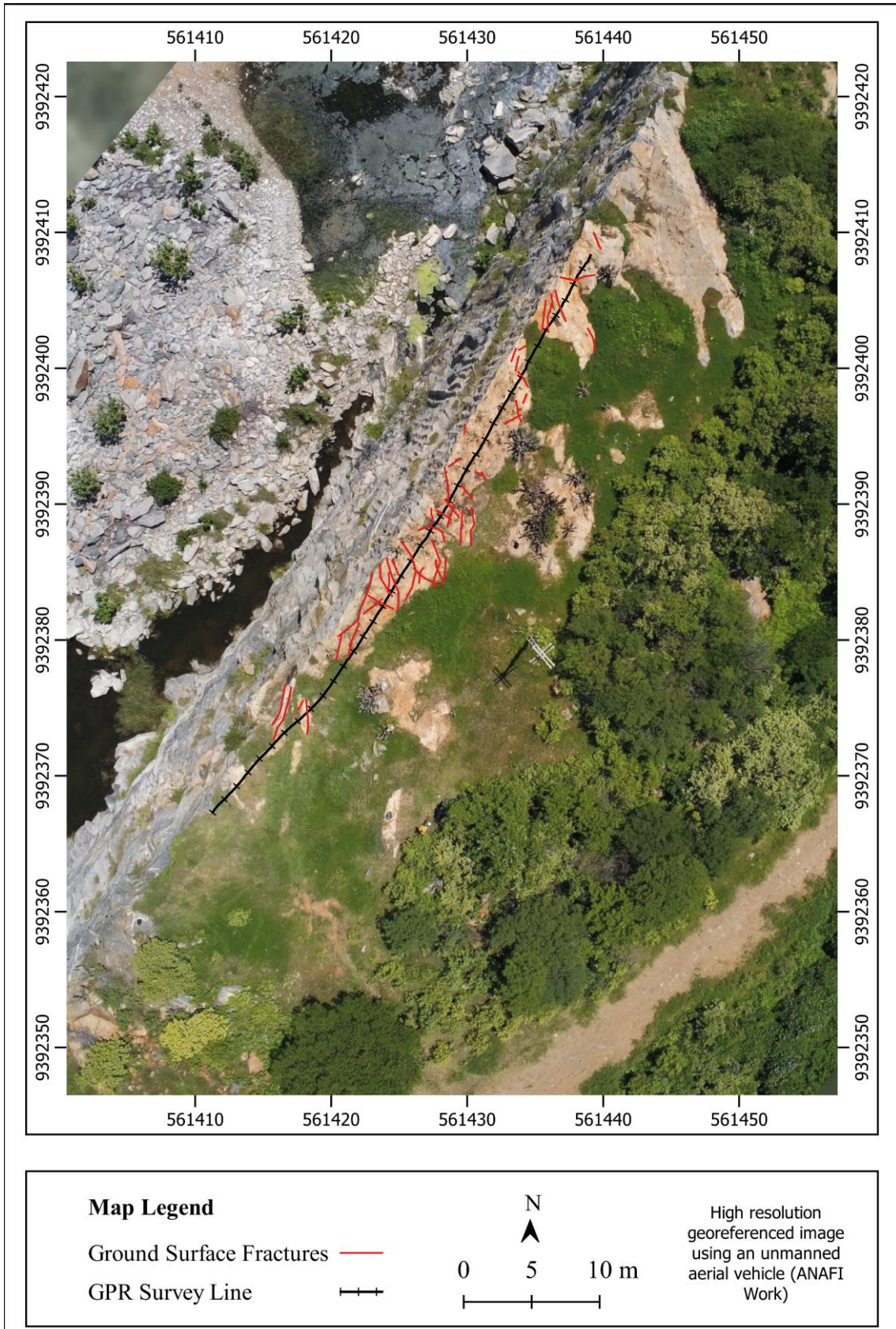
To collect the subsurface information from the selected joint rock slope using the GPR method, it was first positioned a survey line with approximately 50 meters of length where the antennas would be passed to scan the rock mass interior. As a criterion for choosing the best survey line positioning, it was preferred a location where the antennas could be placed in direct contact with the rock, avoiding the maximum loss of GPR signal energy before it be transmitted into the ground due to the presence of vegetation on the ground. Also, it was positioned as close as possible to the edge of the rock mass slope wall, once the fractures observed on it would be used to calibrate the GPR processing data and to promote a better interpretation.

**Figure 4.8** - A topographic survey using geodetic GPS, left, and the elevation measured in which the GPR survey line was positioned, right



Source: elaborated by the author.

**Figure 4.9** - A georeferenced image of the location where the geophysical survey was conducted



Source: elaborated by the author.

Then, a topographic survey was conducted for estimating the terrain elevation where the survey line was laid on the ground, as this information is essential during the processing of the GPR raw data, as discussed earlier. In this regard, it was used a geodetic GPS (Trimble R4 GNSS System) to collect the topographic data. Figure 4.8 shows the geodetic GPS and the elevation measured of the survey line.

Figure 4.9 presents a georeferenced image captured using a UAV with high resolution where it is showed the exact location in which the GPR survey line was positioned.

#### 4.4.2 GPR Data Acquisition

Concerning the GPR data acquisition, the subsurface information was acquired with a SIR-3000 instrument manufactured by GSSI Inc., using two different frequency antennas of 200 and 400 MHz (Figure 4.10). It was only used one survey line of approximately 51.7m, which was positioned in the N35E direction along the outcrop of the jointed rock mass slope at the right margin of the dam spillway.

**Figure 4.10** - GPR survey using the 200 (left) and 400MHz (right) antenna frequency



Source: elaborated by the author.

For this research purpose, the mode of operation of the ground-penetrating radar chosen was the reflection profiling using a constant-offset of the transmitting and receiving antennas (see Figure 4.1a). For the antenna of 200 MHz, in the GPR setup, it was used a time window of 400 nanoseconds (ns) with a sampling of 1024 samples per

trace and 50 traces per meter. While, for the 400 MHz antenna, it was used a time window of 200 ns with a sampling of 1020 samples per trace and 50 traces per meter.

It was also decided not to use any of the two modes of operation for conducting velocity soundings (CMP and WARR methods), as the velocity would be estimated using a hyperbolic fitting method later during the data processing stage. Table 4.5 summarize the GPR data acquisition parameters used in this study.

**Table 4.5** - GPR data acquisition parameters for the 200 and 400 MHz antennas survey

Parameter	Antenna frequency	
	200 MHz	400 MHz
Equipment	GSSI SIR-3000	GSSI SIR-3000
Antennas operation	Bi-static (Tx and Rx)	Bi-static (Tx and Rx)
Mode of data acquisition	Common offset	Common offset
Acquisition data mode	Distance	Distance
Number of survey lines	Single	Single
Trace increment	0.02 m	0.02 m
Sample number	1024 samples	1024 samples
Time window (Range)	400 ns	220 ns
Rate	64 scan/s	64 scan/s
Survey line orientation	N35E	N35E
Survey line length	51.7 m	51.7 m
Velocity analysis	Hyperbolic Fitting	Hyperbolic Fitting

Source: elaborated by the author.

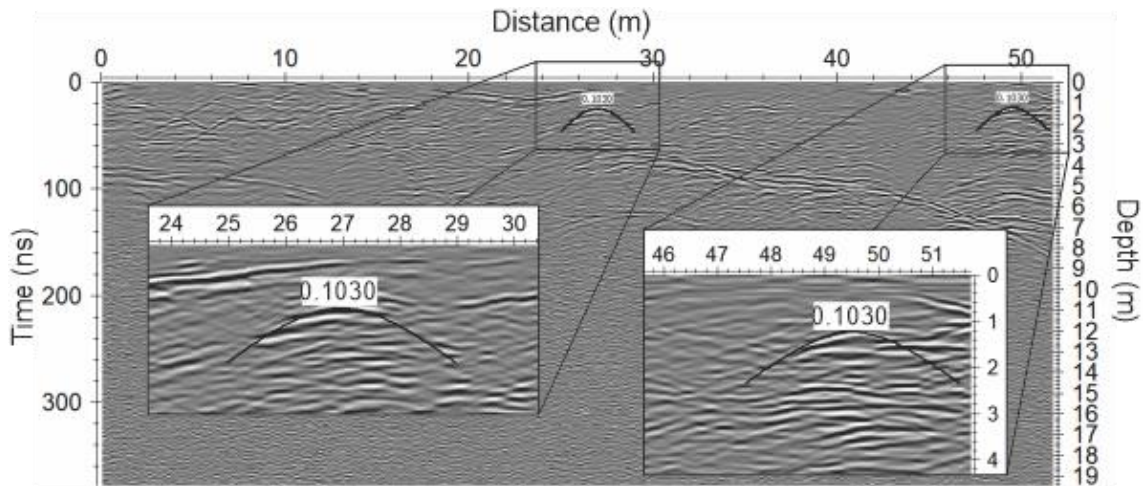
#### 4.4.3 GPR Data Processing

The ground-penetrating radar data involves a set of signal processing techniques that are applied to the raw data obtained after an acquisition survey to make them suitable for visual interpretation, as mentioned briefly earlier in this chapter. Herein, GPR data processing was performed through standard flow steps, similar to presented by Cassidy (2009), Figure 4.4, in order to promote the quality of geophysical responses by eliminating noises and applying gains to compensate for electromagnetic wave (EM) attenuation.

Once the GPR survey was concluded at the site for both 200 and 400 MHz, the raw GPR signal data were processed at Stratigraphic Analysis Laboratory (LAE, acronym in Portuguese for Laboratório de Análises Estratigráficas), in the Department of Geology at the Federal University of Rio Grande do Norte (UFRN), headed by Professor

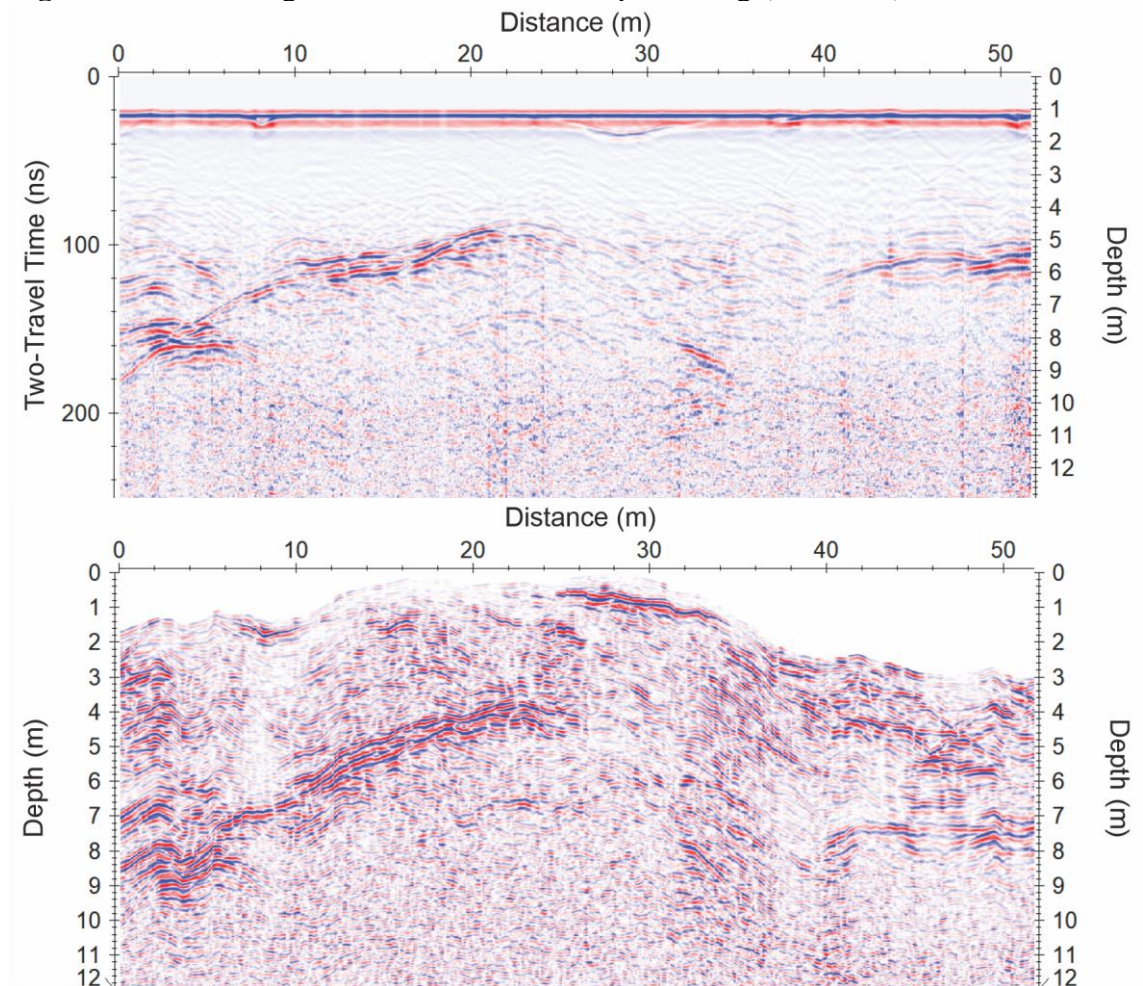
Francisco Pinheiro Lima Filho, co-advisor of this research. The software used for the data processing was the Reflex-Win 8.5.4, which is licensed to the Department of Geology at UFRN.

**Figure 4.11** - Estimation of the velocity using hyperbolic fitting



Source: elaborated by the author.

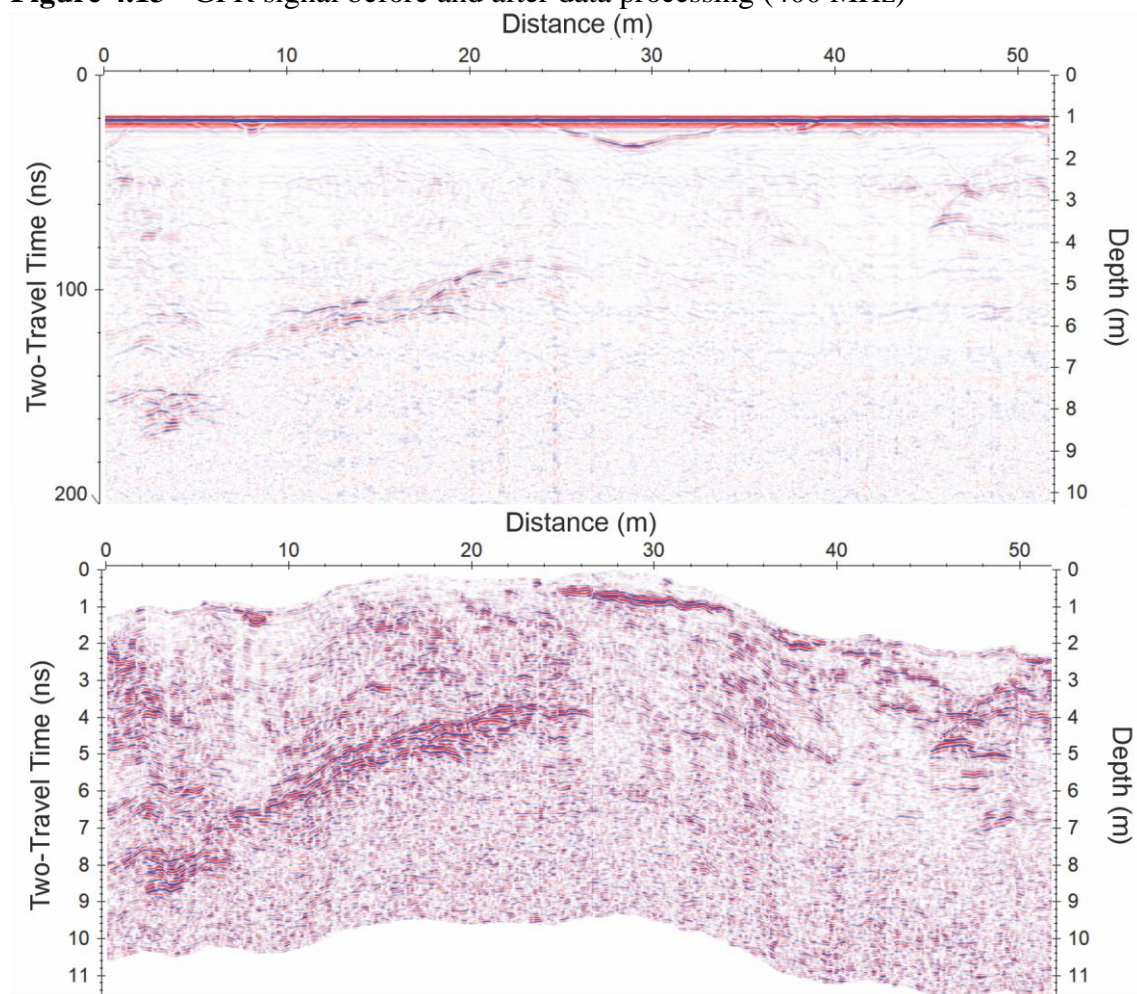
**Figure 4.12** - GPR signal before and after data processing (200 MHz)



Source: elaborated by the author.

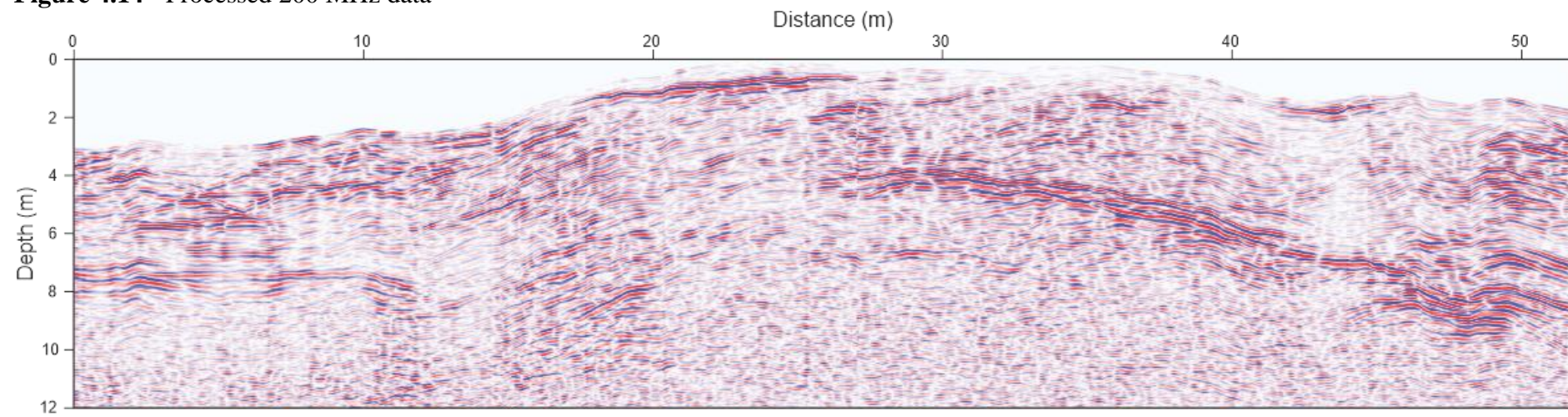
The processing GPR data steps used in this study were the following: zero time correction; (b) attenuation of coherent noise (background removal), (c) dewow, removal of acquisition gains, (d) energy decay compensation, (e) fk filter, (f) topographic correction, and (g) time/depth conversion, besides (h) estimating the propagation velocity using the hyperbolic fitting method. For estimating the propagation velocity, it was used the hyperbolic fitting on the steepest slope to the arms of the inverted U, as suggested by Annan (2003), as shown in Figure 4.11. Figures 4.12 and 4.13 shows the GPR signal before and after basic data processing for the antennas of 200 and 400 MHz, respectively.

**Figure 4.13** - GPR signal before and after data processing (400 MHz)

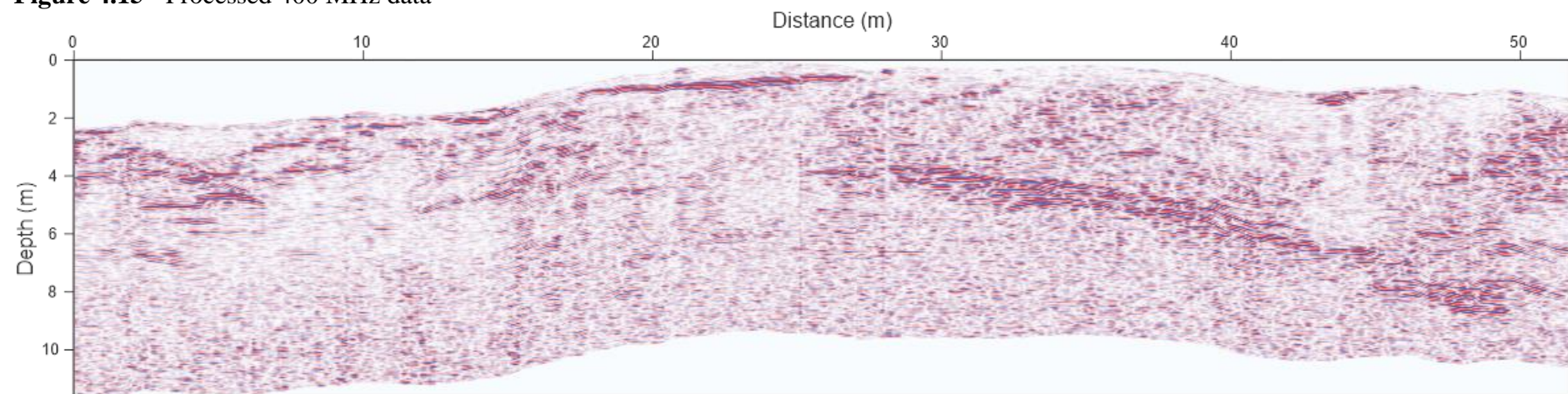


Source: elaborated by the author.

. For the material surveyed in this study, the velocity determined was 0.103 m/ns, where Figures 4.14 and 4.15 shows the radargram results for 200 and 400 MHz antennas. After basic data processing, advanced processing was also performed, where attributes were used to highlight some information obtained from basic processing, using the PETREL software (Figures 4.16 to 4.23).

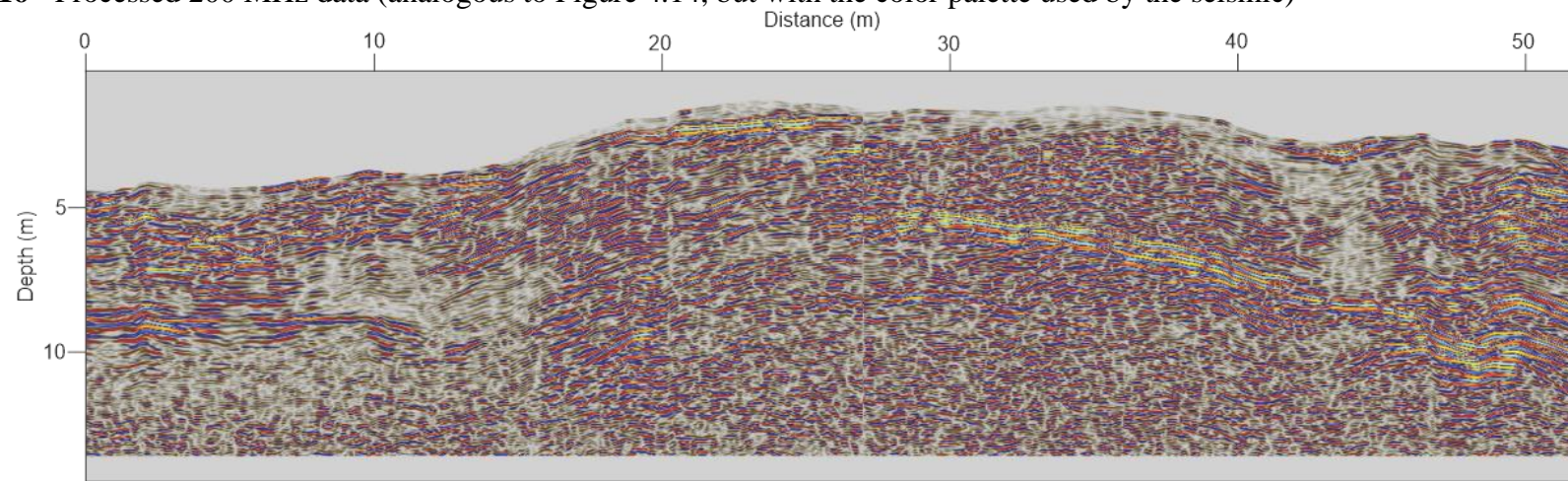
**Figure 4.14** - Processed 200 MHz data

Source: elaborated by the author.

**Figure 4.15** - Processed 400 MHz data

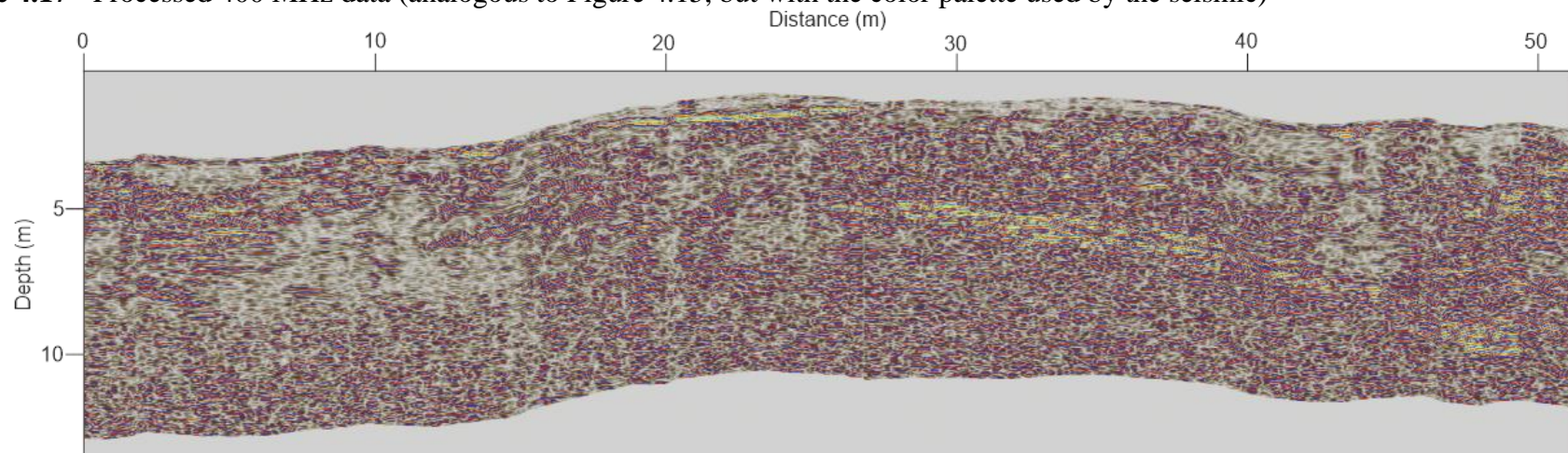
Source: elaborated by the author.

**Figure 4.16** - Processed 200 MHz data (analogous to Figure 4.14, but with the color palette used by the seismic)



Source: elaborated by the author.

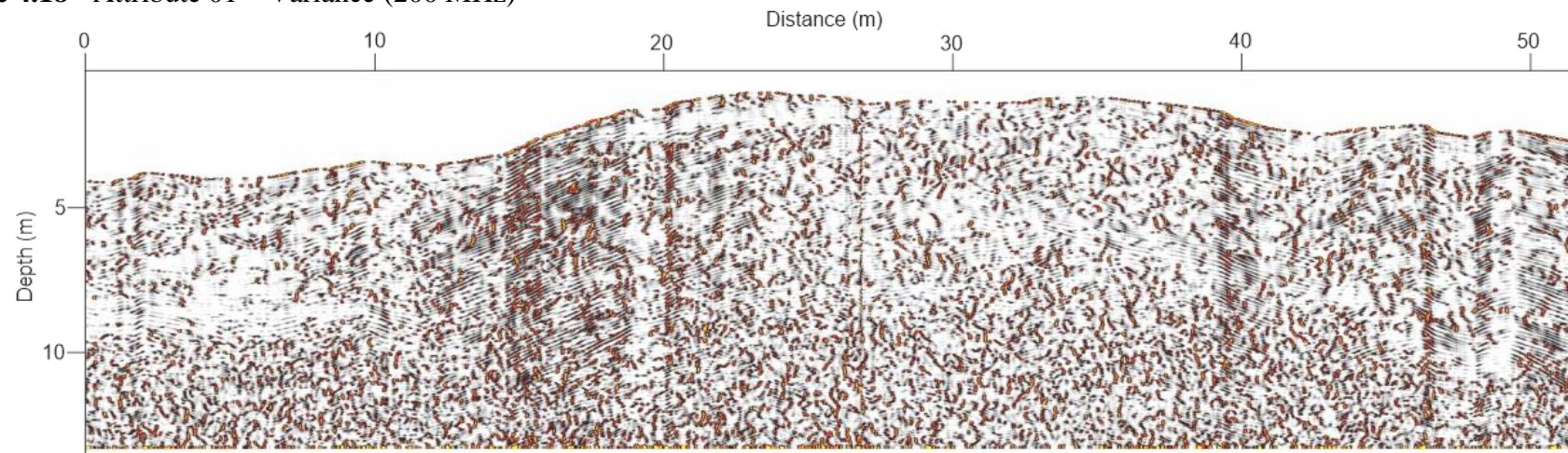
**Figure 4.17** - Processed 400 MHz data (analogous to Figure 4.15, but with the color palette used by the seismic)



Source: elaborated by the author.

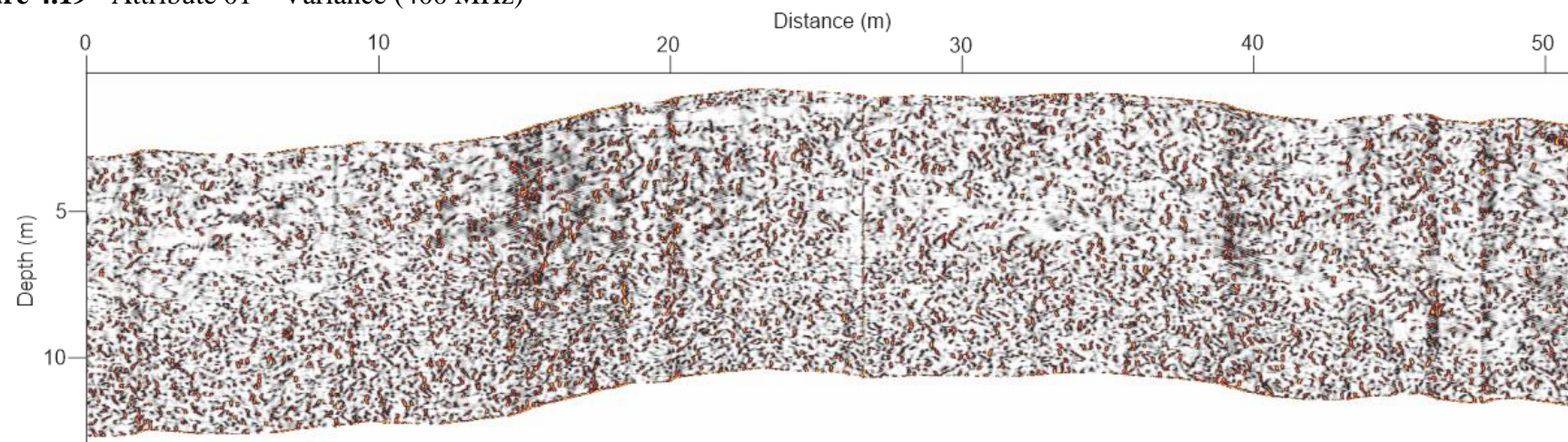


**Figure 4.18** - Attribute 01 – Variance (200 MHz)



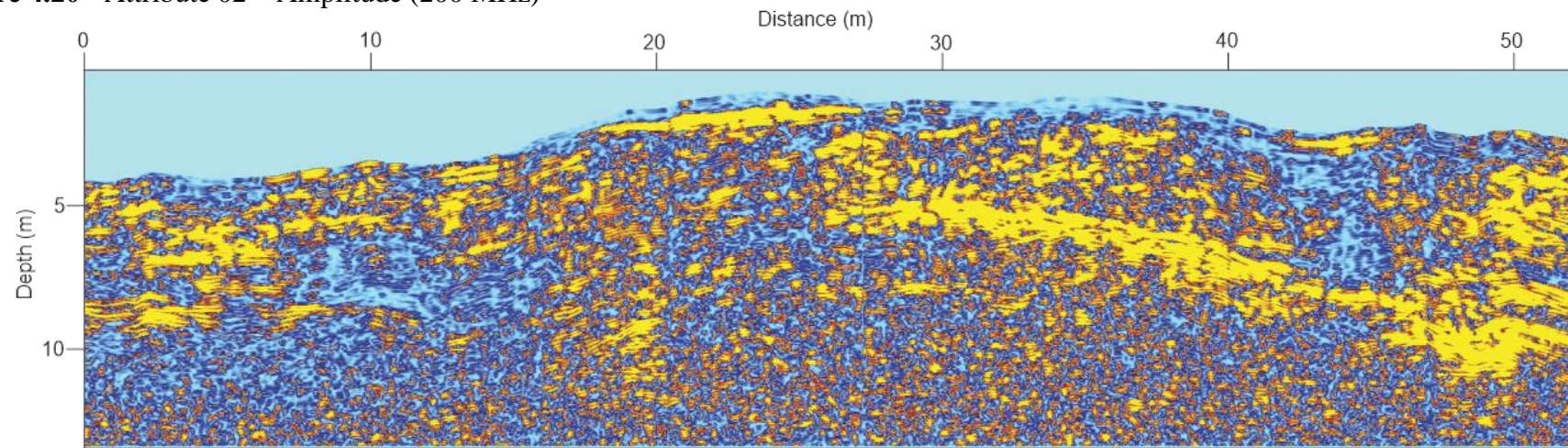
Source: elaborated by the author.

**Figure 4.19** - Attribute 01 – Variance (400 MHz)



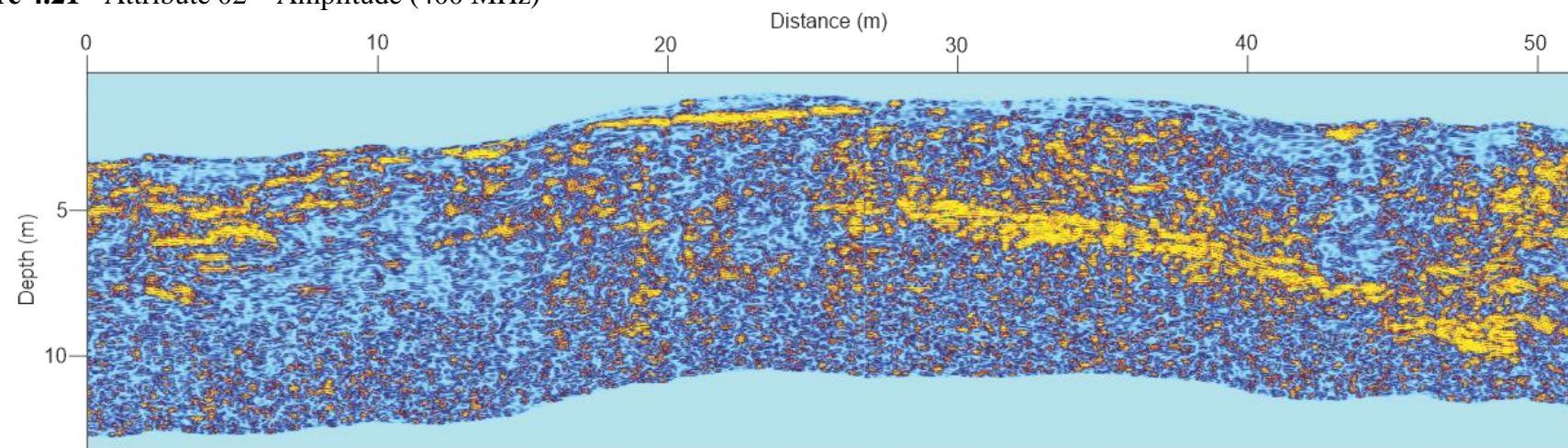
Source: elaborated by the author.

**Figure 4.20** - Attribute 02 – Amplitude (200 MHz)



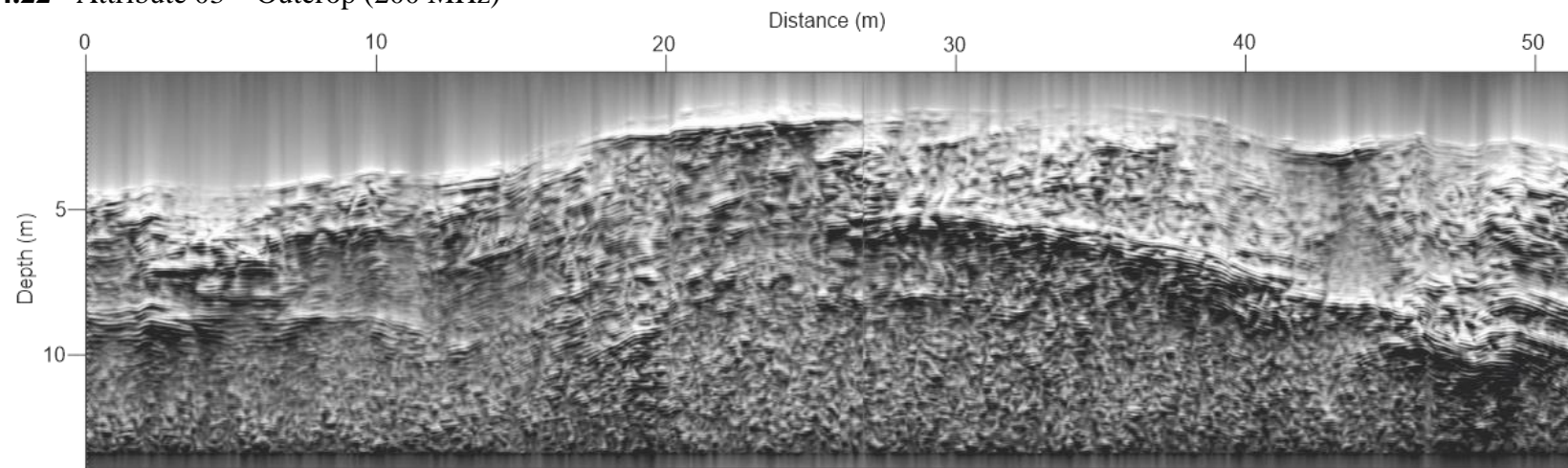
Source: elaborated by the author.

**Figure 4.21** - Attribute 02 – Amplitude (400 MHz)



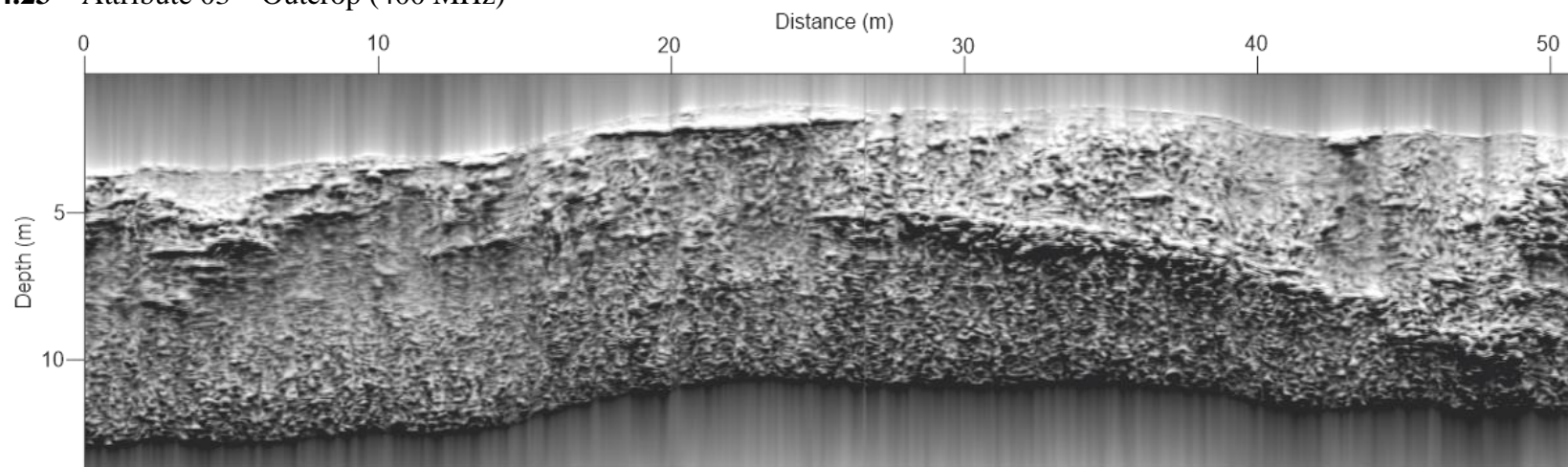
Source: elaborated by the author.

**Figure 4.22** - Attribute 03 – Outcrop (200 MHz)



Source: elaborated by the author.

**Figure 4.23** – Attribute 03 – Outcrop (400 MHz)



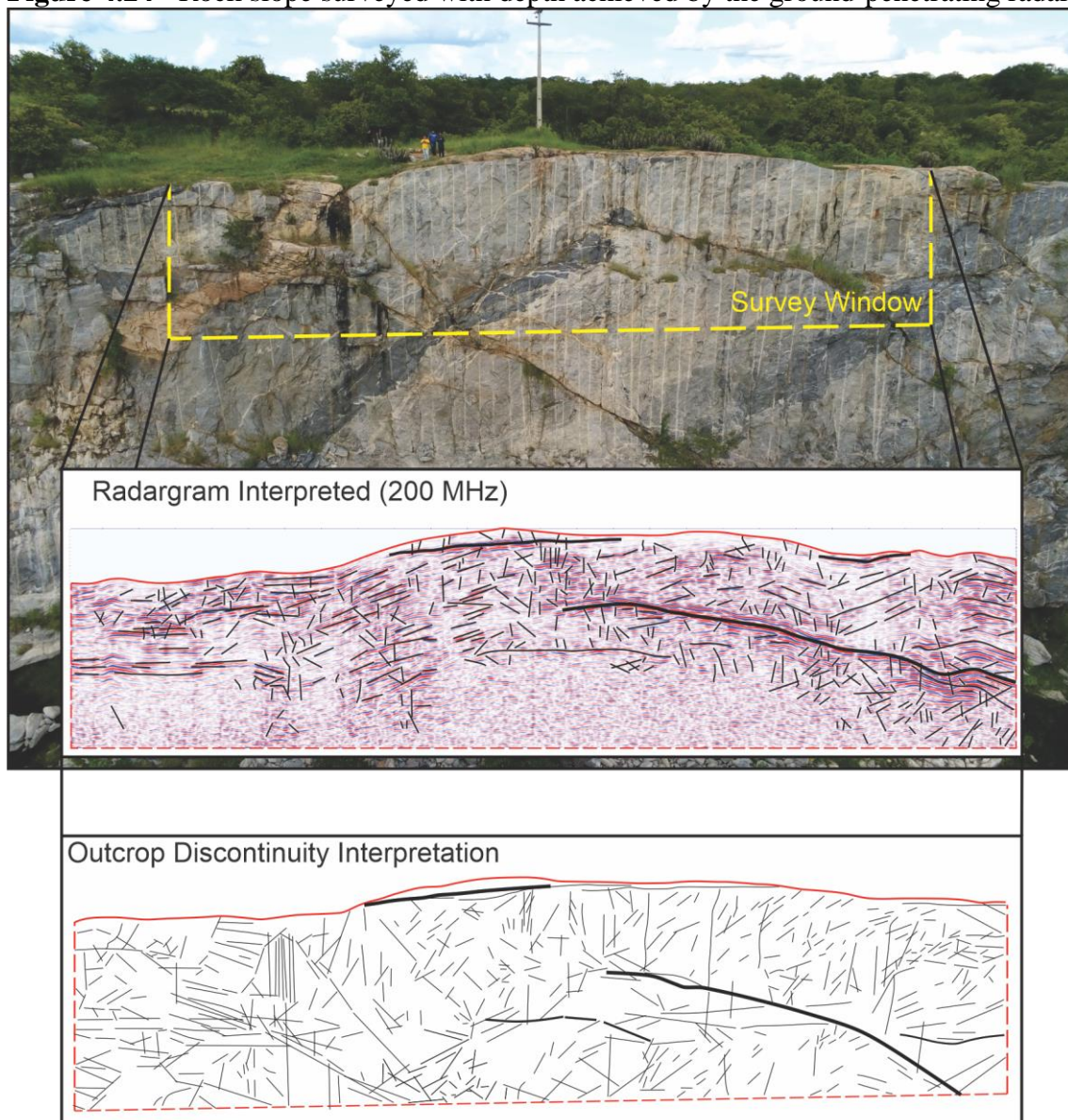
Source: elaborated by the author.

#### 4.4.4 GPR Data Interpretation

For the GPR data interpretation, it was using a direct comparison of outcrop image from an unmanned aerial vehicle (UAV) to the GPR signal processed. It was used as well as the following criteria suggested by Wyatt and Temples (1996), as follow:

- i. A pattern of predominantly straight and relatively continuous reflectors trending at intersecting angles to the horizontal;
- ii. A pattern of predominantly straight and relatively continuous zones of disturbed or missing signal trending at intersecting angles to the horizontal;

**Figure 4.24** - Rock slope surveyed with depth achieved by the ground-penetrating radar



Source: elaborated by the author.

- iii. A pattern of vertical or near-vertical zones of no signal or chaotic signal return;
- iv. Traceable horizontal reflectors exhibiting no apparent offset across the above.

The results of the GPR data interpretation for the jointed rock mass outcrop window using the above methodologies are presented in Figure 4.24. Because of the similarity of the 200 and 400 MHz radargram, it was chosen interpreting the 200 MHz.

#### 4.5 Comparative Analysis

To qualitatively evaluate the potential use of the ground-penetrating radar method as a tool to assist traditional field rock mass characterization, such as geological mapping and drilling exploration surveys, a comparative analysis was conducted using the geological discontinuity conditions observed from the external part of the jointed rock mass outcrop to the subsurface information imaged by the GPR (Figure 4.25). For this analysis, it was chosen using the 200 MHz radargram after basic and advanced data processing, previously presented before (Figures 4.14 and 4.22).

As can be observed in Figure 4.25, four geological features spots (a, b, c, and d) observed on the external outcrop were selected to check the response behavior obtained by the GPR at a similar location. The first spot, a, shows a surface area with the presence of several sub-horizontal fractures intercepted by some vertical fractures, resulting in a disturbed region on the outcrop window surveyed. This region can be easily identified in the radargrams because of the behavior of the reflectors, associating this fractured region with different signal amplitudes response.

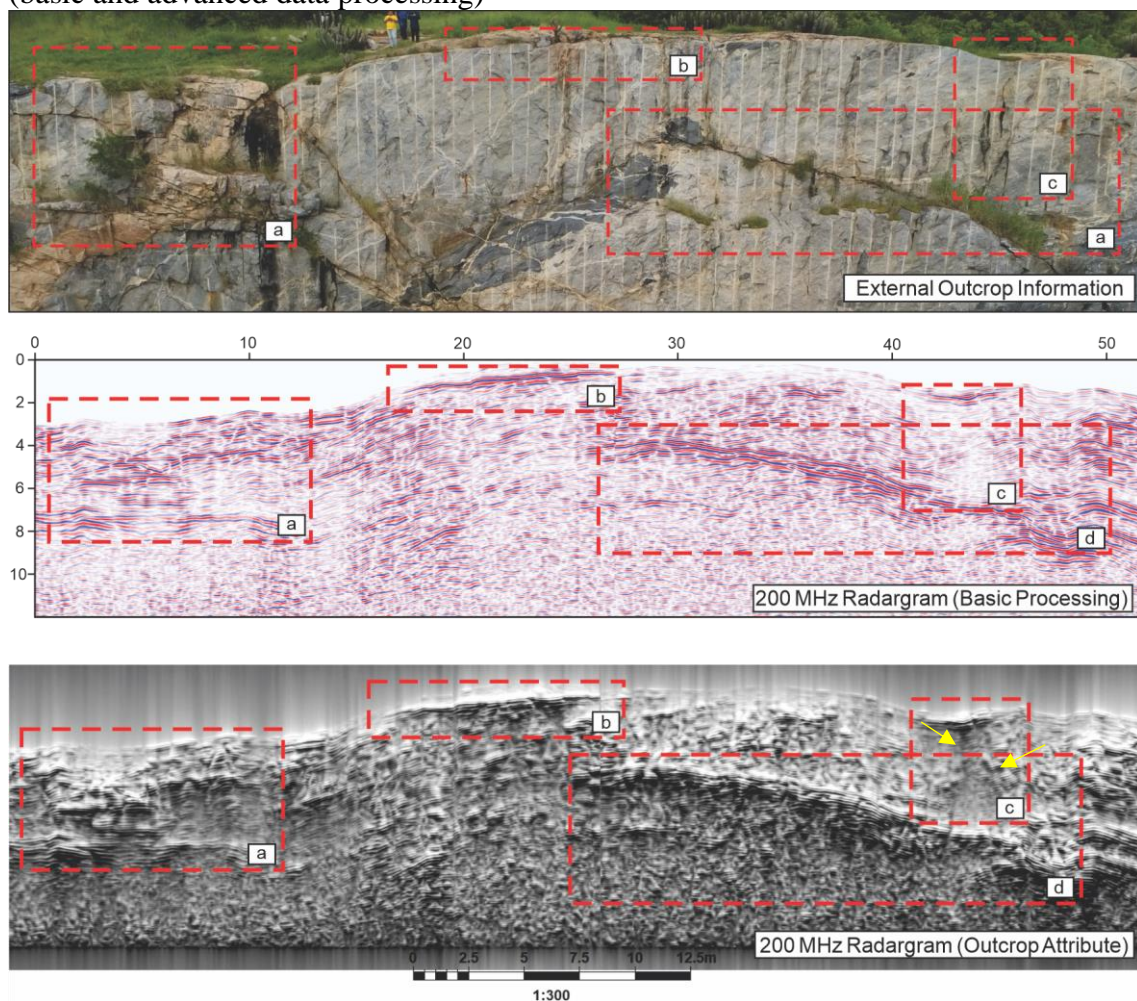
The region of the second spot, b, was selected because of the presence of a horizontal fracture near to the surface, which is clearly identified by the 200 MHz radargram, due to the amount of energy reflected, as observed by the presence of strong reflectors (see Eq. 4.11). Probably, this fracture can be saturated, which would explain the fact of this GPR signal behavior at this location near to the surface.

The third spot, c, also has a similar horizontal fracture near to the surface, however, there are two sub-vertical fractures (yellow arrows) that are only better visualized using the advanced processed 200 MHz radargram. The miss of reflectors

between these discontinuities may be related to the lack of difference of the relative permittivity where the GPR signal is transmitted.

Lastly, the most relevant discontinuity on this outcrop survey window, d, can be seen perfectly through the results obtained from the ground-penetrating radar, as can be observed in Figure 2.25. Because of the presence of strong reflectors in this spot, there is also a high probability that this geological fracture to be filled with organic material or be saturated, which would explain the high dielectric contrast observed in the radargram.

**Figure 4.25** – Comparative analysis between the geological features observed on the external outcrop and its analogs subsurface information imaged by the 200 MHz GPR (basic and advanced data processing)



Source: elaborated by the author.

## 4.6 Conclusions

Geological mapping and drilling survey methodologies have been used for the characterization of rock masses for the purpose of estimating their quality by rock

engineering. Although their wide acceptance in the engineering practices, both methodologies have some limitations that need to be taken into account during the field geological survey. Regarding geological mapping, it relies only on the outcrops information available at the location where the survey is conducted, and, because the process of surface relaxation and weathering that they are submitted to, the geological features derived from this method may not represent the subsurface information, especially due to the anisotropic characteristic of the jointed rock masses. On the other hand, drilling surveys can be used to investigate the subsurface, but they also have some relevant limitations, such as their costs, the uncertainties of the appropriate places to survey and for expressing only 1D subsurface information.

Recently, the construction of the Castanhão dam in the State of Ceará, in Brazil, had its end delayed because of the appearance of undetected geological anomalies, the Paleo Channel and Paleo Channel Jr, at the dam foundation, resulting in also in the change of the original configuration and type of the main dam. If an alternative methodology for subsurface investigation had been used during the feasibility stage of the project, such as using the ground-penetrating radar, these geological anomalies could be identified.

This study presented the potential of using the GPR, which uses short high-frequency-pulsed electromagnetic, EM, waves, normally from 10 to 1000 MHz, to probe the interior of natural geological, as an alternative tool to assist the traditional survey techniques used for rock mass characterization. A jointed rock mass slope at the right margin of the Castanhão dam spillway, located at 561412E and 9392366N (24S), was surveyed using two different antennas frequency 200 and 400 MHz, and, based on images obtained using an unmanned aerial vehicle (UAV), showed the potential of this geophysical method for visualizing important subsurface geological features, such as the fractures conditions within the rock mass.

Among the main experiences that can be drawn from the use of GPR for rock mass characterization, especially for rock mass classification purposes, the following stand out:

- i. Ground-penetrating radar can be used as a quick survey methodology for probing with high resolution the subsurface, especially for improving the conventional methodologies used, i.e., geological mapping and drilling surveys;

- ii. Once the subsurface information is imaged using the GPR, the drilling survey can be made less arbitrarily, consequently, preferred locations may be chosen with less uncertainty;
- iii. Although in this study it was only used a survey line for probing the underground, multiple survey lines, including perpendicular, can be used for a 3D subsurface imaging, which can map better the anisotropic characteristics of discontinuities.



## 5 CONCLUSIONS AND SUGGESTIONS FOR FUTURE RESEARCH

### 5.1 Final Conclusions

The mechanical parameters of the rock masses, such as the unconfined compressive strength,  $\sigma_{cm}$ , and the deformation modulus,  $E_{rm}$ , play an important role in most rock engineering practices. Among the methodologies for estimating  $\sigma_{cm}$  and  $E_{rm}$ , the empirical correlations based on rock mass classification (RMC) systems, i.e., RQD, RMR, Q, and GSI, have been widely used for this purpose, since they are the most cost-effective, especially during the early stages of most projects.

For a comprehensive study of the empirical correlations proposed to estimate  $\sigma_{cm}$  and  $E_{rm}$ , a comparative analysis was conducted here using as database 46 scenarios of rock masses with different quality, which were previously classification and characterized.

Regarding the deformation modulus predicted values using the RMC-based methods, it was possible to notice that non-normalized correlations estimated higher values in comparison to the normalized one, especially for rock mass scenarios with medium-to-better quality. Therefore, the use of non-normalized correlations should be used with caution in cases of good quality rocks, especially with the absence of intact rock stiffness measurements.

Due to the number of proposed expressions to estimate the deformation modulus of rock mass based on rock mass classification schemes, it was observed a significant range of predicted values of  $E_{rm}$  for each rock mass scenario, principally for average-to-good quality rock masses. Thereby, the choice of the correlation depends on the rock mass quality and the classification system used.

Concerning the empirical methods suggested to estimate the unconfined compressive strength, the RMR-based methods estimated the most central values when compared to the other correlations. On the other hand, the RQD-based methods yielded in the highest values of  $\sigma_{cm}$ , while the GSI-based method estimated the most conservative values. Although there is not a particular equation that will be ideal for all rock mass quality scenario, the empirical methods proposed based on Deere's index should be only used for a rough initial estimate in the absence of another classification.

Because of the importance of RMC systems to estimate jointed rock mass mechanical properties, the dissertation discussed the usage of a geophysical method, the

ground-penetrating radar (GPR), to enhance rock mass characterization as an auxiliary tool. Based on a comparative analysis between the discontinuities observed in an outcrop and the discontinuities interpreted using basic and advanced processing techniques, it was possible to notice that ground-penetrating radar is capable to identify almost the same discontinuities features.

Therefore, although the GPR is not self-able to characterize the discontinuities within the rock mass, this geophysical technique can be used to image with high resolution the subsurface fractures without need to excavate or drill, providing extra aid to the conventional characterization methodologies.

## 5.2 Future Research Suggestions

As suggestions for future research based on what was discussed in this dissertation, the author stresses out the following recommendations:

- i. Evaluating the empirical methods to estimate  $E_{rm}$  and  $\sigma_{cm}$  in comparison to the in situ measurements and back-analysis results;
- ii. To study the impact of the rock mass disturbance factor (D) on the empirical methods;
- iii. To verify the GPR sensibility signal behavior for joints that are closed and open;
- iv. Probing a jointed rock mass subsurface using multiple survey lines with different direction (perpendicular and parallel) for rock mass classification purposes.

## REFERENCES

- AASHTO - American Association of State Highway and Transportation Officials. **Standard Specifications for Highway Bridges**, 17th ed. American Association of State Highway and Transportation Officials, Washington, DC, 2002.
- ABAD, J.; CALEDA, B.; CHACON, E.; GUTIEREZ, V.; HIDLGO, E. Application of geomechanical classification to predict the convergence of coal mine galleries and to design their supports. In: 5th ISRM Congress, 10-15 April, Melbourne, Australia, 1983. **Proceedings**. ISRM, p. 15-19, 1983.
- ANNAN, A. P. **Ground penetrating radar principles, procedures and applications**. Sensors and software, 2003.
- ANNAN, A. P. **Ground-penetrating radar**. Society of Exploration Geophysicists, p. 357-438, 2005.
- ANNAN, A. P. **Electromagnetic principles of ground penetrating radar**. Elsevier Science, p. 1-37, 2009.
- AROSIO, D. Rock fracture characterization with GPR by means of deterministic deconvolution. **Journal of Applied Geophysics**, v. 126, p. 27-34, 2016.
- ASTM - American Society for Testing and Material. **Standard guide for using the surface ground penetrating radar method for subsurface investigation**. 2011.
- AYDAN, Ö.; DALGIC, S. Prediction of deformation behavior of 3-lanes Bolu tunnels through squeezing rocks of North Anatolian fault zone (NAFZ). In: Regional Symp. on Sedimentary Rock Eng., Taipei, Taiwan. **Proceedings**. Taipei, p. 228-233, 1998.
- AYDAN, Ö.; KAWAMOTO, T. The Assessment of mechanical properties of rock masses through RMR Rock Classification System. ISRM International Symposium, 19-24 November, Melbourne, Australia. **International Society for Rock Mechanics and Rock Engineering**, 2000.
- BENEDETTO, A.; PAJEWSKI, L. **Civil engineering applications of ground penetrating radar**. Springer, 2015.
- BARTON, N. Review of a new shear-strength criterion for rock joints. **Engineering Geology**, v. 7, n. 4, p. 287-332, 1973.
- BARTON, N. Predicting the behavior of underground openings in jointed rock. In: 4th Manual Rocha Memorial Lecture, Portugal, Lisbon. **Proceedings**. Lisbon, p. 1-28, 1987.
- BARTON, N. The influence of joint properties in modelling jointed rock masses. In: 8th ISRM Congress (Keynote Lecture). **Proceedings**. ISRM, 1995.

BARTON, N. Some new Q-value correlations to assist in site characterisation and tunnel design. **International Journal of Rock Mechanics and Mining Sciences**, v. 39, n. 2, p. 185-216, 2002.

BARTON, N.; CHOUBEY, V. The shear strength of rock joints in theory and practice. **Rock Mechanics**, v. 10, n. 1-2, p. 1-54, 1977.

BARTON, N.; LIEN, R.; LUND, J. Engineering classification of rock masses for the design of tunnel support. **Rock Mechanics**, v. 6, n. 4, p. 189-236, 1974.

BARTON, N.; LOSET, F.; LIEN, R.; LUNDE, J. Application of the Q-system in design decisions concerning dimensions and appropriate support for underground installations. In: Int Conf Subsurface Space, Rockstore, Stockholm, 1980. **Proceedings**. Sub-surface Space, p. 553-561, 1980.

BASARIR, H. Engineering geological studies and tunnel support design at Sulakyurt dam site, Turkey. **Engineering Geology**, v. 86, n. 4, p. 225-237, 2006.

BASARIR, H.; ÖZSAN, A.; KARAKUS, M. Analysis of support requirements for a shallow diversion tunnel at Guledar dam site, Turkey. **Engineering Geology**, v. 81, n. 2, p. 131-145, 2005.

BAUDOIN, Y.; HABIB, M. K. **Using robots in hazardous environments: Landmine detection, de-mining and other applications**. Elsevier, 2010.

BIENIAWSKI, Z. T. Engineering classification of jointed rock masses. **Transaction of the South African Institution of Civil Engineers**, n. 15, p. 335-344, 1973.

BIENIAWSKI, Z. T. Rock mass classification in rock engineering. Exploration for Rock Engineering, **Proceedings** of a Symposium for Rock Engineering Cape Town: Balkema, v. 12, p. 97-106, 1976.

BIENIAWSKI, Z. T. Determining rock mass deformability: experience from case histories. **International Journal of Rock Mechanics and Mining Sciences & Geomechanics Abstracts**, v. 15, n. 5, p. 237-247, 1978.

BIENIAWSKI, Z. T. The geomechanics classification in rock engineering applications. 4th ISRM Congress. **Proceedings**. International Society for Rock Mechanics and Rock Engineering, p. 41-48, 1979.

BIENIAWSKI, Z. T. **Engineering rock mass classifications**. John Wiley & Sons, New York, 1989, 251p.

BIENIAWSKI, Z. T. **Tunnel design by rock mass classifications. Update of Technical Report GL-79-19**. Pennsylvania State Univ University Park Dept of Mineral Engineering, 1990.

BHASIN, R.; GRIMSTAD, E. The use of stress-strength relationships in the assessment of tunnel stability. **Tunnelling and Underground Space Technology**, v. 11, n. 1, p. 93-98, 1996.

BRISTOW, C.; JOL, H. **Ground penetrating radar in sediments**. Geological Society of London, 2003.

CAI, M.; KAISER, P. K.; UNO, H.; TASAKA, Y.; MINAMI, M. Estimation of rock mass deformation modulus and strength of jointed hard rock masses using the GSI system. **International Journal of Rock Mechanics and Mining Sciences**, v. 41, n. 1, p. 3-19, 2004.

CAI, M.; KAISER, P. K.; TASAKA, Y.; MINAMI, M. Determination of residual strength parameters of jointed rock masses using the GSI system. **International Journal of Rock Mechanics and Mining Sciences**, v. 44, n. 2, p. 247-265, 2007.

CASSIDY, N. J. **Ground penetrating radar data processing, modelling and analysis**. Ground penetrating radar: theory and applications, p. 141-176, 2009.

CBDB - Comitê Brasileiro de Barragens. **Main Brazilian Dams III: Design construction and performance**. 2009.

COSAR, S. **Application of rock mass classification systems for future support design of the Dim tunnel near Alanya**. Thesis (Master of Science in Mining Engineering) – The Graduation School of Nature and Applied Sciences of Middle East Technical University, Turkey, 2004.

COON, R. F.; MERRITT A. H. **Predicting in situ modulus of deformation using rock quality indexes**. In: STP477-EB Determination of the In Situ Modulus of Deformation of Rock, ASTM International, p. 154-173, 1970.

CHAMINÉ, H. L.; AFONSO, M. J.; RAMOS, L. R.; PINHEIRO, R. Scanline sampling techniques for rock engineering survey: Insights from intrinsic geologic variability and uncertainty. **Engineering Geology for Society and Territory**, v. 6, p. 357-361, 2015.

DAVIS, J. L.; ANNAN, A. P. Ground-penetrating radar for high-resolution mapping of soil and rock stratigraphy. **Geophysical prospecting**, v. 37, n. 5, p. 531-551, 1989.

DALGIÇ, S. A comparison of predicted and actual tunnel behaviour in the İstanbul Metro, Turkey. **Engineering Geology**, v. 63, n. 1–2, p. 69-82, 2002.

DANIELS, D. J. **Ground Penetrating Radar**. The institution of electrical engineers (IEE), London, UK, 2004, 734p.

DANIELS, D. J. **Ground penetrating radar**. Encyclopedia of RF and Microwave Engineering, 2005.

DEB, D.; VERMA, A. K. **Fundamentals and applications of rock mechanics**. PHI Learning Pvt. Ltd., 2016, 412p.

DEERE, D. U.; MILLER, R. P. **Engineering classification and index properties for intact rock**. Technical Report N. AFWL-TR-65-116, University of Illinois, Urbana, Illinois, 1966, 327p.

- DEERE, D. U., DEERE, D. W. **The rock quality designation (RQD) index in practice.** Rock Classification Systems for Engineering Purposes, ASTM STP 984, Louis Kirkaldie, Ed., American Society for Testing and Materials, Philadelphia, p. 91-101, 1988.
- DEERE, D. U.; DEERE, D. U. **Rock quality designation (RQD) after twenty years.** Department of the Army, US Army Corps of Engineering, Washington, DC, 1989, 100p.
- DEERE, D. U.; HENDRON, A. J.; PATTON, F. D.; CORDING, E. J. Design of surface and near surface construction in rock. In: Eighth US Symposium on Rock Mechanics, Failure and Breakage of Rock, New York, USA. **Proceedings.** New York, p. 237-302, 1967.
- DORN, C.; LINDE, N.; DOETSCH, J.; LE BORGNE, T.; BOUR, O. Fracture imaging within a granitic rock aquifer using multiple-offset single-hole and cross-hole GPR reflection data. **Journal of Applied Geophysics**, v. 78, p. 123-132, 2012.
- DNOCS - Departamento Nacional de Obras Contra as Secas. **Relatório técnico final “as built” da barragem Castanhão.** Ministério da Integração Nacional, Departamento Nacional de Obras contra as Secas (DNOCS), Consórcio AGUASOLOS-HIDROTERRA, Fortaleza-CE, 2004.
- ELKARMOTY, M.; COLLA, C.; GABRIELLI, E.; KASMAEYAZDI, S.; TINTI, F.; BONDUÀ, S.; BRUNO, R. Mapping and modelling fractures using ground penetrating radar for ornamental stone assessment and recovery optimization: Two case studies. **Rudarsko-geološko-naftni zbornik**, v. 32, n. 4, p. 63-76, 2017.
- FRIEDEL, M. J.; JESSOP, J. A.; THILL, R. E. Igneous rock mass fracture delineation using common offset radar reflection. In: SEG Technical Program Expanded Abstracts 1991. **Society of Exploration Geophysicists**, p. 504-506 1991. p. 504-506.
- GALERA, J. M.; ÁLVAREZ, M.; BIENIAWSKI, Z. T. Evaluation of the deformation modulus of rock masses using RMR: comparison with dilatometer tests. In: ISRM Workshop W1, Madrid, Spain, Jul. 6-7, 2007. **Proceedings.** Madrid, p. 71-77, 2007.
- GARDNER, W. S. **Design of drilled piers in the Atlantic Piedmont.** American Society of Civil Engineers (ASCE), p. 62-86, 1987.
- GENIS, M. Assessment of the dynamic stability of the portals of the Dorukhan tunnel using numerical analysis. **International Journal of Rock Mechanics and Mining Sciences**, v. 47, n. 8, p. 1231-1241, 2010.
- GENIS, M., BASARIR, H., OZARSLAN, A., BILIR, A., BALABAN, E. Engineering geological appraisal of the rock masses and preliminary support design, Dorukhan Tunnel, Zonguldak, Turkey. **Engineering Geology**, v. 92, n. 1-2, p. 14-26, 2007.
- GOODMAN, R. E. **Introduction to rock mechanics.** New York: Wiley, 1989, 562p.

GOKCEOGLU, C.; SONMEZ, H.; KAYABASI, A. Predicting the deformation moduli of rock masses. **International Journal of Rock Mechanics and Mining Sciences**, v. 40, n. 5, p. 701-710, 2003.

GRORDNER, M. Delineation of rockburst with ground penetrating radar in the Witwatersrand basin, South Africa. **International Journal of Rock Mechanics and Mining Sciences**, v. 38, n. 6, p. 885-891, 2001.

GRANDJEAN, G.; GOURRY, J. GPR data processing for 3D fracture in marble quarry (Thassos, Greece). **Journal of Applied Geophysics**, v. 61, n. 4, p. 1050-1064, 1996.

GRASMUECK, M. 3-D ground-penetrating radar applied to fracture imaging in gneiss. **Geophysics**, v. 36, n. 1, p. 19-30, 1996.

GRÉGOIRE, C.; HALLEUX, L. Characterization of fractures by GPR in mining environment. **First Break**, v. 20, n. 7, p. 467-471, 2002.

GRIMSTAD, E.; BARTON, N. Updating of the Q-system for NMT. In: Kompen, Opsahl, Berg, editors. **Proceedings**. International Symposium on Sprayed Concrete. Modern Use of Wet Mix Sprayed Concrete for Underground Support, Fagernes, Oslo, 1993.

GUROCAK, Z.; SOLANKI, P.; ZAMAN, M. M. Empirical and numerical analyses of support requirements for a diversion tunnel at the Boztepe dam site, eastern Turkey. **Engineering Geology**, v. 91, n. 2-4, p. 194-208, 2007.

HUDSON, J. A.; HARRISON, J. P. **Engineering rock mechanics: an introduction to the principles**. Elsevier, Amsterdam, 2000, p. 458.

HEYDARI, S.; HAMIDI, J. K.; MONJEZI, M.; EFTEKHARI, A. An investigation of the relationship between muck geometry, TBM performance, and operational parameters: A case study in Golab II water transfer tunnel. **Tunnelling and Underground Space Technology**, v. 88, p. 73-86, 2019.

HOEK, E.; BROWN, E. T. Empirical strength criterion for rock masses. **Journal of the Geotechnical Engineering**, v. 106, p. 1013-1035, 1980.

HOEK, E. **Practical rock engineering**. Rocscience, 2012, 341p.

HOEK, E. Strength of Rock and Rock masses. **ISRM News Journal**, v. 2, n. 2, p. 4-16, 1994.

HOEK, E., BROWN, E. T. Practical estimates of rock mass strength. **International Journal of Rock Mechanics and Mining Sciences**, v. 34, n. 8, p. 1165-1186, 1997.

HOEK, E., BROWN, E. T. The Hoek-Brown failure criterion and GSI - 2018 edition. **Journal of Rock Mechanics and Geotechnical Engineering**, v. 11, n. 3, p. 445-463, 2019.

HOEK E.; KAISER P. K.; BAWDEN W. F. **Support of underground excavations in hard rock**. Rotterdam: A.A. Balkema, 1995, 235p.

HOEK, E.; CARRANZA-TORRES, C.; CURKUM, B. Hoek-Brown failure criterion-2002 edition. In: Mining and tunnelling innovation and opportunity. **Proceedings** of the 5th North American rock mechanics symposium and 17th tunnelling association of Canada conference, University of Toronto, Toronto, Canada, p. 267-273, 2002.

HOEK, E.; DIEDERICHS, M. S. Empirical estimation of rock mass modulus. **International Journal of Rock Mechanics and Mining Sciences**, v. 43, n. 2, p. 203-215, 2006.

HOEK E.; CARTER, T. G.; DIEDERICHS, M. S. Quantification of the geological strength index chart. 47th U.S. Rock Mechanics/Geomechanics Symposium, 23-26 June, San Francisco, California, 2013. **Proceedings**. American Rock Mechanics Association, 2013.

HUDSON, J. A., PRIEST, S. D. Discontinuity and rock mass geometry. **International Journal of Rock Mechanics and Mining Sciences & Geomechanics Abstracts**, v. 16, n. 6, p. 339–362, 1979.

ISRM. Suggested methods for the quantitative description of discontinuities in rock masses. International society for rock mechanics, commission on standardization of laboratory and field tests. **International Journal of Rock Mechanics and Mining Sciences & Geomechanics Abstracts**, v. 15, n. 6, p. 319–368, 1978.

ISRM. Suggested methods for determining the uniaxial compressive strength and deformability of rock materials. International Society for Rock Mechanics, Commission on Standardization of Laboratory and Field Tests. **International Journal of Rock Mechanics and Mining Sciences & Geomechanics Abstracts**, v. 16, n. 2, p. 135–140, 1979.

JOL, H. M. (editor) **Ground penetrating radar theory and applications**. Elsevier, 2009, 524p.

KADIOGLU, S. Photographing layer thicknesses and discontinuities in a marble quarry with 3D GPR visualisation. **Journal of Applied Geophysics**, v. 64, n. 3-4, p. 109-114, 2008.

KALAMARAS, G. S.; BIENIAWSKI, Z. T. A rock mass strength concept for coal seams incorporating the effect of time. 8th ISRM Congress, 25-29 September, Tokyo, Japan, 1995. **Proceedings**. International Society for Rock Mechanics and Rock Engineering, p. 295-302, 1995.

KAYA, A.; BULUT, F.; ALEMDAG, S.; SAYIN, A. Analysis of support requirements for a tunnel portal in weak rock: A case study from Turkey. **Scientific Research and Essays**, v. 6, n. 31, p. 6566-6583, 2011.

KOCBAY, A.; KILIC, R. Engineering geological assessment of the Obruk dam site (Corum, Turkey). **Engineering Geology**, v. 87, n. 3–4, p. 141-148, 2006.



- KULHAWY, F. H.; GOODMAN, E. E. Foundations in rock. In: Bell, F.G. (Ed.), **Ground Engineer's Reference Book**. Butterworths, London, 1987.
- LAI, W. W. L.; DEROBERT, X.; ANNAN, P. A review of Ground Penetrating Radar application in civil engineering: A 30-year journey from Locating and Testing to Imaging and Diagnosis. **NDT & E International**, v. 96, p.58-78, 2018.
- LOWSON, A. R.; BIENIAWSKI, Z. T. Critical assessment of RMR based tunnel design practices: a practical engineer's approach. In: **Proceedings** of the SME, Rapid Excavation and Tunnelling Conference, p. 23-26, 2013.
- MARINOS, P.; HOEK, E. GSI: A geologically friendly tool for rock mass strength estimation. In: ISRM International Symposium, 19-24 November, Melbourne, Australia, 2000. **Proceedings**. International Society for Rock Mechanics and Rock Engineering, 2000, p. 19p.
- MARINOS, P.; HOEK, E. Estimating the geotechnical properties of heterogeneous rock masses such as flysch. **Bulletin of Engineering Geology and the Environment**, v. 60, n. 2, p. 85-92, 2001.
- MARINOS, V.; MARINOS, P.; HOEK, E. The geological strength index: applications and limitations. **Bulletin of Engineering Geology and the Environment**, v. 64, n. 1, p. 55-65, 2005.
- MITRI, H. S.; EDRISSI, R.; HENNING, J. **Finite element modeling of cable-bolted slopes in hard rock ground mines**. 1994.
- MORRIS, I.; ABDEL-JABER, H.; GLISIC, B. Quantitative attribute analyses with ground penetrating radar for infrastructure assessments and structural health monitoring. **Sensors**, v. 19, n. 7, p. 1-17, 2019.
- NASCIMENTO DA SILVA, C.; DE MEDEIROS, W.; DE SÁ, E.; NETO, P. Resistivity and ground-penetrating radar images of fractures in a crystalline aquifer: A case study in Caiçara farm – NE Brazil. **Journal of applied Geophysics**, v. 56, n. 4, p. 295-307, 2004.
- NEAL, A. Ground-penetrating radar and its use in sedimentology: Principles, problems and progress. **Earth-Science Reviews**, v. 66, n. 3-4, p. 261-330, 2004.
- NICHOLSON, G. A.; BIENIAWSKI, Z. T. A nonlinear deformation modulus based on rock mass classification. **International Journal of Mining and Geological Engineering**, v. 8, n. 3, p. 181-202, 1990.
- ÖZSAN, A.; AKIN, M. Engineering geological assessment of the proposed Uruş Dam, Turkey. **Engineering Geology**, v. 66, n. 3-4, p. 271-281, 2002.
- ÖZSAN, A.; KARPUZ, C. Geotechnical rock-mass evaluation of the Anamur dam site, Turkey. **Engineering Geology**, v. 42, n. 1, p. 65-70, 2002.

PALMSTRÖM, A. **RMi - A rock mass classification system for rock engineering Purposes**. PhD Thesis, University of Oslo, 1995, 400p.

PALMSTRÖM, A. C Characterizing rock masses by the RMi for use in practical rock engineering: Part 1: The development of the Rock Mass index (RMi). **Tunnelling and Underground Space Technology**, v. 11, n. 2, p. 175-188, 1996a.

PALMSTRÖM, A. C Characterizing rock masses by the RMi for use in practical rock engineering: part 2: Some practical applications of the rock mass index (RMi). **Tunnelling and Underground Space Technology**, v. 11, n. 3, p. 287-303, 1996b.

PALMSTRÖM, A.; SINGH, R. The deformation modulus of rock masses — comparisons between in situ tests and indirect estimates. **Tunnelling and Underground Space Technology**, v. 16, n. 2, p. 115-131, 2001.

PANTHEE, S.; SINGH, P. K.; KAINTHOLA, A.; DAS, R.; SINGH, T. N. Comparative study of the deformation modulus of rock mass. **Bulletin of Engineering Geology and the Environment**, v. 77, n. 2, p. 751-760, 2018.

PARISEAU, W. G. **Design analysis in rock mechanics**. CRC Press, 2017, 731p.

PORSANI, J. L.; SAUCK, W. A.; JÚNIOR, A. O. GPR for mapping fractures and as a guide for the extraction of ornamental granite from a quarry: A case study from southern Brazil. **Journal of Applied Geophysics**, v. 58, n. 3, p. 177-187, 2006.

PERSICO, R. **Introduction to ground penetrating radar: inverse scattering and data processing**. John Wiley & Sons, 2014.

PRIEST S. D.; HUDSON, J. A. Discontinuity spacing in rock. **International Journal of Rock Mechanics and Mining Sciences & Geomechanics Abstracts**, v. 13, n. 5, p. 135-148, 1976.

PRIEST, S. D. **Discontinuity analysis for rock engineering**. Chapman & Hall, London, 1993, 490p.

RAMAMURTHY, T. Strength and modulus response of anisotropic rocks. In: Hudson JA (ed) **Compressive rock engineering-principle, practice and projects**. Pergamon Press, Oxford, p. 313–329, 1983.

RAMAMURTHY, T. **Stability of rock mass**. In: 8th Indian Geotech. Soc. annual lecture, p. 221–274, 1985.

RAMAMURTHY, T. A geo-engineering classification for rocks and rock masses. **International Journal of Rock Mechanics and Mining Sciences**, v. 41, n. 1, p. 89-101, 2004.

RASOULI, M. Engineering geological studies of the diversion tunnel, focusing on stabilization analysis and support design, Iran. **Engineering Geology**, v. 108, n. 3-4, p. 208-224, 2009.

READ, S. A. L.; PERRIN, N. D.; RICHARDS, L. R. Applicability of the Hoek-Brown Failure Criterion to New Zealand Greywacke Rocks. In: 9th ISRM Congress, 25-28 August, Paris, France, 1999. **Proceedings**. International Society for Rock Mechanics and Rock Engineering, p. 655-660, 1999.

REYNOLDS, J. M. **An introduction to applied and environmental geophysics**. John Wiley & Sons, 2011.

RIAZ, A.; JAMIL, S. M.; ASIF, M.; AKHTAR, K. Tunnel support design by comparison of empirical and finite element analysis of the Nahakki tunnel in Mohmand Agency, Pakistan. **Studia Geotechnica et Mechanica**, v. 38, n. 1, p. 75-84, 2016.

SAPIGINI, M.; LA BARBERA, G.; GHIROTTI, M. Engineering geological characterization and comparison of predicted and measured deformations of a cavern in the Italian Alps. **Engineering Geology**, v. 69, n. 1-2, p. 47-62, 2003.

SARIBUDAK, M. Geophysical mapping of Mount Bonnell fault of Balcones fault zone and its implications on Trinity-Edwards Aquifer interconnection, central Texas, USA. **The Leading Edge**, v. 35, n. 9, p. 752-758, 2016.

SERAFIM, J. L.; PEREIRA, J. P. Consideration of the geomechanical classification of Bieniawski. In: International Symposium on Engineering Geology and Underground Construction. **Proceedings**. Rotterdam: A.A. Balkema, p. 33-44, 1983.

SEN, Z.; KAZI, A. Discontinuity spacing and RQD estimates from finite length scanlines. **Rock Mechanics and Mining Sciences & Geomechanics Abstracts**, v. 21, n. 4, p. 203-212, 1984.

SHAFIEI, A.; DUSSEAULT, M. B.; RAHDAR, H.; MESGARZADEH, S. Rock mass characterization along lot no. 6 of Dez-Qomroud tunnel project in Iran. In: ISRM International Symposium - 5th Asian Rock Mechanics Symposium, 24-26 November, Tehran, Iran, 2008. **Proceedings**. International Society for Rock Mechanics and Rock Engineering, p. 499-510, 2008.

SHAFIEI, A.; DUSSEAULT, M. B. Rock mass characterization at Kangir dam site in Iran. In: ISRM International Symposium - 5th Asian Rock Mechanics Symposium, 24-26 November, Tehran, Iran, 2008. **Proceedings**. International Society for Rock Mechanics and Rock Engineering, p. 483-498, 2008.

SHAFIEI, A.; HEIDARI, M.; DUSSEAULT, M. B. Rock mass characterization at the proposed Khorram-Roud site in western Iran. In: 1st Canada - U.S. Rock Mechanics Symposium, 27-31 May, Vancouver, Canada, 2007. **Proceedings**. American Rock Mechanics Association, 2007.

SHEOREY, P. R. **Empirical Rock Failure Criteria**. CRC Press, 1997, 200p.

SINGH, B. **Workshop on Norwegian Method of Tunnelling**. CSMRS, New Delhi, 1993.

SINGH, B.; VILLADKAR, M. N.; SAMADHIYA, N. K.; MEHROTRA, V. K. Rock mass strength parameters mobilised in tunnels. **Tunnelling and Underground Space Technology**, v. 12, n. 1, p. 47-54, 1997.

SINGH, B.; GOEL, R. K.; MEHROTRA, V. K.; GARG, S. K.; ALLU, M. R. Effect of intermediate principal stress on strength of anisotropic rock mass. **Tunnelling and Underground Space Technology**, v. 13, n. 1, p. 71-79, 1998.

SINGH, M.; RAO, K. S. Empirical methods to estimate the strength of jointed rock masses. **Engineering Geology**, v. 77, n. 1-2, p. 127-137, 2005.

SINGH, B.; GOEL, R. K. **Rock mass classification: a practical approach in civil engineering**. Elsevier, 1999, 282p.

SINGH, B.; GOEL, R. K. **Engineering rock mass classification: Tunneling, foundations and landslides**. Butterworth-Heinemann, 2012, 384p.

SIVAKUGAN, N.; SHUKLA, S. K.; DAS, B. M. **Rock mechanics: an introduction**. CRC Press, 2013, 249p.

SONMEZ, H.; GOKCEOĞU, C.; NEFESLIOĞLU, H. A.; KAYABASI, A. Estimation of rock modulus: For intact rocks with an artificial neural network and for rock masses with a new empirical equation. **International Journal of Rock Mechanics and Mining Sciences**, v. 43, n. 2, p. 224-235, 2006.

SOUFI, A.; BAHI, L.; OUADIF, L.; KISSAI, J. E. Correlation between rock mass rating, Q-system and rock mass index based on field data. In: MATEC Web of Conferences, 2018. **Proceedings**. EDP Sciences, p. 1-17, 2018.

THEUNE, U.; ROKOSH, D.; SACCHI, M. D.; SCHMITT, R. Mapping fractures with GPR: A case study from Turtle Mountain. **Geophysics**, v. 71, n. 5, p. B139-B150, 2006.

TOSHIOKA, T.; TSUCHIDA, T.; SASAHARA, K. Application of GPR to detecting and mapping cracks in rock slopes. **Journal of Applied Geophysics**, v. 33, n. 1-3, p. 119-124, 1995.

TERZAGHI, K. Rock defects and loads on tunnel supports. In: Proctor, R.V. and White, T.L., Eds., **Rock Tunneling with Steel Supports**, Commercial Shearing and Stamping Company, Youngstown, p. 15-99, 1946.

ULUSAY, R.; HUDSON, J. A. **The complete ISRM suggested methods for rock characterization, testing and monitoring: 1974-2006**. ISRM Turkish National Group, Ankara, Turkey, 2007.

ULUSAY, R. **The ISRM suggested methods for rock characterization, testing and monitoring: 2007-2014**. Springer, 2014, 292p.

UTSI, E. C. **Ground penetrating radar: theory and practice**. Butterworth-Heinemann, 2017.

- VALLEJO, L. G.; FERRER, M. **Geological engineering**. CRC Press, 2011, 692p.
- VÁN, P.; B. VÁSÁRHELYI. **Relation of rock mass characterization and damage**. Rock Engineering in Difficult Ground Conditions, Soft Rock and Karst, 2010.
- VÁSÁRHELYI, B.; KOVÁCS, D. Empirical methods of calculating the mechanical parameters of the rock mass. **Periodica Polytechnica Civil Engineering**, v. 61, n. 1, p. 39-50, 2017.
- ZHANG, L.; EINSTEIN, H. H. Using RQD to estimate the deformation modulus of rock masses. **International Journal of Rock Mechanics and Mining Sciences**, v. 41, n. 2, p. 337-341, 2004.
- ZHANG, L. Estimating the strength of jointed rock masses. **Rock Mechanics and Rock Engineering**, v. 43, n. 4, p. 391-402, 2010.
- ZHANG, L. **Engineering properties of rocks**. Butterworth-Heinemann, 2016, 386p.
- ZHANG, L. Evaluation of rock mass deformability using empirical methods – A review. **Underground Space**, v. 2, n. 1, p. 1-15, 2017.
- ZHAO, W.; FORTE, E.; PIPAN, M.; TIAN, G. Ground penetrating radar (GPR) attribute analysis for archaeological prospection. **Journal of Applied Geophysics**, v.97, p. 107-117, 2013.
- ZHAO, W. K.; FORTE, M. D.; PIPAN, M. Integrated attribute analysis for improved GPR data interpretation. In: 2016 16th International Conference on Ground Penetrating Radar (GPR). **Proceedings**. IEEE, p. 1-5, 2016,
- WICKHAM, G. E.; TIEDEMANN, H. R.; SKINNER, E. H. Support determination based on geologic predictions. In: Rapid Excav. Tunneling Conf., American Institute of Mining, Metallurgical and Petroleum Engineers, New York, USA, 1972. **Proceedings**. AMAM, p. 691-707, 1972.
- WICKHAM, G. E.; TIEDEMANN, H. R.; SKINNER, E. H. Ground support prediction model-RSR concept. In: 2nd North American Rapid Excav. Tunneling Conf., San Francisco, 1972. **Proceedings**. American Institute of Mining, Metallurgical and Petroleum Engineers (AIME), New York, p. 691-707, 1972;
- WHITE, R.E. Properties of instantaneous seismic attributes. **The Leading Edge**, v. 10, n. 7, p. 26-32, 1991.
- WYATT, D. E.; TEMPLES, T. J. Ground-penetrating radar detection of small-scale channels, joints and faults in the unconsolidated sediments of the Atlantic Coastal Plain. **Environmental Geology**, v. 27, n. 3, p. 219-225, 1996.
- WYLLIE, D. C. **Rock slope engineering: civil applications**. CRC Press, 2017, 621p.
- YELF, R. J. Application of ground penetrating radar to civil and geotechnical engineering. **Electromagnetic Phenomena**, v. 7, n. 1, 2007.

YUDHBIR, Y.; LEMANZA, W.; PRINZL, F. An empirical failure criterion for rock masses. In: 5th ISRM Congress, 10-15 April, Melbourne, Australia, 1983. **Proceedings**. International Society for Rock Mechanics and Rock Engineering, p. B1-B8, 1983.

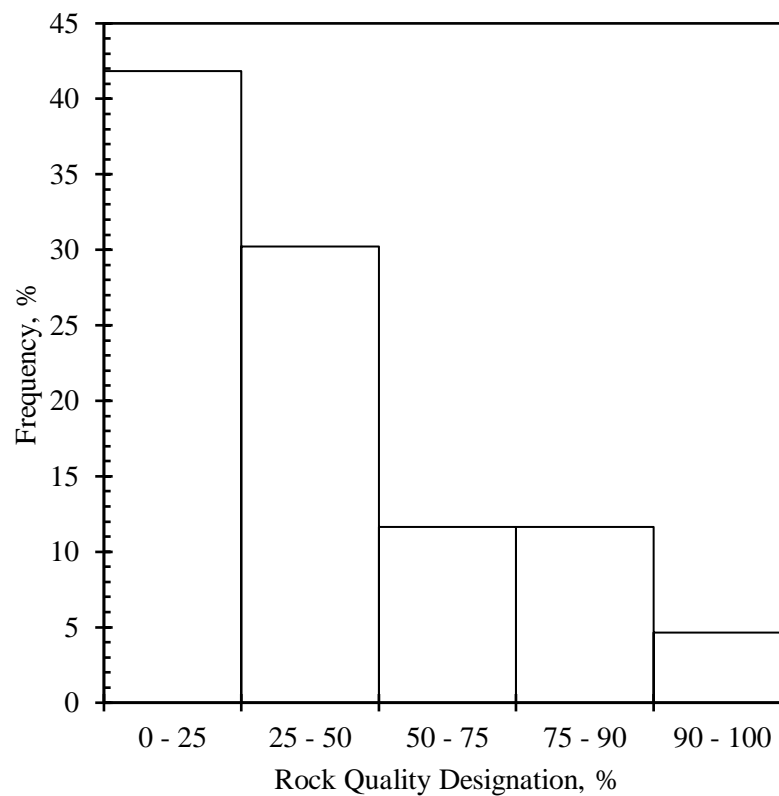
## APPENDIX A - DESCRIPTIVE STATISTICS OF THE DATABASE

**Table A.1** - Descriptive statistics of RQD index database (S1 to S46)

<b>Rock Quality Designation (S1-S46)</b>	
Mean	39.38
Standard Error	4.03
Median	34.00
Mode	10.00
Standard Deviation	26.40
Sample Variance	696.78
Kurtosis	-0.72
Skewness	0.65
Range	92.00
Minimum	2.00
Maximum	94.00
Sum	1693.13
Count	43.00

Source: elaborated by the author.

**Figure A.1** - Frequency histogram of RQD index database (S1 to S46)



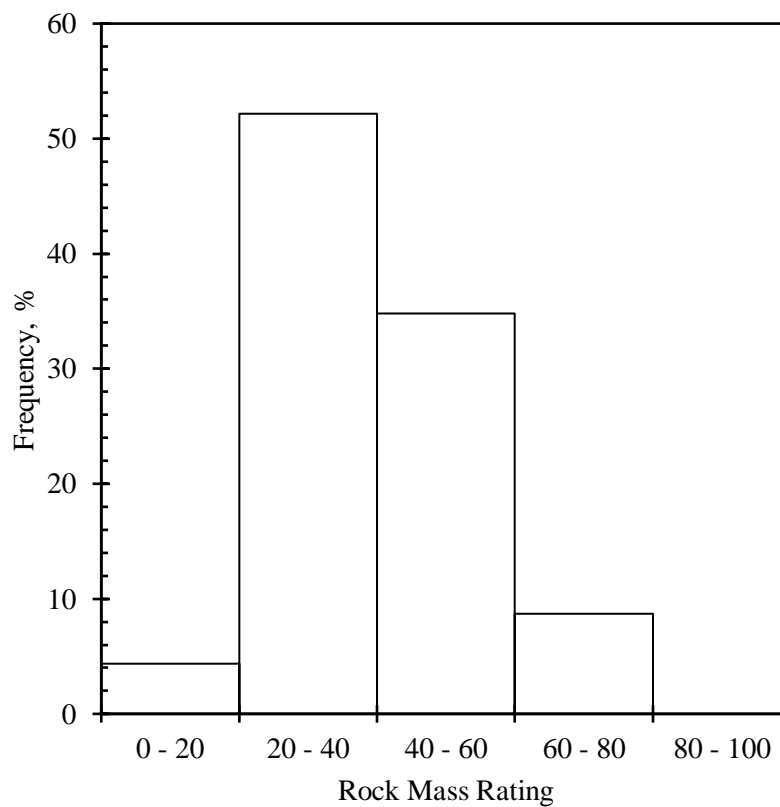
Source: elaborated by the author.

**Table A.2** - Descriptive statistics of RMR number database (S1 to S46)

<b>Rock Mass Rating (S1-S46)</b>	
Mean	39.8
Standard Error	2.18
Median	36
Mode	34
Standard Deviation	14.80
Sample Variance	219.14
Kurtosis	-0.31
Skewness	0.46
Range	63
Minimum	11
Maximum	74
Sum	183
Count	46

Source: elaborated by the author.

**Figure A.2** - Frequency histogram of RMR number database (S1 to S46)



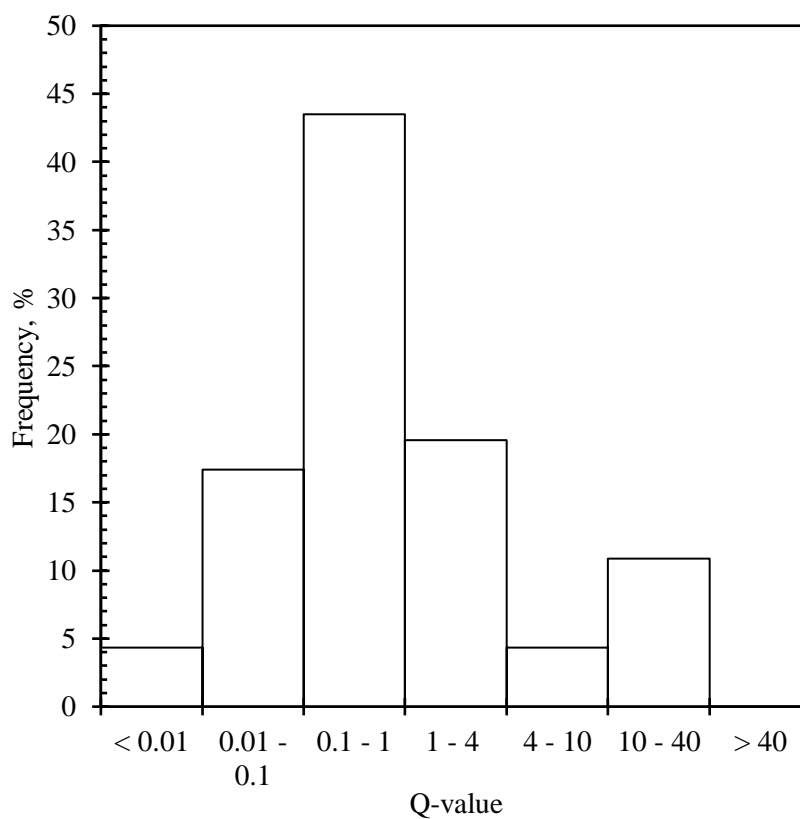
Source: elaborated by the author.



**Table A.3** - Descriptive statistics of Q value database (S1 to S46)

Q (S1-S46)	
Mean	2.483
Standard Error	0.751
Median	0.465
Mode	0.120
Standard Deviation	5.094
Sample Variance	25.949
Kurtosis	5.706
Skewness	2.583
Range	19.988
Minimum	0.002
Maximum	19.990
Sum	114.207
Count	46

Source: elaborated by the author.

**Figure A.3** - Frequency histogram of Q-value database (S1 to S46)

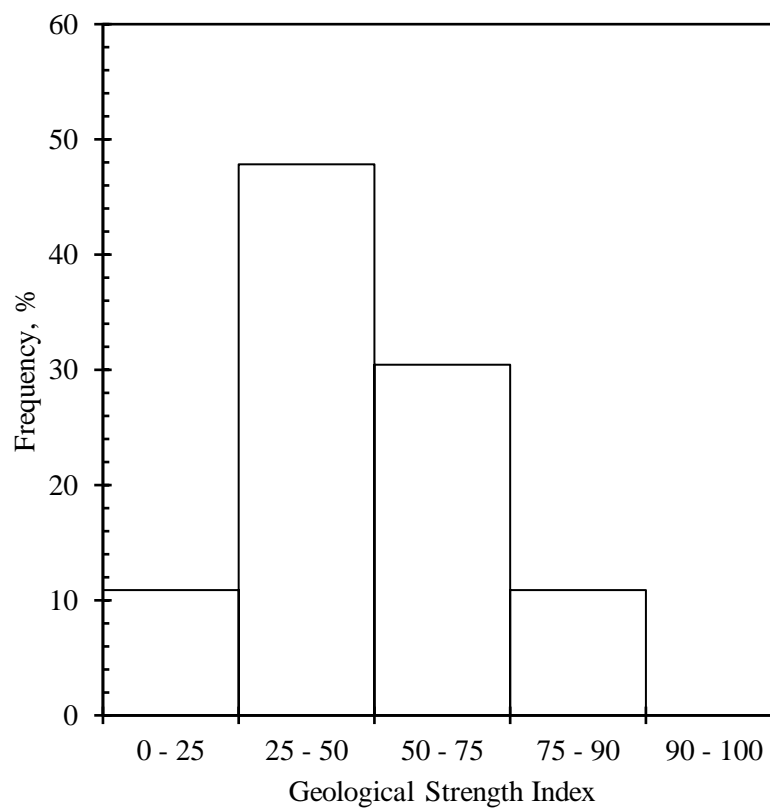
Source: elaborated by the author.

**Table A.4** - Descriptive statistics of GSI number database (S1 to S46)

<b>Rock Mass Rating (S1-S46)</b>	
Mean	39.92
Standard Error	2.35
Median	38.5
Mode	32
Standard Deviation	15.96
Sample Variance	254.62
Kurtosis	0.75
Skewness	0.83
Range	67
Minimum	13
Maximum	80
Sum	1836.5
Count	46

Source: elaborated by the author.

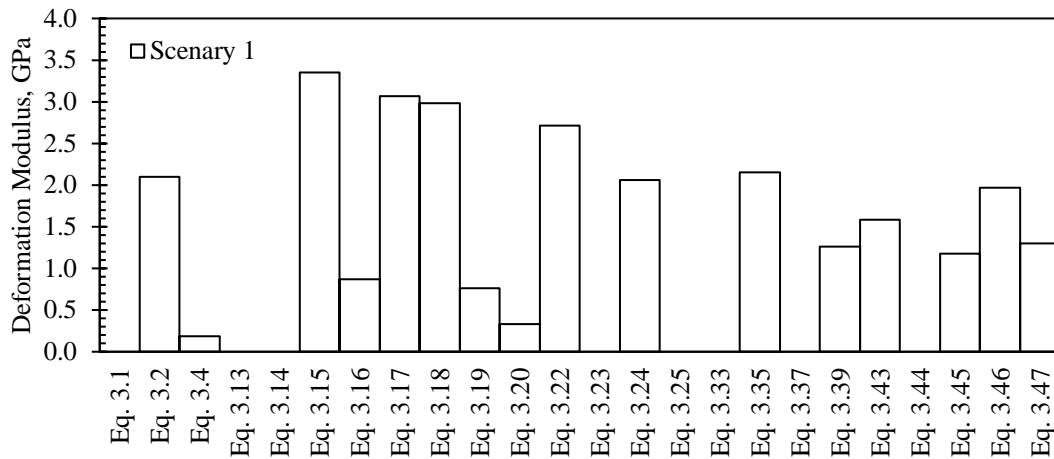
**Figure A.4** - Frequency histogram of GSI number database (S1 to S46)



Source: elaborated by the author.

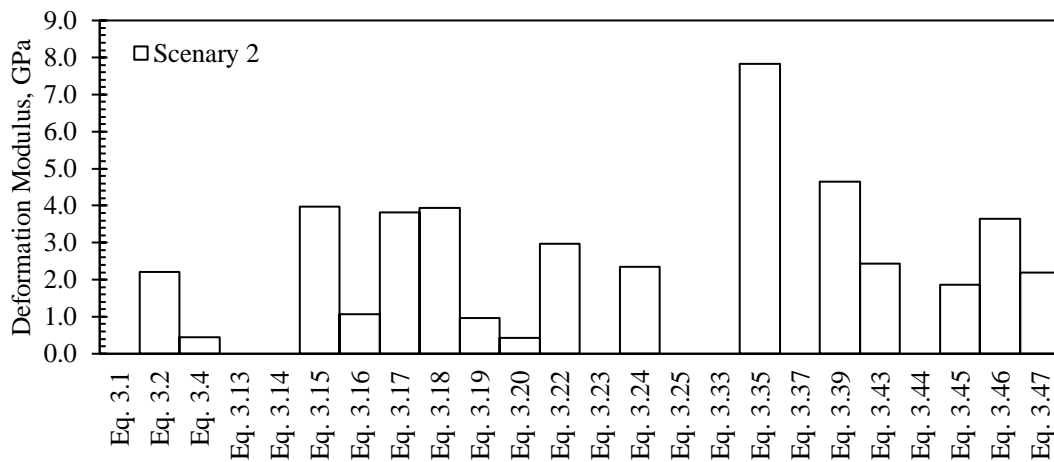
## APPENDIX B - DEFORMATION MODULUS ( $E_{rm}$ ) RESULTS

**Figure B.5** - Deformation modulus calculated for scenario 1



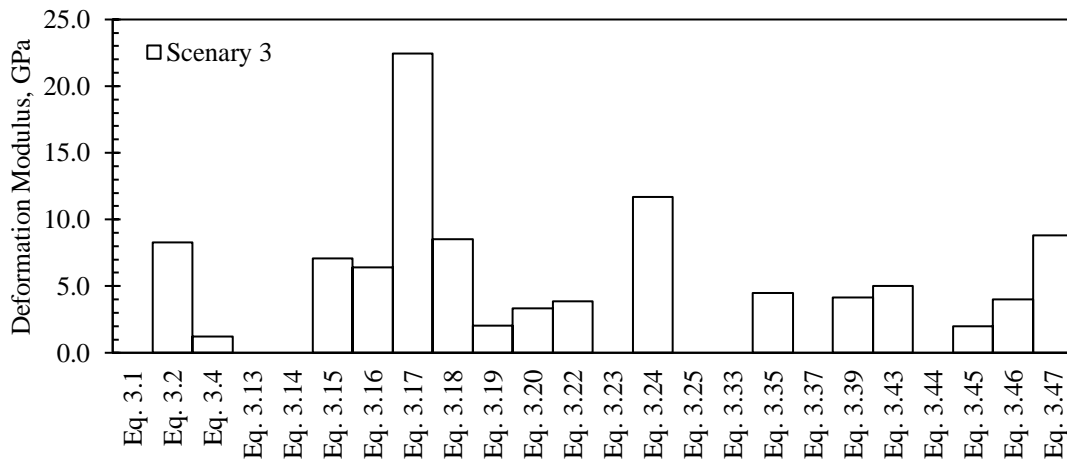
Source: elaborated by the author.

**Figure B.6** - Deformation modulus calculated for scenario 2



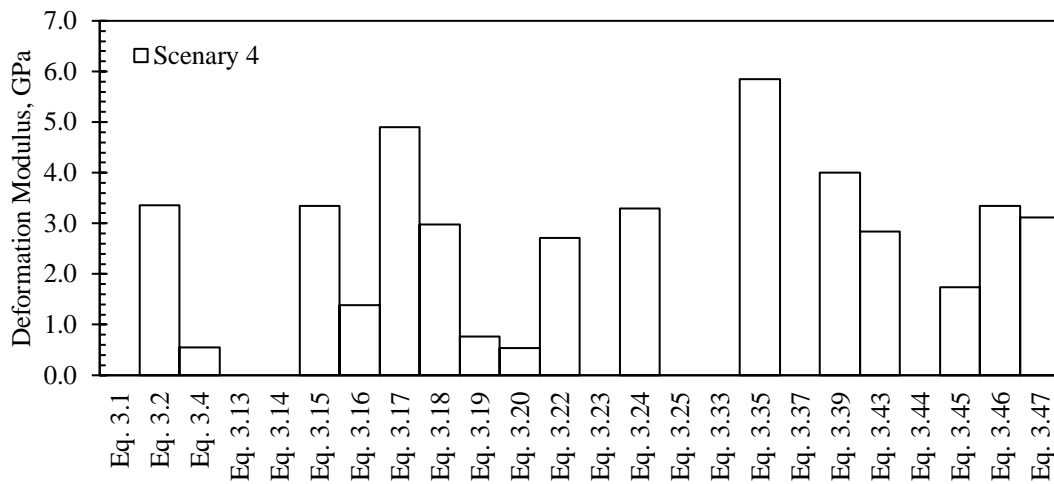
Source: elaborated by the author.

**Figure B.7** - Deformation modulus calculated for scenario 3



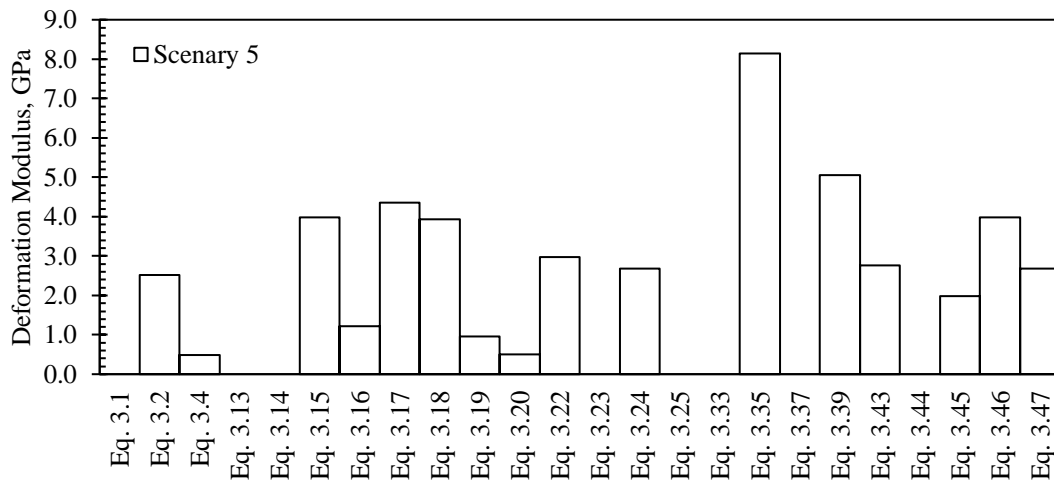
Source: elaborated by the author.

**Figure B.8** - Deformation modulus calculated for scenario 4



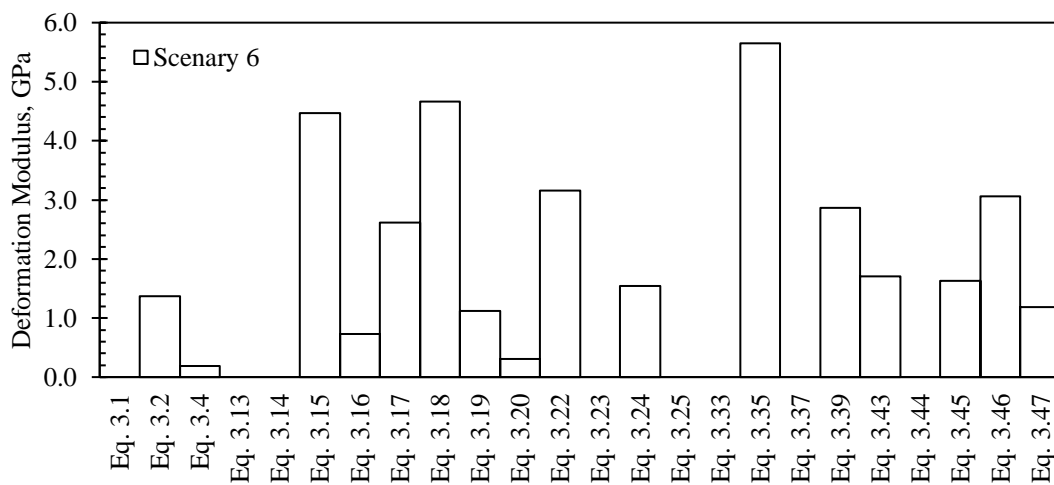
Source: elaborated by the author.

**Figure B.9** - Deformation modulus calculated for scenario 5



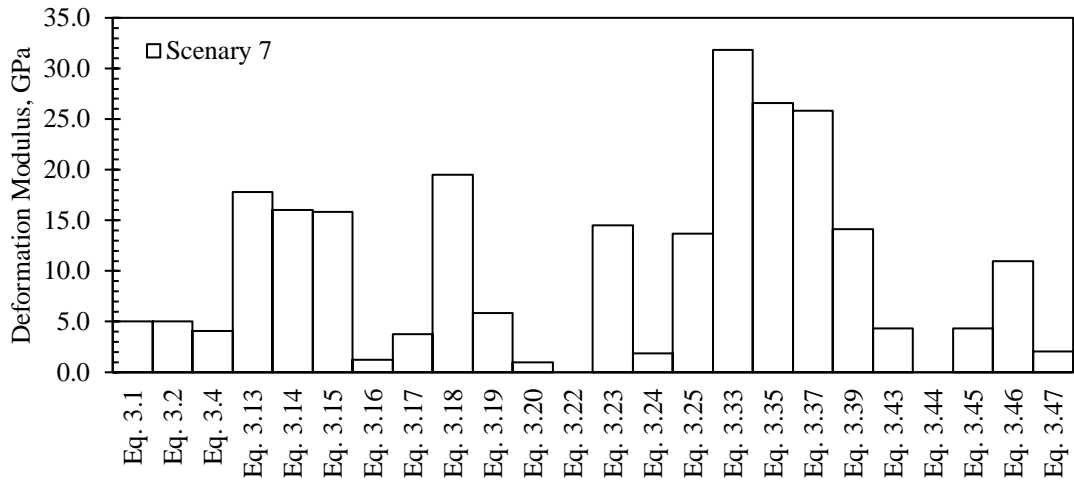
Source: elaborated by the author.

**Figure B.10** - Deformation modulus calculated for scenario 6



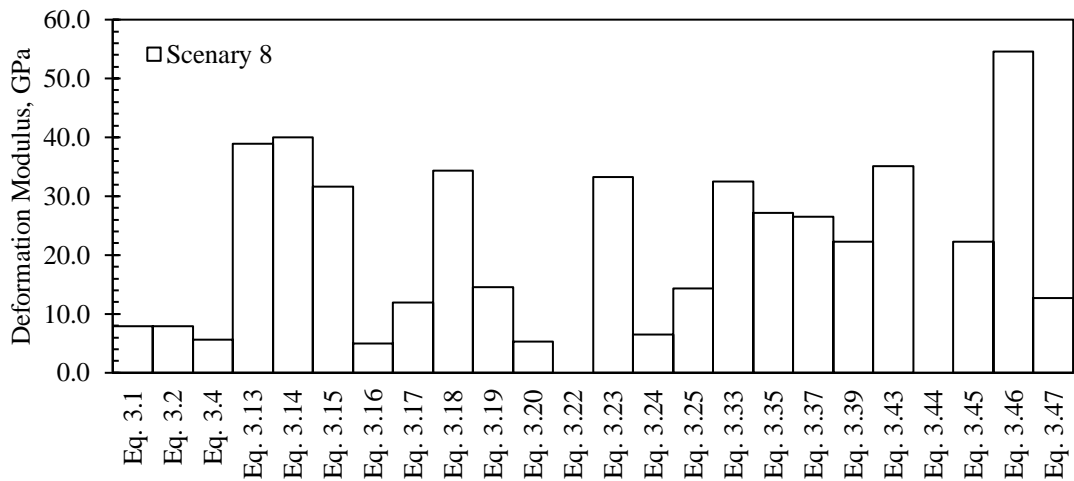
Source: elaborated by the author.

**Figure B.11** - Deformation modulus calculated for scenario 7



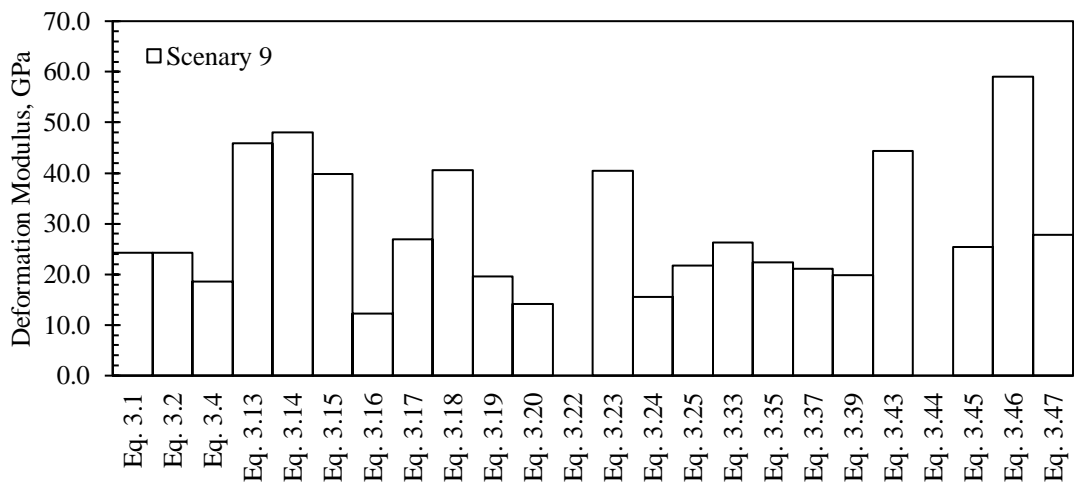
Source: elaborated by the author.

**Figure B.12** - Deformation modulus calculated for scenario 8

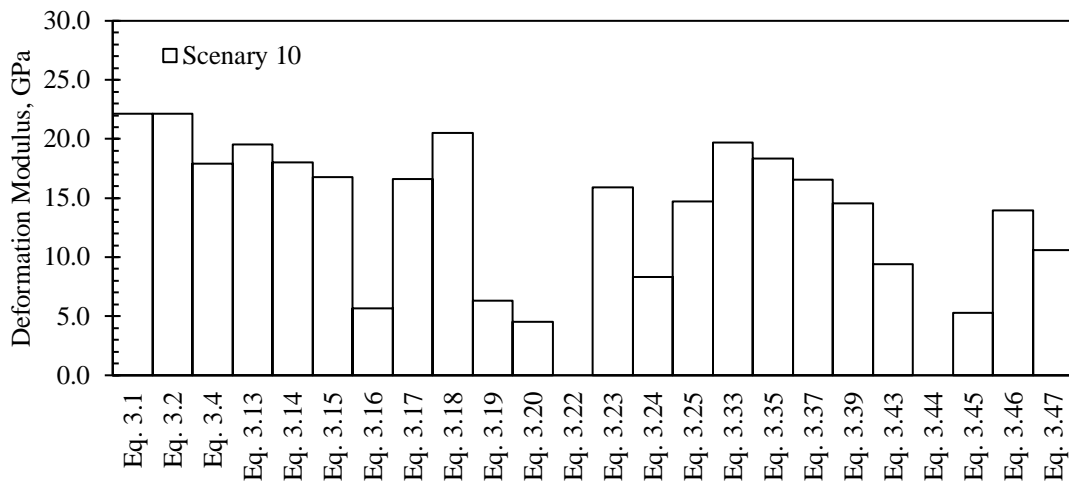


Source: elaborated by the author.

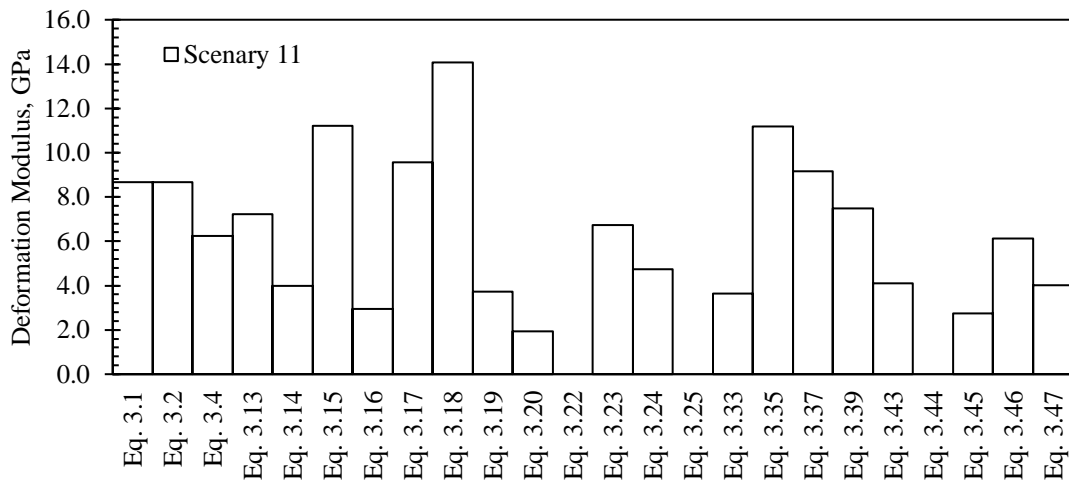
**Figure B.13** - Deformation modulus calculated for scenario 9



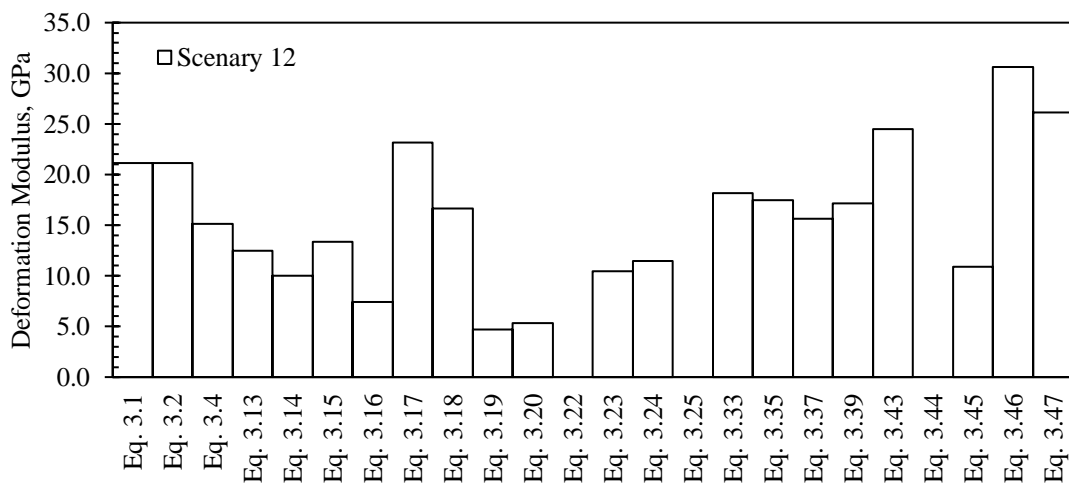
Source: elaborated by the author.

**Figure B.14** - Deformation modulus calculated for scenario 10

Source: elaborated by the author.

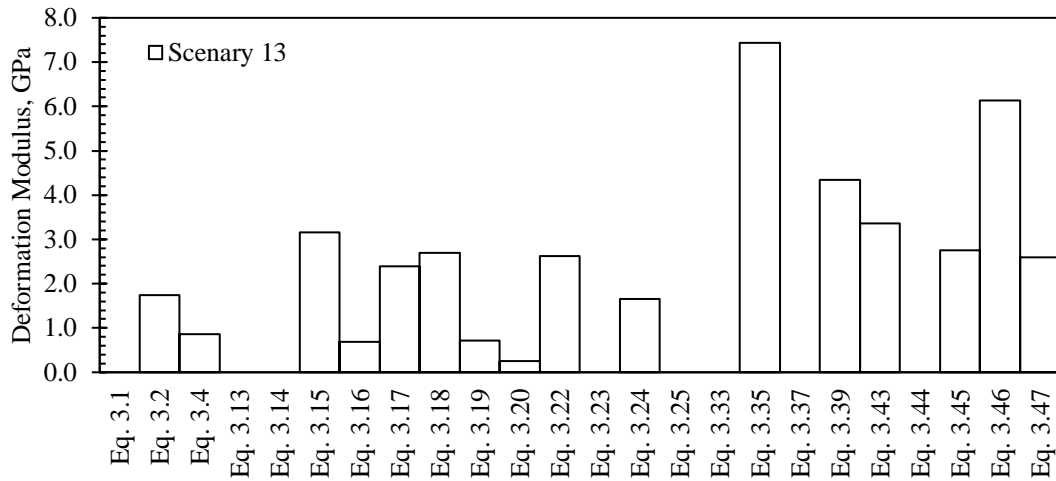
**Figure B.15** - Deformation modulus calculated for scenario 11

Source: elaborated by the author.

**Figure B.16** - Deformation modulus calculated for scenario 12

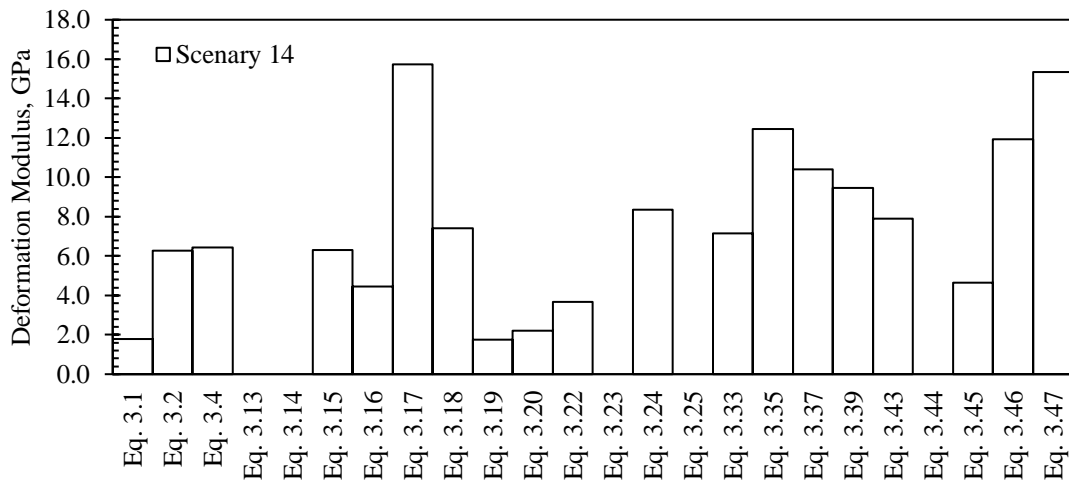
Source: elaborated by the author.

**Figure B.17** - Deformation modulus calculated for scenario 13



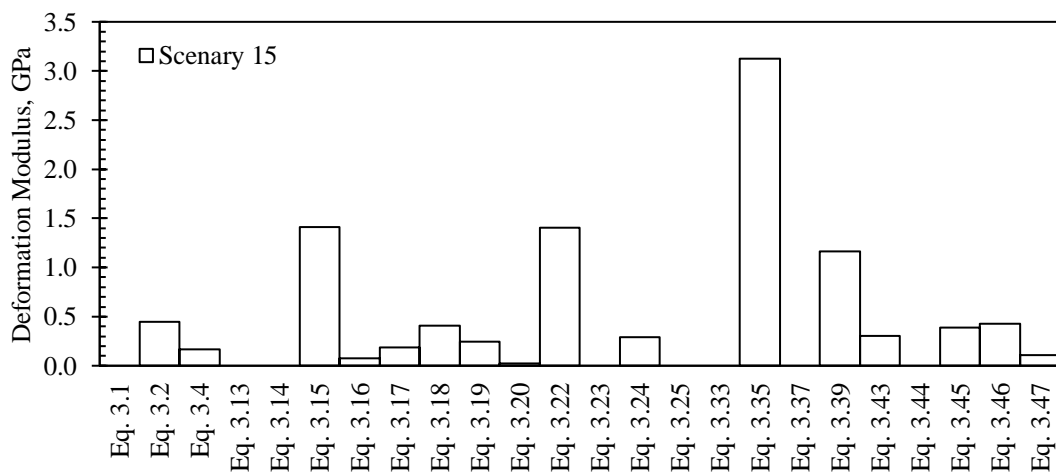
Source: elaborated by the author.

**Figure B.18** - Deformation modulus calculated for scenario 14

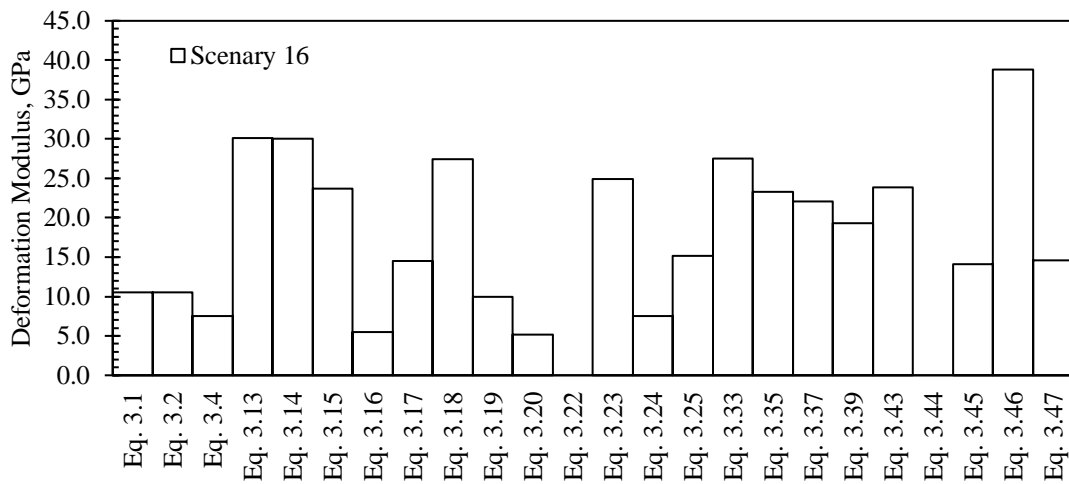


Source: elaborated by the author.

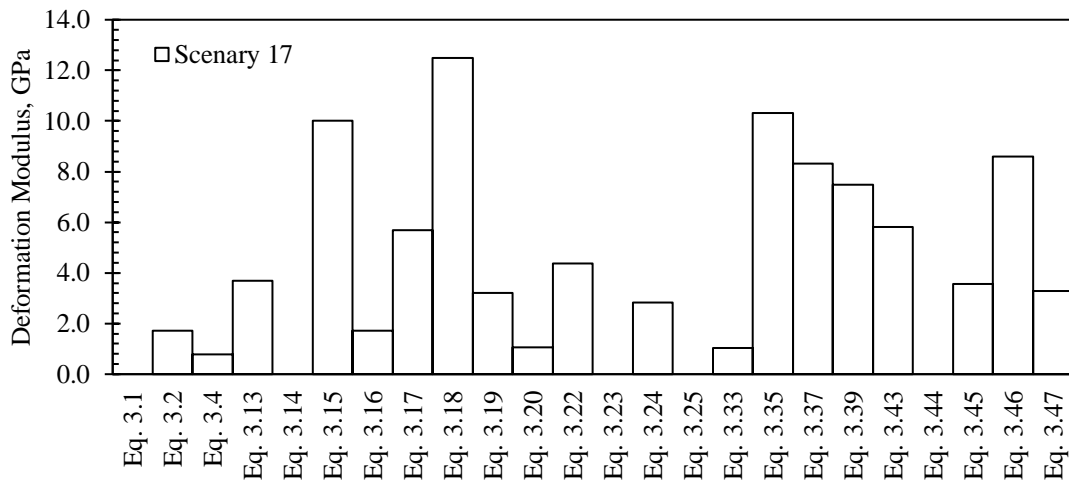
**Figure B.19** - Deformation modulus calculated for scenario 15



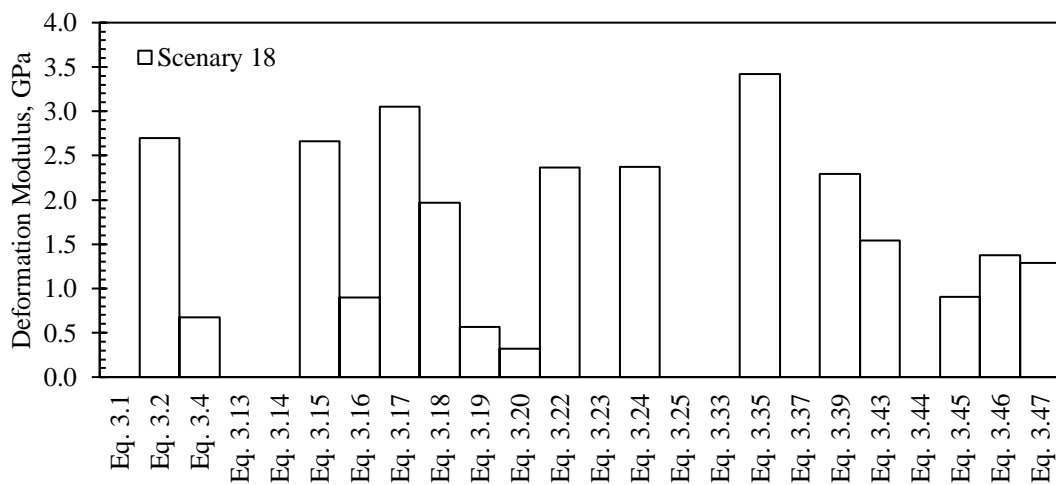
Source: elaborated by the author.

**Figure B.20** - Deformation modulus calculated for scenario 16

Source: elaborated by the author.

**Figure B.21** - Deformation modulus calculated for scenario 17

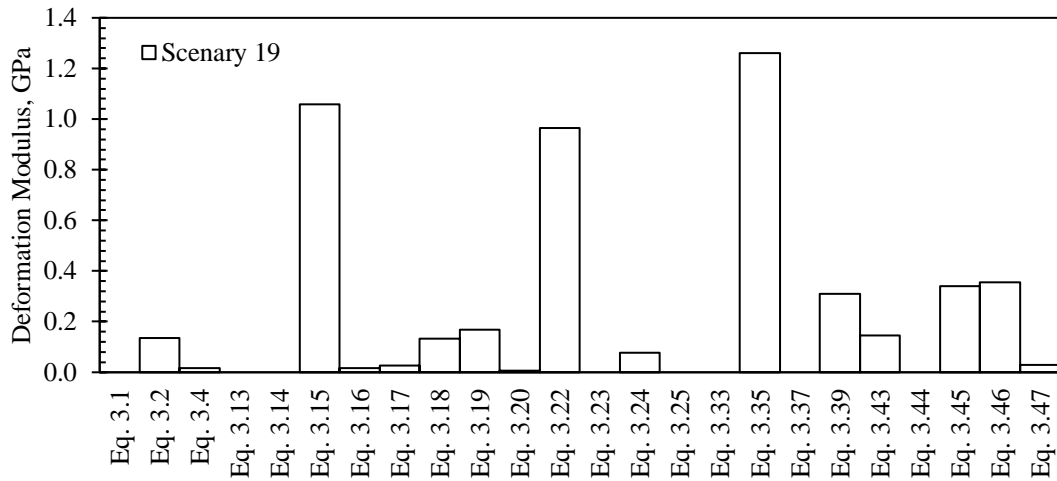
Source: elaborated by the author.

**Figure B.22** - Deformation modulus calculated for scenario 18

Source: elaborated by the author.

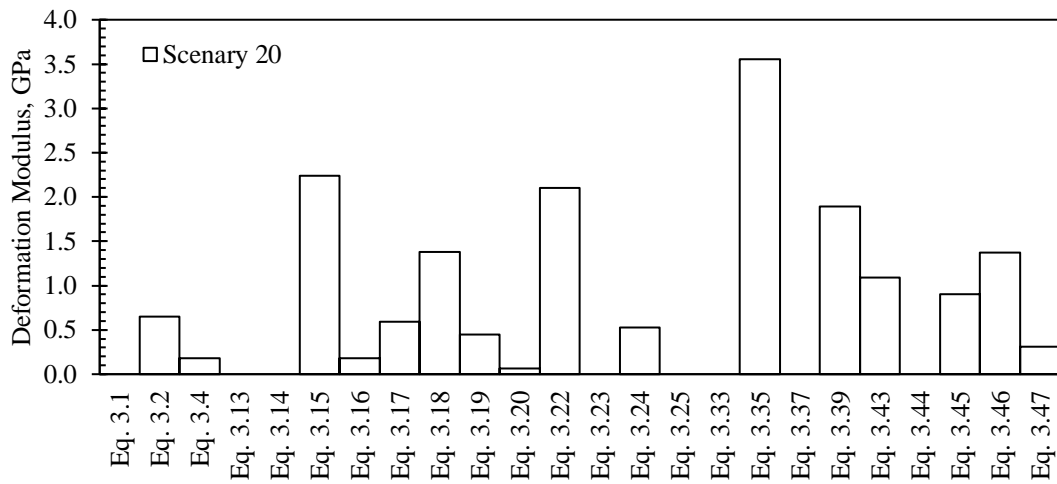


**Figure B.23** - Deformation modulus calculated for scenario 19



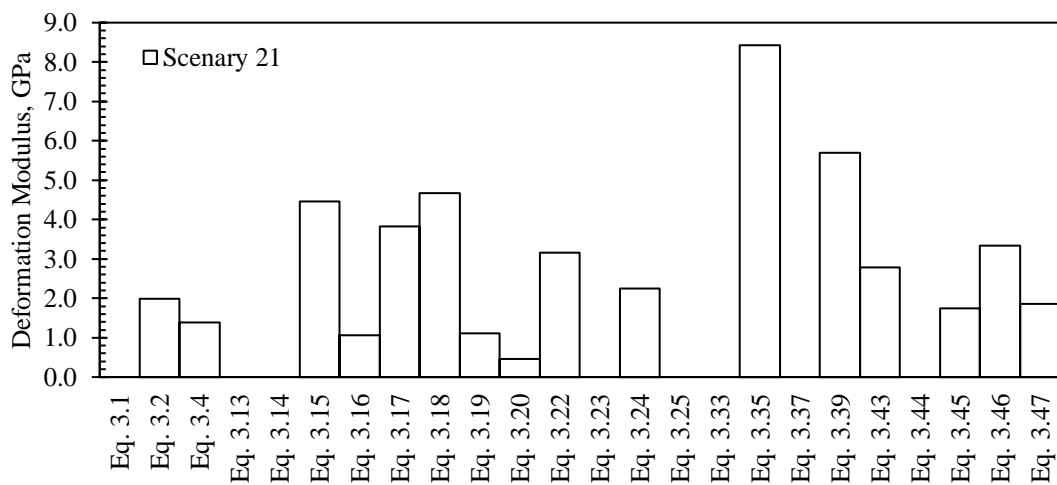
Source: elaborated by the author.

**Figure B.24** - Deformation modulus calculated for scenario 20

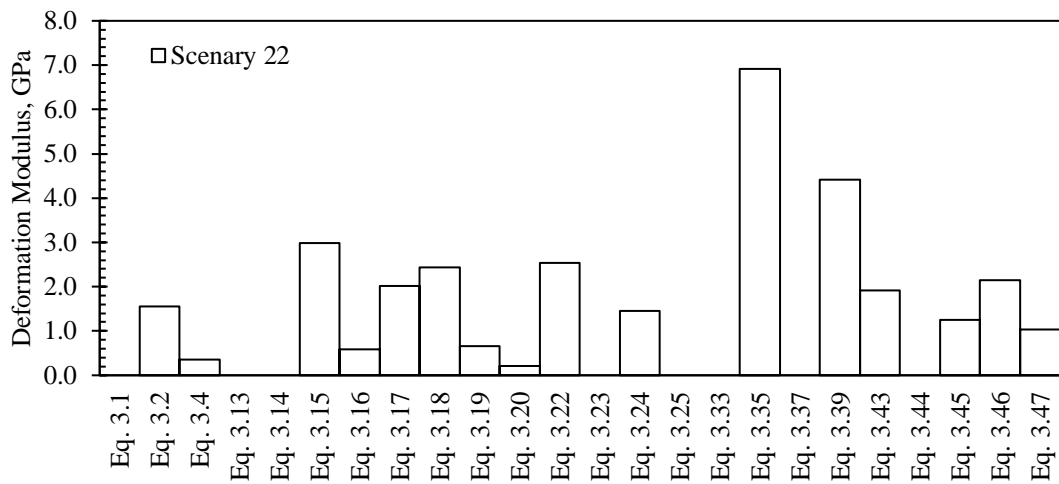


Source: elaborated by the author.

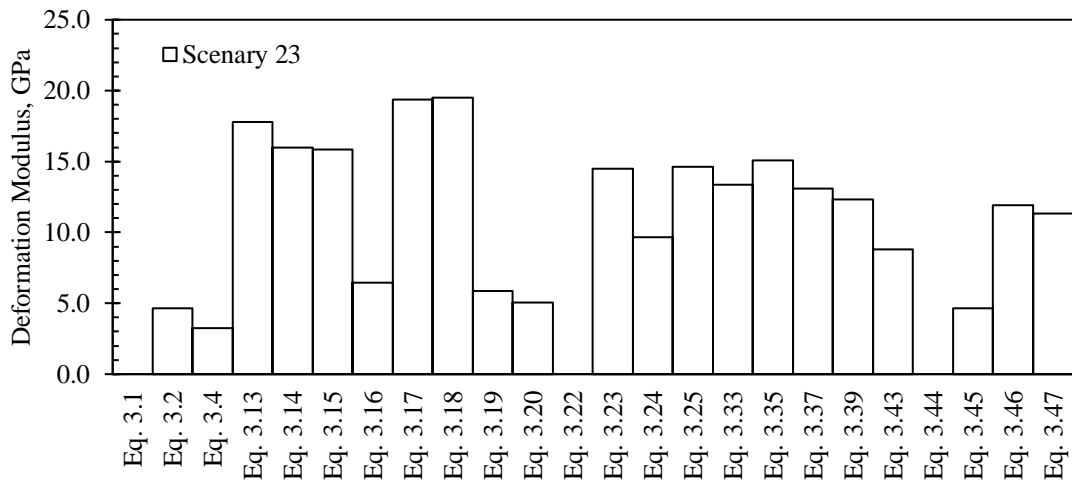
**Figure B.25** - Deformation modulus calculated for scenario 21



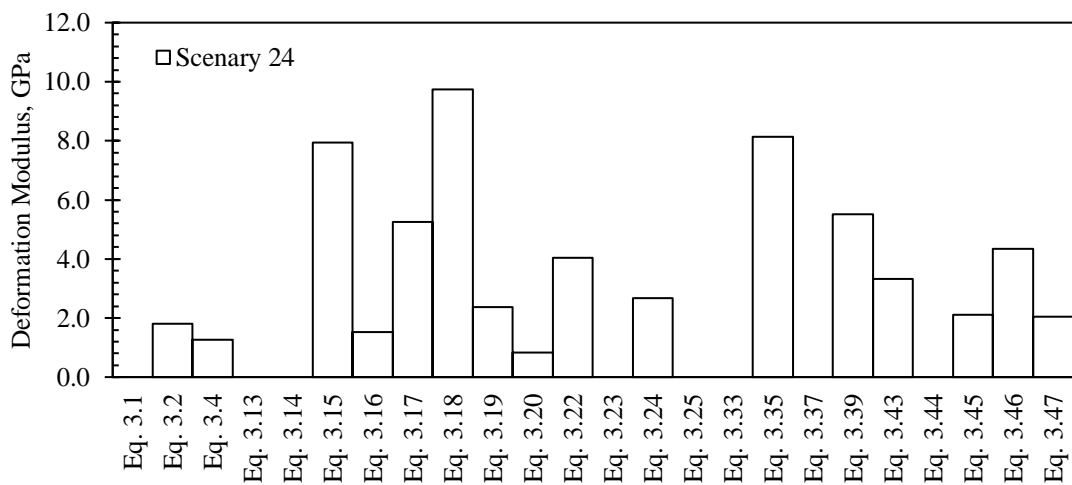
Source: elaborated by the author.

**Figure B.26** - Deformation modulus calculated for scenario 22

Source: elaborated by the author.

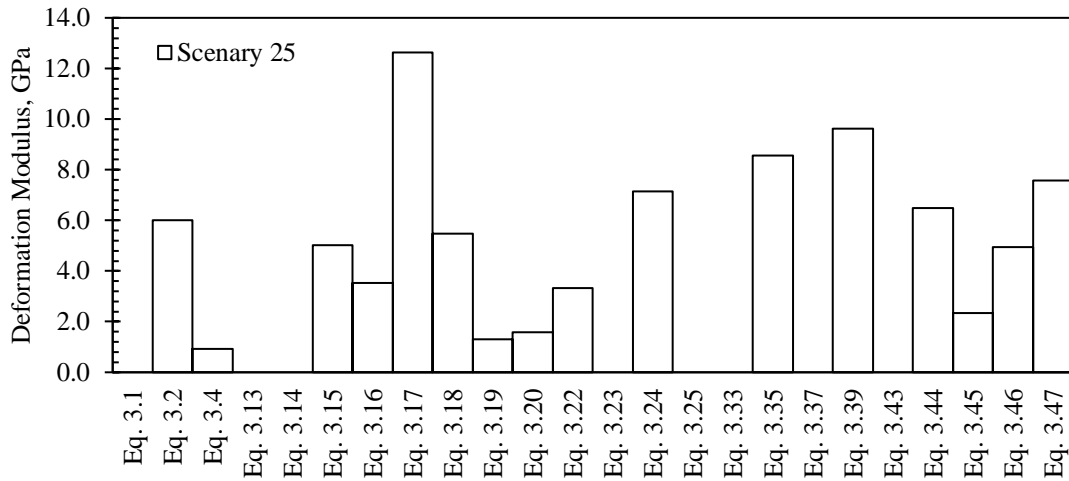
**Figure B.27** - Deformation modulus calculated for scenario 23

Source: elaborated by the author.

**Figure B.28** - Deformation modulus calculated for scenario 24

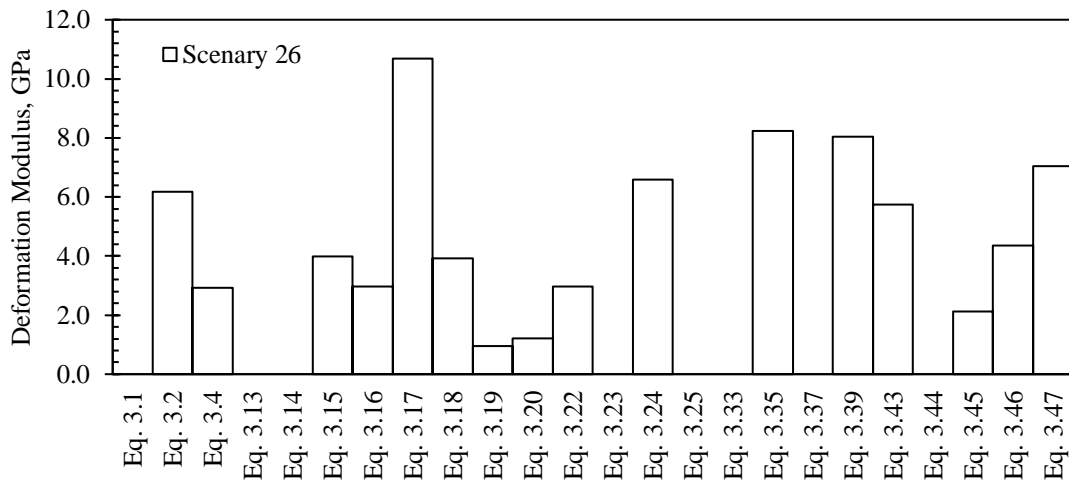
Source: elaborated by the author.

**Figure B.29** - Deformation modulus calculated for scenario 25



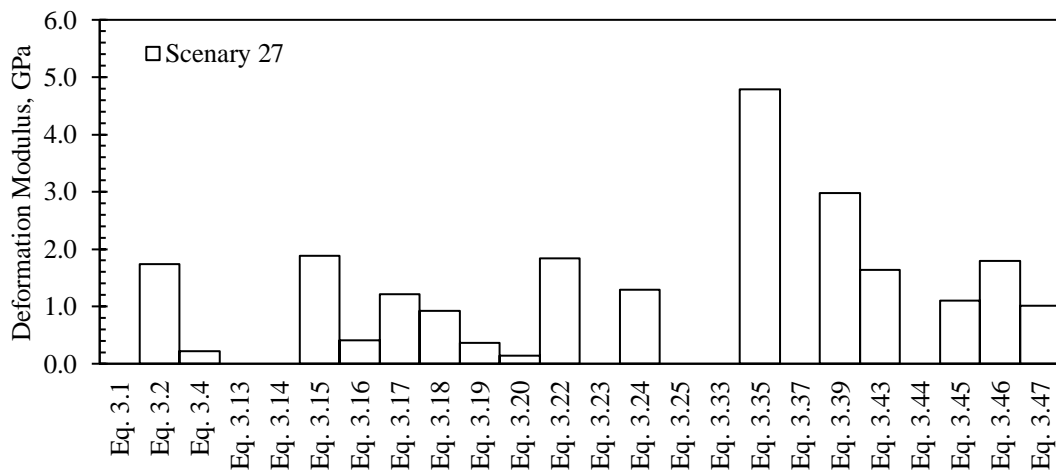
Source: elaborated by the author.

**Figure B.30** - Deformation modulus calculated for scenario 26

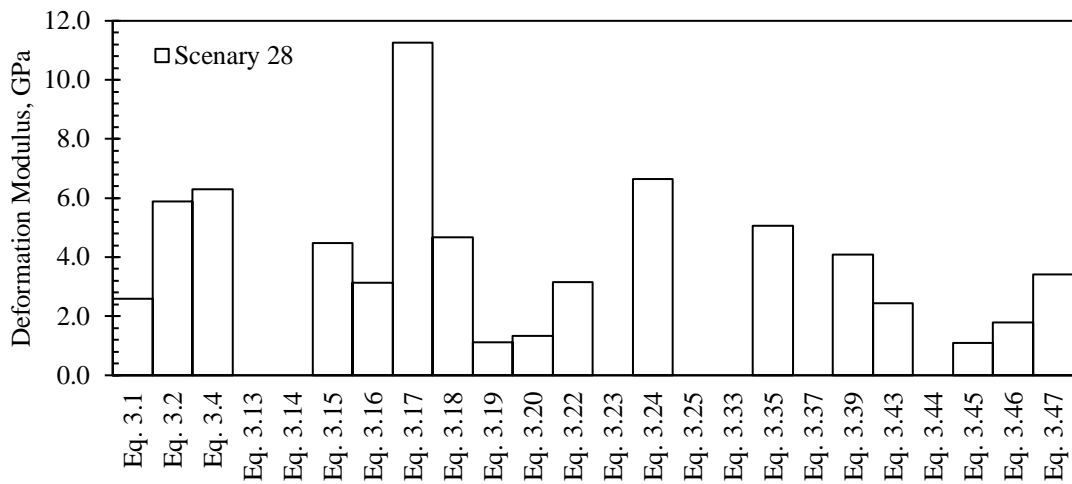


Source: elaborated by the author.

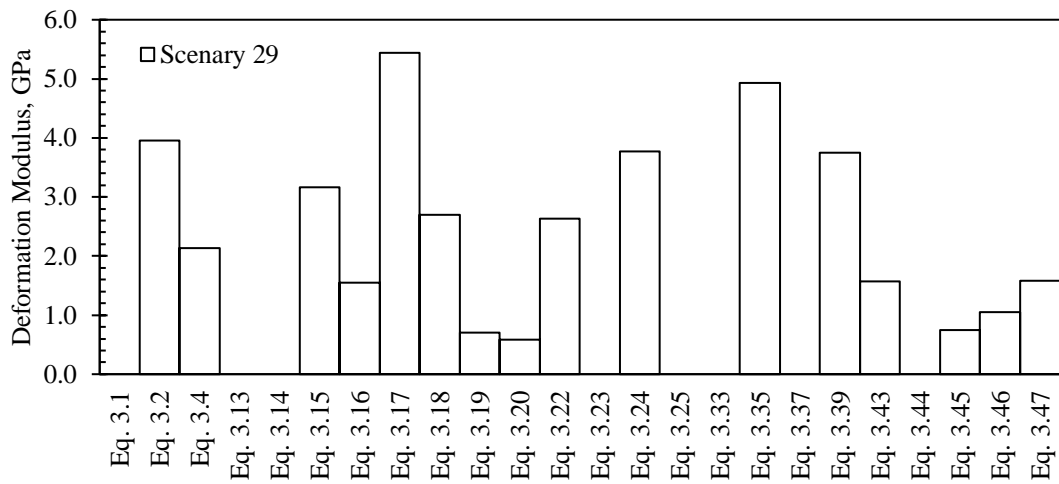
**Figure B.31** - Deformation modulus calculated for scenario 27



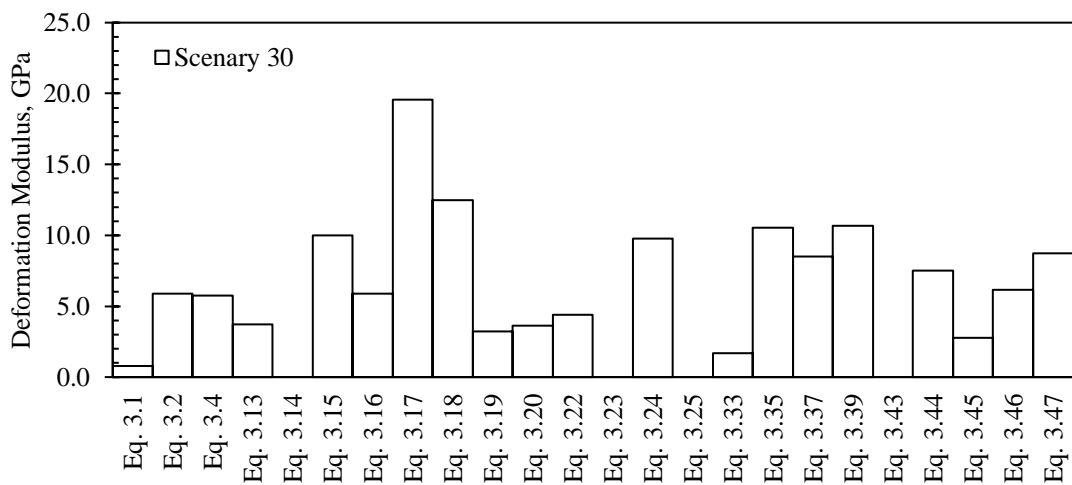
Source: elaborated by the author.

**Figure B.32** - Deformation modulus calculated for scenario 28

Source: elaborated by the author.

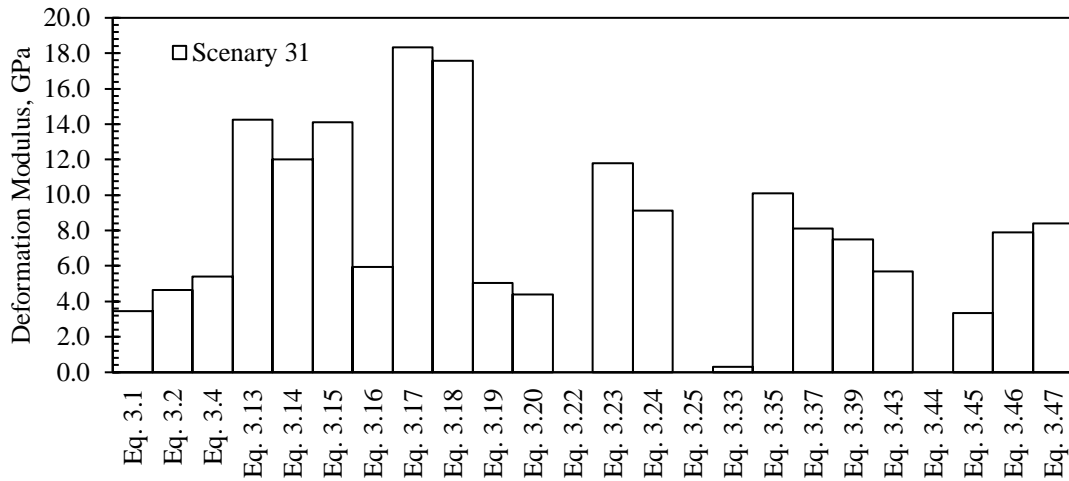
**Figure B.33** - Deformation modulus calculated for scenario 29

Source: elaborated by the author.

**Figure B.34** - Deformation modulus calculated for scenario 30

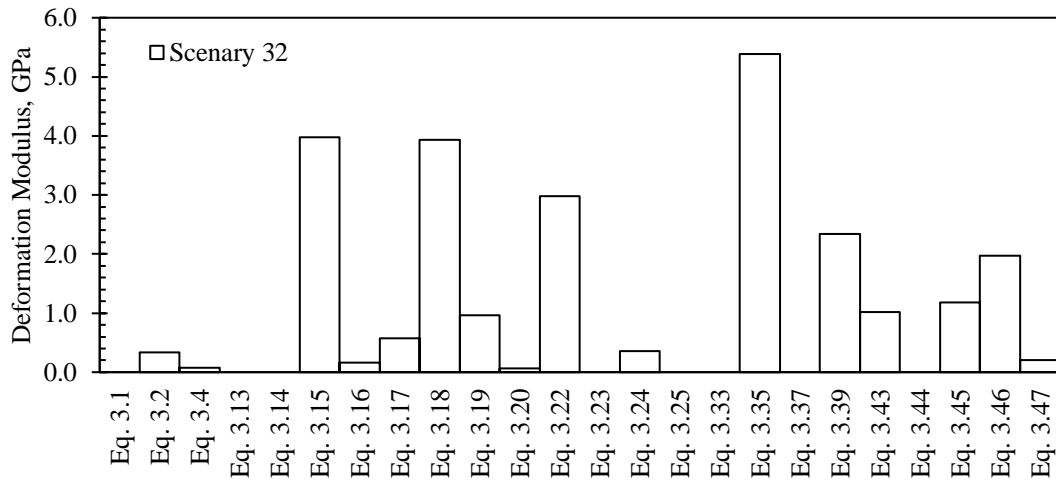
Source: elaborated by the author.

**Figure B.35** - Deformation modulus calculated for scenario 31



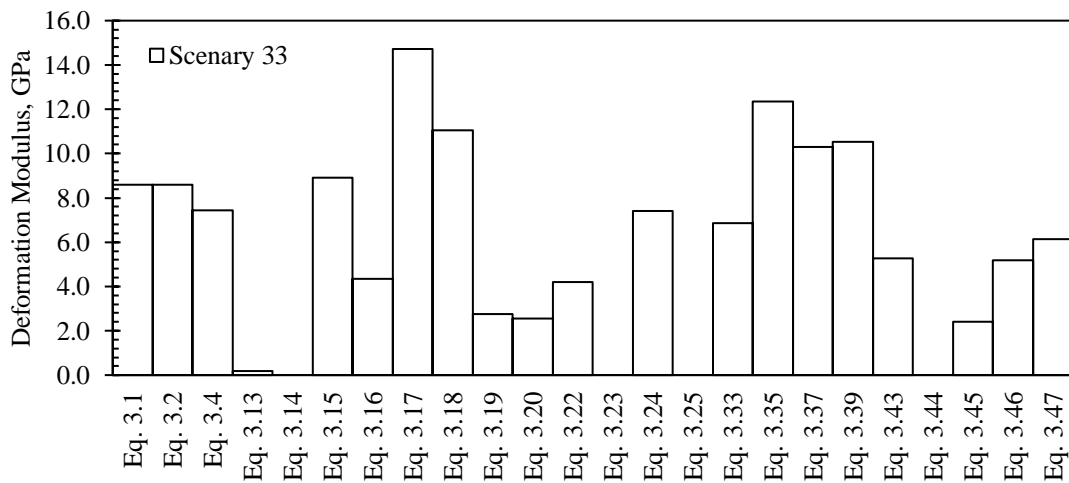
Source: elaborated by the author.

**Figure B.36** - Deformation modulus calculated for scenario 32

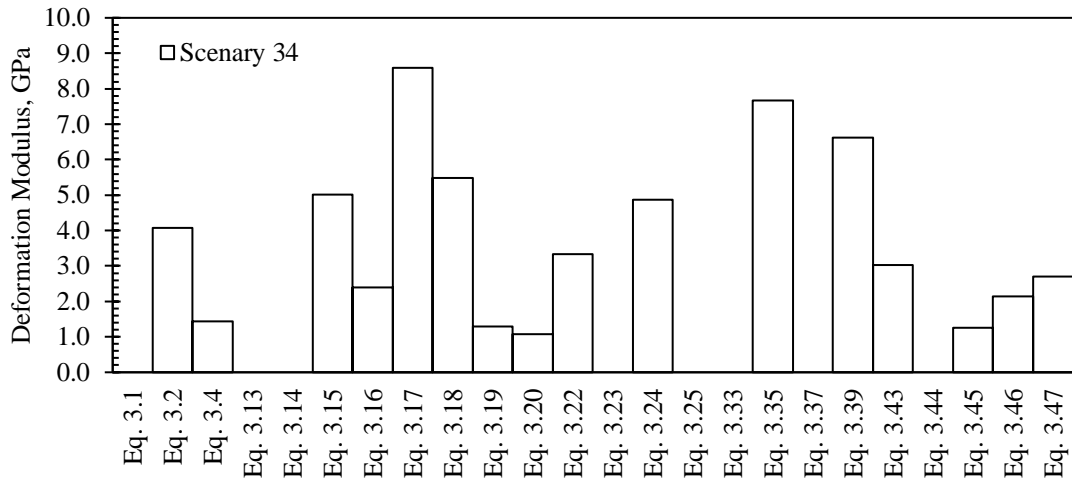


Source: elaborated by the author.

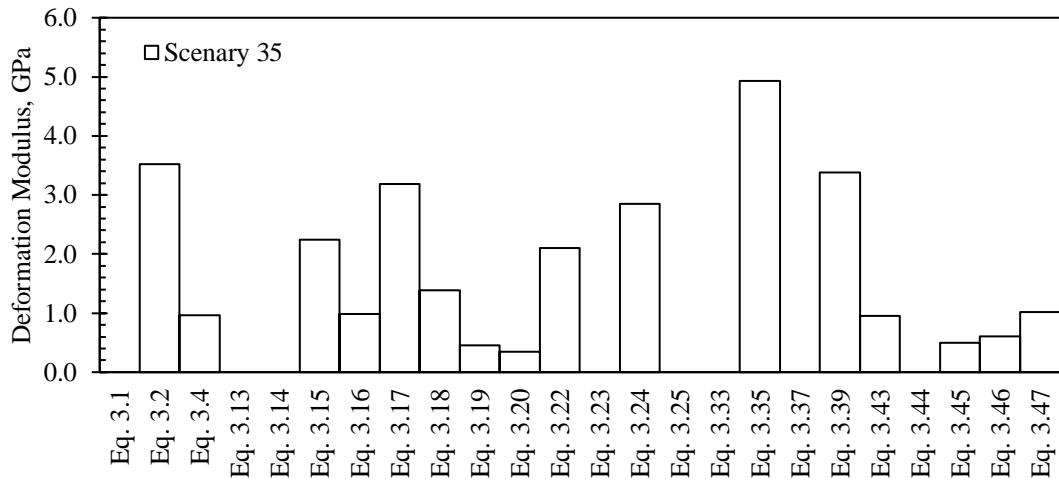
**Figure B.37** - Deformation modulus calculated for scenario 33



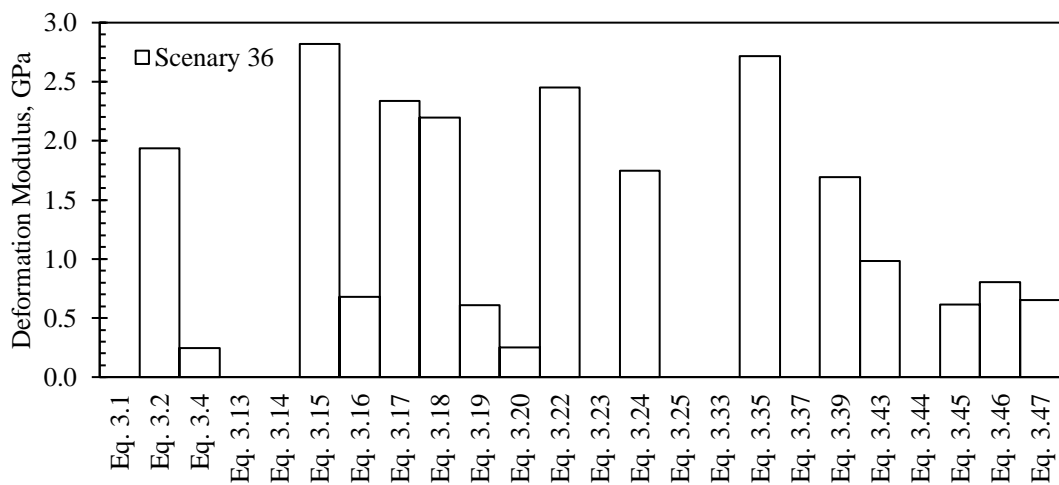
Source: elaborated by the author.

**Figure B.38** - Deformation modulus calculated for scenario 34

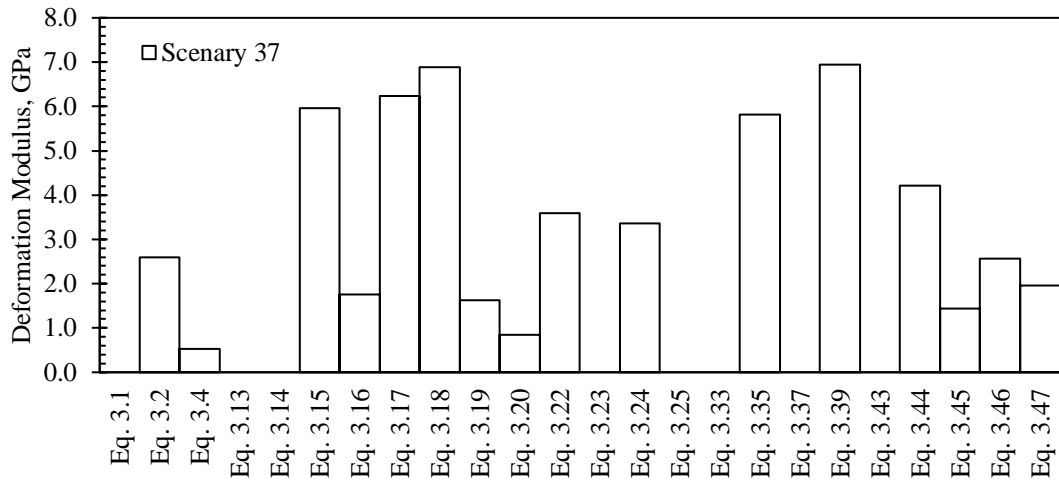
Source: elaborated by the author.

**Figure B.39** - Deformation modulus calculated for scenario 35

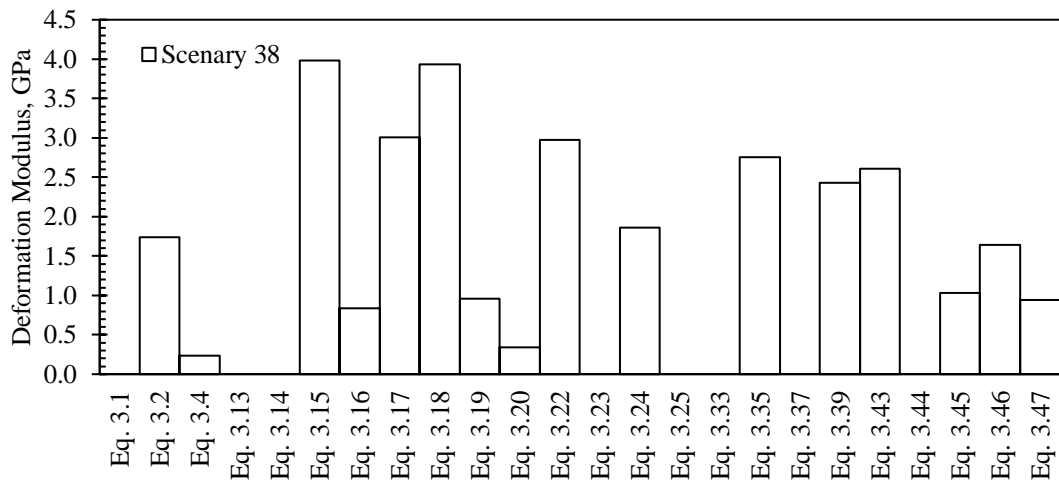
Source: elaborated by the author.

**Figure B.40** - Deformation modulus calculated for scenario 36

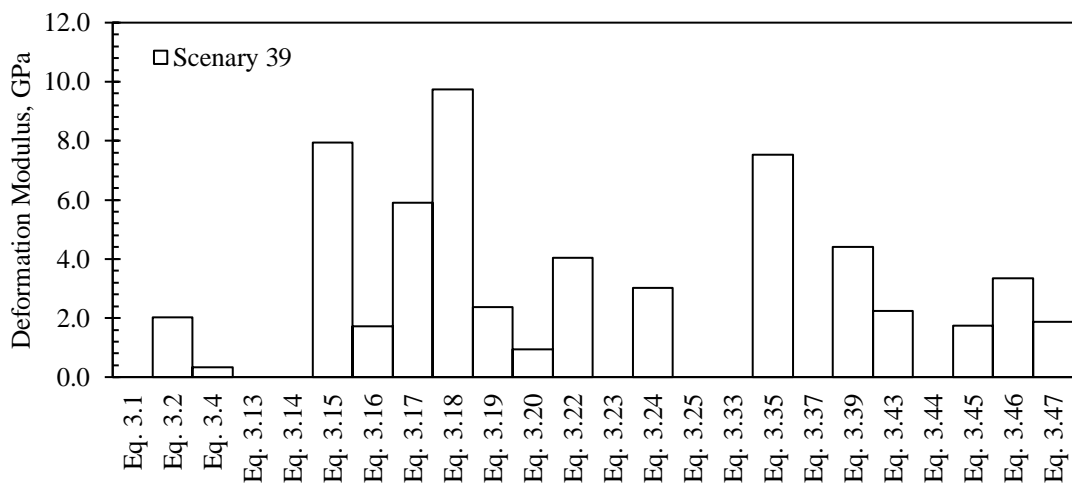
Source: elaborated by the author.

**Figure B.41** - Deformation modulus calculated for scenario 37

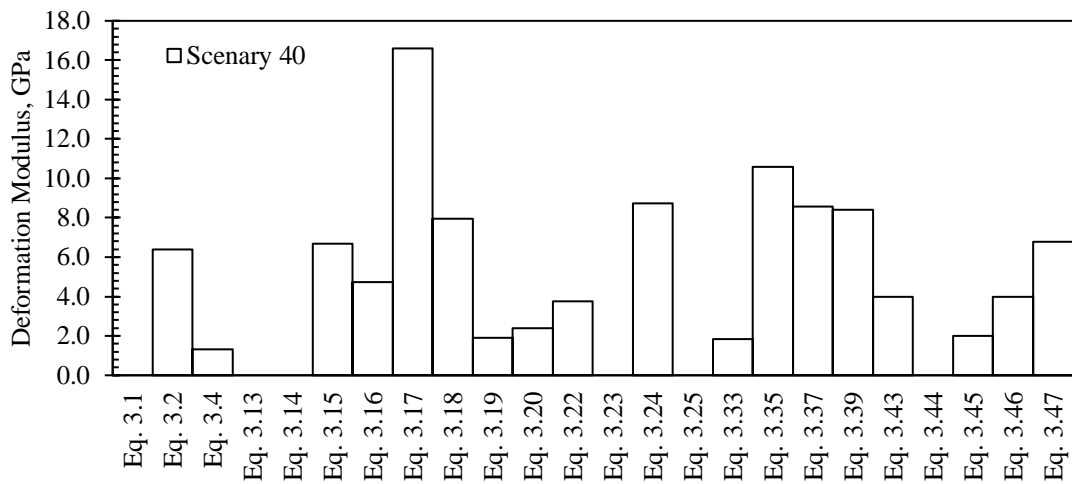
Source: elaborated by the author.

**Figure B.42** - Deformation modulus calculated for scenario 38

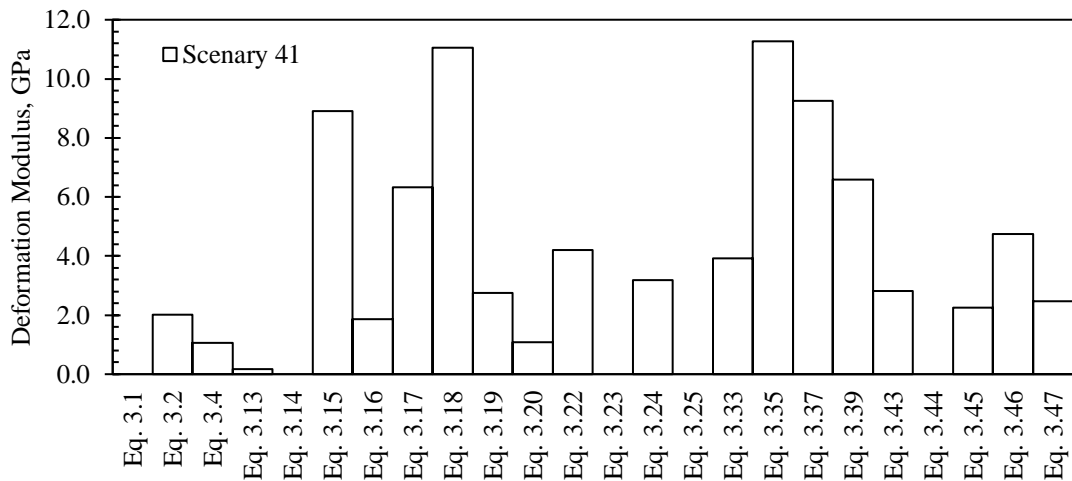
Source: elaborated by the author.

**Figure B.43** - Deformation modulus calculated for scenario 39

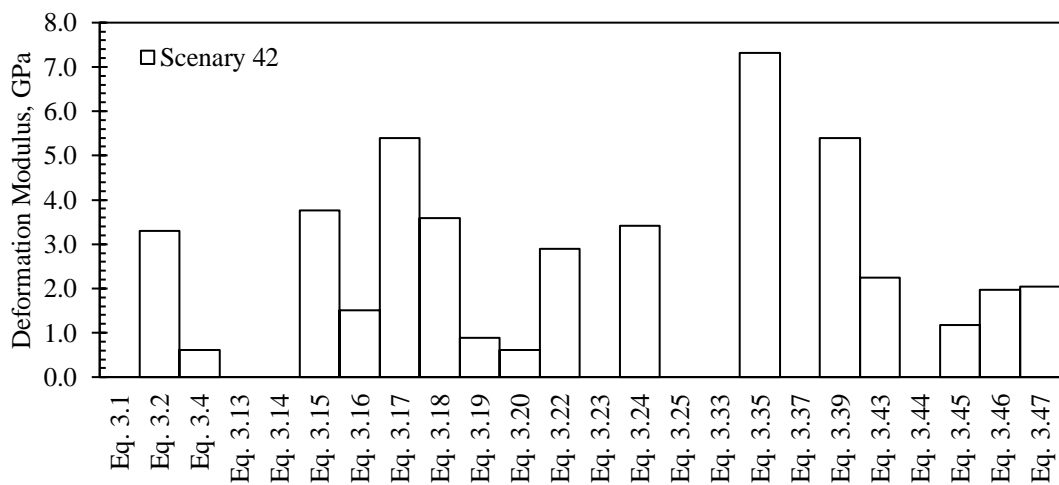
Source: elaborated by the author.

**Figure B.44** - Deformation modulus calculated for scenario 40

Source: elaborated by the author.

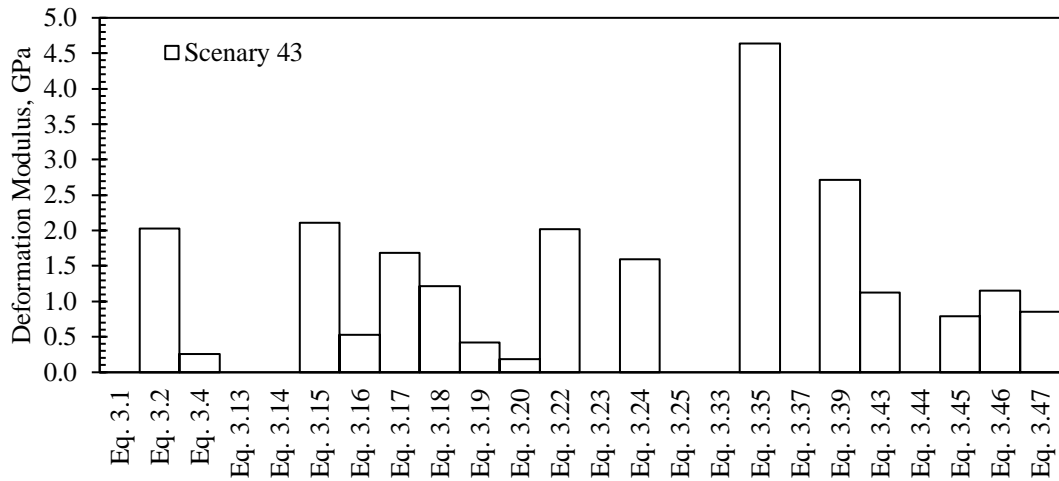
**Figure B.45** - Deformation modulus calculated for scenario 41

Source: elaborated by the author.

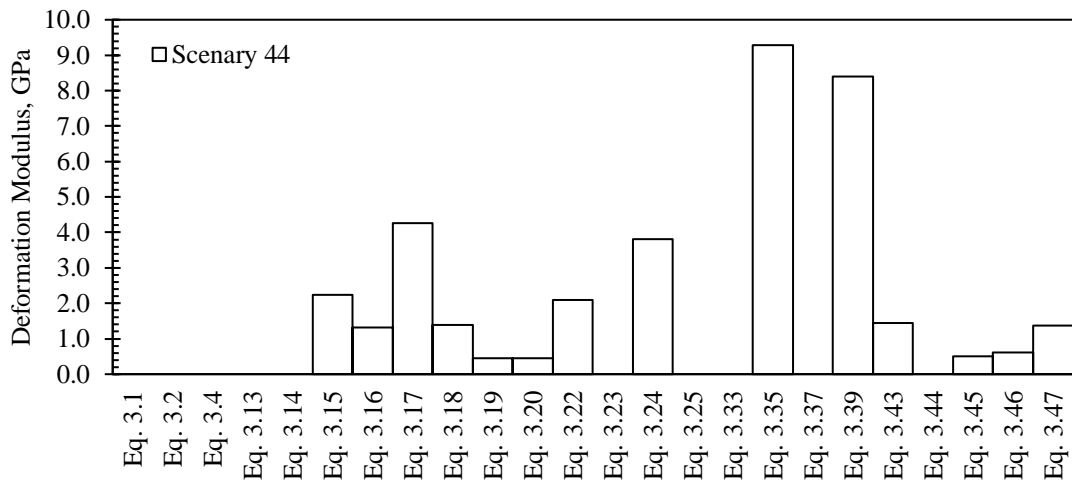
**Figure B.46** - Deformation modulus calculated for scenario 42

Source: elaborated by the author.

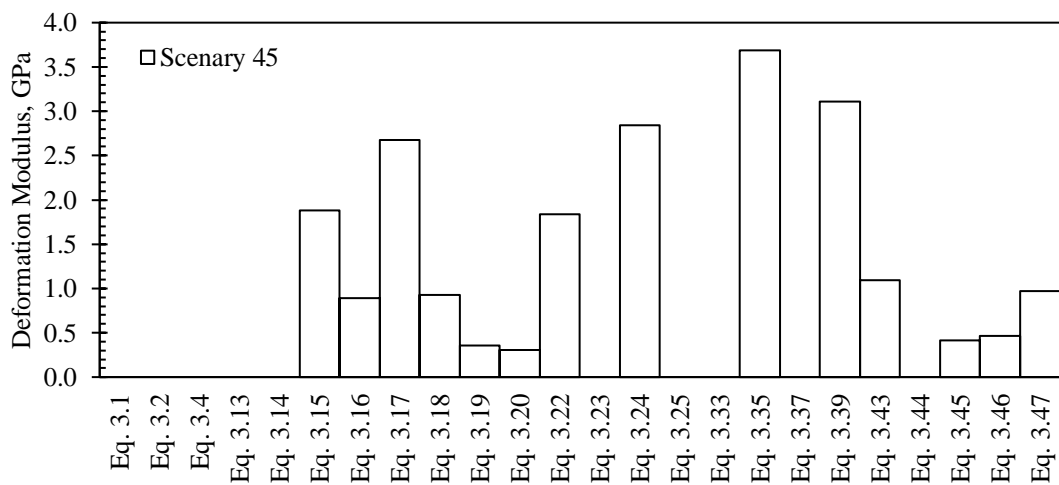


**Figure B.47** - Deformation modulus calculated for scenario 43

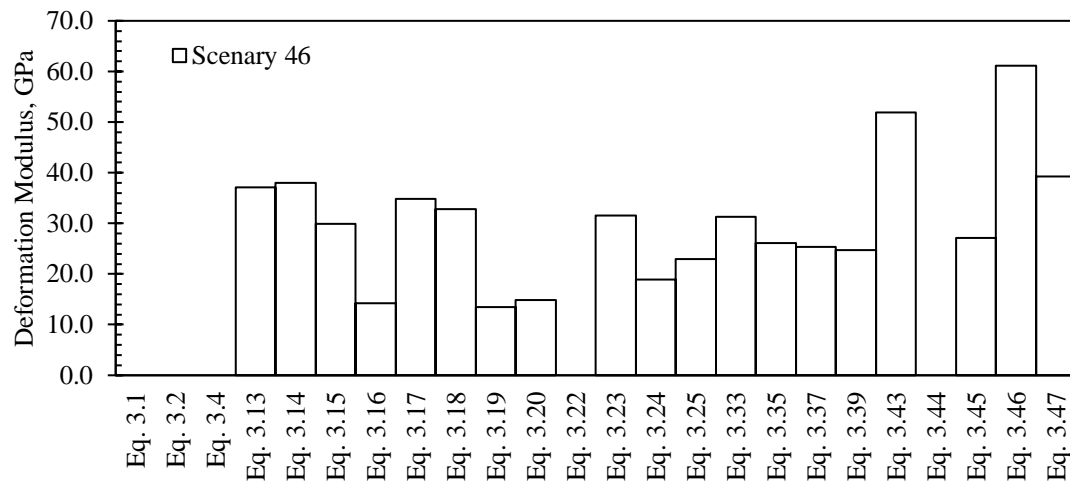
Source: elaborated by the author.

**Figure B.48** - Deformation modulus calculated for scenario 44

Source: elaborated by the author.

**Figure B.49** - Deformation modulus calculated for scenario 45

Source: elaborated by the author.

**Figure B.50** - Deformation modulus calculated for scenario 46

Source: elaborated by the author.

**APPENDIX C - MEAN AND MEDIAN RELATIVE ERROR – DEFORMATION MODULUS**

**Table C.5 - Mean relative error (MRE) of SG-I group in percentage (from deformation modulus estimated data)**

Eq.\ Scenarios	S1	S4	S6	S13	S15	S18	S19	S20	S22	S27	S29	S32	S35	S36	S38	S43	S44	S45
Eq. 3.1	N/A	N/A	N/A	N/A	N/A	N/A	N/A	N/A	N/A	N/A	N/A	N/A	N/A	N/A	N/A	N/A	N/A	N/A
Eq. 3.2	20.6	20.2	-39.7	-35.9	-29.2	52.1	-57.2	-40.3	-23.1	19.3	57.2	-79.0	91.7	36.3	-10.9	-10.9	39.0	N/A
Eq. 3.4	-89.2	-80.4	-91.7	-68.2	-74.0	-62.0	-94.6	-83.8	-82.4	-85.0	-15.1	-95.0	-47.8	-82.8	-87.8	-87.8	-82.5	N/A
Eq. 3.13	N/A	N/A	N/A	N/A	N/A	N/A	N/A	N/A	N/A	N/A	N/A	N/A	N/A	N/A	N/A	N/A	N/A	N/A
Eq. 3.14	N/A	N/A	N/A	N/A	N/A	N/A	N/A	N/A	N/A	N/A	N/A	N/A	N/A	N/A	N/A	N/A	N/A	N/A
Eq. 3.15	92.3	19.8	97.3	16.6	122.1	49.9	236.1	104.7	47.1	29.1	25.6	149.7	21.7	98.4	103.5	103.5	45.0	-16.7
Eq. 3.16	-50.2	-50.4	-67.9	-74.9	-88.1	-49.5	-94.9	-83.3	-71.5	-72.2	-38.5	-89.9	-46.5	-52.2	-57.1	-57.1	-63.4	-51.0
Eq. 3.17	76.0	75.5	15.4	-11.9	-70.8	71.8	-91.6	-46.1	-0.8	-16.6	116.0	-63.8	73.2	64.7	53.9	53.9	15.7	58.6
Eq. 3.18	71.1	6.6	106.0	-0.5	-35.6	10.9	-57.8	26.4	20.2	-36.5	7.3	146.5	-24.8	54.5	100.9	100.9	-16.5	-48.6
Eq. 3.19	-56.1	-72.7	-50.8	-73.9	-61.3	-68.2	-46.4	-58.8	-67.6	-75.4	-71.8	-39.9	-75.5	-57.1	-51.0	-51.0	-71.3	-83.2
Eq. 3.20	-80.8	-80.9	-86.3	-90.5	-96.0	-81.8	-98.2	-94.2	-89.4	-90.5	-76.7	-95.9	-81.3	-82.5	-82.5	-82.5	-87.4	-82.9
Eq. 3.22	55.9	-2.9	39.3	-3.1	120.4	33.3	205.8	92.2	25.2	26.1	4.4	86.8	14.3	72.7	52.3	52.3	38.3	-21.8
Eq. 3.23	N/A	N/A	N/A	N/A	N/A	N/A	N/A	N/A	N/A	N/A	N/A	N/A	N/A	N/A	N/A	N/A	N/A	N/A
Eq. 3.24	18.3	17.9	-32.1	-38.8	-54.2	33.5	-75.9	-51.8	-28.7	-11.4	50.0	-77.6	54.8	23.0	-5.1	-5.1	9.1	41.7
Eq. 3.25	N/A	N/A	N/A	N/A	N/A	N/A	N/A	N/A	N/A	N/A	N/A	N/A	N/A	N/A	N/A	N/A	N/A	N/A
Eq. 3.33	N/A	N/A	N/A	N/A	N/A	N/A	N/A	N/A	N/A	N/A	N/A	N/A	N/A	N/A	N/A	N/A	N/A	N/A
Eq. 3.35	23.7	109.2	149.3	173.9	391.4	92.7	299.8	225.3	240.6	228.5	96.0	237.6	168.2	91.1	41.0	41.0	218.5	245.4
Eq. 3.37	N/A	N/A	N/A	N/A	N/A	N/A	N/A	N/A	N/A	N/A	N/A	N/A	N/A	N/A	N/A	N/A	N/A	N/A
Eq. 3.39	-27.7	43.1	26.3	60.2	82.7	29.0	-1.4	72.8	117.4	104.1	49.0	46.7	84.0	19.2	24.1	24.1	86.3	212.4
Eq. 3.43	-8.9	1.4	-24.7	23.6	-52.5	-13.0	-53.8	-0.2	-5.6	12.5	-37.5	-36.2	-48.1	-30.8	33.4	33.4	-22.9	-46.3
Eq. 3.44	N/A	N/A	N/A	N/A	N/A	N/A	N/A	N/A	N/A	N/A	N/A	N/A	N/A	N/A	N/A	N/A	N/A	N/A
Eq. 3.45	-32.4	-37.7	-28.0	1.5	-39.1	-49.0	7.7	-17.2	-38.1	-24.5	-70.4	-26.2	-72.7	-56.9	-47.2	-47.2	-45.5	-81.3
Eq. 3.46	12.9	19.7	35.3	126.3	-33.0	-22.5	12.7	25.8	5.9	23.3	-58.3	23.3	-66.7	-43.6	-15.9	-15.9	-21.1	-77.2
Eq. 3.47	-25.5	11.5	-47.8	-4.4	-82.8	-27.3	-90.4	-71.5	-49.2	-30.9	-37.3	-87.0	-44.4	-54.0	-51.7	-51.7	-41.2	-49.1

The MRE was calculate using the following relation:  $MRE(\%) = 100 * (x_i + \bar{x})/\bar{x}$ , where  $x_i$  is the  $i^{th}$  estimated value and  $\bar{x}$  is the mean value.

N/A = Not Available (i.e., out of correlation range).

Source: Author (2018).

**Table C.6 - Mean relative error (MRE) of SG-II group in percentage (from deformation modulus estimated data)**

Eq.\ Scenarios	S2	S3	S5	S11	S17	S21	S24	S25	S26	S28	S34	S37	S39	S40	S41	S44
<b>Eq. 3.1</b>	N/A	N/A	N/A	31.7	N/A	N/A	N/A	N/A	N/A	-35.7	N/A	N/A	N/A	N/A	N/A	N/A
<b>Eq. 3.2</b>	-21.2	28.4	-16.4	31.7	-64.4	-33.8	-54.2	11.0	26.8	46.2	7.1	-26.3	-45.2	7.7	-55.3	14.5
<b>Eq. 3.4</b>	-84.0	-81.3	-83.9	-5.0	-83.8	-53.8	-68.0	-82.7	-39.8	56.6	-62.3	-85.1	-91.1	-77.8	-76.4	-78.8
<b>Eq. 3.13</b>	N/A	N/A	N/A	9.7	-22.9	N/A	N/A	N/A	N/A	N/A	N/A	N/A	N/A	N/A	-96.0	N/A
<b>Eq. 3.14</b>	N/A	N/A	N/A	-39.2	-100.0	N/A	N/A	N/A	N/A	N/A	N/A	N/A	N/A	N/A	N/A	N/A
<b>Eq. 3.15</b>	42.3	9.6	32.1	70.4	108.3	48.2	102.0	-7.3	-18.3	10.9	31.5	69.3	114.9	12.9	96.9	30.4
<b>Eq. 3.16</b>	-62.0	-0.6	-59.7	-55.3	-64.3	-64.8	-61.3	-34.9	-38.9	-22.1	-37.2	-50.2	-53.7	-20.3	-58.8	-47.6
<b>Eq. 3.17</b>	36.1	247.9	44.5	45.3	18.7	26.7	33.5	133.8	119.1	179.8	125.5	77.1	59.8	180.8	39.7	87.4
<b>Eq. 3.18</b>	40.4	31.9	30.4	113.6	160.3	54.8	147.5	1.5	-19.3	15.9	44.0	95.9	163.4	34.4	144.3	24.7
<b>Eq. 3.19</b>	-65.7	-68.4	-68.2	-43.3	-33.2	-63.0	-39.7	-76.0	-80.3	-72.3	-66.0	-53.8	-35.8	-68.0	-39.1	-69.2
<b>Eq. 3.20</b>	-84.5	-48.1	-83.5	-70.6	-77.9	-85.0	-78.6	-70.9	-75.0	-66.8	-71.9	-76.0	-74.4	-59.5	-75.9	-79.0
<b>Eq. 3.22</b>	6.4	-40.3	-1.2	N/A	-8.8	4.6	2.5	-38.4	-38.9	-21.7	-12.6	2.1	9.0	-36.3	-7.1	0.3
<b>Eq. 3.23</b>	N/A	N/A	N/A	2.2	N/A	N/A	N/A	N/A	N/A	N/A	N/A	N/A	N/A	N/A	N/A	N/A
<b>Eq. 3.24</b>	-16.0	80.7	-10.9	-27.9	-40.8	-25.4	-31.9	32.2	35.2	64.7	27.5	-4.6	-18.5	47.4	-29.7	18.7
<b>Eq. 3.25</b>	N/A	N/A	N/A	N/A	N/A	N/A	N/A	N/A	N/A	N/A	N/A	N/A	N/A	N/A	N/A	N/A
<b>Eq. 3.33</b>	N/A	N/A	N/A	-44.5	-78.4	N/A	N/A	N/A	N/A	N/A	N/A	N/A	N/A	-69.2	-13.4	N/A
<b>Eq. 3.35</b>	179.8	-30.6	170.2	69.9	115.0	179.9	107.1	58.6	69.2	25.8	101.1	65.4	103.4	78.7	149.1	153.9
<b>Eq. 3.37</b>	N/A	N/A	N/A	39.0	73.1	N/A	N/A	N/A	N/A	N/A	N/A	N/A	N/A	44.6	104.2	N/A
<b>Eq. 3.39</b>	66.3	-35.9	67.9	13.8	55.7	89.0	40.2	78.2	65.1	1.6	73.9	97.3	19.0	41.9	45.7	87.1
<b>Eq. 3.43</b>	-13.1	-22.6	-8.6	-37.6	21.2	-7.7	-15.7	N/A	17.9	-39.6	-20.7	N/A	-39.4	-32.8	-37.7	-22.1
<b>Eq. 3.44</b>	N/A	N/A	N/A	N/A	N/A	N/A	N/A	20.1	N/A	N/A	N/A	19.8	N/A	N/A	N/A	N/A
<b>Eq. 3.45</b>	-33.6	-69.3	-34.1	-58.2	-25.5	-42.2	-46.1	-56.8	-56.5	-72.6	-67.0	-59.3	-52.9	-66.5	-50.0	-59.2
<b>Eq. 3.46</b>	30.5	-38.3	32.3	-6.8	79.1	11.0	10.6	-8.4	-10.8	-55.3	-43.6	-27.0	-9.5	-32.7	4.8	-31.8
<b>Eq. 3.47</b>	-21.7	36.7	-11.0	-38.9	-31.4	-38.6	-47.8	40.0	44.5	-15.4	-29.3	-44.3	-49.1	14.7	-45.4	-29.2

The MRE was calculate using the following relation:  $MRE(\%) = 100 * (x_i + \bar{x})/\bar{x}$ , where  $x_i$  is the  $i^{\text{th}}$  estimated value and  $\bar{x}$  is the mean value.

N/A = Not Available (i.e., out of correlation range).

Source: Author (2018).

**Table C.7** - Mean relative error (MRE) of SG-III group in percentage (from deformation modulus estimated data)

Eq.\ Scenarios	S7	S8	S9	S10	S12	S14	S16	S23	S30	S31	S33	S46
<b>Eq. 3.1</b>	-54.8	-64.4	-16.3	53.4	33.2	-76.2	-42.9	N/A	-88.5	-59.0	23.1	N/A
<b>Eq. 3.2</b>	-54.8	-64.4	-16.3	53.4	33.2	-16.9	-42.9	-59.8	-13.0	-45.1	23.1	N/A
<b>Eq. 3.4</b>	-63.7	-74.5	-36.0	24.2	-4.5	-14.7	-59.1	-72.0	-14.5	-36.0	6.2	N/A
<b>Eq. 3.13</b>	59.5	74.6	58.3	35.4	-21.1	N/A	63.0	53.6	-45.1	68.8	-97.4	22.6
<b>Eq. 3.14</b>	43.5	79.5	65.4	24.7	-36.9	N/A	62.5	38.2	-100.0	42.0	N/A	25.5
<b>Eq. 3.15</b>	42.2	41.9	37.2	16.3	-15.9	-16.6	28.5	36.9	48.3	67.2	27.5	-1.4
<b>Eq. 3.16</b>	-88.8	-77.7	-57.7	-60.9	-53.3	-41.2	-70.4	-44.2	-12.7	-29.6	-37.9	-53.1
<b>Eq. 3.17</b>	-66.4	-46.5	-7.1	15.2	45.9	108.1	-21.4	67.2	190.0	117.2	110.6	15.1
<b>Eq. 3.18</b>	75.0	54.0	39.6	42.3	5.0	-2.0	48.8	68.5	85.4	107.9	58.2	8.5
<b>Eq. 3.19</b>	-47.3	-34.8	-32.3	-56.1	-70.5	-76.8	-46.1	-49.3	-52.4	-40.3	-60.5	-55.5
<b>Eq. 3.20</b>	-91.2	-76.3	-51.2	-68.6	-66.5	-70.9	-72.0	-56.3	-45.9	-48.0	-63.7	-51.1
<b>Eq. 3.22</b>	N/A	N/A	N/A	N/A	N/A	-51.3	N/A	N/A	-35.1	N/A	-39.9	N/A
<b>Eq. 3.23</b>	30.0	49.3	39.4	10.1	-33.9	N/A	34.9	25.1	N/A	39.5	N/A	4.1
<b>Eq. 3.24</b>	-83.2	-70.7	-46.4	-42.3	-27.7	10.6	-59.1	-16.6	44.6	7.8	6.0	-37.7
<b>Eq. 3.25</b>	22.9	-35.7	-25.3	1.8	N/A	N/A	-18.0	26.5	N/A	N/A	N/A	-24.2
<b>Eq. 3.33</b>	185.4	46.0	-9.4	36.6	14.7	-5.6	49.0	15.3	-74.7	-96.2	-2.0	3.2
<b>Eq. 3.35</b>	138.3	21.8	-22.8	26.9	10.3	64.6	26.1	30.1	56.3	19.5	76.5	-13.8
<b>Eq. 3.37</b>	131.8	19.0	-27.4	14.6	-1.4	37.6	19.4	13.0	26.3	-4.2	47.3	-16.4
<b>Eq. 3.39</b>	26.6	-0.2	-31.4	0.8	8.4	25.2	4.5	6.6	58.5	-11.5	50.8	-18.3
<b>Eq. 3.43</b>	-61.0	57.5	53.1	-34.7	54.5	4.2	29.3	-23.9	N/A	-32.7	-24.5	71.2
<b>Eq. 3.44</b>	N/A	N/A	N/A	N/A	N/A	N/A	N/A	N/A	11.2	N/A	N/A	N/A
<b>Eq. 3.45</b>	-61.0	0.2	-12.3	-63.3	-31.4	-38.6	-23.5	-59.9	-59.2	-60.4	-65.4	-10.3
<b>Eq. 3.46</b>	-1.4	144.8	103.3	-3.2	93.1	57.6	110.3	3.0	-9.0	-6.4	-26.0	102.0
<b>Eq. 3.47</b>	-81.4	-43.2	-4.2	-26.5	64.8	102.8	-20.8	-2.0	29.7	-0.7	-12.0	29.7

The MRE was calculate using the following relation:  $MRE(\%) = 100 * (x_i + \bar{x})/\bar{x}$ , where  $x_i$  is the  $i^{\text{th}}$  estimated value and  $\bar{x}$  is the mean value.

N/A = Not Available (i.e., out of correlation range).

Source: Author (2018).

**Table C.8 - Median relative error (MdRE) of SG-I group in percentage (from deformation modulus estimated data)**

Eq.\ Scenarios	S1	S4	S6	S13	S15	S18	S19	S20	S22	S27	S29	S32	S35	S36	S38	S43	S44	S45
<b>Eq. 3.1</b>	N/A	N/A	N/A	N/A	N/A	N/A	N/A	N/A	N/A	N/A	N/A	N/A	N/A	N/A	N/A	N/A	N/A	N/A
<b>Eq. 3.2</b>	18.2	10.2	-18.2	-33.4	30.6	53.8	-3.8	-16.2	-10.3	38.7	66.1	-66.1	193.2	44.6	-3.2	71.2	N/A	N/A
<b>Eq. 3.4</b>	-89.4	-82.0	-88.7	-67.0	-52.1	-61.6	-87.9	-77.2	-79.4	-82.5	-10.3	-91.9	-20.2	-81.8	-86.7	-78.5	N/A	N/A
<b>Eq. 3.13</b>	N/A	N/A	N/A	N/A	N/A	N/A	N/A	N/A	N/A	N/A	N/A	N/A	N/A	N/A	N/A	N/A	N/A	N/A
<b>Eq. 3.14</b>	N/A	N/A	N/A	N/A	N/A	N/A	N/A	N/A	N/A	N/A	N/A	N/A	N/A	N/A	N/A	N/A	N/A	N/A
<b>Eq. 3.15</b>	88.5	9.9	167.7	21.1	309.8	51.5	655.1	187.4	71.8	50.1	32.7	303.1	86.2	110.5	121.2	78.7	58.4	82.6
<b>Eq. 3.16</b>	-51.2	-54.5	-56.4	-73.9	-78.0	-49.0	-88.5	-76.6	-66.7	-67.7	-35.0	-83.7	-18.1	-49.2	-53.3	-55.0	-6.8	-13.6
<b>Eq. 3.17</b>	72.5	60.9	56.6	-8.4	-46.2	73.6	-81.0	-24.3	15.8	-3.0	128.3	-41.5	164.9	74.8	67.2	42.6	201.6	159.4
<b>Eq. 3.18</b>	67.7	-2.3	179.6	3.4	18.8	12.1	-5.1	77.4	40.3	-26.2	13.3	297.9	15.0	64.0	118.4	2.9	-2.2	-10.2
<b>Eq. 3.19</b>	-57.0	-74.9	-33.2	-72.9	-28.5	-67.8	20.4	-42.2	-62.2	-71.4	-70.2	-2.9	-62.5	-54.5	-46.7	-64.7	-68.1	-65.2
<b>Eq. 3.20</b>	-81.2	-82.5	-81.4	-90.1	-92.6	-81.6	-96.0	-91.8	-87.6	-89.0	-75.4	-93.3	-71.5	-81.4	-81.0	-84.4	-67.5	-70.6
<b>Eq. 3.22</b>	52.9	-10.9	89.0	0.6	306.7	34.7	586.9	169.9	46.2	46.6	10.3	201.5	74.9	83.2	65.5	70.3	48.8	78.4
<b>Eq. 3.23</b>	N/A	N/A	N/A	N/A	N/A	N/A	N/A	N/A	N/A	N/A	N/A	N/A	N/A	N/A	N/A	N/A	N/A	N/A
<b>Eq. 3.24</b>	15.9	8.1	-7.8	-36.4	-15.6	34.9	-45.9	-32.4	-16.7	3.0	58.4	-63.9	136.7	30.5	3.2	34.4	169.5	175.5
<b>Eq. 3.25</b>	N/A	N/A	N/A	N/A	N/A	N/A	N/A	N/A	N/A	N/A	N/A	N/A	N/A	N/A	N/A	N/A	N/A	N/A
<b>Eq. 3.33</b>	N/A	N/A	N/A	N/A	N/A	N/A	N/A	N/A	N/A	N/A	N/A	N/A	N/A	N/A	N/A	N/A	N/A	N/A
<b>Eq. 3.35</b>	21.3	91.8	238.4	184.5	806.5	94.8	798.1	356.6	297.6	281.9	107.0	445.0	310.3	102.8	53.3	292.4	556.9	257.2
<b>Eq. 3.37</b>	N/A	N/A	N/A	N/A	N/A	N/A	N/A	N/A	N/A	N/A	N/A	N/A	N/A	N/A	N/A	N/A	N/A	N/A
<b>Eq. 3.39</b>	-29.1	31.2	71.4	66.4	237.0	30.4	121.5	142.6	153.7	137.3	57.4	136.9	181.5	26.5	34.9	129.5	494.1	201.3
<b>Eq. 3.43</b>	-10.7	-7.0	2.2	28.4	-12.3	-12.1	3.8	40.1	10.3	30.8	-34.0	2.9	-20.6	-26.5	45.0	-5.0	2.2	6.1
<b>Eq. 3.44</b>	N/A	N/A	N/A	N/A	N/A	N/A	N/A	N/A	N/A	N/A	N/A	N/A	N/A	N/A	N/A	N/A	N/A	N/A
<b>Eq. 3.45</b>	-33.8	-42.9	-2.2	5.4	12.3	-48.4	142.1	16.2	-27.7	-12.2	-68.8	19.1	-58.2	-54.3	-42.7	-32.8	-64.4	-59.9
<b>Eq. 3.46</b>	10.7	9.7	83.6	135.1	23.6	-21.7	153.3	76.5	23.7	43.3	-55.9	99.1	-49.1	-40.1	-8.6	-2.9	-56.7	-54.8
<b>Eq. 3.47</b>	-26.9	2.3	-29.1	-0.6	-68.3	-26.5	-78.3	-60.0	-40.7	-19.7	-33.7	-79.1	-15.0	-51.2	-47.5	-27.6	-3.2	-6.1

The MdRE was calculate using the following relation:  $MdRE(\%) = 100 * (x_i + x_{med})/x_{med}$ , where  $x_i$  is the  $i^{th}$  estimated value and  $x_{med}$  is the median value.

N/A = Not Available (i.e., out of correlation range).

Source: Author (2018).

**Table C.9** - Median relative error (MdRE) of SG-II group in percentage (from deformation modulus estimated data)

Eq.\ Scenarios	S2	S3	S5	S11	S17	S21	S24	S25	S26	S28	S34	S37	S39	S40	S41	S44
<b>Eq. 3.1</b>	N/A	N/A	N/A	38.7	N/A	N/A	N/A	N/A	N/A	-24.0	N/A	N/A	N/A	N/A	N/A	N/A
<b>Eq. 3.2</b>	-7.8	75.0	-7.4	38.7	-53.0	-20.7	-39.9	14.3	48.4	72.7	28.5	-12.8	-24.8	14.9	-36.4	28.5
<b>Eq. 3.4</b>	-81.3	-74.6	-82.2	0.0	-78.6	-44.6	-58.1	-82.2	-29.5	85.1	-54.8	-82.4	-87.8	-76.3	-66.4	-76.2
<b>Eq. 3.13</b>	N/A	N/A	N/A	15.5	1.7	N/A	N/A	N/A	N/A	N/A	N/A	N/A	N/A	N/A	-94.3	N/A
<b>Eq. 3.14</b>	N/A	N/A	N/A	-36.0	-100.0	N/A	N/A	N/A	N/A	N/A	N/A	N/A	N/A	N/A	N/A	N/A
<b>Eq. 3.15</b>	66.5	49.4	46.3	79.4	174.9	77.6	165.0	-4.5	-4.4	31.1	57.8	100.3	195.0	20.5	179.9	46.4
<b>Eq. 3.16</b>	-55.6	35.5	-55.4	-52.9	-52.8	-57.8	-49.2	-32.9	-28.5	-8.0	-24.6	-41.1	-36.4	-14.9	-41.4	-41.1
<b>Eq. 3.17</b>	59.3	374.0	60.0	53.0	56.7	51.9	75.1	140.7	156.3	230.6	170.6	109.5	119.3	199.6	98.7	110.3
<b>Eq. 3.18</b>	64.3	79.7	44.5	124.9	243.6	85.5	224.8	4.5	-5.6	36.9	72.8	131.7	261.5	43.3	247.3	40.0
<b>Eq. 3.19</b>	-59.9	-57.0	-64.8	-40.3	-11.8	-55.7	-20.8	-75.3	-77.0	-67.3	-59.2	-45.3	-11.9	-65.9	-13.4	-65.4
<b>Eq. 3.20</b>	-81.9	-29.3	-81.8	-69.1	-70.8	-82.0	-72.0	-70.0	-70.8	-60.8	-66.3	-71.6	-64.9	-56.8	-65.7	-76.5
<b>Eq. 3.22</b>	24.5	-18.7	9.5	N/A	20.4	25.4	34.5	-36.6	-28.5	-7.5	4.8	20.8	49.7	-32.1	32.0	12.6
<b>Eq. 3.23</b>	N/A	N/A	N/A	7.6	N/A	N/A	N/A	N/A	N/A	N/A	N/A	N/A	N/A	N/A	N/A	N/A
<b>Eq. 3.24</b>	-1.7	146.3	-1.3	-24.1	-21.9	-10.6	-10.7	36.1	58.2	94.6	53.0	12.8	11.9	57.3	0.0	33.2
<b>Eq. 3.25</b>	N/A	N/A	N/A	N/A	N/A	N/A	N/A	N/A	N/A	N/A	N/A	N/A	N/A	N/A	N/A	N/A
<b>Eq. 3.33</b>	N/A	N/A	N/A	-41.6	-71.6	N/A	N/A	N/A	N/A	N/A	N/A	N/A	N/A	-67.1	23.1	N/A
<b>Eq. 3.35</b>	227.4	-5.5	199.3	78.9	183.7	235.4	171.7	63.3	97.9	48.6	141.3	95.6	179.3	90.7	254.2	185.1
<b>Eq. 3.37</b>	N/A	N/A	N/A	46.4	128.4	N/A	N/A	N/A	N/A	N/A	N/A	N/A	N/A	54.3	190.3	N/A
<b>Eq. 3.39</b>	94.6	-12.6	86.0	19.8	105.5	126.5	83.9	83.6	93.2	20.1	108.7	133.4	63.3	51.3	107.1	110.0
<b>Eq. 3.43</b>	1.7	5.5	1.3	-34.3	60.0	10.6	10.7	N/A	37.9	-28.7	-4.8	N/A	-16.7	-28.3	-11.4	-12.6
<b>Eq. 3.44</b>	N/A	N/A	N/A	N/A	N/A	N/A	N/A	23.7	N/A	N/A	N/A	41.8	N/A	N/A	N/A	N/A
<b>Eq. 3.45</b>	-22.2	-58.1	-27.0	-56.0	-1.7	-30.7	-29.3	-55.5	-49.1	-67.7	-60.5	-51.9	-35.3	-64.2	-28.9	-54.2
<b>Eq. 3.46</b>	52.7	-15.9	46.5	-1.8	136.4	33.0	45.1	-5.7	4.4	-47.2	-32.3	-13.7	24.2	-28.1	48.9	-23.4
<b>Eq. 3.47</b>	-8.4	86.3	-1.4	-35.6	-9.5	-26.4	-31.6	44.2	69.1	0.0	-15.1	-34.1	-30.2	22.3	-22.4	-20.5

The MdRE was calculate using the following relation:  $MdRE(\%) = 100 * (x_i + x_{med})/x_{med}$ , where  $x_i$  is the  $i^{th}$  estimated value and  $x_{med}$  is the median value.

N/A = Not Available (i.e., out of correlation range).

Source: Author (2018).

**Table C.10** - Median relative error (MdRE) of SG-III group in percentage (from deformation modulus estimated data)

Eq.\ Scenarios	S7	S8	S9	S10	S12	S14	S16	S23	S30	S31	S33	S46
<b>Eq. 3.1</b>	-40.3	-64.4	-2.3	36.5	35.1	-74.8	-38.8	N/A	-86.8	-56.2	20.7	N/A
<b>Eq. 3.2</b>	-40.3	-64.4	-2.3	36.5	35.1	-12.0	-38.8	-62.3	-0.3	-41.4	20.7	N/A
<b>Eq. 3.4</b>	-52.0	-74.5	-25.3	10.5	-3.2	-9.6	-56.1	-73.7	-2.0	-31.6	4.1	N/A
<b>Eq. 3.13</b>	110.8	74.6	84.8	20.5	-20.1	N/A	74.8	44.0	-37.1	80.3	-97.5	24.4
<b>Eq. 3.14</b>	89.7	79.6	93.1	11.0	-36.0	N/A	74.3	29.6	-100.0	51.7	N/A	27.3
<b>Eq. 3.15</b>	87.9	41.9	60.1	3.5	-14.7	-11.6	37.7	28.4	69.9	78.6	25.0	0.0
<b>Eq. 3.16</b>	-85.2	-77.7	-50.6	-65.2	-52.7	-37.7	-68.3	-47.6	0.0	-24.8	-39.1	-52.4
<b>Eq. 3.17</b>	-55.6	-46.5	8.4	2.5	47.9	120.5	-15.8	56.8	232.2	132.0	106.4	16.7
<b>Eq. 3.18</b>	131.3	54.0	63.0	26.7	6.4	3.8	59.5	58.1	112.4	122.0	55.1	10.0
<b>Eq. 3.19</b>	-30.4	-34.8	-21.0	-61.0	-70.1	-75.4	-42.2	-52.4	-45.5	-36.2	-61.3	-54.9
<b>Eq. 3.20</b>	-88.4	-76.3	-43.1	-72.0	-66.1	-69.2	-70.0	-59.0	-38.1	-44.5	-64.4	-50.4
<b>Eq. 3.22</b>	N/A	N/A	N/A	N/A	N/A	-48.5	N/A	N/A	-25.6	N/A	-41.0	N/A
<b>Eq. 3.23</b>	71.8	49.3	62.8	-2.0	-33.0	N/A	44.7	17.4	N/A	48.9	N/A	5.6
<b>Eq. 3.24</b>	-77.8	-70.7	-37.5	-48.7	-26.7	17.2	-56.2	-21.8	65.7	15.1	3.9	-36.8
<b>Eq. 3.25</b>	62.4	-35.7	-12.8	-9.4	N/A	N/A	-12.1	18.6	N/A	N/A	N/A	-23.2
<b>Eq. 3.33</b>	277.3	46.0	5.7	21.6	16.3	0.0	59.8	8.2	-71.0	-95.9	-3.9	4.7
<b>Eq. 3.35</b>	215.0	21.8	-9.9	13.0	11.8	74.4	35.2	22.1	79.0	27.7	73.0	-12.5
<b>Eq. 3.37</b>	206.4	19.0	-15.3	2.0	0.0	45.8	28.0	6.0	44.7	2.3	44.4	-15.2
<b>Eq. 3.39</b>	67.4	-0.2	-20.0	-10.3	9.9	32.6	12.1	0.0	81.5	-5.4	47.8	-17.2
<b>Eq. 3.43</b>	-48.5	57.5	78.6	-41.9	56.6	10.4	38.7	-28.6	N/A	-28.2	-26.0	73.7
<b>Eq. 3.44</b>	N/A	N/A	N/A	N/A	N/A	N/A	N/A	N/A	27.4	N/A	N/A	N/A
<b>Eq. 3.45</b>	-48.4	0.2	2.3	-67.3	-30.5	-34.9	-18.0	-62.4	-53.2	-57.7	-66.1	-9.0
<b>Eq. 3.46</b>	30.4	144.8	137.3	-13.9	95.8	67.0	125.5	-3.4	4.3	0.0	-27.5	104.9
<b>Eq. 3.47</b>	-75.4	-43.2	11.9	-34.5	67.1	114.9	-15.1	-8.1	48.6	6.1	-13.8	31.6

The MdRE was calculate using the following relation:  $MdRE(\%) = 100 * (x_i + x_{med})/x_{med}$ , where  $x_i$  is the  $i^{th}$  estimated value and  $x_{med}$  is the median value.

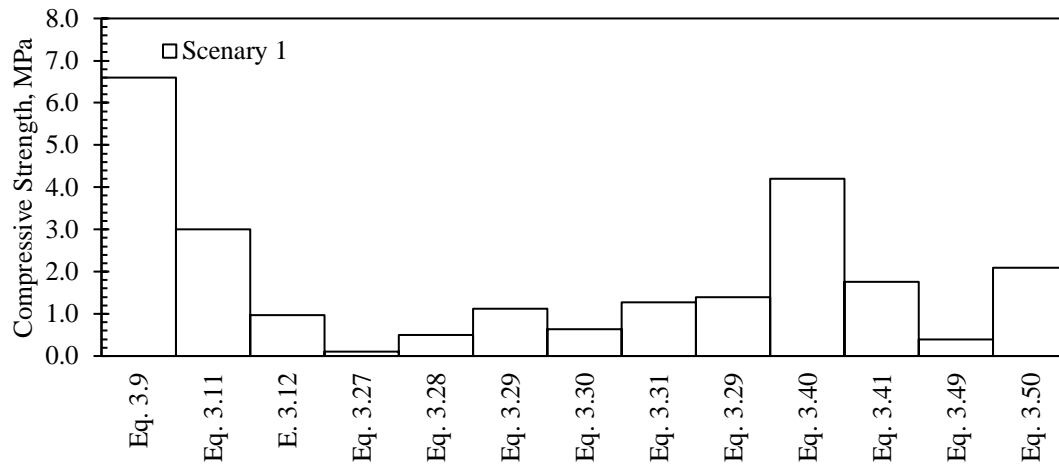
N/A = Not Available (i.e., out of correlation range).

Source: Author (2018).



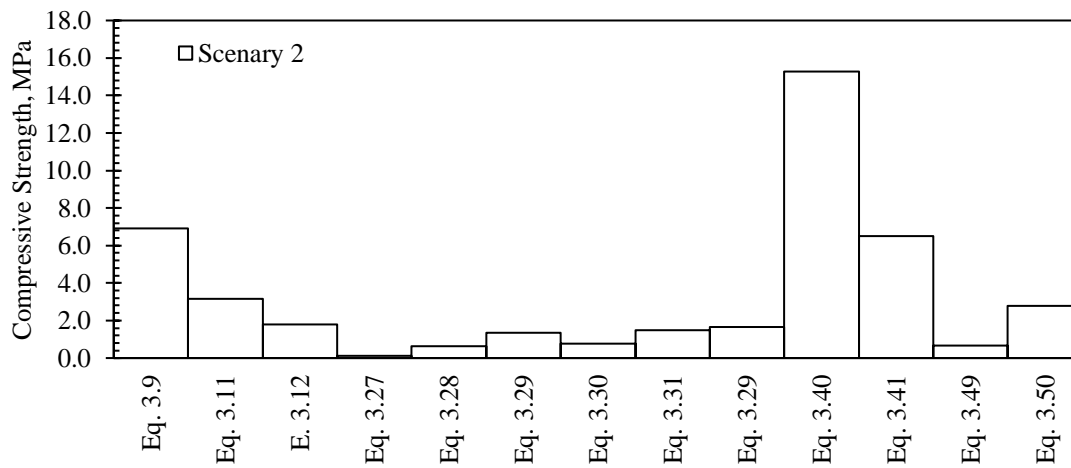
## APPENDIX D - COMPRESSIVE STRENGTH ( $\sigma_{cm}$ ) RESULTS

**Figure D.51** - Compressive strength calculated for scenario 1



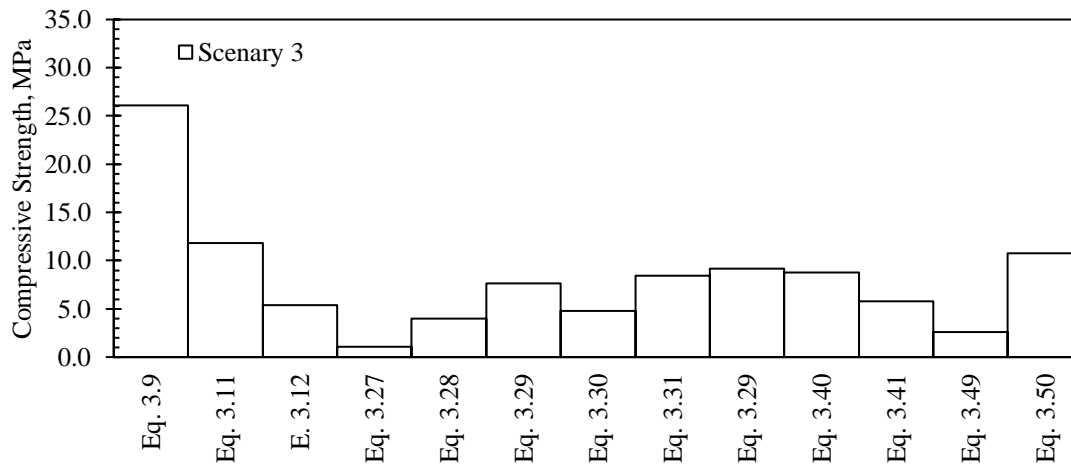
Source: elaborated by the author.

**Figure D.52** - Compressive strength calculated for scenario 2

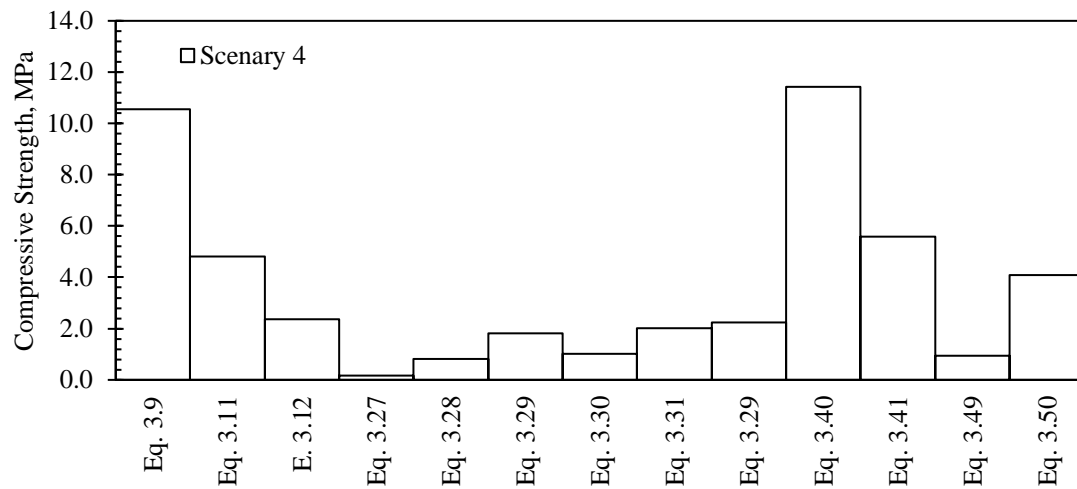


Source: elaborated by the author.

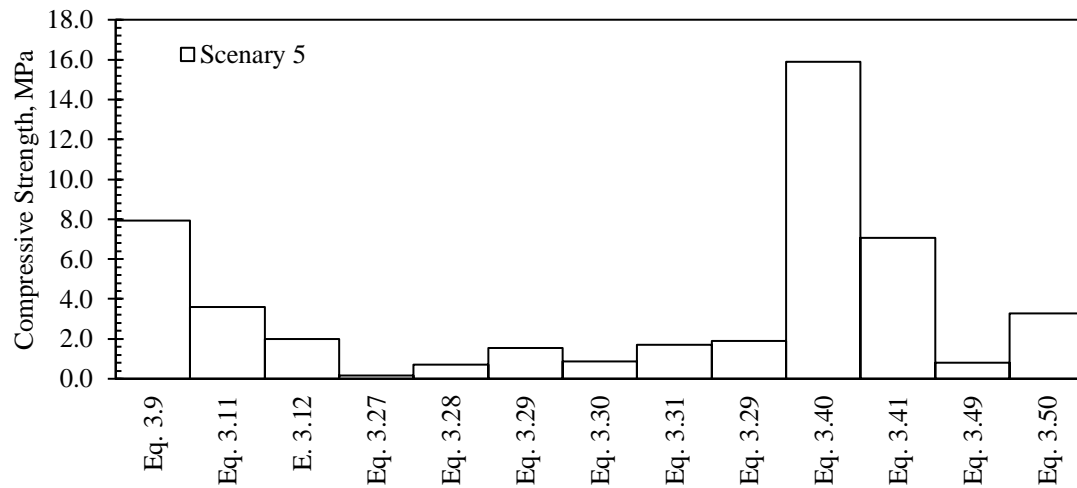
**Figure D.53** - Compressive strength calculated for scenario 3



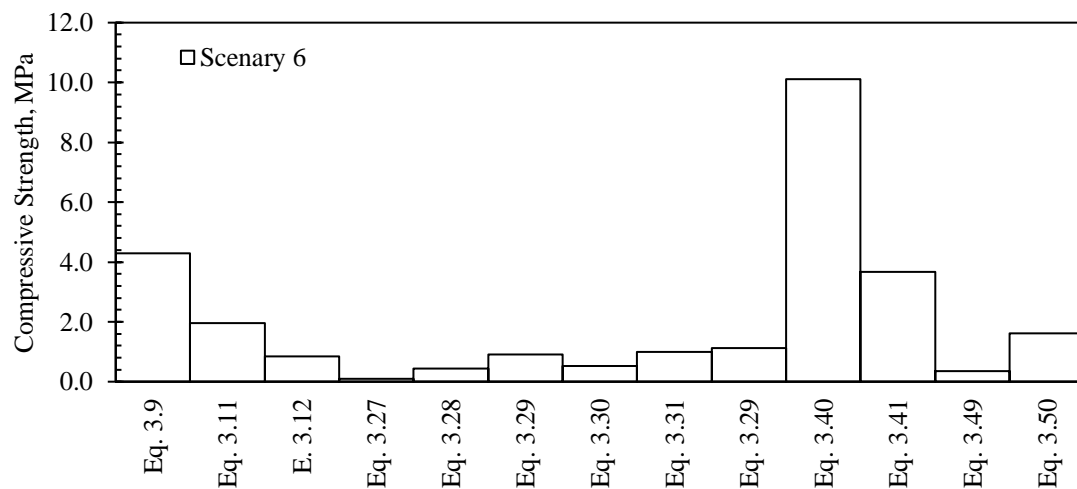
Source: elaborated by the author.

**Figure D.54** - Compressive strength calculated for scenario 4

Source: elaborated by the author.

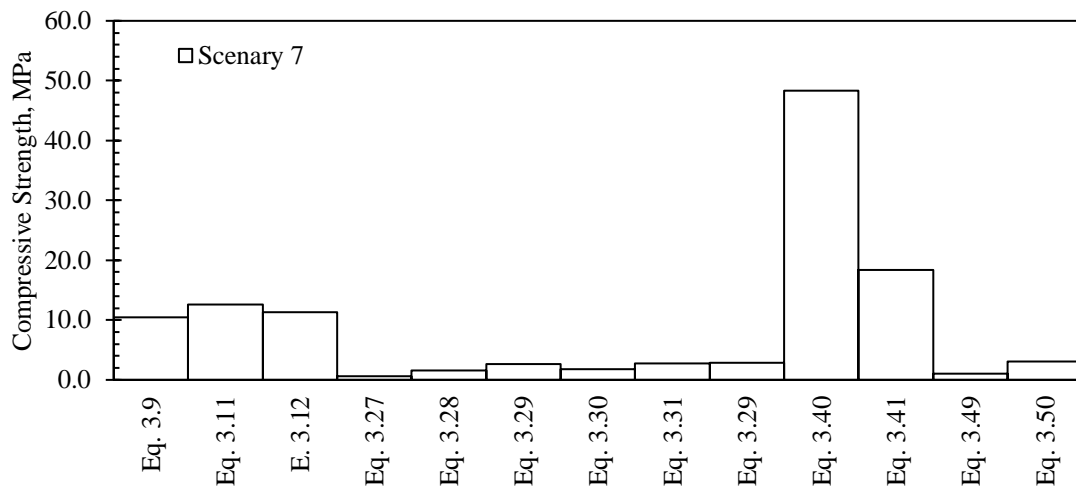
**Figure D.55** - Compressive strength calculated for scenario 5

Source: elaborated by the author.

**Figure D.56** - Compressive strength calculated for scenario 6

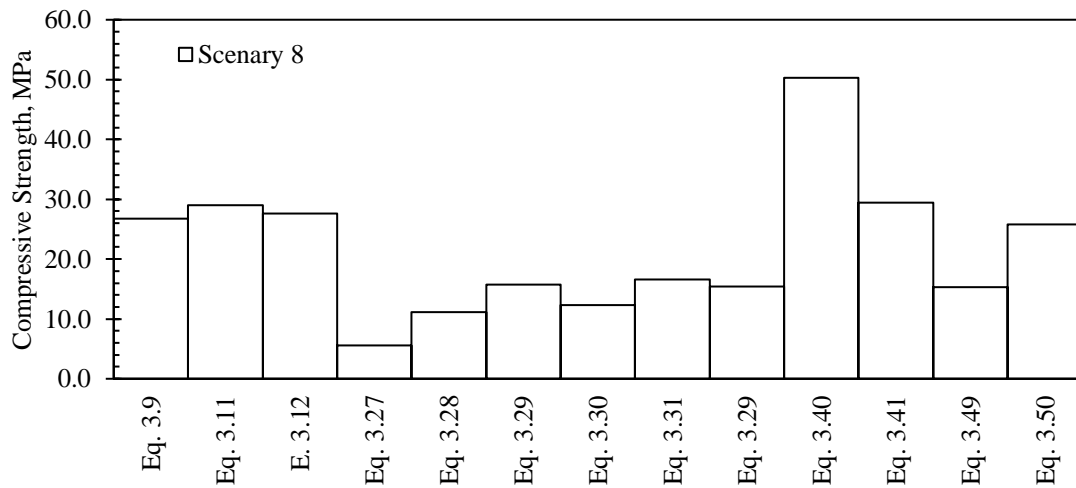
Source: elaborated by the author.

**Figure D.57** - Compressive strength calculated for scenario 7



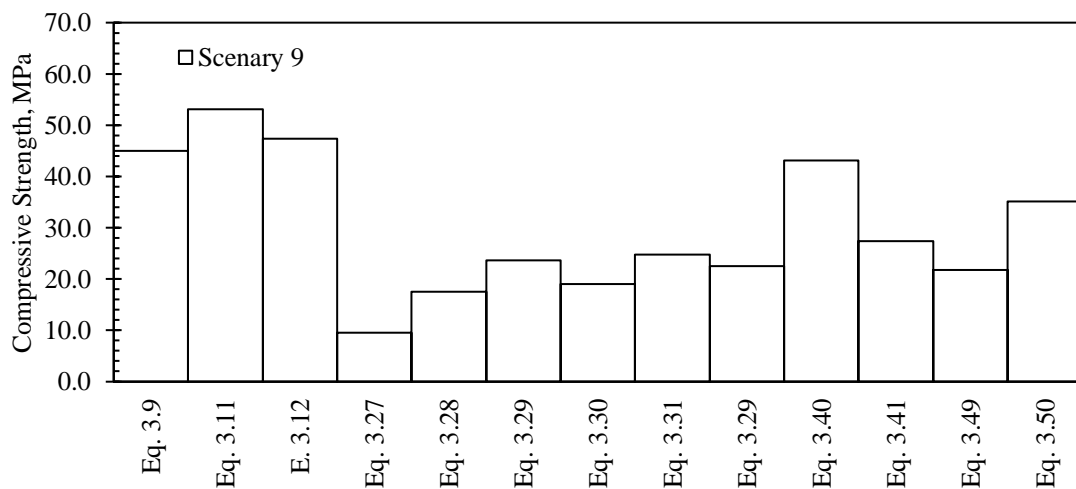
Source: elaborated by the author.

**Figure D.58** - Compressive strength calculated for scenario 8



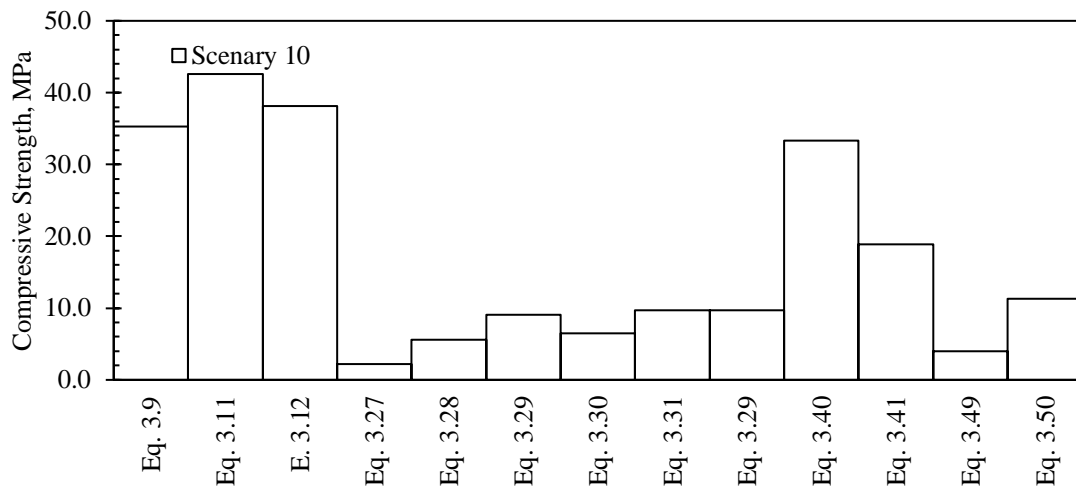
Source: elaborated by the author.

**Figure D.59** - Compressive strength calculated for scenario 9



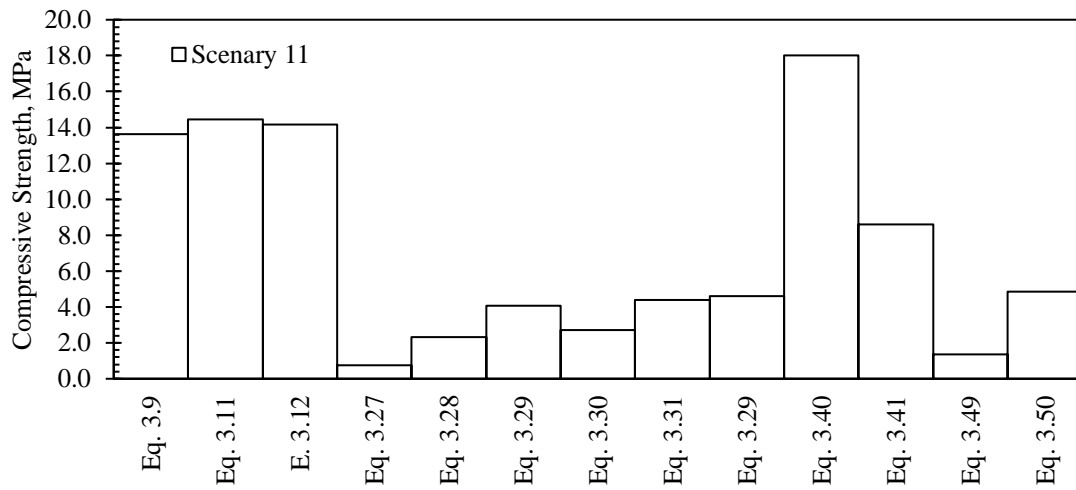
Source: elaborated by the author.

**Figure D.60** - Compressive strength calculated for scenario 10



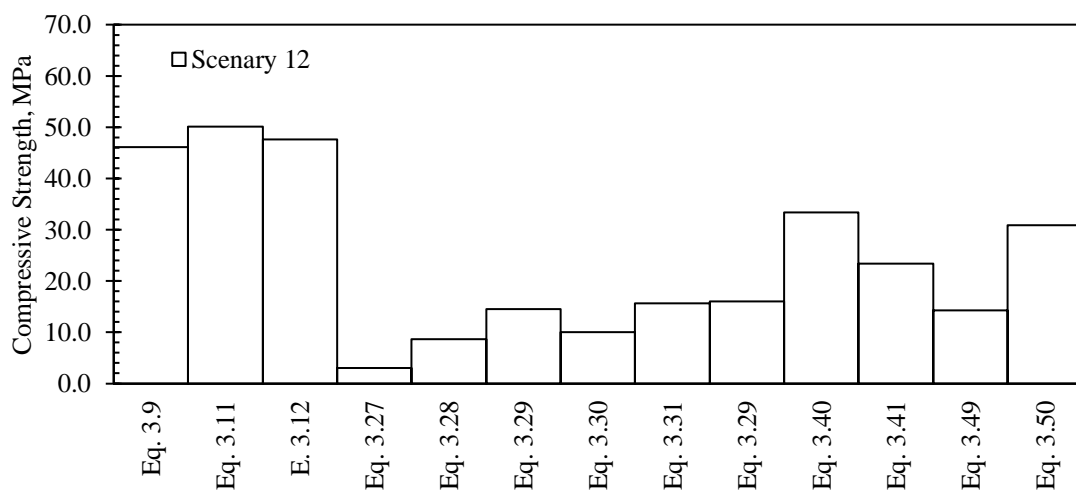
Source: elaborated by the author.

**Figure D.61** - Compressive strength calculated for scenario 11



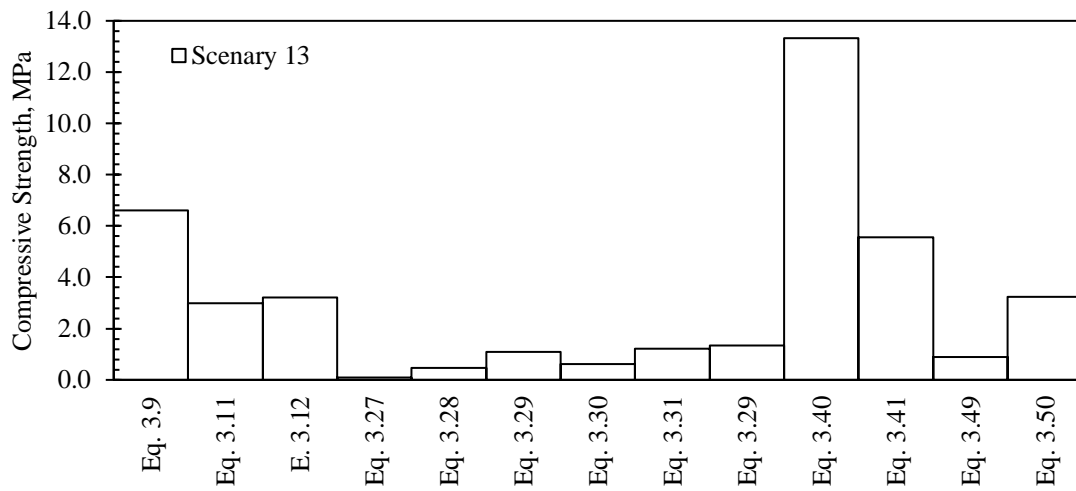
Source: elaborated by the author.

**Figure D.62** - Compressive strength calculated for scenario 12



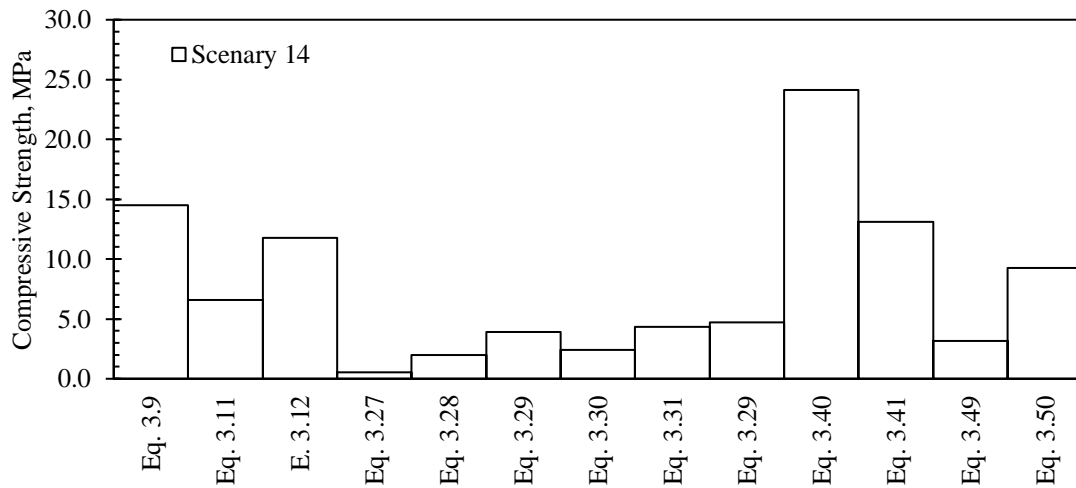
Source: elaborated by the author.

**Figure D.63** - Compressive strength calculated for scenario 13



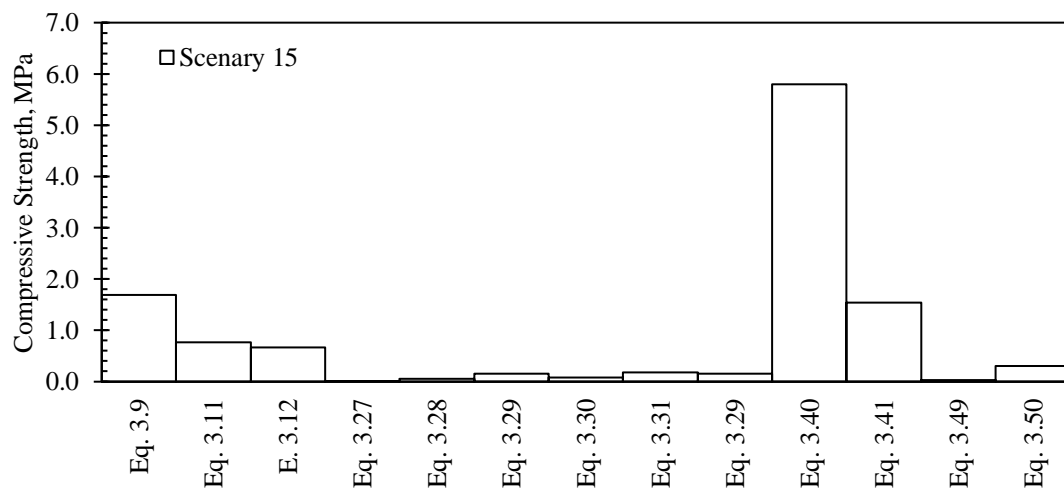
Source: elaborated by the author.

**Figure D.64** - Compressive strength calculated for scenario 14



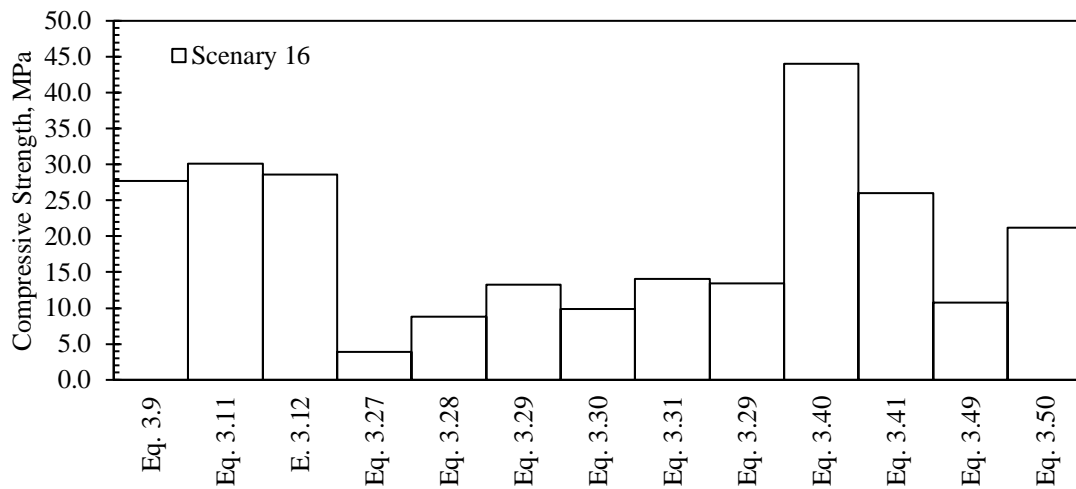
Source: elaborated by the author.

**Figure D.65** - Compressive strength calculated for scenario 15



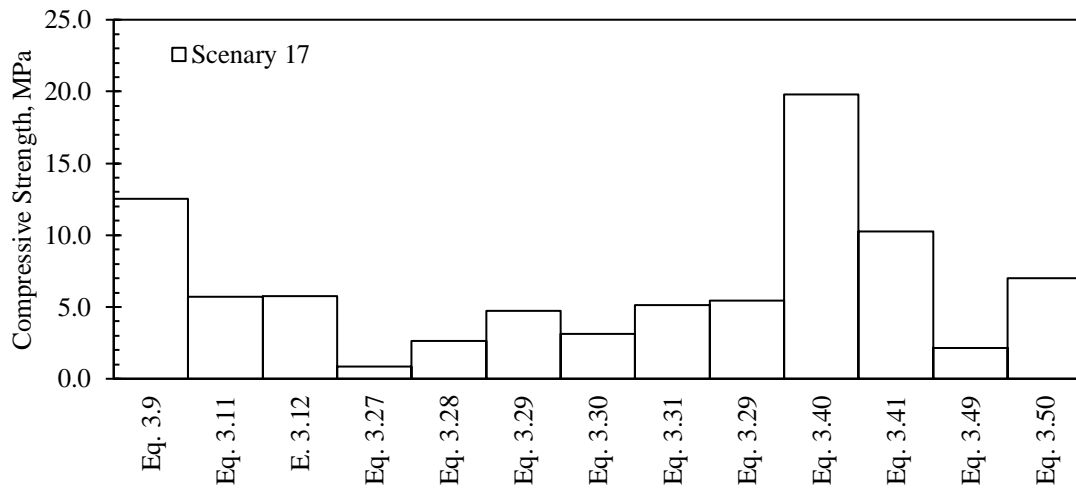
Source: elaborated by the author.

**Figure D.66** - Compressive strength calculated for scenario 16



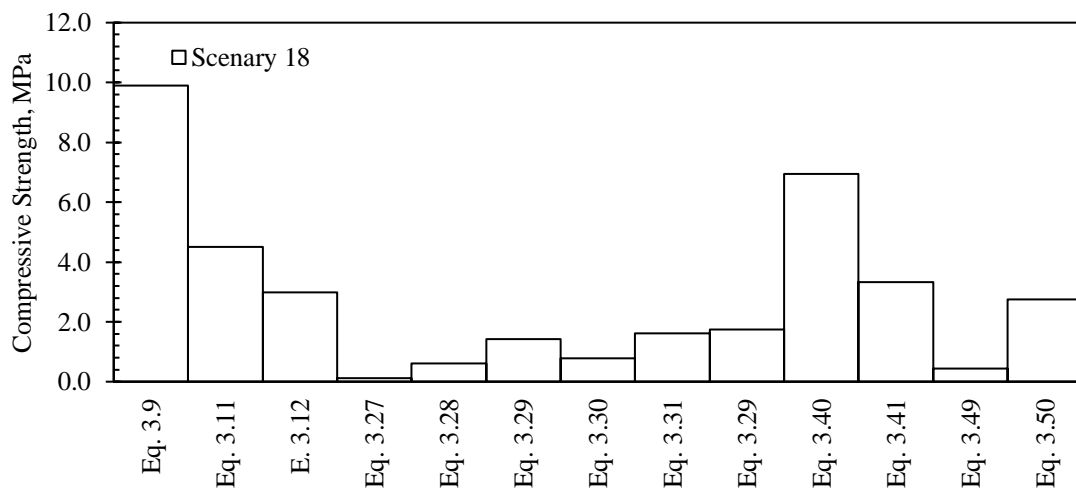
Source: elaborated by the author.

**Figure D.67** - Compressive strength calculated for scenario 17



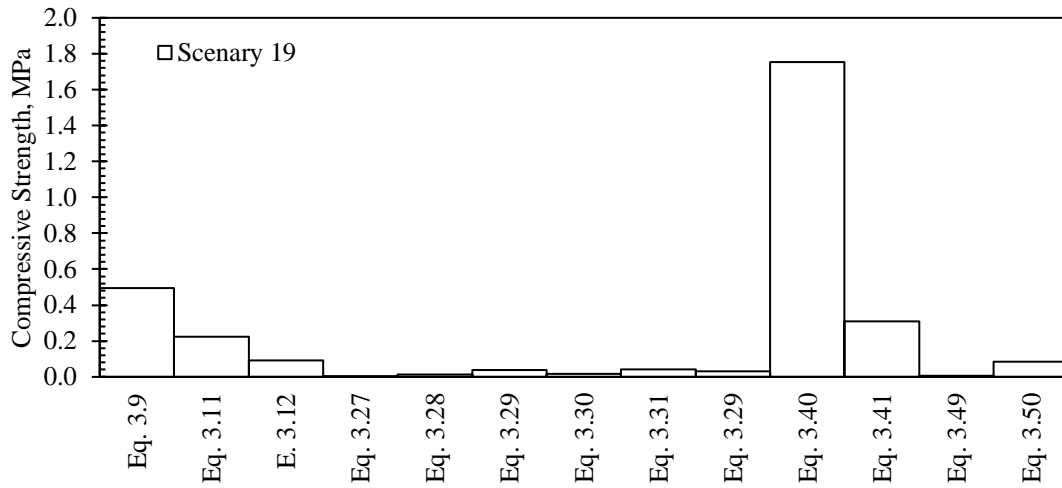
Source: elaborated by the author.

**Figure D.68** - Compressive strength calculated for scenario 18



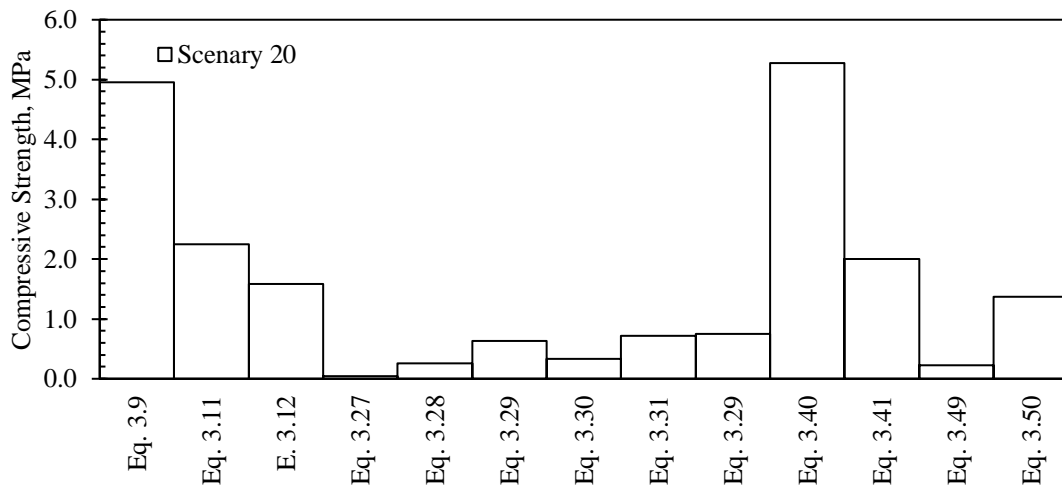
Source: elaborated by the author.

**Figure D.69** - Compressive strength calculated for scenario 19



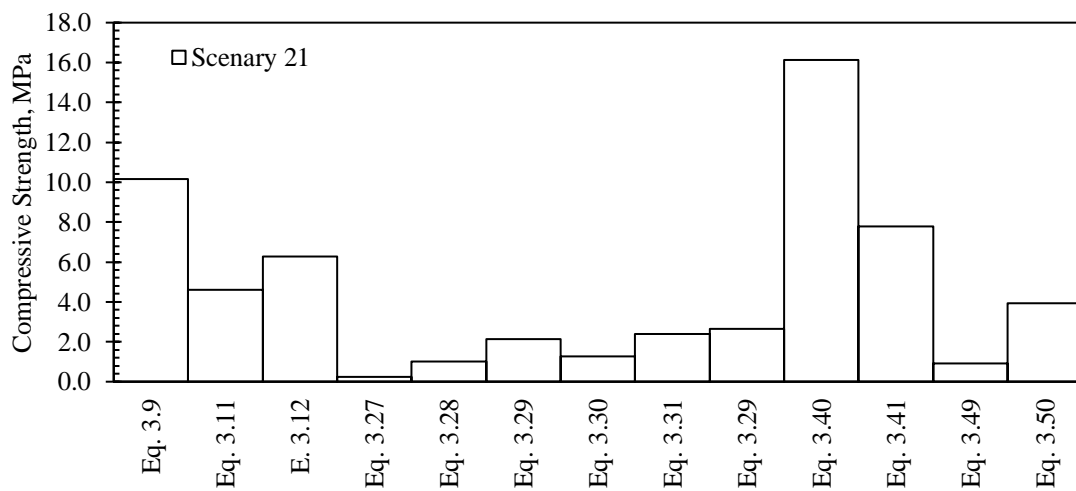
Source: elaborated by the author.

**Figure D.70** - Compressive strength calculated for scenario 20



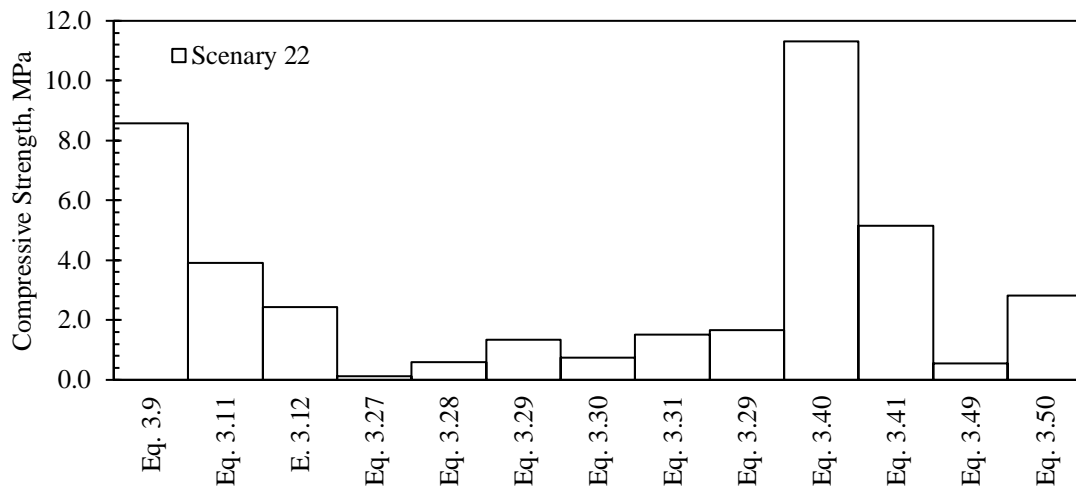
Source: elaborated by the author.

**Figure D.71** - Compressive strength calculated for scenario 21



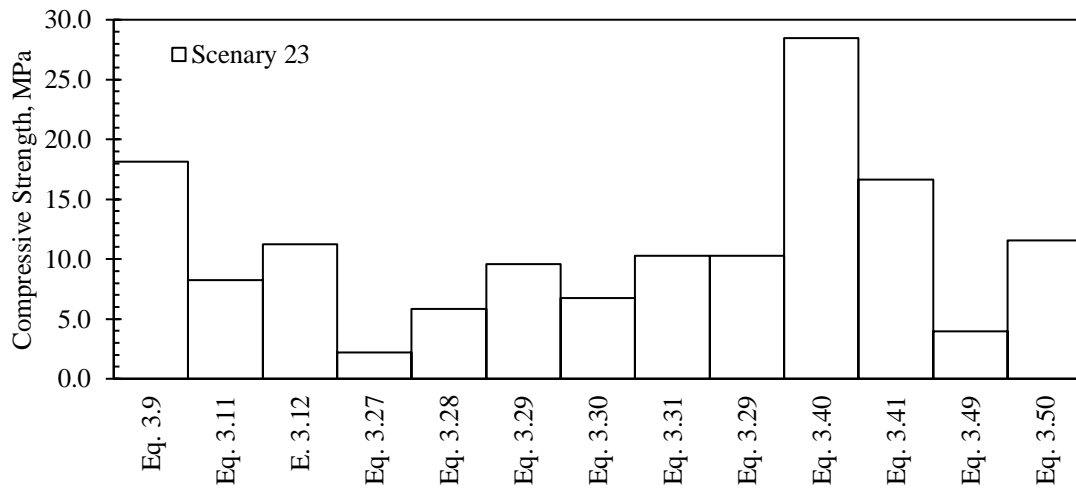
Source: elaborated by the author.

**Figure D.72** - Compressive strength calculated for scenario 22



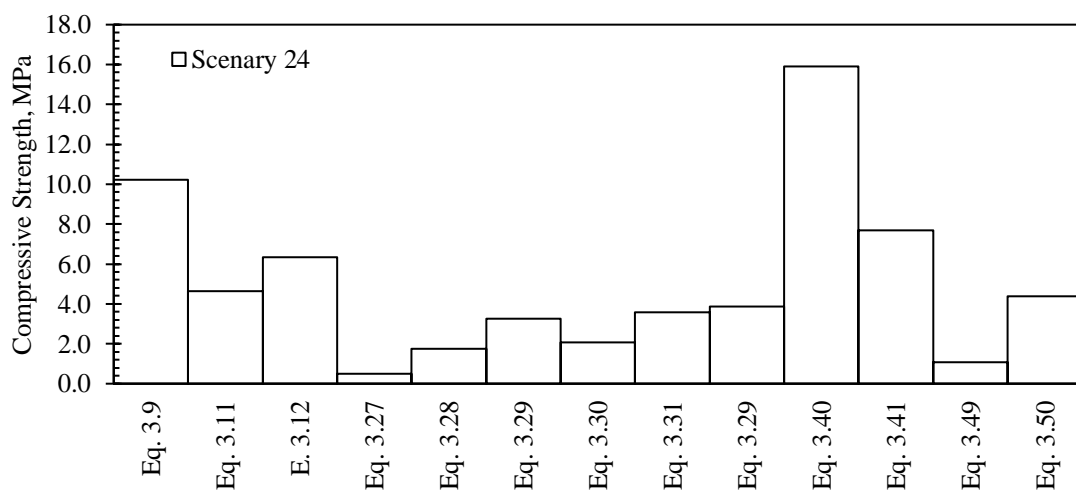
Source: elaborated by the author.

**Figure D.73** - Compressive strength calculated for scenario 23



Source: elaborated by the author.

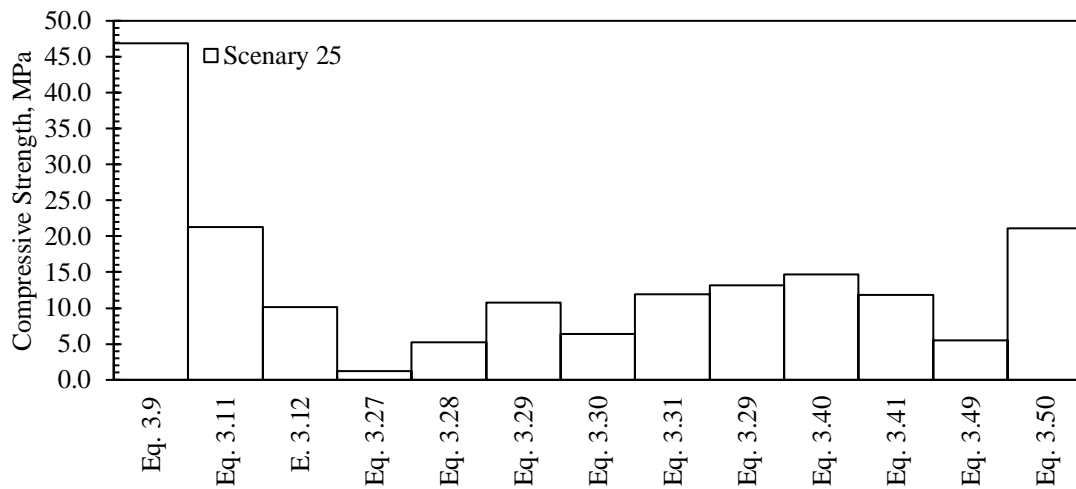
**Figure D.74** - Compressive strength calculated for scenario 24



Source: elaborated by the author.

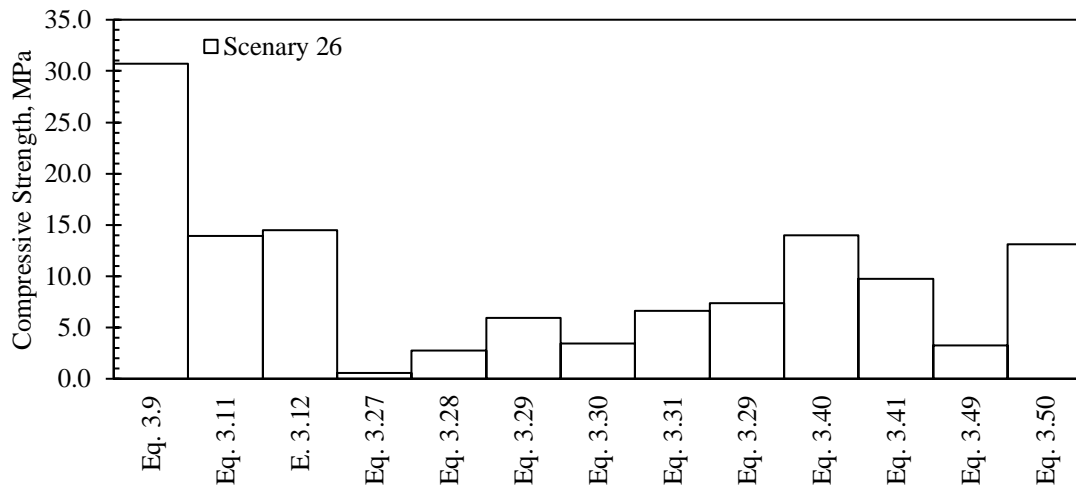


**Figure D.75** - Compressive strength calculated for scenario 25



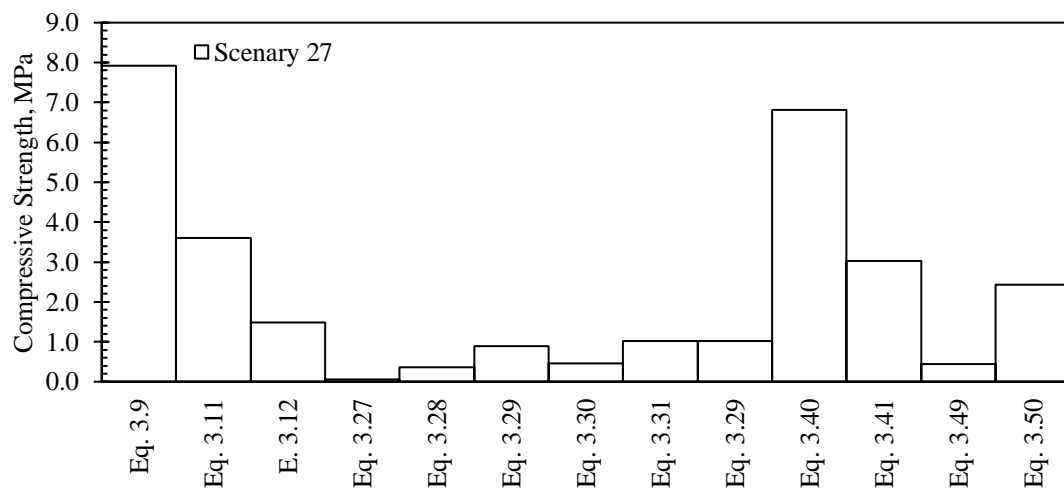
Source: elaborated by the author.

**Figure D.76** - Compressive strength calculated for scenario 26



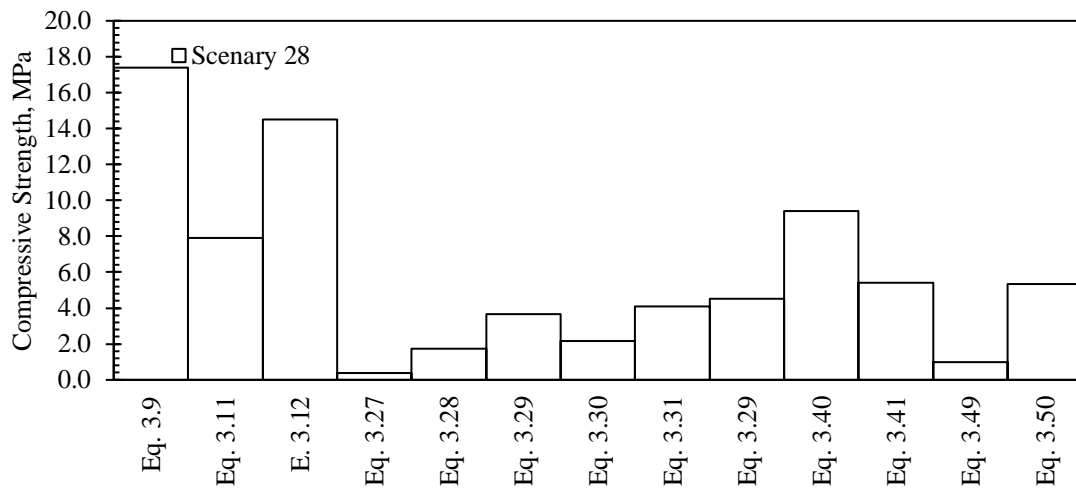
Source: elaborated by the author.

**Figure D.77** - Compressive strength calculated for scenario 27



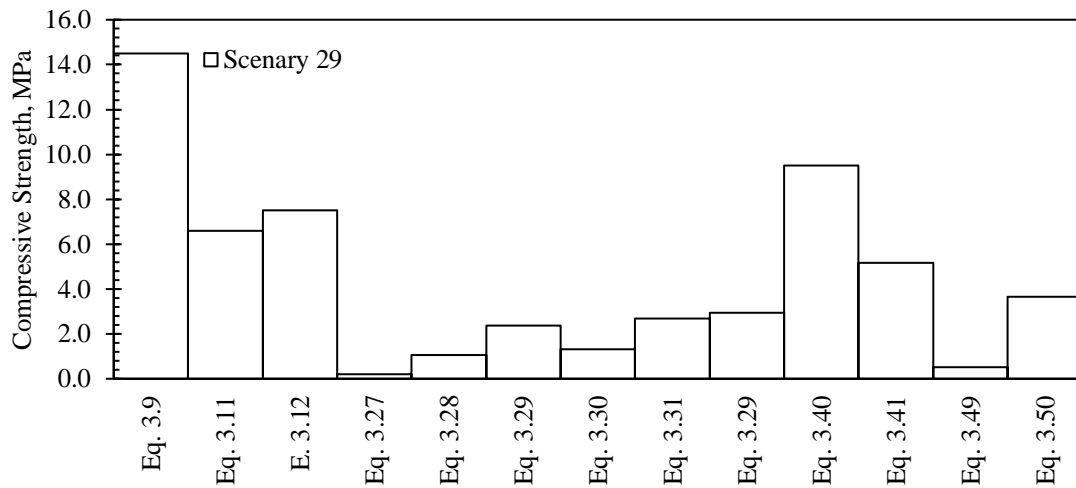
Source: elaborated by the author.

**Figure D.78** - Compressive strength calculated for scenario 28



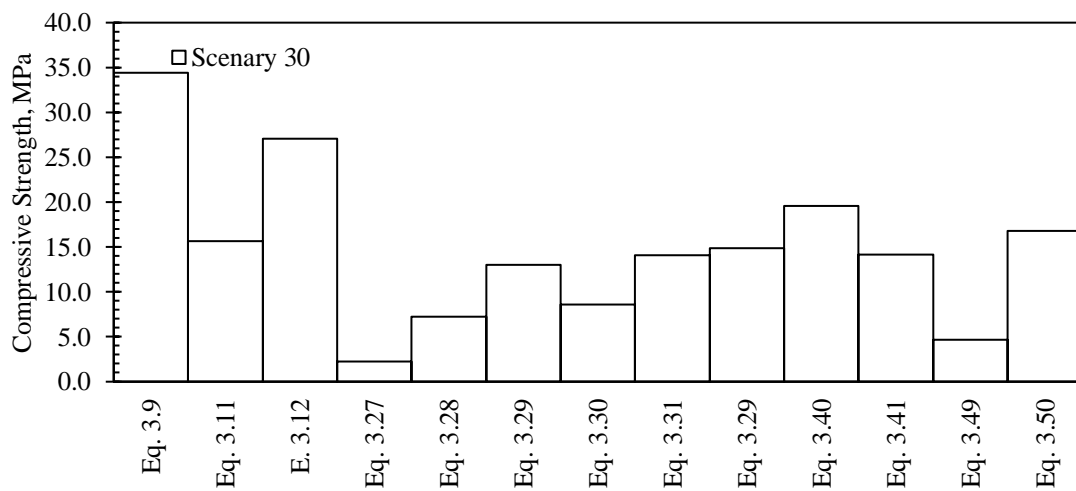
Source: elaborated by the author.

**Figure D.79** - Compressive strength calculated for scenario 29

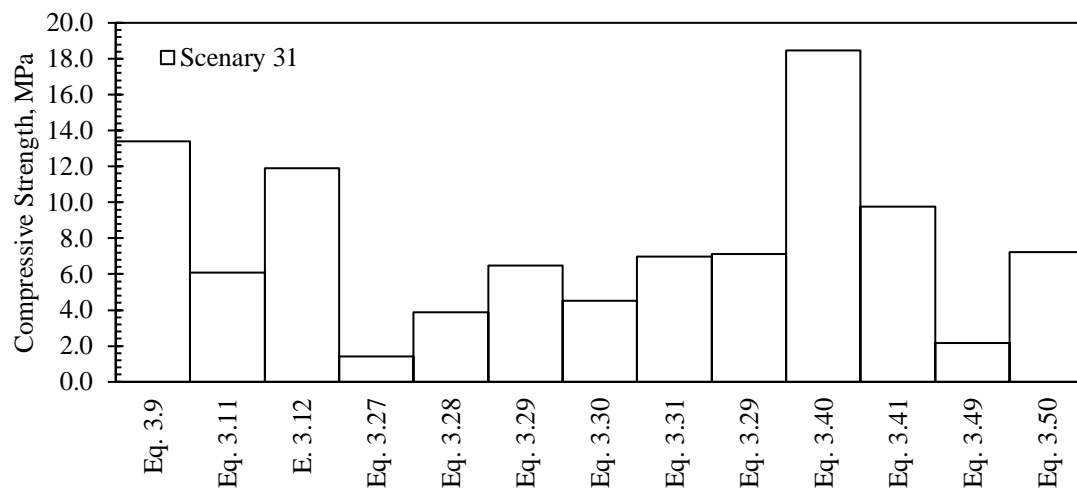


Source: elaborated by the author.

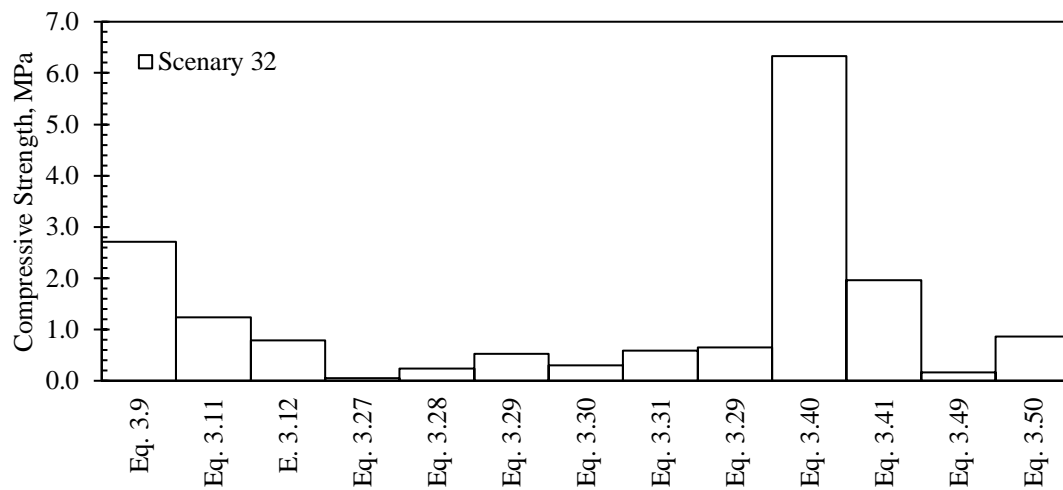
**Figure D.80** - Compressive strength calculated for scenario 30



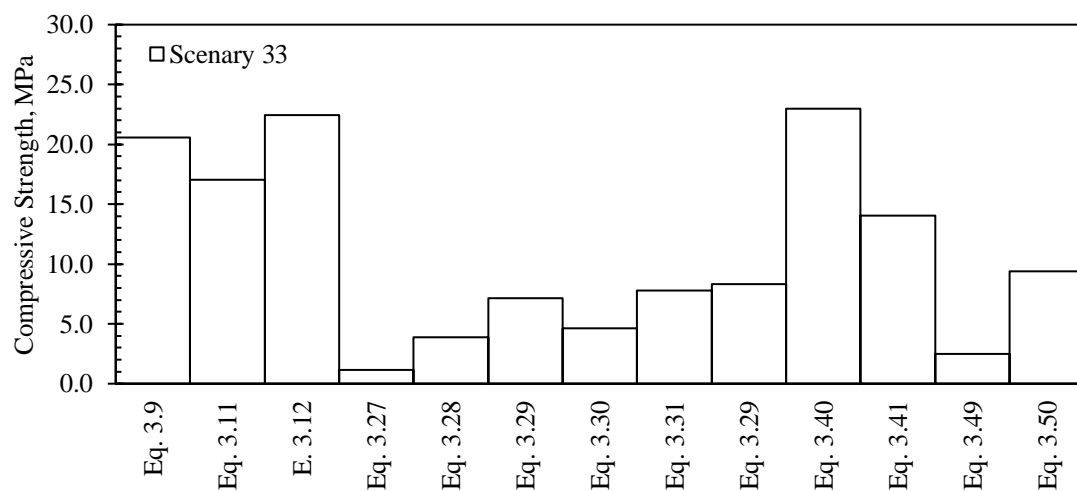
Source: elaborated by the author.

**Figure D.81** - Compressive strength calculated for scenario 31

Source: elaborated by the author.

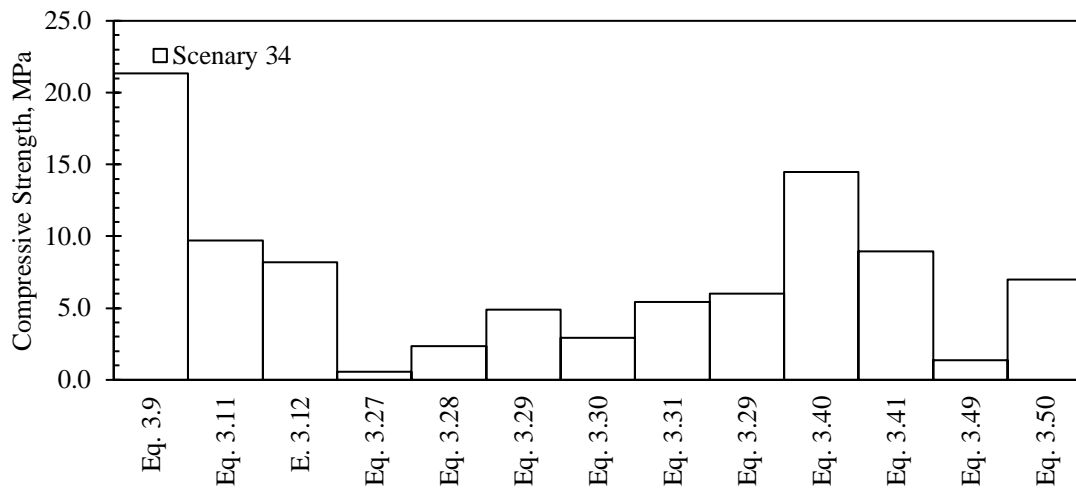
**Figure D.82** - Compressive strength calculated for scenario 32

Source: elaborated by the author.

**Figure D.83** - Compressive strength calculated for scenario 33

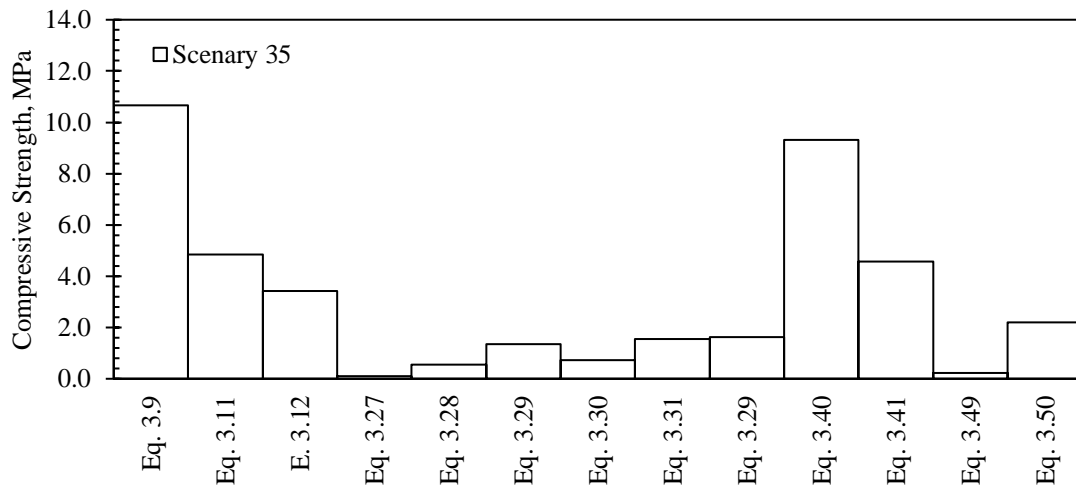
Source: elaborated by the author.

**Figure D.84** - Compressive strength calculated for scenario 34



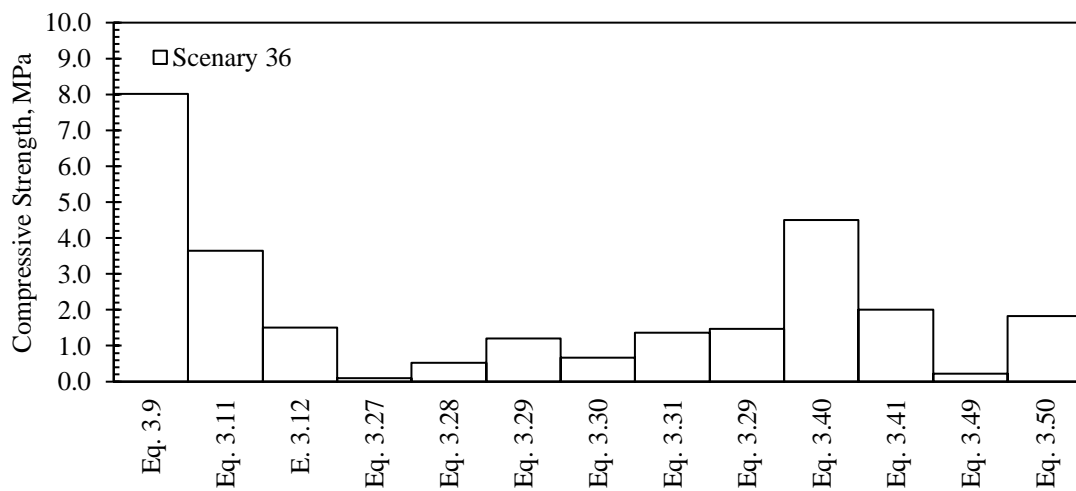
Source: elaborated by the author.

**Figure D.85** - Compressive strength calculated for scenario 35



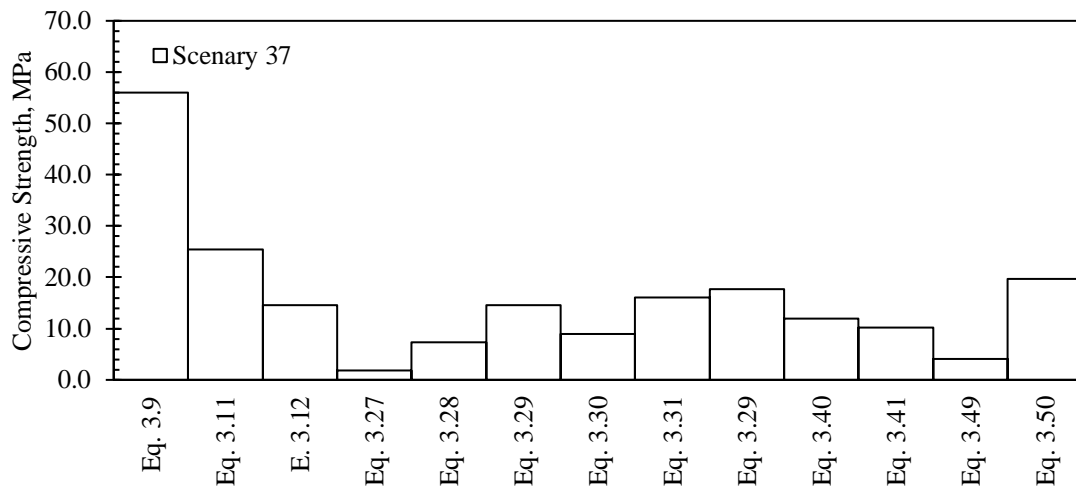
Source: elaborated by the author.

**Figure D.86** - Compressive strength calculated for scenario 36



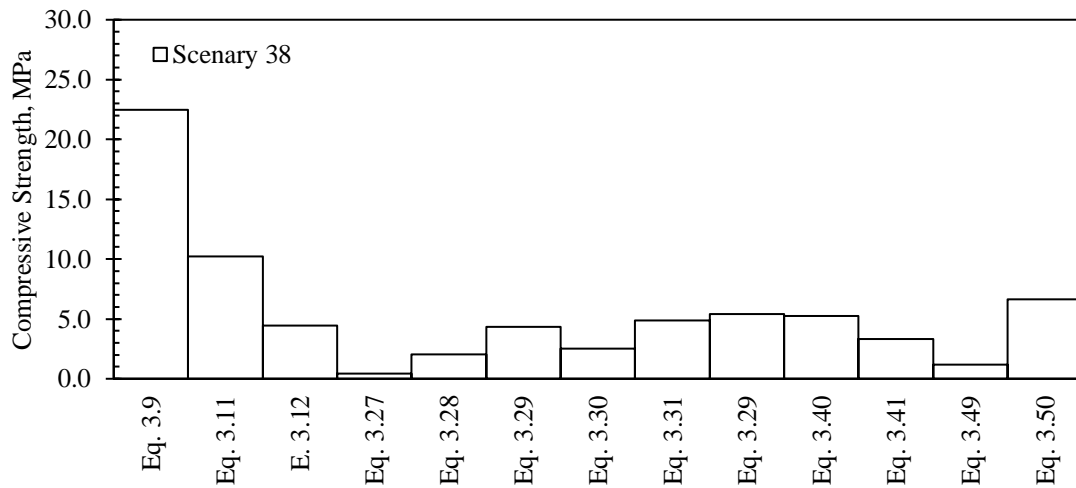
Source: elaborated by the author.

**Figure D.87** - Compressive strength calculated for scenario 37



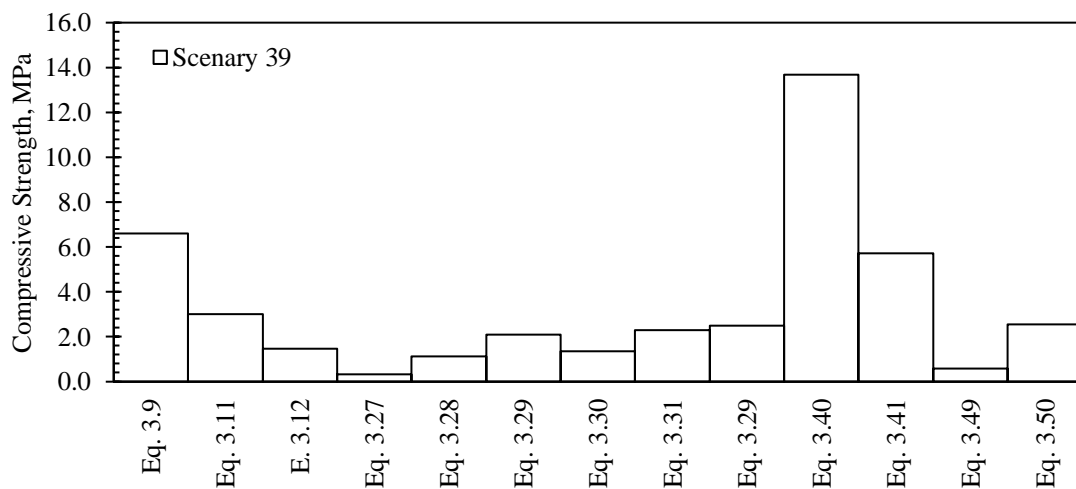
Source: elaborated by the author.

**Figure D.88** - Compressive strength calculated for scenario 38



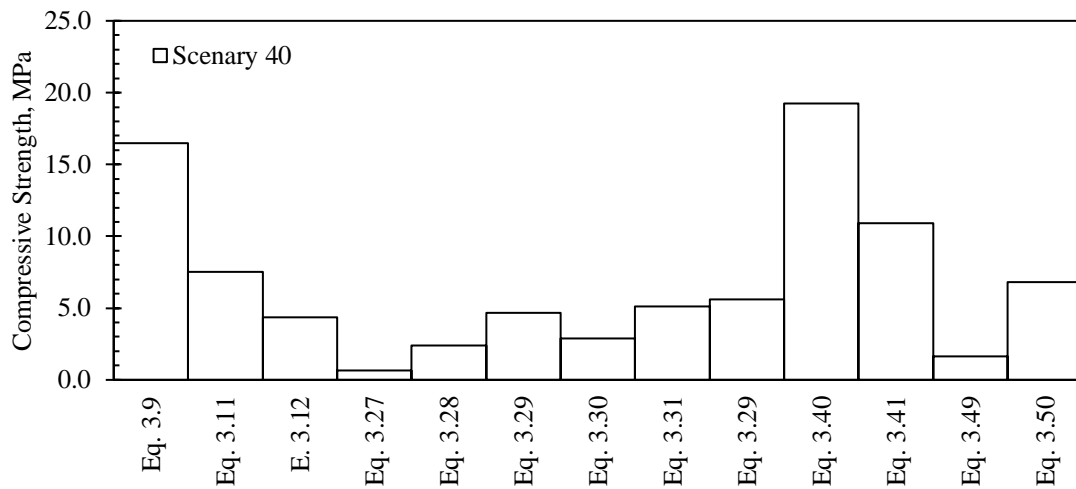
Source: elaborated by the author.

**Figure D.89** - Compressive strength calculated for scenario 39



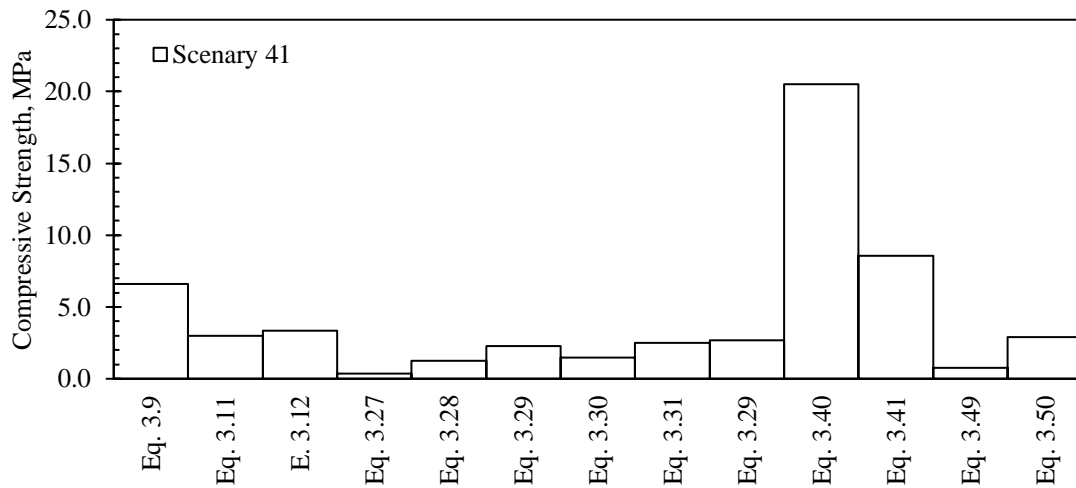
Source: elaborated by the author.

**Figure D.90** - Compressive strength calculated for scenario 40



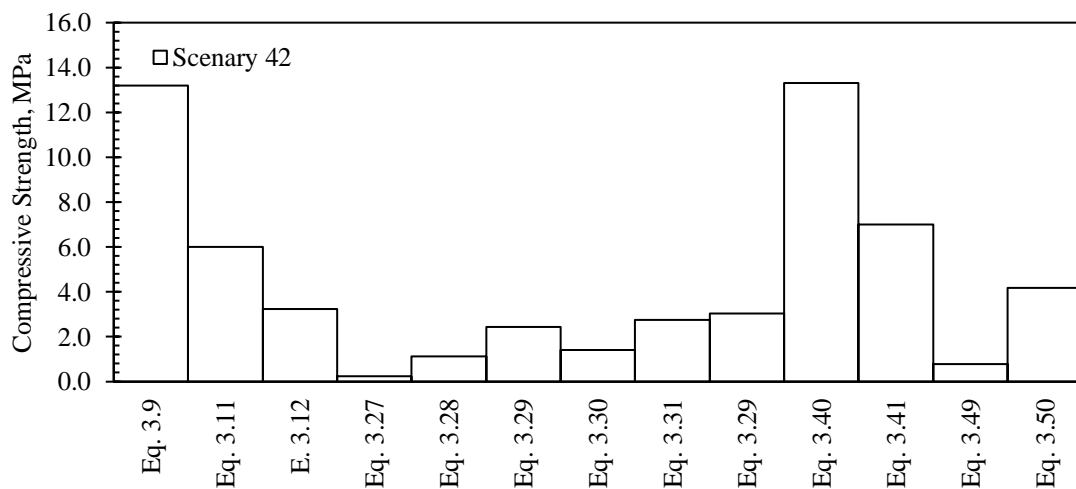
Source: elaborated by the author.

**Figure D.91** - Compressive strength calculated for scenario 41



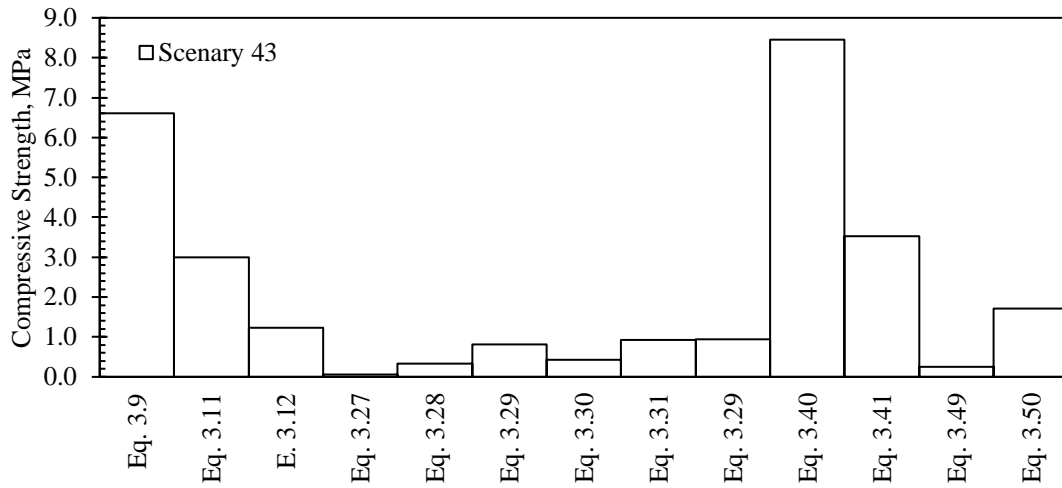
Source: elaborated by the author.

**Figure D.92** - Compressive strength calculated for scenario 42



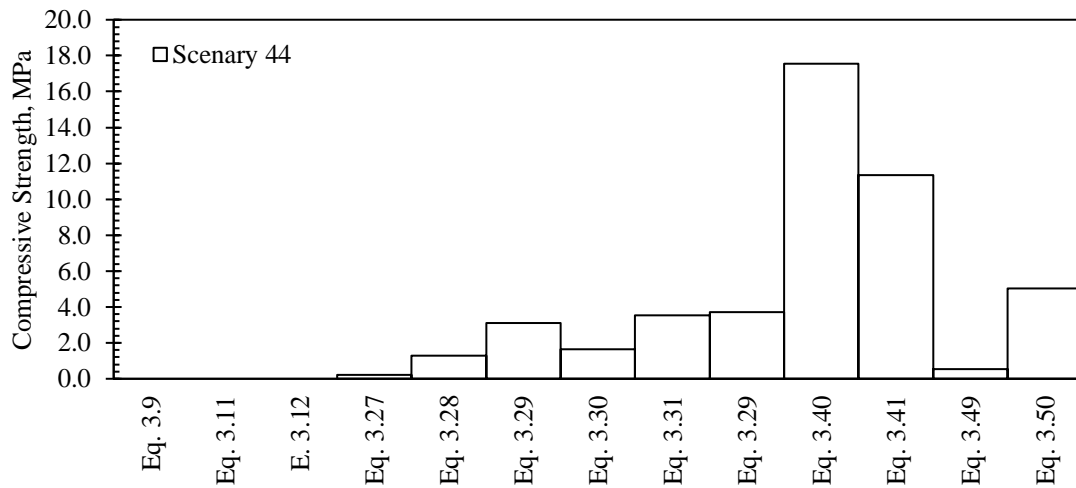
Source: elaborated by the author.

**Figure D.93** - Compressive strength calculated for scenario 43



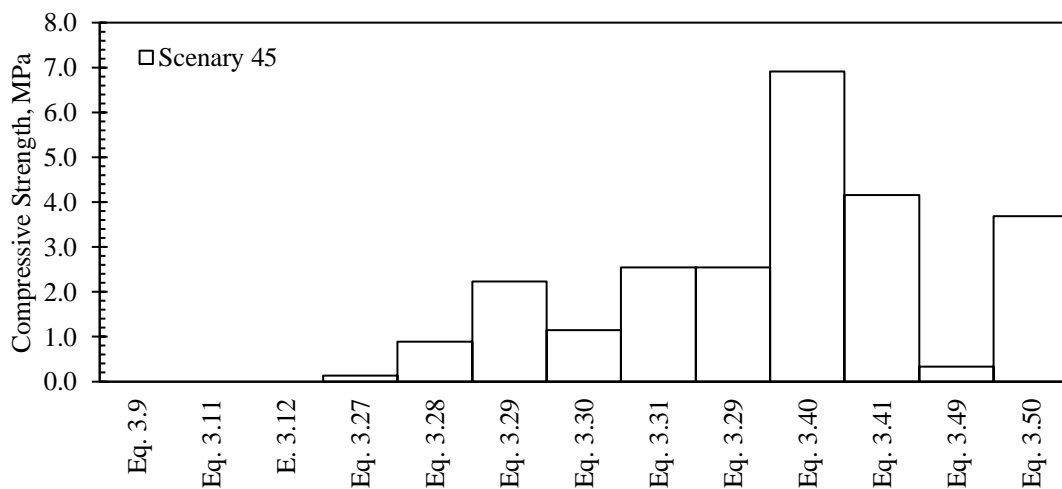
Source: elaborated by the author.

**Figure D.94** - Compressive strength calculated for scenario 44

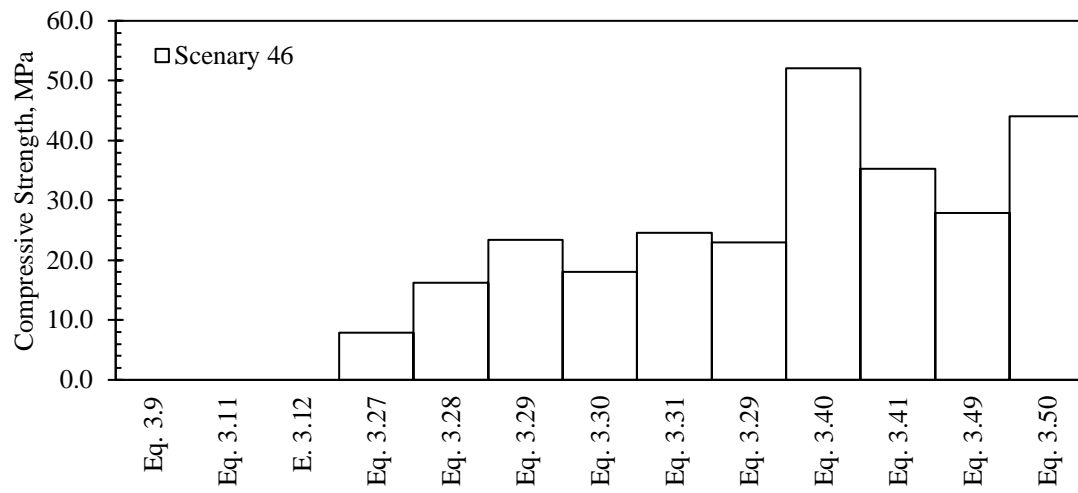


Source: elaborated by the author.

**Figure D.95** - Compressive strength calculated for scenario 45



Source: elaborated by the author.

**Figure D.96** - Compressive strength calculated for scenario 46

Source: elaborated by the author.



**APPENDIX E - MEAN AND MEDIAN RELATIVE ERROR – COMPRESSIVE STRENGTH**

**Table E.11** - Mean relative error (MRE) of SG-I group in percentage (from compressive strength estimated data)

Eq.\ Scenarios	S1	S4	S6	S13	S15	S18	S19	S20	S22	S27	S29	S32	S35	S36	S38	S43	S44	S45
<b>Eq. 3.9</b>	256.7	187.2	107.2	111.2	92.8	246.5	107.0	215.4	173.8	249.0	225.2	114.6	236.9	285.2	299.5	203.5	N/A	N/A
<b>Eq. 3.11</b>	62.2	30.5	-5.8	-4.0	-12.4	57.5	-5.9	43.4	24.5	58.6	47.8	-2.4	53.1	75.1	81.6	38.0	N/A	N/A
<b>Eq. 3.12</b>	-47.5	-35.6	-58.7	2.9	-23.9	4.5	-61.3	1.0	-22.2	-34.8	68.1	-37.2	7.9	-28.0	-20.8	-43.3	N/A	N/A
<b>Eq. 3.27</b>	-94.5	-95.6	-95.3	-97.0	-99.1	-96.1	-99.3	-97.1	-96.4	-97.5	-95.3	-95.8	-97.0	-95.3	-92.2	-97.5	-95.4	-94.2
<b>Eq. 3.28</b>	-72.7	-78.0	-79.3	-84.7	-93.4	-78.6	-94.6	-83.4	-81.2	-84.4	-76.4	-80.7	-82.3	-74.9	-64.2	-84.9	-73.2	-63.9
<b>Eq. 3.29</b>	-39.0	-50.9	-56.4	-65.4	-82.4	-49.9	-84.6	-59.7	-56.9	-60.7	-46.7	-58.4	-57.0	-41.9	-22.6	-62.8	-35.0	-9.3
<b>Eq. 3.30</b>	-65.7	-72.4	-74.4	-80.7	-91.2	-72.7	-92.7	-78.6	-76.2	-79.6	-70.2	-76.0	-77.2	-68.1	-55.3	-80.4	-65.5	-53.0
<b>Eq. 3.31</b>	-31.6	-44.9	-51.5	-61.1	-79.7	-43.4	-82.2	-54.3	-51.5	-55.1	-40.1	-53.6	-51.2	-34.5	-13.6	-57.7	-26.2	3.5
<b>Eq. 3.29</b>	-24.7	-39.4	-46.2	-57.3	-82.0	-39.0	-87.3	-52.2	-47.1	-55.1	-34.3	-48.6	-49.0	-28.9	-4.3	-56.4	-22.9	3.5
<b>Eq. 3.40</b>	127.4	210.6	388.7	326.1	558.7	143.0	634.1	236.3	261.2	200.0	112.8	401.5	194.6	116.3	-6.3	288.5	265.8	181.0
<b>Eq. 3.41</b>	-5.0	51.8	76.8	78.0	74.9	16.2	29.3	27.6	64.7	33.2	15.6	55.7	44.4	-3.6	-41.1	62.3	136.4	69.3
<b>Eq. 3.49</b>	-78.7	-74.6	-82.8	-71.3	-97.1	-84.3	-97.5	-85.7	-82.5	-80.5	-88.2	-87.2	-92.6	-89.0	-79.2	-88.1	-88.7	-86.5
<b>Eq. 3.50</b>	13.1	11.2	-22.4	3.3	-65.3	-3.9	-65.2	-12.5	-10.3	7.0	-18.4	-32.0	-30.8	-12.5	18.5	-21.2	4.6	49.7

The MRE was calculate using the following relation:  $MRE(\%) = 100 * (x_i + \bar{x})/\bar{x}$ , where  $x_i$  is the  $i^{\text{th}}$  estimated value and  $\bar{x}$  is the mean value.

N/A = Not Available (i.e., out of correlation range).

Source: Author (2018).

**Table E.12** - Mean relative error (MRE) of SG-II group in percentage (from compressive strength estimated data)

Eq.\ Scenarios	S2	S3	S6	S13	S15	S18	S19	S20	S22	S27	S29	S32	S35	S36	S38	S43
<b>Eq. 3.9</b>	108.9	218.7	117.0	88.8	91.6	122.2	103.7	238.4	216.7	191.9	197.9	250.1	98.1	143.0	52.4	192.2
<b>Eq. 3.11</b>	-5.1	44.9	-1.3	100.1	-12.9	1.0	-7.4	53.8	44.0	32.7	35.4	59.2	-9.9	10.5	-30.7	32.8
<b>Eq. 3.12</b>	-45.5	-34.2	-45.5	96.0	-12.1	37.5	26.0	-26.6	49.7	143.6	14.2	-9.1	-55.7	-35.9	-22.4	-28.5
<b>Eq. 3.27</b>	-95.9	-86.7	-95.8	-89.4	-87.3	-95.0	-90.1	-91.1	-93.8	-93.4	-92.1	-88.4	-90.4	-90.6	-91.4	-94.7
<b>Eq. 3.28</b>	-81.3	-51.3	-80.5	-67.9	-59.7	-77.8	-65.3	-62.4	-71.6	-70.9	-66.9	-54.4	-66.3	-64.8	-71.2	-75.2
<b>Eq. 3.29</b>	-59.5	-6.3	-58.0	-43.8	-27.7	-53.2	-34.9	-22.5	-38.6	-38.5	-31.8	-9.2	-36.7	-31.5	-47.1	-45.7
<b>Eq. 3.30</b>	-76.7	-41.3	-75.7	-62.3	-52.3	-72.6	-58.5	-53.8	-64.6	-63.9	-59.3	-44.5	-59.6	-57.4	-65.7	-68.9
<b>Eq. 3.31</b>	-54.8	2.8	-53.1	-39.1	-21.4	-47.9	-28.8	-14.1	-31.5	-31.6	-24.4	0.2	-30.8	-24.7	-42.3	-39.3
<b>Eq. 3.29</b>	-50.0	11.8	-48.0	-36.5	-17.1	-42.3	-23.3	-4.9	-24.1	-24.2	-16.3	10.1	-25.4	-17.8	-38.4	-32.8
<b>Eq. 3.40</b>	360.9	7.0	335.8	149.3	202.5	252.4	216.7	6.2	44.1	57.7	102.1	-25.7	310.8	183.5	374.0	194.9
<b>Eq. 3.41</b>	95.7	-29.3	93.5	19.2	56.5	70.0	53.1	-14.8	0.5	-9.0	24.8	-36.7	71.6	60.7	98.0	55.2
<b>Eq. 3.49</b>	-80.3	-68.1	-78.2	-81.4	-67.0	-80.3	-78.3	-60.5	-66.2	-83.7	-80.9	-74.4	-82.5	-75.6	-82.7	-82.5
<b>Eq. 3.50</b>	-16.4	31.9	-10.2	-33.0	7.0	-14.0	-12.8	52.2	35.5	-10.5	-2.4	22.7	-23.3	0.6	-32.6	-7.4

The MRE was calculate using the following relation:  $MRE(\%) = 100 * (x_i + \bar{x})/\bar{x}$ , where  $x_i$  is the  $i^{\text{th}}$  estimated value and  $\bar{x}$  is the mean value.

N/A = Not Available (i.e., out of correlation range).

Source: Author (2018).

**Table E.13** - Mean relative error (MRE) of SG-III group in percentage (from compressive strength estimated data)

Eq.\ Scenarios	S7	S8	S9	S10	S12	S14	S16	S23	S30	S31	S33	S46
<b>Eq. 3.9</b>	16.0	23.7	50.1	102.9	91.2	87.8	43.1	64.8	132.5	75.4	88.4	N/A
<b>Eq. 3.11</b>	39.6	34.4	77.1	144.7	107.7	-14.6	55.4	-25.1	5.7	-20.3	56.4	N/A
<b>Eq. 3.12</b>	24.8	27.6	57.8	119.0	97.2	52.2	47.6	1.9	82.8	55.4	105.8	N/A
<b>Eq. 3.27</b>	-93.3	-74.3	-68.1	-87.5	-87.4	-93.3	-79.8	-79.9	-84.6	-81.7	-89.3	-70.9
<b>Eq. 3.28</b>	-82.3	-48.6	-41.7	-67.7	-64.3	-74.2	-54.5	-46.8	-51.0	-49.2	-64.3	-40.3
<b>Eq. 3.29</b>	-71.1	-27.1	-21.0	-47.9	-39.7	-49.2	-31.5	-13.2	-12.3	-15.0	-34.6	-14.3
<b>Eq. 3.30</b>	-79.7	-43.2	-36.4	-63.0	-58.5	-68.7	-48.8	-38.9	-42.2	-41.1	-57.6	-33.8
<b>Eq. 3.31</b>	-69.0	-23.3	-17.5	-44.2	-35.0	-44.1	-27.4	-6.9	-4.6	-8.6	-28.7	-9.7
<b>Eq. 3.29</b>	-68.9	-28.7	-24.9	-44.4	-33.4	-38.7	-30.4	-6.6	0.7	-7.0	-23.9	-15.6
<b>Eq. 3.40</b>	435.6	133.0	43.8	91.7	38.3	212.3	127.2	158.5	32.1	141.3	110.6	91.1
<b>Eq. 3.41</b>	103.3	36.4	-8.8	8.7	-2.9	69.7	34.5	51.3	-4.3	27.6	28.5	29.3
<b>Eq. 3.49</b>	-88.8	-29.2	-27.4	-76.9	-40.9	-59.2	-44.6	-64.2	-68.4	-71.5	-77.3	2.5
<b>Eq. 3.50</b>	-66.1	19.3	17.0	-35.3	27.8	19.9	9.3	5.2	13.7	-5.2	-13.8	61.6

The MRE was calculate using the following relation:  $MRE(\%) = 100 * (x_i + \bar{x})/\bar{x}$ , where  $x_i$  is the  $i^{\text{th}}$  estimated value and  $\bar{x}$  is the mean value.

N/A = Not Available (i.e., out of correlation range).

Source: Author (2018).

**Table E.14** - Median relative error (MdRE) of SG-I group in percentage (from compressive strength estimated data)

Eq.\ Scenarios	S1	S4	S6	S13	S15	S18	S19	S20	S22	S27	S29	S32	S35	S36	S38	S43	S44	S45
<b>Eq. 3.9</b>	421.4	373.7	326.9	395.0	850.0	468.3	1060.4	560.0	417.8	677.8	395.0	317.4	560.0	442.1	404.1	595.9	N/A	N/A
<b>Eq. 3.11</b>	137.0	115.3	94.0	125.0	331.8	158.3	427.4	200.0	135.3	253.6	125.0	89.7	200.0	146.4	129.1	216.3	N/A	N/A
<b>Eq. 3.12</b>	-23.3	6.2	-14.9	141.0	275.2	71.4	116.8	111.4	47.1	45.3	155.9	22.2	111.4	1.3	0.0	30.0	N/A	N/A
<b>Eq. 3.27</b>	-91.9	-92.7	-90.3	-92.9	-95.3	-93.5	-96.1	-94.0	-93.1	-94.4	-92.9	-91.9	-94.0	-93.3	-90.2	-94.2	-93.4	-94.0
<b>Eq. 3.28</b>	-60.1	-63.8	-57.4	-64.1	-67.4	-64.9	-69.5	-65.3	-64.4	-65.1	-64.1	-62.6	-65.3	-64.7	-54.8	-65.3	-61.4	-62.8
<b>Eq. 3.29</b>	-10.9	-19.0	-10.1	-18.8	-13.1	-17.8	-13.8	-15.7	-18.6	-12.3	-18.8	-19.2	-15.7	-18.2	-2.3	-14.8	-6.3	-6.6
<b>Eq. 3.30</b>	-49.8	-54.4	-47.3	-54.7	-56.8	-55.2	-58.9	-55.3	-54.9	-54.6	-54.7	-53.4	-55.3	-55.1	-43.7	-55.1	-50.3	-51.6
<b>Eq. 3.31</b>	0.0	-9.1	0.0	-8.8	0.0	-7.1	0.0	-4.3	-8.3	0.0	-8.8	-9.7	-4.3	-7.8	9.0	-3.1	6.3	6.6
<b>Eq. 3.29</b>	10.1	0.0	10.9	0.0	-11.4	0.0	-29.0	0.0	0.0	0.0	0.0	0.0	0.0	0.0	20.8	0.0	11.1	6.6
<b>Eq. 3.40</b>	232.4	412.3	906.8	898.5	3146.2	298.6	4014.3	603.8	583.1	568.7	223.9	875.2	477.2	204.5	18.3	790.7	427.0	189.4
<b>Eq. 3.41</b>	38.8	150.3	264.3	317.1	762.1	90.6	624.8	167.1	211.4	196.8	75.9	202.7	182.9	35.7	-25.7	272.1	240.5	74.3
<b>Eq. 3.49</b>	-68.8	-58.1	-64.6	-32.8	-85.6	-74.3	-85.8	-70.1	-66.9	-56.5	-82.1	-75.0	-85.4	-84.5	-73.7	-72.8	-83.8	-86.1
<b>Eq. 3.50</b>	65.3	83.4	59.9	142.0	70.9	57.7	95.2	83.1	69.7	138.5	24.3	32.3	35.6	23.1	49.5	80.6	50.7	54.2

The MdRE was calculate using the following relation:  $MdRE(\%) = 100 * (x_i + x_{med})/x_{med}$ , where  $x_i$  is the  $i^{th}$  estimated value and  $x_{med}$  is the median value.

N/A = Not Available (i.e., out of correlation range).

Source: Author (2018).

**Table E.15** - Median relative error (MdRE) of SG-II group in percentage (from compressive strength estimated data)

Eq.\ Scenarios	S2	S3	S6	S13	S15	S18	S19	S20	S22	S27	S29	S32	S35	S36	S38	S43
<b>Eq. 3.9</b>	317.4	240.3	317.4	197.2	131.0	285.0	165.4	297.0	317.4	285.0	256.1	285.6	186.1	222.6	147.5	335.0
<b>Eq. 3.11</b>	89.7	54.7	89.7	215.0	5.0	75.0	20.7	80.5	89.7	75.0	61.8	75.3	30.1	46.7	12.5	97.7
<b>Eq. 3.12</b>	8.8	-29.7	4.8	208.7	5.9	138.2	64.2	-13.8	97.2	221.3	36.5	0.1	-36.0	-14.9	26.1	6.4
<b>Eq. 3.27</b>	-91.9	-85.8	-91.9	-83.4	-84.7	-91.3	-87.1	-89.5	-91.9	-91.3	-90.6	-87.2	-86.1	-87.5	-86.0	-92.2
<b>Eq. 3.28</b>	-62.6	-48.0	-62.6	-49.5	-51.4	-61.6	-54.8	-55.9	-62.6	-61.6	-60.5	-49.8	-51.3	-53.2	-53.2	-63.0
<b>Eq. 3.29</b>	-19.2	0.0	-19.2	-11.5	-12.8	-18.9	-15.2	-9.1	-19.2	-18.9	-18.5	0.0	-8.6	-9.1	-14.1	-19.2
<b>Eq. 3.30</b>	-53.4	-37.3	-53.4	-40.7	-42.5	-52.4	-45.9	-45.8	-53.4	-52.4	-51.4	-38.8	-41.7	-43.4	-44.3	-53.8
<b>Eq. 3.31</b>	-9.7	9.8	-9.7	-4.1	-5.3	-9.8	-7.2	0.7	-9.7	-9.8	-9.6	10.3	0.0	0.0	-6.3	-9.6
<b>Eq. 3.29</b>	0.0	19.4	0.0	0.0	0.0	0.0	0.0	11.5	0.0	0.0	0.0	21.3	7.8	9.2	0.0	0.0
<b>Eq. 3.40</b>	820.9	14.2	738.1	292.5	264.7	510.5	312.7	24.6	89.9	108.0	141.5	-18.2	493.3	276.4	669.8	339.0
<b>Eq. 3.41</b>	291.0	-24.6	272.0	87.7	88.7	194.5	99.5	0.0	32.4	20.0	49.2	-30.3	147.8	113.4	221.6	131.0
<b>Eq. 3.49</b>	-60.7	-65.9	-58.2	-70.7	-60.2	-66.0	-71.7	-53.6	-55.5	-78.5	-77.2	-71.9	-74.7	-67.7	-72.0	-74.0
<b>Eq. 3.50</b>	67.1	40.8	72.7	5.5	29.0	49.1	13.6	78.6	78.6	18.0	16.7	35.1	10.8	33.5	9.5	37.9

The MdRE was calculate using the following relation:  $MdRE(\%) = 100 * (x_i + x_{med})/x_{med}$ , where  $x_i$  is the  $i^{th}$  estimated value and  $x_{med}$  is the median value.

N/A = Not Available (i.e., out of correlation range).

Source: Author (2018).

**Table E.16** - Median relative error (MdRE) of SG-III group in percentage (from compressive strength estimated data)

Eq.\ Scenarios	S7	S8	S9	S10	S12	S14	S16	S23	S30	S31	S33	S46
<b>Eq. 3.9</b>	273.0	61.4	81.9	263.9	187.2	206.4	97.1	77.1	143.1	91.8	147.5	N/A
<b>Eq. 3.11</b>	348.9	75.3	114.7	338.9	212.0	39.3	114.1	-19.5	10.5	-12.8	105.4	N/A
<b>Eq. 3.12</b>	301.3	66.4	91.3	292.9	196.2	148.2	103.2	9.6	91.1	70.0	170.4	N/A
<b>Eq. 3.27</b>	-78.5	-66.5	-61.3	-77.6	-81.1	-89.0	-72.1	-78.4	-83.9	-79.9	-86.0	-66.9
<b>Eq. 3.28</b>	-43.1	-33.0	-29.3	-42.1	-46.4	-57.9	-37.3	-42.9	-48.8	-44.4	-53.2	-32.1
<b>Eq. 3.29</b>	-7.1	-4.9	-4.2	-6.6	-9.4	-17.2	-5.7	-6.8	-8.3	-7.1	-14.1	-2.6
<b>Eq. 3.30</b>	-34.5	-25.9	-22.9	-33.6	-37.7	-48.9	-29.5	-34.3	-39.5	-35.6	-44.3	-24.8
<b>Eq. 3.31</b>	-0.4	0.0	0.0	0.0	-2.3	-8.7	0.0	0.0	-0.3	0.0	-6.3	2.6
<b>Eq. 3.29</b>	0.0	-7.0	-9.0	-0.3	0.0	0.0	-4.1	0.4	5.2	1.7	0.0	-4.1
<b>Eq. 3.40</b>	1622.9	203.9	74.3	243.8	107.8	409.5	212.9	177.8	38.1	163.9	176.7	117.2
<b>Eq. 3.41</b>	553.9	77.9	10.6	94.9	45.9	176.8	85.3	62.6	0.0	39.6	68.8	47.0
<b>Eq. 3.49</b>	-63.8	-7.7	-12.0	-58.5	-11.2	-33.4	-23.8	-61.5	-67.0	-68.9	-70.2	16.5
<b>Eq. 3.50</b>	8.9	55.6	41.8	16.1	92.0	95.6	50.5	13.0	18.8	3.6	13.2	83.7

The MdRE was calculate using the following relation:  $MdRE(\%) = 100 * (x_i + x_{med})/x_{med}$ , where  $x_i$  is the  $i^{th}$  estimated value and  $x_{med}$  is the median value.

N/A = Not Available (i.e., out of correlation range).

Source: Author (2018).